Laboratoire d'Études Spatiales et d'Instrumentation en Astrophysique

HABILITATION À DIRIGER DES RECHERCHES

Présentée par
Thibault CAVALIÉ
LESIA - Observatoire de Paris

Millimeter/submillimeter observations and modeling of chemistry and dynamics in Giant Planet atmospheres

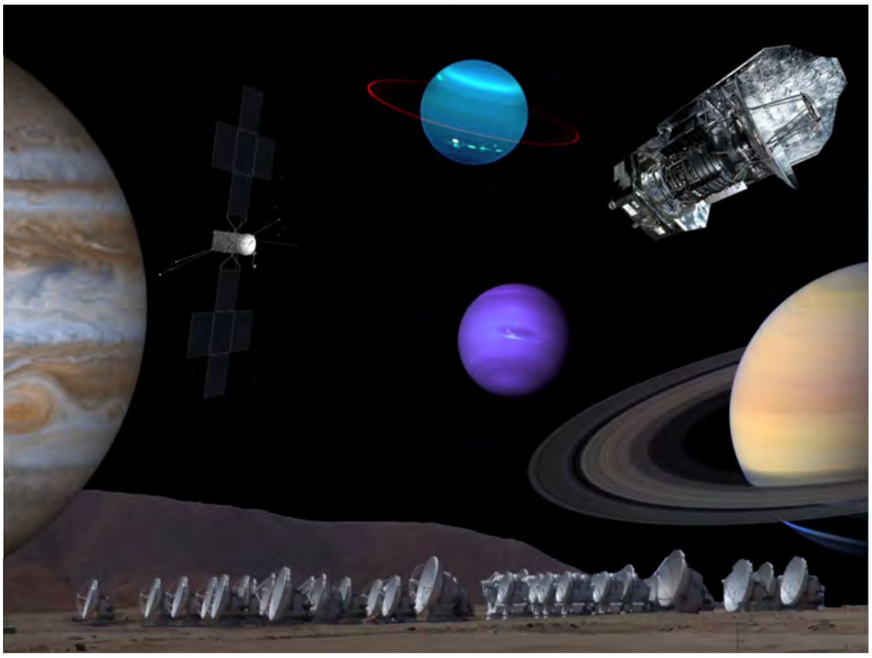

Soutenue le 27 Septembre 2018
Devant le jury composé de :

Benoît Mosser	Professeur, LESIA, Observatoire de Paris	Président
Jean-Christophe Loison	Directeur de Recherche, ISM, Université de Bordeaux	Rapporteur
Darrell Strobel	Senior Scientist, Johns Hopkins University	Rapporteur
Charlotte Vastel	Astronome, IRAP	Rapporteur
Sandrine Guerlet	Chargée de Recherche, LMD	Examinateur
Paul Hartogh	Senior Scientist, Max Planck Institut für Sonnensystemforschung	Examinateur
Olivier Mousis	Professeur, LAM	Examinateur
Aymeric Spiga	Maître de Conférences, LMD	Examinateur

Abstract

How did the Solar System Giant Planets form and how do they evolve?
We can obtain part of the answers to these outstanding questions with in situ measurements, remote sensing observations either with telescopes or planetary missions, and modeling. While more and more exoplanets are discovered every day and while we will better characterize them with new observatories like JWST, the planets of the Solar System remain our local laboratory for studying formation and evolution of such bodies. The (sub)millimeter domain, owing to the very high spectral resolution of the heterodyne technique and to the ever increasing spatial resolution and sensitivity of new observatories like ALMA, is suitable for determining planetary atmospheric composition and dynamics when coupled with appropriate radiative transfer, photochemical or thermochemical modeling.

In this habilitation thesis, I summarize 10 years of observations of the Solar System Giant Planets with ground-based and space-based observatories, like IRAM-30m, JCMT, Odin, Herschel, and more recently ALMA. With thermochemical modeling of the deep tropospheres of the Giant Planets, I have participated in trying to establish their deep composition to constrain their formation processes. The next natural step is the participation in an atmospheric probe proposal for the Ice Giants, and the development of its mass spectrometer, in preparation for a NASA-ESA joint flagship mission to these distant worlds. With time-dependent 1D or 2D photochemical modeling, I have contributed to a better understanding of how the composition and chemistry in the stratospheres of the Giant Planets are altered by seasons and external sources. With ALMA, it is now possible to measure directly winds in the stratospheres of the Giant Planets to constrain their stratospheric circulation. Our first Jupiter and Saturn map will contribute to this effort. In a decade from now, the european JUICE mission to Jupiter and its moons will enable me to monitor Jupiter's atmosphere with the SWI instrument, both in terms of chemistry and dynamics, and with spectral and spatial resolutions and temporal coverage never achieved before.

Acknowledgments

I would like to thank all the jury members for accepting to evaluate my work, Benoît Mosser for accepting to preside this jury, and Charlotte Vastel, Darrell Strobel and Jean-Christophe Loison for their review. I am glad I could bring together world experts to cover each aspect of my scientific activities: Sandrine Guerlet, Charlotte Vastel, Darrell Strobel and Paul Hartogh for observations, Jean-Christophe Loison, Olivier Mousis and Aymeric Spiga for modeling, and Darrell Strobel, Paul Hartogh and Olivier Mousis again for space missions.

My gratitude goes also to Raphael Moreno, Emmanuel Lellouch and Thierry Fouchet for the friendly working atmosphere in Meudon and for the top-level science discussions we have had over the years. I will miss working on a daily basis with such a great team. I will not forget that Thérère Encrenaz has conveyed her passion for observations to me at the very start of my PhD thesis at the IRAM-30m. This certainly was a cornerstone in my career. Without Pierre Drossart, this habilitation thesis manuscript would not (yet) exist. He encouraged me to start its preparation when I joined LESIA.

The present manuscript tries to capture and summarize a 10 year journey in planetary sciences that started after the completion of my PhD. This journey would never have been possible without the continued trust over the years of my PhD advisors Françoise Billebaud and Michel Dobrijevic and two-times postdoc advisor Paul Hartogh.

I am also grateful to be working with my friends Olivia Venot, Ladislav Řezáč and Vincent Hue, who have been kind enough to convince me I could understand their models and involve me in their work. I am really happy Olivia could enter CNRS one year ago, and I am amazed of the trajectory Vincent is currently taking. He started as a brilliant PhD student six years ago, and he is now an even more brilliant research scientist who has established himself as an expert in photochemical modeling and UV observations (not mentioning his work on planning and calibrating Juno/UVS observations). No wonder his colleagues at SwRI do not want him to leave! I wish him the best for the years to come. So do I regarding Ladi and his lovely family.

I have been working in several teams in the past 10 years. I can only be thankful for all the things I have learned regarding planetary sciences, observations, instrumentation, modeling, project management, etc., from the people composing these teams, especially the HssO, SWI, and Hera teams.

More generally, I wish to thank all my collaborators, including the engineers, technicians and people from the administrations. Science could not work without them.

Last but not least, I would like to thank my wife, children and family for their continued support, understanding, and love. At last, we are reunited after so many years. This habilitation thesis is dedicated to them.

Contents

Curriculum Vitæ

Personal details

Name	Thibault Cavalié
Date of birth	August 8, 1982
Place of birth	Talence, France
Family status	Married, 2 children
Languages	French, English, German
Address	LESIA – Observatoire de Paris-Meudon, 5 place Jules Janssen, 92195 Meudon
Phone	+33.(0)1.45.07.77.94 / +33.(0)7.86.09.44.30
Email	thibault.cavalie@obspm.fr
Website	https://sites.lesia.obspm.fr/thibault-cavalie/

Work experience

2015-present	CNRS scientist (Chargé de Recherche) at the Laboratoire d'Études Spatiales et d'Instrumentation en Astrophysique (LESIA)
2013-2015	Postdoc, Max Planck Institute for Solar System Research (MPS, Germany) Title: Preparation of JUICE/SWI Funding: MPS Supervisor: P. Hartogh
2010-2013	Postdoc, Laboratoire d'Astrophysique de Bordeaux (LAB) Title: 2D photochemical modeling of Giant Planet atmospheres in the framework of the Herschel HssO program Funding: CNES, ERC E_3ARTHS, Fondation des Amis des Sciences Supervisors: M. Dobrijevic and F. Selsis
2008-2010	Postdoc, MPS Title: Observations of the Giant Planets with Herschel Funding: MPS, Deutsche Forschungsgemeinschaft (DFG) Supervisor: P. Hartogh
2005-2008	PhD student, LAB Title: Observations millimétriques et submillimétriques des composés oxygénés dans les atmosphères planétaires. Préparation aux missions Herschel et ALMA Funding: Ministry of Research Supervisors: F. Billebaud and M. Dobrijevic

Responsibilities

Missions Co-I of the Submillimetre Wave Instrument (SWI) of the JUICE mission
Co-I of the ESA-M5 mission proposal "Hera Saturn probe" (not selected)

Observations PI of 4 ALMA programs
PI of 2 Herschel Open Time programs
PI of 10 other programs (SMA, IRAM-30m, JCMT)
co-I of 8 programs (ALMA, Herschel, SOFIA)
Associate scientist of the Herschel HssO Key Program
Associate scientist of the JWST Early release Science program "The Jovian System"

Coordination Co-lead of ESA Working Group "Jovian atmosphere" (JUICE mission)
Lead of SWI Working Group "Jovian atmosphere" (JUICE mission)
Chair (2015) and Deputy Chair (2014) of the CASA Users Committee
SOC/LOC of the SWI Science consortium meeting #1 (Bordeaux, 03/2015)
SOC/LOC of the HssO Team Meeting (Bordeaux 09/2011, Lindau 12/2008) and of the HssO/TNOs Meeting (Lindau 06/2009)
SOC/LOC of the Young European Radio Astronomers Conference 2007 (Carcans, France)

Education

2008 PhD in Astrophysics, Bordeaux University (UB)

2005 Master 2 Research in Astrophysics, UB

2000 Baccalaureate in Science, Lycée Jean Moulin, Langon

Prizes and Awards

2011 Best poster, Journée de l'Institut de Physique Fondamentale, UB

2005 University fellowship for best students, UB

2005 "Prix de la Ville de Pessac aux Étudiants", City of Pessac

2002 Janus programme fellowship, IN2P3

Research

Themes Formation of the Giant Planets

- What are the physico-chemical conditions for the formation of planetesimals?
- Under which process did the primordial ices condense?

Spatio-temporal evolution of the Giant Planet atmospheres

- What are the interaction between the Giant Planets atmospheres and their environment?
- How do seasons and dynamics influence the atmospheric composition of Giant Planets?

Dynamics of the Giant Planet atmospheres

- Do the tropospheric winds extend to the stratosphere?
- What is the origin of the atmospheric oscillations of Jupiter and Saturn?

Expertise Ground- and space-based (sub)millimeter observations
Radiative transfer modeling in 3D ellipsoidal geometry
Photochemical modeling of upper atmospheres
Thermochemical modeling of deep atmospheres
Science implementation of a space mission

Publications 36 refereed publications, 10 as 1st author, 4 highlights in A&A
38 conference papers as 1st author, 4 invited talks
7 Minor Planet Center Circulars (astrometry of asteroids)
Reviewer for Icarus, A&A, The Astrophysical Journal, and Planetary and Space Science

Teaching

Supervision of students

PhD thesis V. Hue (LAB), 2012-2015. Title: “Modélisation physico-chimique 3D des atmosphères des planètes géantes”

Master

1. Y. Guimard, 2018, Master 1 Informatique des Organisations, PSL Research University, 2 months. Title: “Optimisation d’un code de modélisation atmosphérique des planètes géantes”
2. L. Brouillard, 2018, Licence 3 Physique, UB, 5 weeks. Title: “L’abondance interne de l’eau dans les planètes géantes Uranus et Neptune”
3. S. Cuzacq, 2018, Master 1 Physique, UB, 2 months. Title: “Modélisation du spectre submillimétrique de l’atmosphère de Titan dans le contexte d’Herschel et d’ALMA”
4. K. Bermudez-Diaz, 2018, Master 2 Physique, University of Montpellier (UM), 4 months. Title: “Évolution temporelle de l’abondance de l’eau dans la stratosphère de Jupiter”
5. S. Branchu, 2014, Master 1 Physique, UB, 2 months. Title: “Modélisation du spectre submillimétrique de l’atmosphère de Titan dans le contexte d’Herschel et d’ALMA”
6. V. Hue, 2012, Master 2 Astrophysique, UB, 4 months. Title: “Modélisation physico-chimique 3D des atmosphères des planètes géantes”
7. U. Hincelin, 2008, Master 1 Physique, UB, 3 months. SFP Prize “Stage de Master 1 de Physique”. Title: “Propriétés observables des atmosphères de Jupiters froids autour d’autres ̀etoiles”

8. É. Bernard, 2007, Master 2 Pro Informatique pour les Sciences, UM, 6 months. title: “Validation et optimisation d’un code de transfert radiatif infrarouge pour les planétes géantes”
9. A. Dubrouil, 2006, Master 1 Physique, UB, 3 months. Title: “Les composés oxygénés dans les atmosphères des planètes géantes et leur observabilité”

University teaching

2010-2015	Part-time teacher (8hrs/year)
2005-2008	Part-time teacher “Moniteur du CIES” (64h/year)
2002-2004	Tutor
Topics	Initiation à l’Astrophysique (CM), Optique Géométrique (CM, TD, TP), Mécanique du point (TP), Méthodologie (TD), Projet Professionnel (TD) for Licence student

Outreach

Schools Interactive lectures from 1st to 5th grade (CP–CM2) in the elementary school of Cabanac-et-Villagrains (France), 2018
Project referent for the 1st grade class in the elementary school of Cabanac-et-Villagrains (France), 2018. Project awarded with the 2018 SF2A “Découvrir l’Univers” Prize.
Conferences in middle and high schools of Aquitaine (Lycée Max Linder in Libourne in 2008, Collège Léo Drouyn in Vérac in 2012)

UTL Coordinator of the “Université du Temps Libre d’Aquitaine – Astronomie” (UTL), 2011-2016
UTL lecturer (2x2hrs in 2005-2006, 3x2hrs/yr in 2006-2008 and 2010-2016)
UTL observation tutor (6-8x2hrs/yr in 2005-2008 and 2010-2016)
Topics: La recherche de l’eau sur Mars, les exoplanètes, l’observation millimétrique des planètes, les atmosphères planétaires, la Grande Tempête de Saturne de 2010-2011, Pluton, la Machine d’Anticythère, la conquête spatiale, l’eau dans le Systéme solaire, la mission JUICE, le programme HssO, Observer dans un observatoire professionnel, la radioastronomie

Astronomy clubs Conferences in amateur astronomy clubs: Jalles Astro (2008, 2012 and 2014), Observatoire de Dax (2013 and 2016), Rencontres Astronomiques de Classun (2011)

Learned societies Conferences in learned societies: Société Française de Physique (2014), Société Astronomique de Nantes (2014), Société Astronomique de Bordeaux (2008 and 2014)

Other conferences Herschel Day at the Bordeaux University (2009), Association Universitaires d’Astronomie (2018)

Open days Open days at LAB (2007, 20011, 2013) and MPS (2009)

Observatory visits Bordeaux observatory visits (2005-2008, and 2010-2013)

Accompanying note

Foreword

In this accompanying note, I present a summary of my career history to put into perspective how I have developed and conducted my research so far, my services to the community, as well as supervision of students, teaching, and outreach activities.

Note: All acronyms not explicitly defined in the text can be found in Appendix C.

"Come on, let's go space truckin' "
(Deep Purple)

Introduction

My interest for the Solar System started back to my youth and is tied to space exploration and amateur astronomy. I was captivated by the first incredible images of the Outer Solar System taken by the Voyager 2 mission and the new images of Mars when the space exploration of the red planet resumed in the nineties. I would also be looking for all kind of space conquest documents (books, biographies, documentaries, movies, etc.). Like many other professional astronomers, I started in amateur astronomy and joined a local club in the mid-nineties. I was the annoying kid who always wanted to look at planets and who had a more limited interest for the deep sky... The nineties were incredibly dense in terms of observable events in the Solar System and space exploration that would keep me thrilled for the years to come: the Shoemaker-Levy 9 impacts, comets Hale-Bopp and Hyakutake, the 1999 solar eclipse in France, the first Mars rover, Mars Global Surveyor, and the launch of Cassini-Huygens. All these events have kept me excited about the Solar System and all amateur observations I made during that time probably explain my primary interest for observations rather than modeling.

Even if I had no idea until very late in my studies what job I wished to do, I always had space exploration and planetary sciences somewhere in the back of my head. I remember a day in last year in middle school when I first had to write down on a form what I wanted to do for a living. I wrote down "astrophysicist", even though I had not a clue what it meant... Years later, for my first internship (during my second year at university), I gave a try at something different from planetary sciences. I worked for a couple of months in the astroparticle group of the CENBG laboratory, observing and analyzing Cherenkov emissions from the Crab Nebula. This was a confirmation that nothing would get me more interested in sciences than planets. I was very lucky to find a friendly and enthusiastic group of scientists at LAB that understood my interest, took me under its wings for two additional undergraduate internships, and finally proposed me a thesis subject that was different from anything I would have expected in the first place. Even if observations were a central part of my subject, "nice" images of the planets were indeed quite rare in the (sub)millimeter domain ten years ago, as a big limitation for planetary observations was spatial resolution. However, the perspective of working with a space observatory like Herschel and getting among the first images of the planets with ALMA in a not so distant future was always a great motivation. For the time being, I would benefit from the very high spectral resolution offered by heterodyne spectroscopy to characterize planetary atmospheres, in terms of composition and dynamics.

PhD thesis at LAB

I started my PhD in 2005 in the Planetology Team of LAB, under the supervision of Françoise Billebaud and Michel Dobrijevic. Anticipating the arrival of the revolutionary observatories that Herschel and ALMA would be for the (sub)millimeter domain, the Planetology Team wished to develop an observational counterpart to its photochemical modeling work. My main task was therefore to get prepared for Herschel and ALMA observations of the Solar System planets. I have developed my observational and radiative transfer expertise in the (sub)millimeter domain leading several observation projects from the ground with the IRAM-30m and at the JCMT (Cavalié et al., 2008a,b, 2009), and with the Odin space telescope (Cavalié et al., 2008c). With these observations, I started studying the origin of water in the stratosphere of Jupiter and obtained the first submillimeter observation of CO in Saturn.In parallel, I have participated in the preparation of the Herschel HssO Key Program (PI P. Hartogh, MPS) by providing numerous observation simulations of the Giant Planets. My effort was rewarded when I was offered the chance to lead one of the science themes of the project. Because my long term goal was to get ready for spatially-resolved observations of the Giant Planets, I chose the theme: "Spatial distribution of water in Jupiter and Saturn". The observations of this theme were the most exciting in my opinion and would force me to prepare the software tools to simulate and analyze such data.

Between 2005 and 2008, I have also been a part-time teacher ("Moniteur") at the Bordeaux University (64hrs/year). During my PhD thesis, I have given lectures in physics and astronomy, and overseen tutorial and practical classes in physics. I have also supervised three undergraduate students during their Master 1 and Master 2 internships. I had them work on various topics which are listed in my CV. All of them completed their work packages. I have continued teaching at the Bordeaux University during my CNES and 2nd MPS postdocs (see below).

Postdoc at MPS

After the completion of my thesis in October 2008, I joined the microwave group of P. Hartogh at MPS in Lindau (Germany) for a first postdoc, to be in the core of the HssO group and as close as possible to the HssO data. I started with the coordination of the paper presenting the HssO program (Hartogh et al., 2009), additional observation preparation (Sagawa et al., 2010), and with more ground-based observations with the JCMT (Cavalié et al., 2010). It was also the time when I joined the Submillimetre Wave Instrument (SWI) project as co-I in the framework of what would become the JUICE mission (Jupiter Icy Moons Explorer), and contributed to the instrument design and development study. This enabled me to fulfill another of my personal goals: to work on a space mission! While I was contributing to papers on the first results of the HssO program on Mars, Saturn and Neptune (Hartogh et al., 2010c,a,b, 2011; Swinyard et al., 2010; Lellouch et al., 2010) and to the HIFI inflight calibration paper (Roelfsema et al., 2012), I started collecting the Jupiter and Saturn water maps I was in charge of. In parallel of the data analysis itself for which I had already developed the relevant radiative transfer tool, and because there were no spatially-resolved photochemical models that would help me interpret the data later on, I proposed a new project in the framework of a CNES fellowship with the aim of developing an altitude-latitude photochemical model for the Giant Planets.

CNES postdoc at LAB

I obtained a CNES postdoc fellowship to return at LAB at the end of 2010 and start the development of a 2D photochemical model. The choice of the LAB was guided by the already existing expertise in photochemistry (M. Dobrijevic) and dynamics (F. Hersant). Before putting together the model, we completed a mandatory first step which consisted in reducing the large chemical schemes of 1D models to make computational time for a 2D model reasonable (Dobrijevic et al., 2010, 2011). In parallel, I obtained my first ALMA spatially-resolved map of Saturn (to study Saturn's 2010-2011 Great Storm) and this underlined even more the need for such kind of model. I also managed to publish a follow-up study to my initial observations of water in Jupiter with Odin (Cavalié et al., 2012a) and the Herschel water maps of Jupiter (Cavalié et al., 2013).

Co-supervision of V. Hue's PhD thesis

In the spring of 2012, M. Dobrijevic and I had co-advised V. Hue, a brilliant student, for his undergraduate internship. Our initial development results, my fresh ALMA data, and the interest shown by V. Hue (and his excellent results at the university), triggered the start of a PhD thesis. I have been extremely lucky to co-supervise the thesis of V. Hue on the development of the 2D model. He managed to complete the development in a very short time (less than a year), such that he could even add a time dimension to the model to make it seasonal. Despite the lack of spectacular results in the first papers using a simplified version of this model on Saturn (Hue et al., 2015, 2016), the next one on Jupiter (Hue et al., 2018), only recently published, paves the way for future research on Jupiter's dynamics and auroral chemistry.

During his PhD, he won a fellowship to visit a foreign institute and I strongly encouraged him to visit SwRI as I had started working with T. Greathouse (SwRI) on my Herschel data interpretation. Among many other projects, T. Greathouse is conducting a long-lasting temperature mapping of Jupiter and Saturn and he has developed a climate model for Saturn. V. Hue was therefore be able to couple the required thermal modeling with his own model. He visited SwRI for 6 months in 2014 and he started a fruitful collaboration with T. Greathouse. This collaboration, combined with his need to understand the auroral chemistry of Jupiter, led him to apply for a postdoc position on Juno/UVS data analysis at SwRI. He got a position at the end of 2015 and he even got promoted Research Scientist in 2018 at SwRI. He is still analyzing Juno/UVS data and improving his 2D seasonal model.

Back to MPS

In 2013, i.e. before the end of V. Hue's PhD thesis, my contract at LAB was coming to an end. I contacted P. Hartogh to ask him for a new postdoc at MPS, centered on the preparation of JUICE/SWI this time. At the end of 2013, I returned to MPS to continue working on the Herschel data and to start the science preparation of SWI. In my two years at MPS, I published the first detection in the submillimeter range of CO in the stratosphere of Uranus with Herschel (Cavalié et al., 2014), demonstrating it has an external source, and a photochemical study on the chemical response to the temperature increase in Saturn's hot stratospheric vortex following the Great Storm of 2010-2011 (Cavalié et al., 2015). In this time frame, I also joined the Hera Science Definition Team and co-proposed this mission to ESA for the M4 mission (Mousis et al., 2014). It was not selected at this time and we reworked the project (Mousis et al., 2016) to submit it to ESA for the M5 slot. I also managed to complete the upgrade of my radiative transfer code to a new version that accounts for the ellipsoidal geometry of giant planets. This code can simulate (sub)millimeter observations and maps for any geometry, spectral and spatial resolution. It can also produce fits files for ALMA mapping simulations with CASA. I use this code routinely ever since and I managed to win 3 ALMA proposals in Cycle 4 and 5, and contributed to another successful one in Cycle 5.

After my successful application at CNRS for a permanent position scientist in the Spring of 2015, I was appointed as co-lead of the JUICE Working Group "Jovian atmosphere" by the JUICE Project Scientist (O. Witasse).

CNRS position at LESIA

I joined LESIA and its Planetology group on October 1st, 2015. My main research topics are the formation of the Giant Planets, and the chemical, dynamical and seasonal evolution of their atmospheres. I continue to use (sub)millimeter observations as a baseline of my work, and I am now involved in thermochemical and photochemical modeling of the Giant Planets. For instance, I have coordinated a study on the modeling of the deep composition of Uranus and Neptune (Cavalié et al., 2017b). In parallel, I am deeply involved in the science preparation of the JUICE mission, with the coordination of the "Jovian atmosphere" Working Group with L. Fletcher (Leicester University), and of SWI. My role in the SWI consortium during the implementation phase is threefold: observation plan optimization, operational script development and validation, and ground calibration.

In 2018, I have advised and co-advised several undergraduate students. K. Bermudez (Montpellier University) has worked on the calibration and analysis of the data from our Odin temporal monitoring of water in the stratosphere of Jupiter. He was supervised by N. Biver (LESIA) for the data calibration. S. Cuzacq (Bordeaux University) has successfully adapted my radiative transfer model to Titan. The ASP Team will now be able to propose and analyze Titan observations and confront observations to its photochemical model simulations. L. Brouillard (Bordeaux University) has applied our thermochemical model to Uranus and Neptune with a chemical scheme in which the methanol block has been fully updated by R. Bounaceur (LRGP). The goal was to compare with our previous results and assess the impact of the update on our former conclusions on deep water abundances in these planets. Y. Guimard (Paris Dauphine University) is working (at the time of writing) on the optimization of our photochemical and thermochemical codes with the aim of parallelizing them.

With this continued will to be involved in space missions, I have been working for several years in the Hera mission proposal to send an atmospheric probe to Saturn. Unfortunately, and despite a high scientific merit, it has recently been declined by ESA for its M5 mission, mostly for programmatic reasons: there is no foreseen mission that could carry the probe to Saturn and serve as relay in the timeframe of the M5 mission. Now, the goal of our team is to adapt the concept of Hera to the exploration of Uranus and/or Neptune in the frame of an anticipated ESA-NASA joint flagship mission. We have recently published the science goals of a Hera probe adapted to the Ice Giants (Mousis et al., 2018). In 2018, and for family reasons, I have asked CNRS for returning to LAB. It has been approved and should be effective on September 1st, 2018. Following my application and a subsequent decision of the Paris Observatory Scientific Council, I will remain affiliated to the Paris Observatory at least until the end of 2020, and plan to as for renewal of this affiliation when required to keep strong ties with the LESIA Planetology Team. Now, in the frame of my return to Bordeaux, I have proposed a hardware contribution of the LAB Electronics Team to the Hera Mass Spectrometer that would be led by P. Wurz (Bern University). LAB would therefore design and produce the electronics and firmware of the mass spectrometer and I would continue to participate in the science. The mass spectrometer data would actually provide me with ground truth measurements I could compare with my thermochemical model predictions (e.g. Cavalié et al. 2017b).

Service to the community

In 2014, I have been nominated as representative of the european ALMA community in the first CASA Users Committee by B. Glendenning, Director for Data Management and Software at NRAO (Socorro). I have served the ALMA and VLA observer communities within this committee for three years, including as Deputy Chair in 2014 and Chair in 2015. The tasks of this committee were to (i) collect user concerns and needs, (ii) assess the capabilities, usability, reliability, and performance of CASA, and (iii) propose development priorities.

As mentioned above, I have been involved in the implementation of the JUICE/SWI instrument since its selection in 2013. In the Spring of 2015, I have been nominated as “Jupiter atmosphere” Working Group co-lead for the JUICE mission by O. Witasse, the JUICE Project Scientist. My past, current and future work regarding the implementation of JUICE and SWI is detailed in Section 4.3.

Outreach

Coming from the amateur astronomy community, it has always seemed natural to me to come back to the public to teach and explain what we do in planetary sciences and present recent discoveries and future projects. This is why I have regularly visited schools, astronomy clubs, and learned societies in the past 10 years (details are given in my CV). I also participate in outreach events organized by my institute/university (public conference for Herschel launch, Café Sciences for the 2015 partial solar eclipse, etc.).

I have also publicized my results several times through press releases (A&A, ESA, CNRS), radio interviews and I try to maintain a personal webpage (https://sites.lesia.obspm.fr/thibault-cavalie/) in which I present my results in short posts. The press releases, radio interviews, etc. can be easily accessed to through this webpage.

I have given lectures in planetary sciences and space exploration, and organized observations on the Bordeaux Observatory site, for the Université du Temps Libre for more than ten years (2005-2016) and coordinated its astronomy program for six years (2011-2016). I also often take part in Open Days events in the places I work. In 2017-2018, I have supervised an astronomy project for the 1st grades at my town’s ground school, titled “Our Earth, a planet in the Solar System”, in which the pupils have been introduced to the following concepts: the day/night cycle, the moon phases, the solar and moon eclipses, gravity, the other planets of the Solar System, etc. They have been awarded with the 2018 SF2A Prize “Découvrir l’Univers”. I have also proposed and given a series of interactive lectures for all grades.I am now planning to expand this series of lectures and come back every year to present a new topic to the pupils. Next year, I intend to propose this series of lectures to the ground and middle schools where I have grown.

Introduction: 10 years observing Giant Planets... and so many more to come!

A revolution in exoplanetary science in the past two decades has shown that giant gaseous worlds appear commonplace in our galaxy. To unveil how giant planets form and how they work, we have to measure their composition, structure, and seasonal evolution. The Giant Planets in our own Solar System now serve as ideal benchmarks for understanding the origins and evolution of these worlds.

The variety found in these distant worlds raises the question of how planetary systems form. Planetary formation is currently explained by two competing models: the core accretion model (Mizuno, 1980; Pollack et al., 1996) and the gravitational instability model (Boss, 1997, 2002). In the first model, a planetary core forms from the accretion of planetesimals. When its mass reaches a critical mass of $\sim$10-15 Earth masses, it captures the surrounding gas from the protoplanetary nebula which is mainly composed of hydrogen and helium. In the gravitational instability model, a giant planet forms after the local collapse of the gas in the protoplanetary disk. These two scenarios can be differentiated by measuring the abundances of heavy elements ($Z > 2$) in the planets. In the gravitational instability model, the heavy element abundances should be protostellar unless photoevaporation occurred due to a nearby OB star. The latter effect would result in a uniform enrichment factor with respect to protostellar abundances (Boss et al., 2002). In the core accretion model, the heavy element abundances primarily depend on the way protoplanetary ices condensed and trapped the volatiles bearing the heavy elements. If ices condensed in amorphous form (Owen et al., 1999), then a uniform enrichment factor is expected, possibly similar to the disk instability+photoevaporation model. If ices condensed in crystalline form (hydrate clathrates) (Gautier et al., 2001; Gautier and Hersant, 2005), then the O abundance should be highly superstellar (because of the need for H_2O molecules to build the trapping cages), Ar and possibly Kr and N should be depleted because of their lower clathrate formation temperature compared to other volatiles (Hersant et al., 2004; Mousis et al., 2018). Alternatives to these two classes of models exist. Guillot and Hueso (2006) proposed that Giant Planets could have formed in a chemically evolved disk in which the hydrogen and helium gas would already have started being lost because of photoevaporation. This scenario can explain the low enrichment of noble gases seen in Jupiter. A similar enrichment is expected at Saturn and a higher one in the ice giants, but these enrichment factors are all supposed to be smaller than those predicted by accretion of solids containing C, O, N and S. Finally, Ali-Dib et al. (2014) proposed that ice giants formed on the CO snowline. This model results in highly enriched O and C abundances, moderately enriched Kr, Xe, S and P, and Ar and N only in stellar abundances owing to their low trapping temperatures. The main issue with this model is the assumption of a stationary disk during the formation of these planets.

Each heavy element abundance measurements, as well as isotopic ratios (although not detailed in this introduction), are crucial to shed light on the giant planet formation processes. A good example is O in water, which plays a central role in the trapping of volatiles either by adsorption on amorphous ice or in clathrates during the formation of planetesimals. Depending on the condensation process and the heliocentric distance of formation of the ices, the enrichment in O could range from protostellar to highly superstellar. The O abundance is thus one of the main measurement that can help differentiate models. Unfortunately, the Galileo probe probably failed at measuring the deep O abundance in Jupiter by entering dry zone and thus not reaching the levels where H_2O is well-mixed (Wong et al., 2004). It is one of the Juno mission goals to derive Jupiter's deep O abundance from microwave observations (Matousek, 2007). For other planets, and in the absence of Galileo-like probes, heavy element abundances must be deduced from the composition of the observable part of their atmospheres.

Yet, Lellouch et al. (1995) and Feuchtgruber et al. (1997) have discovered that a number of species, including H_2O, are delivered to the Giant Planets by external sources, like interplanetary dust particles (IDP), icy rings/satellites, and large comet impacts. It is thus essential to measure and model the interactions existing between planets and their local/distant environment, with the aim of quantifying the effect of these external sources on composition. Doing so, it is then possible to disentangle external from internal sources in atmospheric composition and thus better understand giant planet formation. These studies, still limited to Solar System Giant Planets, are important in the perspective of exoplanet atmospheric characterization, since external sources are likely to exist in extrasolar systems (Kiefer et al., 2014a,b).

The Solar System is the only local laboratory we have within our reach to study the origin and evolution of giant planets and their atmospheres, by means of ground-based and space-based telescopes, and planetary missions. It is thus essential to better understand how our Solar System formed and works to be able to transpose this knowledge to exoplanetary systems. The latter in return, owing to their diversity, can broaden our views on planetary formation and evolution, even if the data remain limited for now. However, Giant Planets have only been visited by a limited number of space missions, and even fewer orbiting probes (Galileo, Cassini, and now Juno). This is even truer for the Ice Giants Uranus and Neptune which have only been flown-by once each by the Voyager 2 probe. As a consequence, their temporal and meridional coverage is quite poor and little is known about their composition and dynamics. Remote sensing thus remains our best option for studying these worlds.

The (sub)millimeter domain is an ideal observation window for measuring the composition of planetary atmospheres as numerous molecules have rotational lines in this wavelength range. Observations with the very high spectral resolution enabled by the heterodyne technique, and the high spatial resolution enabled by large telescopes (e.g. IRAM-30m) and interferometers (e.g. NOEMA and ALMA), are key in deciphering not only composition, but also dynamics (i.e. winds) of these atmospheres. (Sub)millimeter observations coupled with thermochemical modeling of tropospheres are powerful tools for deep composition determination, until in situ measurements can be carried out by Galileo-like atmospheric probes. When coupled with photochemical modeling of upper tropospheres and of stratospheres, (sub)millimeter observations help us to better understand the chemical complexification of giant planet atmospheres. Eventually, wind measurements from line Doppler shifts are key constraints for the GCMs in development for giant planets (Medvedev et al., 2013; Guerlet et al., 2014).

In the past 10 years, I have observed the atmospheres of the Giant Planets in the submillimeter domain with facilities that have enabled me to ever increase spatial resolution: I have started with large ground-based single dishes (JCMT and IRAM-30m), continued with the Herschel Space Observatory, and eventually started using the more complex interferometers (SMA and ALMA). I am now anticipating the next step in term of spatial resolution at Jupiter with the preparation of the JUICE mission, especially with its submillimeter sounder (SWI). In parallel, I have contributed to a long-term time series of observations of post-SL9 species in Jupiter with observatories like IRAM-30m, and mostly the Odin space telescope. With the very high spectral resolution, the ever increasing spatial resolution, and the building of time series, I have developed and contributed to new (sometimes) multi-dimensional and (always) time-dependent models to interpret these data. In the following manuscript, I first present these new models I have developed or contributed to. Then, I summarize the results I have obtained regarding the formation, chemical and dynamical evolution of the Giant Planets. After the conclusion of this manuscript, I outline my main science objectives for the next years.

Chapter 1

New atmosphere models for the Giant Planets

1 Radiative transfer models

1.1 Introduction

The analysis of spectra recorded in the (sub)millimeter domain requires radiative transfer modeling adapted to the observatory and instrument used for the observations. The radiative transfer equation is generally solved in one dimension, and the spectral radiance I_ν is computed along a line-of-sight:

$$I_\nu(z) = I_\nu(0)\, \mathrm{e}^{-\tau_\nu(z)} + \int_0^{\tau_\nu(z)} B_\nu(T(z))\, \mathrm{e}^{-\tau_\nu}\, d\tau_\nu \tag{1.1}$$

where z is altitude, τ_ν is the optical thickness, T is the atmospheric temperature, and B_ν is the Planck function. A proper averaging of several lines-of-sight is then necessary when modeling spatially unresolved observations, to account for air mass variations from nadir to limb, as well as temperature and abundance variability. While the heterodyne spectroscopy technique provides us with very high spectral resolution data ($R \geqslant 10^6$), single dish observatories generally have a limited spatial resolution compared to Solar System planets. At best, they only enable us to roughly map Venus, Mars, or Jupiter. This is why the majority of such observations have been analyzed with disk-averaged condition models (e.g. Marten et al. 1993; Bergin et al. 2000). Besides, interferometers which enable reaching spatial resolutions of $1''$ or better, had rarely been used to study Giant Planets (Moreno et al., 2007) before the arrival of ALMA.

1.2 Radiative transfer in spherical geometry

My first radiative transfer model was a 1D line-by-line model, developed during my thesis, and written in spherical geometry to naturally account for airmass variations and limb emissions. In this model, first presented in Cavalié et al. (2008a), temperature or abundance variability within one telescope beam could not be accounted for. The planetary disk was sampled radially with a number of lines-of-sight, which were then averaged with proper weights when applying the telescope beam pattern. I have used this model successfully in several studies, all of which including disk-averaged or low spatial resolution observations (Cavalié et al., 2008c, 2009, 2010, 2012a, 2013, 2014). In the case of disk-averaged spectra, I performed my analyses by simply using disk-averaged vertical profiles for temperature and abundance. On the other hand, in the rare cases where I had some spatial resolution (e.g. Cavalié et al. 2013), I adapted the profiles from one beam to another to derive either the observed temperature or abundance fields. Results obtained with this model are presented in the next chapters of this document.

1.3 Radiative transfer with 3D ellipsoidal geometry

With the rise of ALMA and the access to very high spatial resolution, I felt the need to develop a new model that would enable me not only to simulate high spectral resolution data, but also full maps with high spatial resolution or maps in which there is a high spatial variability of temperature and/or abundance. This model would have to be flexible enough to allow modeling observations of (i) any planet and carried out by any (sub)millimeter facility (single dish or interferometer), and (ii) any rotational line emission at very high spectral resolution over a limited bandwidth (heterodyne spectra) or at a lower spectral resolution over a very large bandwidth (e.g. PACS/SPIRE spectra).

With this assessment in mind, I have developed a new version of my radiative transfer model in which the 3D ellipsoidal geometry of the giant planets is computed. Accounting for the planet true geometry is guided by my will to compare Jupiter and Saturn observed maps with simulations (these planets have a flattening of 10%), and to be able to include 2D/3D photochemical models or GCM results as input parameters. With this model, I can account not only for the altitudinal variability of temperature and abundance in equation 1.1, but also for any latitudinal and longitudinal variability of these fields. The planetary ellipse is sampled on a 2D irregular grid of lines-of-sight, with a denser sampling close to the limb. The radiative transfer equation is solved on each one of them on an irregular grid of frequencies, with a denser sampling around rotational lines. Before applying a telescope beam, the results are interpolated on a regular spectral and spatial grid to facilitate the 2D beam convolution. The rapid rotation of the planets, which tends to broaden and/or Doppler shift observed spectral lines (depending on the spectral and spatial resolutions), is included. Ring emission/absorption is also modeled for Saturn, following prescriptions of Guerlet et al. (2014) and with input data from de Pater et al. (1991), Flandes et al. (2010), and Spilker et al. (2003, 2005). To allow for rapid computations of any spectral/spatial configuration, I have parallelized this code with OpenMP.

On each single line-of-sight accounted for in the modeling, the local temperature and abundance information is used. This is key when analyzing spatially-resolved maps in which there is latitudinal/longitudinal/altitudinal variability in temperature and/or abundance. For instance, accounting for latitudinal and longitudinal variability in temperature is mandatory for the interpretation of Saturn data, like my H_2O map and the 2010-2011 Storm H_2O and CH_4 maps. These observations are presented in sections 1.5 and 2.3 of chapter 3. Meridional variability in both temperature and abundance is also required to analyze the distributions of SL9 species in Jupiter's stratosphere. Relevant ALMA observations are described in section 3.2 of chapter 3.

Recently, I have interfaced my model with CASA, the data reduction software for ALMA data. I have added a module to the code that enables me to output simulated data cubes into fits files. They are subsequently fed into CASA, with the aim of simulating ALMA observations from my model results (see Fig. 1.1). It helps making the ALMA proposals I am leading or associated to easier to prepare and more convincing.

1.4 Conclusion et perspectives

My first 1D radiative transfer model, written in spherical geometry, was adapted to the high spectral resolution provided by heterodyne spectroscopy, but not to high spatial resolution mapping. My radiative transfer model development strategy has always been twofold: enable observation modeling and simulation in conditions that are relevant to the new observatories like ALMA. This has been the driver for the development of my latest model, in which the 3D ellipsoidal geometry is fully implemented. This model is now my baseline model for spatially-resolved data interpretation. It is also interfaced with CASA to simulate ALMA observations.

In the case of orbiter or flyby observations, the observer can get very close to the target (i.e. Juno). In such cases, and only if the telescope beam is sufficiently broad, my model would need to be generalized with lines-of-sight that are focusing on a close-by observer. This is currently not the case and the lines-of-sight are parallel, as the observer is assumed to be at an infinite distance.

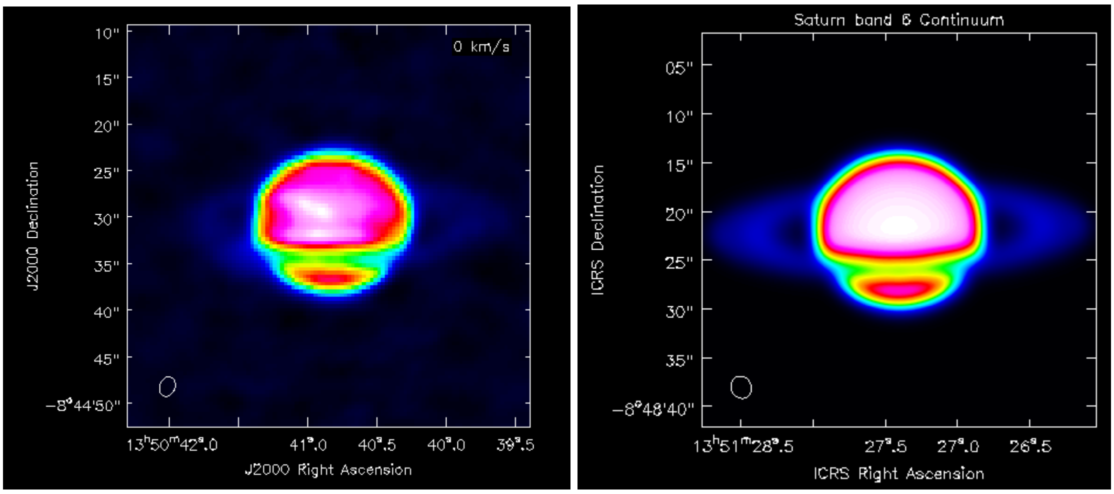

Figure 1.1: (Left) Observed and (Right) simulated image of the continuum emission of Saturn and its ring system in ALMA band 6 (230 GHz) in January 2012 (Cycle 0 project presented in section 2.3 of chapter 1). The image is produced after using the CASA simulation task on a data cube computed with my radiative transfer model that accounts for the 3D ellipsoidal geometry of the planet and its rings.

My main development goal for the next few years are to:

1. Account for frequency dependent Doppler shifts induced by a vertically variable wind profile in the computation of spectra. This will enable me to constrain winds from ALMA and JUICE/SWI observations.

2. Interface my model with an inversion model, like the ones that use optimal estimation (Rengel et al., 2008; Rezac et al., 2014). This would enable me to retrieve automatically the abundance/temperature/wind parameters of the model.

3. Adapt the model to Titan, to enable my colleagues in Bordeaux to simulate their photochemical model results and compare them with observations. Together with M. Dobrijevic, we have supervised an undergraduate student (S. Cuzacq) during the spring of 2018 on this topic and a first version of the model now exists. A thorough validation now needs to be performed before the model can be used for observation simulation and analysis.

2 Photochemical and transport models

2.1 Introduction

Photochemical models are key tools to understand the physico-chemical processes in the giant planet stratospheres. The level of complexity of such models obviously depends on the type of observations that have to be interpreted. In what follows, I present the two types of models that I have used over the years: a 1D time-dependent model and a 2D seasonal model. The latter was developed to have the means to interpret spatially-resolved data obtained (or to be obtained) with ALMA, JSWT, JUICE, etc. Finally, I conclude and propose development goals for the future.

2.2 1D time-dependent photochemistry

Pre-existing model

The Bordeaux 1D time-dependent photochemical model was first developed for Titan and Neptune (Toublanc et al., 1995; Dobrijevic et al., 1995; Dobrijevic and Parisot, 1998) and solves the continuity equation:

$$\frac{\partial n_i}{\partial t} = P_i - n_i L_i - \nabla \cdot \mathbf{\Phi_i} \tag{1.2}$$

where n_i is the number density of species i, t is time, P_i and L_i are the chemical production and loss rates, and $\mathbf{\Phi_i}$ is the molecular flux. This equation must be solved for all species i, at all altitudes and as a function of time. It thus results in a large system of non-linear heavily coupled partial derivative equations. The model was then adapted to Saturn (Ollivier et al., 2000). The specificity of this model is that it has the capability to account for uncertainties of kinetic rates and propagate them when computing the vertical profiles of the various species of the model (Dobrijevic et al., 2003). When analyzing the resulting uncertainties in the abundance vertical profiles with a global sensitivity method, it is possible to identify the reactions that are responsible for causing the uncertainties. This subsequently points chemists to study the identified reactions (Leonori et al., 2014; Homayoon et al., 2014; Cunha de Miranda et al., 2015; Bourgalais et al., 2016; Sleiman et al., 2016) for us to eventually improve the predictability of the models (Hébrard et al., 2009).

Time-dependent modeling

I have quickly sensed the potential the Bordeaux model had to help me study the temporal evolution of the SL9-derived species in the stratosphere of Jupiter. Indeed, the SL9 impacts were by definition sporadic events, and the observations had already spanned over about 15 years when I started working on this topic. This warranted the use of a time-dependent model. Moreover, almost all the available observations were spatially-unresolved, thus justifying the use of a 1D model. While only permanent influxes were coded in the model, I added the possibility to have material supplied by a sporadic event like a comet impact. I finally interfaced this model with my 1D radiative transfer model (described in section 1.2 in this chapter) to interpret Jupiter observations of SL9 species. The papers I have published on this topic with this model are summarized in section 1.3 of chapter 3.

I have also used this model to study the temporal evolution of the composition in the stratospheric vortex that was formed subsequently to the Saturn's Storm of 2010-2011. This work is presented in section 2.2 of chapter 3.

Transport-only modeling

The versatility of the Bordeaux model enables the user to turn chemistry or transport off. In the case were the observational data was either of limited S/N or targeted a chemically stable species, I chose to simplify the model by not accounting for chemical processes and focus only on transport processes. I applied this simplified model to the interpretation of CO observations in Saturn (Cavalié et al., 2009, 2010) and Uranus (Cavalié et al., 2014). These studies are presented in section 1.4 of chapter 3.

2.3 Seasonal altitude-latitude photochemical model

Modeling and observational context

Models always have to be adapted to the kind of data they are used for. With the dramatic increase in sensitivity and spatial resolution in the submillimeter domain[1] seen in the past 10 years, a new generation of models had to be developed.

With the huge amount of spatially resolved data collected by the Cassini mission over about half a Saturnian year, several teams (Guerlet et al., 2014; Medvedev et al., 2013; Friedson and Moses, 2012) started to develop GCMs with the aim to understand the mechanisms at play in the atmosphere of Saturn (and other Giant Planets). These 3D and time-dependent hydrodynamical models are extremely helpful to understand the atmospheric dynamics and to model spatially resolved data. However, Giant Planets have

[1] Spectral resolution was already very high thanks to heterodyne spectroscopy.

small Rossby numbers (ratio of inertial forces to Coriolis forces) because of their size and short rotation periods. The atmospheric structures that have to be modeled thus require a high spatial resolution which makes the computations very time-consuming. This is the main reason why these models generally neglect atmospheric chemistry and use meridionally uniform distributions for the species that contribute to the stratospheric thermal balance. This is a serious limitation knowing that the abundances of C_2H_2 and C_2H_6, i.e. the main stratospheric coolants, vary with latitude and season in Jupiter and Saturn (Nixon et al., 2007; Guerlet et al., 2009).

The majority of Herschel observations from the HssO program or Open Time programs I am involved in are disk-averaged observations. The use of the 1D photochemical model thus remained pertinent to interpret these data. However, Herschel also first enabled us to map Jupiter and Saturn with a moderate spatial resolution. As soon as I realized that Herschel would give us for the first time spatial resolution on Jupiter and Saturn in frequency bands where all previous observations were disk-averaged (Feuchtgruber et al., 1997; Lellouch et al., 2002; Bergin et al., 2000), I jumped on the occasion that was given to me in January 2007 to obtain the PI-ship on the science theme “Spatial distribution of water in Jupiter and Saturn” of the HssO program. This topic would be challenging not only regarding the data reduction and analysis, but mostly because the 1D photochemical model would obviously become of limited interest to analyze the maps. Finally, and with the start of operations of the ALMA observatory in 2011 and the high spatial resolution becoming accessible for all Giant Planets (down to less than 1”), the need for a more realistic photochemical model was becoming more and more significant. For my postdoc time in Bordeaux, my colleagues from the former “Solar System and Exoplanets” Team and I thus decided to develop a spatially-resolved photochemical model to complement GCM simulations.

A two-step development project

To complement GCM results and to interpret my spatially resolved Herschel and ALMA data, we started the development of a 2D photochemical model for the Giant Planets in 2011. Because Giant Planets are relatively homogeneous in longitude, and to keep the computational time reasonable, we decided not to account for the longitudinal dimension at this time, and only deal with altitude and latitude. But, because Cassini made us enter into an era in which we can study planets over seasonal timescales, we had to keep the time-dependency of the 1D model and even turn it into a dimension of the model that could be controlled to account for orbital parameters of the planets.

However, and despite limiting the spatial dimensions of the model to altitude and latitude, the very complex chemical network used in 1D models could not be transposed to a new 2D model, because of computational time limitations. Chemical networks indeed contain about 1000 reactions that couple more than 100 species in non-linear differential equations. The first step of our development work has thus consisted in defining an objective methodology to build a simpler, i.e. reduced, chemical network that could then be used in our future 2D photochemical model. This was the main reason why I got a CNES postdoc fellowship in Bordeaux in 2010-2012. The Bordeaux team, with its 1D photochemical model, had the tools to build such a network. By running uncertainty propagation and sensitivity analyses, it was possible to identify and extract the key reactions that controlled the vertical profiles of a subset of selected species of interest, like the hydrocarbons responsible for the heating/cooling of the stratosphere (i.e. CH_4, C_2H_6, C_2H_2), and later the main oxygen species (H_2O, CO, and CO_2). Our methodology was published in Dobrijevic et al. (2011). Starting from the vertical profiles of Guerlet et al. (2009, 2010), we showed that we could reduce the initial chemical network from $\sim$100 species and $\sim$600 reactions by 60% and 90%, respectively, and still keep the vertical profiles of the species of interest within error bars. An example for C_2H_2 in Saturn is shown in Fig. 1.2. More recently, after an update of the full chemical network by Hébrard et al. (2013), Dobrijevic et al. (2014), and Loison et al. (2015), we have updated our reduced chemical network for Giant Planets (see Cavalié et al. 2015, and Hue et al. 2015, 2016).

With these initial results, the concomitant award of ALMA time in Cycle 0 (see section 2.3) and will of V. Hue to start working with our team, we obtained funding for a PhD thesis for him to continue

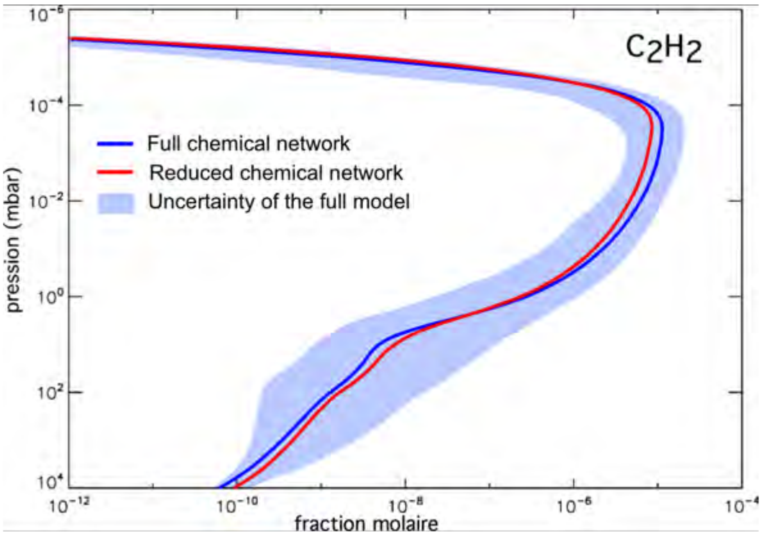

Figure 1.2: Vertical profile of C_2H_2 in Saturn's stratosphere, as computed with the 1D photochemical model and the full chemical network (blue line) and the reduced chemical network (red line). The envelope of uncertainty on the vertical profile, as deduced from kinetic rate uncertainty propagation, is displayed with light blue. The profile is very well reproduced by the reduced network. This figure is adapted from Dobrijevic et al. (2011).

the development of the 2D seasonal photochemical model, in the second step of our model development project. I have co-supervised his thesis work from 2012 to 2015. The model we have successfully put together is detailed in Hue et al. (2015). In short, it has the following characteristics:

- The model solves the continuity equation for altitudes (resolution $\sim H/3$), latitudes (resolution $\sim 5°$), and as a function of time (resolution of 10° in heliocentric longitude), using spherical geometry.
- The chemical network includes 22 C, H, and O species, 33 reactions and 24 photodissociations.
- The temporal evolution of the local solar declination is computed from the orbital parameters (e.g., period, eccentricity, obliquity).
- The actinic flux is computed with a full-3D spherical radiative transfer model.
- The model can be fed with a seasonal and latitude-altitude thermal field directly simulated by a GCM or retrieved from observations.
- Vertical and meridional eddy diffusion (K_{zz} and K_{yy}) and advective transport are implemented.
- Ring shadowing effects are included for Saturn.

So far, three papers using this model have been published. I present the first three in the following paragraphs.

Pseudo-2D seasonal model of Saturn

In Hue et al. (2015, 2016), we have first applied our new model to the study of the seasonal evolution of the abundances of the main C_2 hydrocarbons. In Hue et al. (2015), we have taken the seasonal thermal model of Greathouse et al. (2005, 2008) and shown that we could fairly well reproduce the meridional distributions of C_2H_2 and C_2H_6 from the low to the mid-latitudes in the mbar region, i.e. where the Cassini observations probe the stratosphere, even without meridional transport (Fig. 1.3). In the equatorial region, the main difference with the data was the absence of the signature of the Saturn Quasi-Periodic Oscillation (QPO). The QPO is inherently a dynamical phenomenon and only a GCM can reproduce it. At high southern latitudes and at $L_S = 320°$, the abundance of C_2H_6 is underestimated by a factor of 2-3. This could be the indication that there is an advective cell in the southern hemisphere, with downwelling motions above the southern polar region.

In the course of his thesis, Vincent won funding from the Bordeaux University IdEx program to have a visiting scientist period. Benefiting from the collaboration I had started with T. Greathouse from the SwRI (USA) on the analysis of my Herschel maps of Jupiter's H_2O (see section 1.3), he spent 6 months at SwRI in 2014 to study the feedback between the temperature field computed with the model of Greathouse et al. (2005) with the seasonal 2D abundance distributions of the species responsible for the control of the temperature in Saturn's stratosphere, i.e. CH_4, C_2H_2, and C_2H_6. This work, presented in Hue et al. (2016), shows that such coupling has a significant influence on temperature, but not on abundances. For pressures lower than 0.5 mbar and polar latitudes, the seasonal temperature peaks occur half a season earlier than in the Hue et al. (2015) model. The equator-to-pole thermal gradient is thus significantly impacted at low pressures. The next logical step is to test advective transport patterns that could help reconcile the model results with the C_2H_2 and C_2H_6 data,.

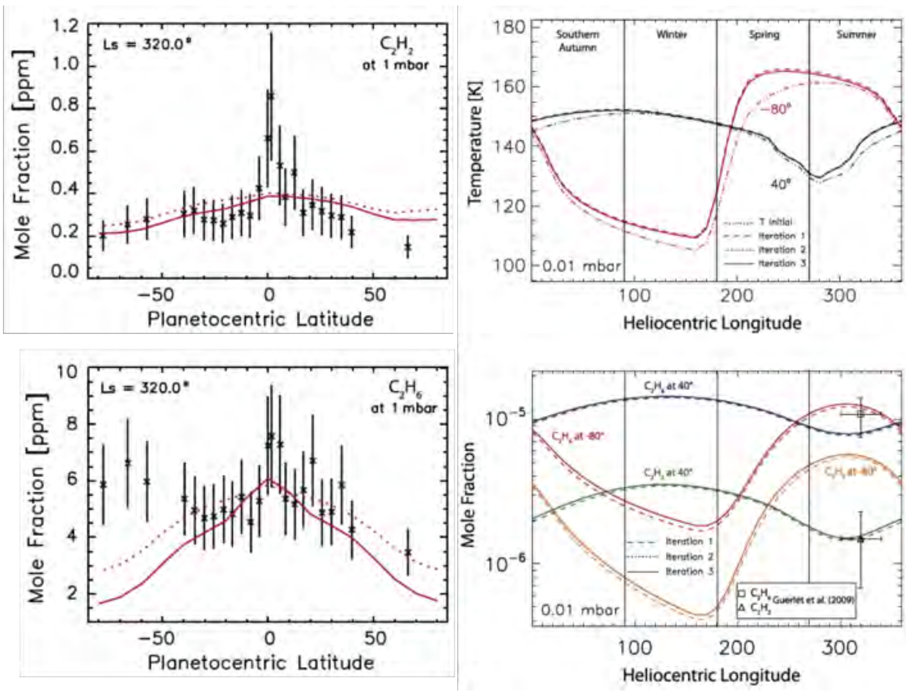

Figure 1.3: (Left) Meridional distributions of C_2H_2 and C_2H_6 in Saturn at1 mbar from Cassini/CIRS observations compared to the pseudo-2D photochemical models simulations of Hue et al. (2015). The two models were obtained with different thermal fields (seasonal in solid lines and uniform in dashed lines). (Right) Feedback between composition and temperature as a function of season. The effect becomes significant at high latitudes where seasonal variability in abundances of C_2H_2 and C_2H_6 are most noticeable. Figures extracted from Hue et al. (2015, 2016).

2D seasonal model of Jupiter

Cassini measured the meridional distribution of C_2H_2 and C_2H_6 in Jupiter during its flyby in December 2000 (Nixon et al., 2007, 2010). It has revealed a striking difference between the two species at the millibar level, with the abundance of C_2H_2 decreasing poleward and the abundance of C_2H_6 increasing poleward. In Hue et al. (2018), we have used our model to try to reproduce these distributions. With the pseudo-2D model, in which the meridional transport is turned off, only the C_2H_2 distribution can be fitted as it follows the mean insolation. When adding meridional diffusion, all distributions are flattened, which improves the fit to C_2H_6 (but obviously not the one to C_2H_2), but never enables to get an increase of its abundance at high latitudes. With 2D advective transport cells between 30 mbar and 0.01 mbar, in which there are upwelling motions over the equator and downwelling motions over the poles, we manage to increase the abundance of C_2H_6 at high latitudes for the first time. However, C_2H_2 then follows the same trend, which is incompatible with the data. This proves that chemistry and 2D diffusion/advection are not sufficient to explain the observations. This hints at auroral processes taking place in Jupiter's upper stratosphere. This conclusion was the driver that made Vincent apply for a postdoc position at SwRI in the Juno/UVS Team. He would be able to work on Jupiter auroral data and continue in parallel the development of his model by adding ion-neutral chemistry.

2.4 Conclusion and perspectives

In the past 8 years, we have managed to develop a full 2D seasonal photochemical and transport model for giant planet atmospheres. This model has now been published several times, in different flavors, and the development objectives are relatively clear:

- Short-to-mid term: Include ion-neutral chemistry to the chemical network to assess whether auroral chemistry can explain the high latitude distributions of C_2 hydrocarbons in Jupiter and Saturn. The main difficulty, besides building the network itself, resides in the fact that we will probably have to leave aside the concept of reduced chemical network and work with a full network. This may result in a significant increase of the computational time and would then imply trying to parallelize it. I have already taken action on this side by supervising an undergraduate student (Y. Guimard) in computational sciences over the summer of 2018. His task consists in re-writing the model solver in Fortran 90. It is in Fortran 77 for now which prevents the parallelization of the whole code.
- Long term: Couple our photochemical model to a GCM (e.g. Guerlet et al. 2014, Medvedev et al. 2013). There are two options: (i) study the feedback between the two models by providing chemical species distributions to the GCM and use their atmospheric circulation in our model, (ii) include a chemistry module to a GCM an use a reduced chemical network. I am currently planning to ask for funding for a thesis or a postdoc to start in 2019 in co-supervision with P. Hartogh (PI of JUICE/SWI) and A. Medvedev (MPS GCM main developer) at MPS to work on (ii). This funding could be obtained in the framework of the current partnership between the Bordeaux and Göttingen universities.

In parallel, we will now regularly use the model to interpret spatially-resolved data that I obtain and will continue to obtain with ALMA and later with JUICE/SWI (e.g., refer to sections 1.3, 1.5 and 3.2).

3 Thermochemical models

3.1 Introduction

Thermochemistry has been used for decades to model the conditions in the deep tropospheres of the giant planets, with the aim of constraining the deep composition of giant planets and thus their formation processes. By coupling thermochemistry with the vertical transport caused by convection, it is possible to link the upper tropospheric abundances of observed species with other species that reside deep in the atmosphere, at levels that cannot be probed. The main example is the derivation of the deep H_2O abundance from upper tropospheric CO observations (Fegley and Prinn, 1988; Lodders and Fegley, 1994) to constrain primordial ices condensation processes (Owen et al., 1999; Gautier et al., 2001). Tropospheric H_2O is very difficult or nearly impossible to observe directly with remote sensing techniques in the tropospheres of the Giant Planets (Larson et al., 1975; de Graauw et al., 1997; de Pater and Richmond, 1989) because it condenses at fairly deep levels already. However, the abundances of H_2O and CO are linked by the equilibrium reaction $H_2O + CH_4 = 3H_2 + CO$ in the deep tropospheres of Giant Planets. As the temperature cools down with altitude, the equilibrium moves towards the left hand side of the equation. The upper tropospheric abundance of CO is finally fixed at a level where the timescale of the reaction equals the vertical diffusion timescale: thermochemical equilibrium is quenched. The main unknowns in this problem are the magnitude of the deep tropospheric vertical diffusion and the thermal profile. Usually, dry or wet adiabats are used to extrapolate upper tropospheric temperatures to deeper levels.

3.2 Quench level approximation and comprehensive thermochemical/transport models

Until recently, only quench level approximation models were used to try and constrain the deep H_2O abundance in Giant Planets (Lodders and Fegley, 1994; Bézard et al., 2002; Visscher and Fegley, 2005; Visscher et al., 2010; Luszcz-Cook and de Pater, 2013). In these models, the quench level is derived by equating the chemical timescale for the conversion of H_2O into CO with the diffusion timescale. The chemical lifetime is obtained from the assumed rate-limiting reaction. I have used this technique in Cavalié et al. (2009) to derive an upper limit on the deep H_2O abundance of Saturn from our tropospheric CO upper limit, and found that it was $<$26 times the solar value.

The detection of hot Jupiters and subsequent characterization work has increased the interest for high temperature chemistry models. It has led to the release of comprehensive 1D thermochemistry and transport models, in which the continuity equation is solved at all altitudes using a full chemical network. These comprehensive models (Moses et al., 2011; Venot et al., 2012) can then be transposed to Solar System Giant Planet deep and hot tropospheres. In Cavalié et al. (2014), I have first used the model of Venot et al. (2012) to derive an upper limit on the deep H_2O abundance of Uranus from an upper limit derived by Teanby and Irwin (2013), and found that is was $<$500 times the solar value. I chose to collaborate with O. Venot (LISA) on these aspects, because her model benefits from an extensive experimental and modeling work done by the combustion community to validate a chemical network with H, C, O, and N species in the temperature and pressure range relevant to Giant Planet deep tropospheres. To speed up the calculations, the atmospheric composition is first estimated with a thermochemical equilibrium model of Agúndez et al. (2014), in which the Gibbs energy is minimized. Once this starting point is obtained, the thermochemical and transport model can be efficiently applied.

3.3 A new methodology to extrapolate deep temperatures - Consequences

Giant planet deep tropospheres are supposedly water-rich (Owen and Encrenaz, 2003; Gautier and Hersant, 2005) and H_2O condenses more or less deep in their tropospheres. The mean molecular weight gradient produced by the condensation of H_2O can be significant and has the effect of stabilizing the atmosphere with respect to convection. If the deep H_2O abundance exceeds a threshold, a thin radiative layer appears in which the temperature can increase dramatically over a small altitude range. I have applied this principle, published by Leconte et al. (2017), to Uranus and Neptune in Cavalié et al. (2017b), because these planets have the highest anticipated H_2O deep abundances among the Solar System Giant Planets. I expected the effect of the mean molecular weight gradient at the level where H_2O condenses to be maximal. The thermal profiles depart from dry or wet adiabats in this regions, as shown in Fig. 1.4. They consist of a wet adiabat in the upper troposphere, a radiative layer at the level of H_2O condensation, and a dry adiabat in the hot layers. A consequence of the higher deep temperatures obtained in such profiles, the deep H_2O abundance required to produce the observed upper tropospheric CO is lower than in calculations using simple wet or dry adiabats. For Uranus and Neptune, the nominal deep H_2O abundances in Uranus and Neptune are then $<$160 times solar and 480 times solar. These results are discussed in chapter 2 section 3.2.

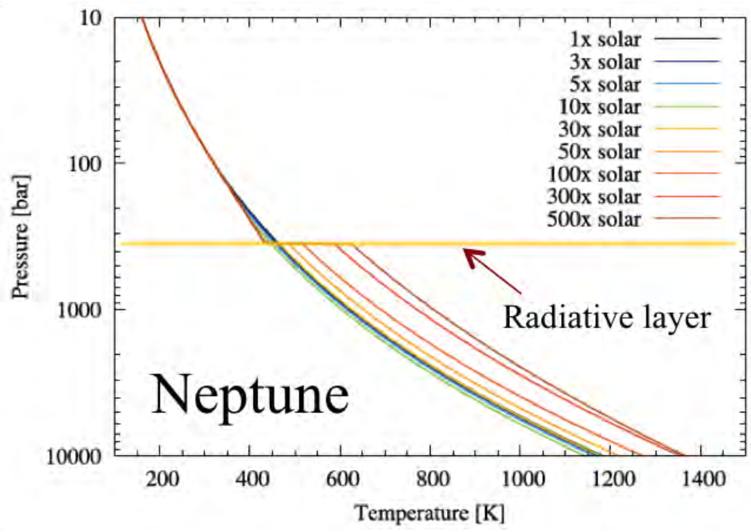

Figure 1.4: Tropospheric temperature profiles of Neptune obtained for various deep H_2O abundances, when applying the prescription of Leconte et al. (2017). Above a given threshold, the mean molecular weight gradient in the H_2O condensation region stabilizes the atmosphere with respect to convection and produces a thin radiative layer in which the temperature dramatically increases. Figure adapted from Cavalié et al. (2017b).

3.4 Conclusion and perspectives

The results and conclusion of this work will be detailed in section 3.2. Here, we list and briefly discuss the modeling limitation raised by this study:

- Does the radiative layer act as a transport barrier? The radiative layer produced by the mean molecular weight gradient could, in principle, be the siege of a drastic decrease of vertical mixing despite the thinness of the layer ($\sim$1 km). Vertical mixing could be as low as that of molecular diffusivity. It would result in a gradient in the CO profile. As CO has an external source at the top of the atmosphere (Cavalié et al., 2014), such a stringent transport barrier could mean that at least part of upper tropospheric CO could be produced from the external source. This is only true if vertical mixing is as low as that of molecular diffusivity. If so, the upper tropospheric CO measurement would no longer be a diagnostic of the deep H_2O abundance. Experimental or theoretical work on these aspects would be valuable.

- It has been noticed by Moses (2014) that the chemical scheme we use has a major difference in the timescales over which CH_3OH, an intermediate species in the equilibrium reaction, is converted into H_2O. This causes about an order of magnitude differences in the upper tropospheric CO abundance for a given deep H_2O abundance. O. Venot (LISA) and I are currently collaborating with R. Bounaceur (LRGP) to revisit the thermochemistry of CH_3OH. He has updated the CH_3OH block of the network in early 2018. O. Venot and I have supervised undergraduate students to test this new scheme on exoplanets and Uranus/Neptune. Preliminary results obtained by L. Brouillard (Bordeaux University) indicate that the deep H_2O abundance in Uranus and Neptune decreases to <45 and 250 times solar, respectively, to reproduce the tropospheric CO observations. A more thorough study is required to confirm these results.

- An ideal gas equation of state was implicitly used in this study, which is questionable under high pressure conditions in water-rich environments. Recent theoretical work indicate a rather limited impact of a more realistic equation of state under jovian conditions (Karpowicz and Steffes, 2013), but the departure from an ideal gas remains unconstrained under uranian/neptunian pressure/H_2O conditions. Theoretical work is needed to better assess this issue. In any case, our chemical network would then need to be fully updated as the ideal gas law is implicitly used in the derivation of kinetic rates.

- Other condensates (made of NH_4SH, NH_3 or H_2S) are expected in the tropospheres of Uranus and Neptune. The impact of latent heat release by these phases would need to be properly estimated, even though the abundances at work should be rather small.

Finally, a goal for the next few years is to extend the chemical network of the model beyond H, C, O, and N species. The element which is the main candidate is P, as it has been predicted by Visscher and Fegley (2005) that P species could be used to constrain the deep H_2O abundance in Giant Planets, in the same way CO is currently used. O. Venot and I are currently collaborating with J.C. Loison (ISM) and M. Dobrijevic (LAB) in this respect.

4 Conclusion and perspectives

In this first chapter, I have presented all the different types of models I have developed or contributed to develop. These are radiative transfer, photochemical and thermochemical models. The development work has always been (and will keep on being) guided by my will to stick to the properties (spectral and spatial resolution mostly) of the observation data at hand: 1D models when the data are poorly resolved horizontally, and more complex 2D or 3D models for the newest spatially-resolved data obtained with Herschel and ALMA. The most recent models are: (i) a radiative transfer model written in full 3D ellipsoidal geometry to enable the modeling of highly resolved ALMA maps, (ii) a seasonal altitude-latitude photochemical model to interpret these same data and constrain processes like external supplies of material by dust, comets, satellites and rings, and (iii) a 1D thermochemical and transport model to constrain the deep composition of Giant Planets.

For each type of model, I have described the development perspectives for the short-to-long term. In my opinion, the top priorities are the following:

1. Radiative transfer model: couple the existing model to a retrieval model to automatize the retrieval of physical parameters from high signal-to-noise ratio observations.

2. Photochemical model: include auroral chemistry to understand the high latitude composition of Jupiter and Saturn.

3. Thermochemical model: revisit the chemistry of CH_3OH to waive the discrepancy between the models of Moses (2014) and Venot et al. (2012).

Each one of them is currently being worked on and I expect the first results not later than in 2019.

Chapter 2

New constraints on the formation of Giant Planets

1 Introduction

The formation of the Giant Planets in the Solar System, as well as in extrasolar systems, remains one of the most outstanding question in planetary science. All four giants of our system are different from one another, even if they can be split into two distinct families: gas giants (Jupiter and Saturn) and ice giants (Uranus and Neptune). The gas giants have most of their mass in their atmospheres, while ice giants have a significant solid interior. This major difference, alongside numerous other ones, imply formation environments and timescales with distinct properties. Only observations of the deep composition of the Giant Planets in combination with formation and evolution models can help us to unveil the processes that led to the formation of these planets.

I have worked on questions related to the formation of the Giant Planets only for a few years, i.e. much less than compared to the other science themes described in chapter 3. This explains why this chapter is shorter than the next ones. In this chapter, I present two observables in giant planet atmospheres that can help shed light on the formation of these bodies. I first discuss the importance of the deuterium abundance and how it can be linked to the environment in which protoplanetary ices formed. Then, I describe how the deep oxygen abundance can help us to constrain the processes under which these primordial ices condensed and trapped heavy elements. Finally, I give my conclusion and perspectives in terms of modeling, observations and space missions.

2 The deuterium abundance

2.1 Introduction

According to laboratory experiments and measurements made in the interstellar medium, the ion-molecule interactions and grain-surface reactions at low temperature contribute in the enrichment in deuterium of ices. As a result, the D/H ratio increases when temperature decreases (Watson, 1974; Brown and Millar, 1989). Measuring the D/H ratio in Solar System bodies helps us to constrain the physico-chemical conditions under which H_2O formed (Gautier et al., 2001; Owen et al., 1999). For instance, the D/H ratio in Jupiter and Saturn seems to be representative of the protosolar value (Lellouch et al., 2001). On the other hand, the mixing of D-enriched grains coming from the cores of Uranus and Neptune with their atmospheres results in a higher D/H value in these planets (Feuchtgruber et al., 1999). The accurate knowledge of the D/H ratio in Giant Planets helps us to understand the composition of the grains in the protoplanetary disk as well as their link to comets (Hersant et al., 2001). The D/H value found in comets ranges from the earth ocean value (Lis et al., 2013) to three times this value (Altwegg et al., 2015).

2.2 Herschel observations and open questions

In the framework of the Herschel HssO Key Program, several measurements of the D/H ratio in comets have been obtained (Hartogh et al., 2011; Bockelée-Morvan et al., 2012; Lis et al., 2013). In parallel, we have performed new observations of the rotational lines of HD at 56 and 112 μm in all Giant Planets to improve on the accuracy of the ISO measurements (Feuchtgruber et al., 1999; Lellouch et al., 2001).

At Jupiter and Saturn, a recent work by Pierel et al. (2017) confirms previous ISO findings (Lellouch et al., 2001) that the jovian D/H is protosolar and that the value at Saturn is slightly lower. It is still not understood how Saturn, which formed at a larger heliocentric distance that Jupiter and was thus confronted to lower temperatures, could end up with a lower D/H ratio than Jupiter. Our Herschel observations, which are still being analyzed by F. Billebaud (LAB) with my radiative transfer model, combined with new formation and evolution models may help solve this issue in the future.

So far, we have published the results for Uranus and Neptune in Lellouch et al. (2010) and Feuchtgruber et al. (2013). The observations indicate that the D/H ratio in these planets is $(4.4\pm0.4)\times10^{-5}$ and $(4.1\pm0.4)\times10^{-5}$, respectively, which is consistent with the previous determination from ISO data (Feuchtgruber et al., 1999), although nominally lower. It thus remains difficult to explain how Uranus and Neptune could end up having a D/H ratio lower than Oort cloud comets, when the cores of these planets are supposedly made of the same material as these comets. In the paper, we propose as an alternative that Uranus and Neptune have a high rock-to-ice ratio in their interior, for their D/H to remain compatible with that of Oort cloud comets. Other explanations, like Ali-Dib et al. (2014), have been proposed to reconcile the D/H ratio seen in Uranus and Neptune with the Oort cloud comet value, by proposing that the ices in Uranus and Neptune are mostly composed of CO ice rather than cometary H_2O ice. However this model fails at explaining the high deep H_2O abundance expected from tropospheric observations of CO in Neptune.

However, the thermal structure of Uranus, as derived by Orton et al. (2014a) from Spitzer observations, is incompatible with our D/H values at a level of 10% or more. Although still unpublished, the equivalent Neptune model leads to the same assessment. Thus, additional modeling work is required to both fit the atmospheric temperature and the D/H ratio with the combined Spitzer and Herschel datasets.

3 The deep oxygen abundance

3.1 Introduction

There are two classes of formation models for the giant planets: core accretion (Pollack et al., 1996) and disk gravitational instability (Boss, 1997). The processes at play to form a giant planet are drastically different. In the core accretion scenario, a $\sim$10-15 $M_\oplus$ core forms in less than 1 My from the accretion of planetesimals. This initial phase is followed by a long transition period of several My during which the core continues to accrete solids but starts also capturing gas from the surrounding nebula. After reaching a given mass threshold, the surrounding nebula gas collapses on the core and forms a gas giant like Jupiter or Saturn before the nebula gas dissipates. Ice giants are supposedly "unfinished" gas giants. According to this model, ice giants never got massive enough in time to have the nebula gas collapse on their cores before the dissipation of the nebula gas. On the other hand, the disk instability model supposes that clumps of nebula material (dust, planetesimals and gas) suddenly collapse (possibly because of a propagating density wave) to form a giant planet. In this scenario, the formation time is much shorter than in the core accretion model: it only takes about 1 My to fully form a giant. As a consequence, these two models differ in the final composition of the formed planets. While disk gravitational instability predicts abundances in stellar proportions for heavy elements because of the short formation time, the core accretion model predicts superstellar abundances, with enrichment factors increasing with heliocentric distance.

Constraining the history and thus the processes that led to the formation of the giant planets remains a real challenge for observers and modelers. The composition of their deep atmospheres is assumed to be a good diagnostic of their state right after their formation was completed, but it is very difficult to measure it. Probing the deep atmospheric layers of these planets to measure their composition can, in principle, be achieved by 3 techniques: (i) in situ measurements, (ii) direct measurement with remote sensing observations, and (iii) indirect measurement with context observations and atmosphere models.

Jupiter's deep composition was established in situ with the successful dive of the Galileo probe into the atmosphere of Jupiter in 1995. An overall enrichment factor of 4±2 was observed in most heavy elements (Fig. 2.1 left), notably except oxygen (carried by H_2O) which was surprisingly found significantly subsolar (Atreya et al., 1999, 2003; Wong et al., 2004). This is explained by the fact that Galileo entered a 5 μm hot spot, a region depleted in volatiles. So the H_2O value cannot be blindly trusted and should be regarded as a lower limit. Moreover, this observable is another key to the understanding of giant planet formation. H_2O is supposedly very abundant at the time of the formation of the Solar System. As the temperature cools down both with heliocentric distance and time, H_2O starts to condense and to agglomerate with dust to form planetesimals. This species also acts as a trap for heavy elements. Depending on the amount of available H_2O and the temperature/pressure conditions at play in these stages of the planetary formation, heavy element can be trapped either by adsorption onto amorphous ice (Bar-Nun et al., 1988; Owen et al., 1999) or by clathrate hydrates (Lunine and Stevenson, 1985; Gautier et al., 2001). The main difference between the two processes is that clathrates require a significantly higher abundance of H_2O, since 5.75 (or 5.66, depending on the clathrate type) H_2O molecules are required to trap a molecule that carries a heavy element (Gautier et al., 2001). Measuring not only heavy elements, but also specifically H_2O is thus crucial for better understanding giant planet formation. Fig. 2.1 (right) shows qualitatively the expected heavy element enrichments at Uranus/Neptune expected from various models.

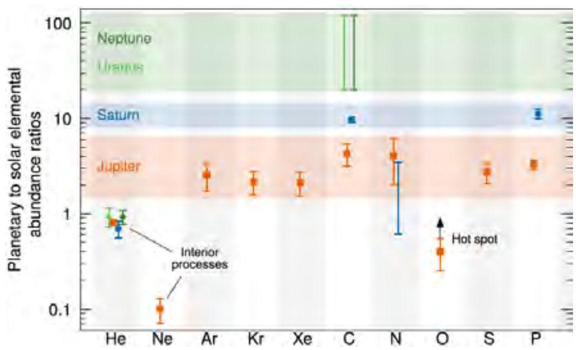

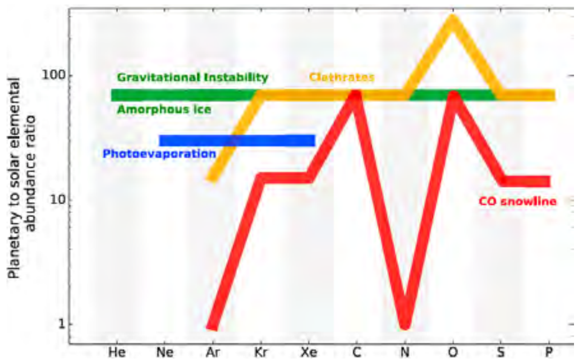

Figure 2.1: (Left) Heavy element measurements in the Giant Planets. An overall enrichment factor if 4±2 was observed in Jupiter by Galileo. The lack of measurements in the other giants is the main motivation for proposing atmospheric probes like Hera (see section 4). (Right) Qualitative enrichment factor for heavy elements in Uranus/Neptune as expected from various formation models. Both figures are taken from Mousis et al. (2018).

A difficulty in Solar System Giant Planets if that H_2O condenses relatively deep in the tropospheres of the Giant Planets and is therefore difficult to measure, even with an in situ probe. The probable failure of Galileo at measuring the deep H_2O, was one of the main motivations to send the Juno mission (Matousek, 2007; Bolton et al., 2017). Juno orbits Jupiter on a polar orbit that has a perijove only a few 1000 km above Jupiter's cloud top. It embarks a microwave radiometer (MWR) among other instruments. The main goal of this instrument is to observe the 22 GHz H_2O absorption and measure the deep oxygen abundance of Jupiter (Janssen et al., 2005, 2017) to constrain formation models (Helled and Guillot, 2017). However, this technique is very challenging for several reasons: H_2O is not the only absorber in this spectral region (e.g. NH_3 - see Bolton et al. 2017), the temperature profile is not measured but extrapolated form previous measurements, and the calibration of the observations has to be extremely good. My feeling is that it will be difficult to measure the deep oxygen abundance of Jupiter with Juno.

In the absence of atmospheric probes for Saturn, Uranus and Neptune, we are left for now with the last technique for these planets. It provides us with an indirect measurement of the deep H_2O abundance by using an upper tropospheric species that does not condense, and link it back to H_2O with thermo-chemistry and transport calculations. The principle is presented in section 3.1. This type of calculations can be performed either in the framework of an approximation, i.e. the quench level approximation (e.g. Lodders and Fegley 1994), or with comprehensive thermochemical and diffusion models as described in section 3.2 of chapter 1 (e.g., Moses et al. 2011). In the course of my work, I have used both techniques, as is described in the next sections.

3.2 Observations and modeling

Saturn

In Cavalié et al. (2009), I have determined an upper limit on the tropospheric CO abundance in Saturn from the observation of the CO(3-2) line. I have applied the quench level approximation to derive its deep O/H ratio, and found that H_2O should be less than 26 times solar. This result is not constraining in itself, as both sequestration of heavy elements by crystalline and amorphous ice are compliant with this number. Following these results, I have participated as co-I in a VLT observation program that targeted infrared lines of CO in Saturn. The first results have been presented recently at the DPS by Fouchet et al. (2017). We have obtained the first detection of tropospheric CO in Saturn with a mole fraction of $\sim$1 ppb (see Fig. 2.2). After refining the model results, I will use my thermochemical and transport model to constrain the deep oxygen abundance in Saturn.

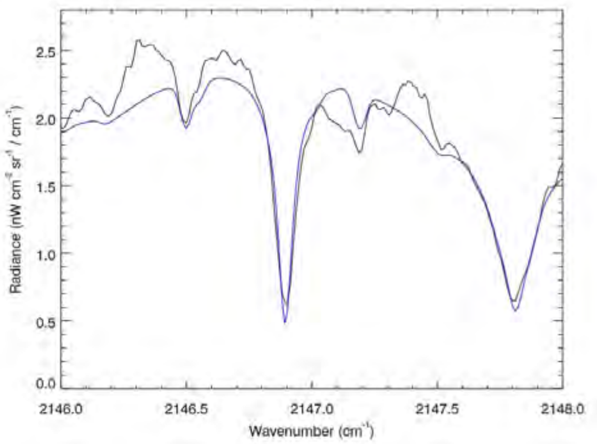

Figure 2.2: First detection of tropospheric CO in Saturn with the VLT. The model in blue has a tropospheric CO mole fraction of 1.2 ppb. Figure taken from Fouchet et al. (2017).

Uranus and Neptune

After a first attempt to detect CO in Uranus with Herschel/HIFI and the HssO program, I have managed to detect CO in the framework of my Herschel Open Time progam. While the CO line was formed in the stratosphere, the observation enabled me to derive an upper limit on the tropospheric CO (Cavalié et al., 2014). However, the upper limit of 2.1 ppb derived from Herschel/SPIRE observations by Teanby and Irwin (2013) was significantly more constraining. Using a first version of the thermochemical model and a dry adiabat, I derived an upper limit of 500 times solar for the deep oxygen abundance in Uranus.

At Neptune, the most recent published work indicates that tropospheric CO has a mole fraction of $0.1^{+0.2}_{-0.1}$ ppm (Luszcz-Cook and de Pater, 2013). Using a quench level approximation and dry/wet adiabats, they derive a deep oxygen abundance of at least 400 times solar. In the meantime, the HssO Team has observed CO in Neptune with SPIRE. These observations, completed by ground-based observations of R. Moreno (LESIA) with the IRAM-30m, indicate a tropospheric mole fraction of 0.20±0.05 ppm (Moreno et al., 2011). These observational results remain to be published.

After the release of the new tropospheric temperature extrapolation model of Leconte et al. (2017), I applied their prescription to Uranus and Neptune in conjunction with the latest observational data presented above. The details of the thermal modeling are given in section 3.3 of chapter 1. According to the model, the tropospheric CO abundance not only depends on the deep H_2O abundance, but also on other observables like the tropospheric temperature, vertical transport, and the CH_4 abundance. I have explored this space parameter within the boundaries of existing observation error bars (of CO and CH_4) and estimates (for tropospheric temperature and transport). The nominal results, obtained with the 3-layer temperature profiles of Leconte et al. (2017), indicate that Uranus and Neptune should be highly enriched in oxygen, with <160 times the solar value in Uranus and 480 times the solar value in Neptune. However, and as previously stated in section 3.4 of chapter 1, we have updated the CH_3OH chemistry from our chemical network following a recommendation of Moses (2014). Using the chemical rates of Moses et al. (2011) for the reaction $H+CH_3OH \rightarrow CH_3+H_2O$ significantly changes our results to <55 and 280 times the solar value for Uranus and Neptune, respectively. This theoretical, experimental, and modeling work is currently ongoing and involves R. Bounaceur (LRGP), O. Venot (LISA). The preliminary results obtained by L. Brouillard (Bordeaux University) show that using our new CH_3OH block results in deep oxygen abundances of <45 and 250 times the solar value for Uranus and Neptune, respectively, which is in broad agreement with expectations. I need to confirm these results with more simulations and to assess the implications on the formation of the Ice Giants.

4 Conclusion and perspectives

In this chapter, I have summarized the work I have led and contributed to concerning the determination of the deep composition of Giant Planets, in an attempt to improve our knowledge on their formation processes. This work involves ground-based and space-based observations, as well as thermochemical modeling.

We have determined the D/H ratios in Uranus and Neptune in Feuchtgruber et al. (2013), but we may need to revise our results in order to get a consistent match of both Herschel and Spitzer spectra (Orton et al., 2014b). For now, the D/H values are significantly below cometary values (Lis et al., 2013) for these planets and remain difficult to understand. In parallel, I will continue to support F. Billebaud in her Herschel HD observation analysis for Jupiter and Saturn.

We have recently detected tropospheric CO in Saturn with the VLT (Fouchet et al., 2017). Once the tropospheric CO abundance will be established, I will run my thermochemical model to constrain the deep oxygen abundance in this planet. This result will hopefully be obtained when the Juno MWR Team will be able to constrain the jovian deep oxygen abundance from their radiometric observations.

From CO observations and new thermochemical models, I have estimated the deep oxygen abundance of Uranus and Neptune to be <160 and 480 times solar, respectively, but large uncertainties in the modeling remain to be waived. The most important step to improve the predictability of the model consists in updating and validating our CH_3OH chemistry, and this work is ongoing at the time of writing. Preliminary results indicate that the deep oxygen abundance is lower than in my previous work (i.e., <45 and 250 times solar, resp.) and implications on formation scenarios have to be reevaluated.

Formation and interior modelers try to put together scenarios that fit all observational data (mass, radius, luminosity, composition, etc.). There is currently no model that can explain the formation of the Giant Planets, especially the Ice Giants regarding their observed composition (Helled et al., 2011; Helled and Lunine, 2014; Nettelmann et al., 2013; Ali-Dib et al., 2014). To improve this situation, measurements are required for all Giant Planets. Isotopic, helium, noble gases, and other heavy element abundances are key in constraining the formation environment and processes of the giant planets, as demonstrated by the Galileo probe measurements in Jupiter (von Zahn et al., 1998; Niemann et al., 1998; Mahaffy et al., 2000; Atreya et al., 2003; Wong et al., 2004). This is why I have contributed in starting the Hera project, led by O. Mousis (LAM). Hera was a planetary probe project which aimed at measuring the heavy element abundances, isotopic ratios and physical properties of Saturn's atmosphere down to the 20 bar level (Mousis et al., 2014). After a first unsuccessful attempt with the ESA M4 selection, we reworked the technical aspects of the project (Mousis et al., 2016) and proposed it for the M5 selection. Hera was part of the 13 finalists considered by ESA for a phase A study, but was eventually not selected as there was no identified mission to carry the probe to Saturn. The Dragonfly mission to Titan, selected by NASA as candidate for the New Frontiers 4 mission, was not retained as possible carrier.

In the meantime, NASA has released a study of concepts to explore the Ice Giants (https://www.lpi.usra.edu/icegiants/mission_study/Full-Report.pdf). The favored mission architecture is composed of an orbiter and a probe which could be provided by ESA, in the same spirit that led to the very successful Cassini-Huygens mission. Following these results, we have undertaken a new study to prove that the Hera concept can be adapted to Uranus and Neptune (Mousis et al., 2018). In parallel, I have started discussions involving S. Gauffre (head of the Electronics Team at LAB), and P. Wurz (PI of the mass spectrometer of Hera), for LAB to contribute not only scientifically but also on the hardware side to the mass spectrometer of the probe. It has been agreed that LAB would provide the electronics and firmware of the instrument, if the mission gets selected. We are now awaiting the kick-off of an ESA-led Ice Giant study, focused on exploring how ESA could best contribute to a NASA-led Ice Giant mission, to propose an atmospheric probe in the spirit of Hera.

Chapter 3

Seasonal chemistry and dynamics in the stratospheres of the Giant Planets

1 Supply of exogenic material to the stratospheres of the Giant Planets

1.1 Introduction

A major discovery of the Infrared Space Observatory (ISO) was the detection of H_2O in the stratospheres of the Giant Planets and Titan (Feuchtgruber et al., 1997; Coustenis et al., 1998). This discovery has proven the existence of external sources of H_2O, as this species condenses at the tropopauses of these planets and can therefore not come from their deeper tropospheric layers. This supply of oxygen material that manifests itself not only through H_2O but also CO and CO_2 has several possible sources: (i) an influx of interplanetary dust particles (IDP) produced by collisions of asteroids and by the activity of comets (Prather et al., 1978; Landgraf et al., 2002; Moses and Poppe, 2017), (ii) icy rings and satellites (Strobel and Yung, 1979; Prangé et al., 2006), and (iii) impact of Shoemaker-Levy 9 (SL9) type comets (Lellouch et al., 1995). Fig. 3.1 displays these sources, taking Saturn as an example. It is important to assess the relative magnitude of each of these sources to better understand phenomena like the production of dust at high heliocentric distances (Kidger, 2003; Poppe, 2016), the ionisation and/or transport of solid and gaseous material from rings and satellites to upper atmospheres (Connerney, 1986; Cassidy and Johnson, 2010; Moore et al., 2015), and the frequency of comet impacts in the outer Solar System (Zahnle et al., 2003).

In the following sections, I describe the various studies I have been leading and involved in regarding the determination of the origin of exogenic species observed in the stratospheres of the Giant Planets. Most of the results have been obtained with the Herschel Space Observatory.

1.2 The Herschel Space Observatory

The Herschel Space Observatory (Pilbratt et al., 2010) was launched in 2009 to study the universe in the submillimeter domain. It carried three instruments onboard: the Heterodyne Instrument for the Far Infrared (HIFI, de Graauw et al. 2010), the Photodetector Array Camera and Spectrometer (PACS, Poglitsch et al. 2010), and the Spectral and Photometric Imaging Receiver (SPIRE, Griffin et al. 2010). The main goal of the Herschel mission was to map water in the Universe. This space observatory completed its mission in April 2013.

The Herschel Guaranteed Time Key Program "Water and related chemistry in the Solar System"' (PI P. Hartogh, MPS), also known as HssO (Herschel Solar System Observations), proposes to determine the origin, the distribution, and the evolution of H_2O and of its isotopes in the atmospheres of Mars, the Giant Planets, Titan, and comets (Hartogh et al., 2009). I have been involved in this program since 2005. I started working with the HssO Team producing numerous observation simulations to optimize

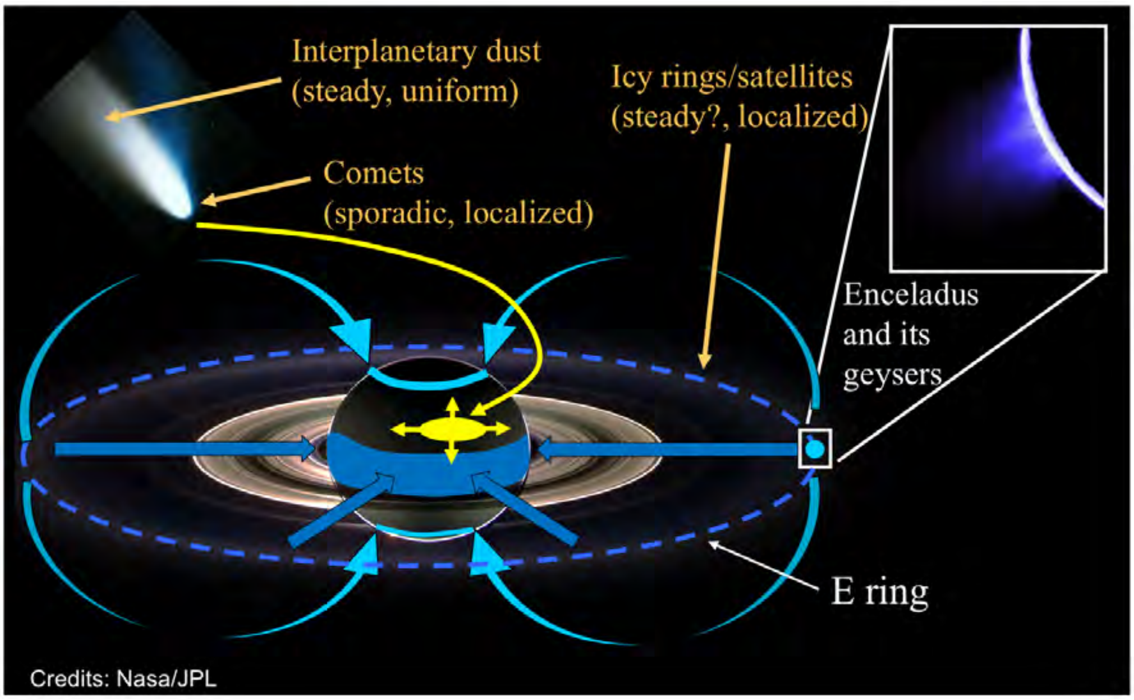

Figure 3.1: Possible external sources of exogenic material for Giant Planets, with Saturn and its system taken as an example. Each source has its own spatio-temporal properties that can be used by observers as diagnostics.

our observation program. I have also coordinated the paper that presents the HssO program (Hartogh et al., 2009), and I am leading the science theme "Spatial distribution of H_2O in Jupiter and Saturn" of this program.

1.3 The origin of H_2O in the stratosphere of Jupiter

Introduction

According to the joint analysis of H_2O and CO_2 observations carried out with ISO in 1997, the majority of the observed H_2O seemed to be originating from the SL9 impacts in July 1994 in Jupiter's stratosphere (Lellouch et al., 2002). However, Submillimeter Wave Astronomy Satellite (SWAS) observations in 1999 could be modeled with an steady source (IDP-like) model (Bergin et al., 2000), which seemed contradictory.

Odin observations and modeling

In 2002, the Odin space telescope recorded a spectrum with the H_2O line at 557 GHz of Jupiter's stratosphere. I have analyzed the Odin and SWAS data with the coupled photochemical and radiative transfer models of sections 1.2 and 2.2 of chapter 1. The photochemical model has enabled me to account for the time variability of the H_2O vertical profile, from the impact date to the observations. The first results, presented in Cavalié et al. (2008c), displayed in Fig. 3.2 (top left) show narrower wings for the line in the SL9 model. It comes from the slow downward diffusion of H_2O from its deposition level of 0.1 mbar (Lellouch et al., 1995; Moreno et al., 2003). Contrary to the IDP model, H_2O had not yet reached the condensation level (at $\sim$ few 10 mbar) at the time of the observations. The models thus seemed to confirm the SL9 source, even if the IDP model remained within 3-σ of the noise.

This initial Odin observation was then followed by numerous observations between 2003 and 2018, especially after the first analysis in 2006. Jupiter has now been observed one or two times a year in the past 10 years with Odin. The main idea driving these observations is to obtain the evidence for temporal variability of the H_2O vertical profile, as expected if H_2O was brought by comet SL9. The analysis of the data ranging from 2002 to 2009, shown in Fig. 3.2 (bottom left), indeed indicates a decrease of $\sim$15% of the line-to-continuum ratio of the 557 GHz line (Cavalié et al., 2012a). The rest of the data has just been reduced this year by K. Bermudez (Montpellier University) who I have co-advised with N. Biver (LESIA) during his undergraduate internship. The preliminary analysis unambiguously confirms the temporal decrease of the water abundance in Jupiter's stratosphere, especially when Herschel/HIFI observations of the same line are added (Fig. 3.2 bottom left). The line-to-continuum ratio of the 557 GHz line has decreased by $\sim$40% between 1999 and 2018. Long-term photochemical modeling is required before publication of these data. Refined models will serve to predict the H_2O abundance in 2030, when JUICE/SWI observations will become available (see section 4).

Herschel observations and modeling

I have obtained the first resolved maps of Jupiter's stratospheric H_2O with the HIFI and PACS instruments of Herschel in the framework of the HssO program (Fig. 3.2). I have shown, by combining the observations with Jupiter thermal infrared maps retrieved from NASA IRTF observations, that the factor of 2-3 North-South asymmetry in terms of H_2O column abundance was not caused by a thermal asymmetry. Because the PACS maps reveal an overabundance in the southern hemisphere, the hemisphere in which SL9 fell, and because HIFI spectra show that H_2O resides at pressures lower than 2 mbar, i.e. inconsistent with an IDP source because it is significantly above the H_2O condensation level, I have proven that the 3D distribution of H_2O is a remnant of the SL9 impacts (Cavalié et al., 2013).

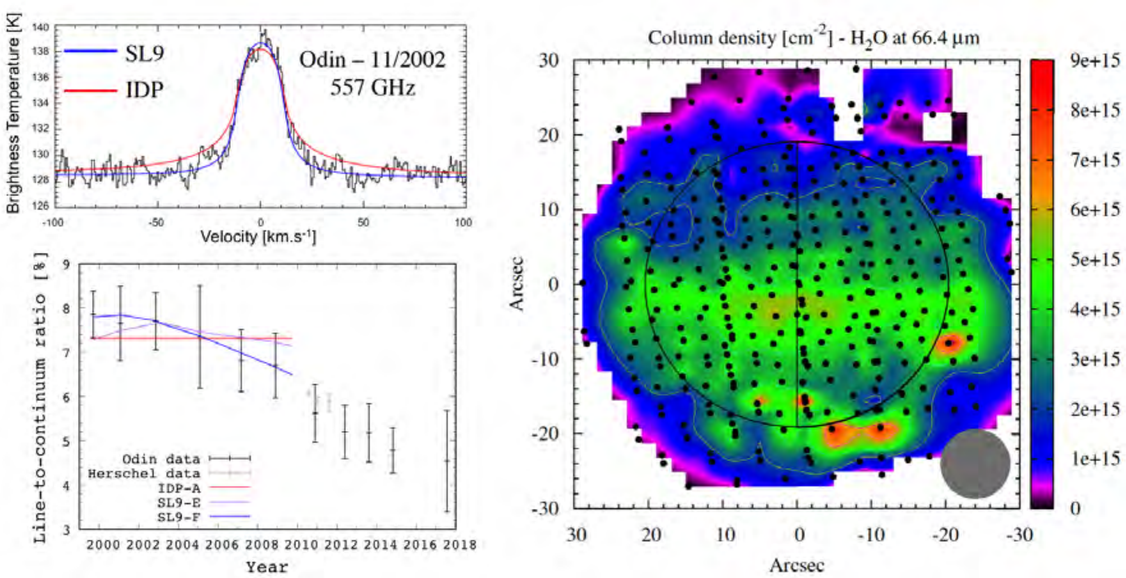

Figure 3.2: Observations of H_2O in Jupiter's stratosphere: (Top left) Odin observations of 2002 (Cavalié et al., 2008c) and (Bottom left) temporal evolution of the H_2O line-to-continuum ratio between 1999 and 2009 observed by Odin and compared to photochemical models (Cavalié et al., 2012a). We have completed this dataset with 2010-2018 Odin and 2010-2011 Herschel observations. (Right) Spatial distribution of H_2O in 2010 from Herschel/PACS data (Cavalié et al., 2013). The temporal evolution and spatial distribution demonstrate the SL9 origin of H_2O in Jupiter's stratosphere.

Conclusions et perspectives

While there was already observational proof of the cometary origin of CO, HCN, CS, and CO_2, in Jupiter' stratosphere, H_2O was the missing piece. With a 10-year effort combining Odin and Herschel observations, as well as time-dependent photochemical modeling, I have managed to prove the cometary origin of H_2O in Jupiter's stratosphere.

The remaining Odin observations, most of them being post-Herschel observations, will now serve to monitor the temporal decay of the H_2O abundance. This work will lead us, the JUICE/SWI Team, to better constrain the photochemical losses and vertical transport in Jupiter's stratosphere. It will enable us to make predictions on the distribution of H_2O that SWI will observe in 2030 (see section 4). We will thus be able to improve our observation time estimates and optimize our observation strategy.

In the meantime, I have obtained ALMA Cycle 5 observation time to map H_2O in band 5 (at 183 GHz) in July 2018. If measured, this map will complement my HCN and CO maps, obtained with ALMA in Cycle 4 in March 2017, and help me to understand why the HCN, CO, and CO_2 distributions are so different when these species are all supposed to come from SL9 (see section 3.2, and refer to Lellouch et al. 2006 for the discovery of this discrepancy between HCN and CO_2).

1.4 The origin of CO in Saturn and Uranus

Introduction

CO was detected in Saturn in 1986 in the infrared by Noll et al. (1986) at the $\sim$1 ppb level. Complementary observations of Noll and Larson (1991) could not help to determine the origin of this compound and the question remained open ever since. In Uranus, Encrenaz et al. (2004) first detected CO in the atmosphere of Uranus with the VLT at the level of 20-30 ppb, but could also not state on its origin. Determining the origin of CO in the Giant Planets is more complex than for H_2O as this species does not condense at the tropopauses of these planets and can therefore originate not only for external sources (IDP, comets, rings/satellites), but also from the deep oxygen-rich interiors of these planets. Studying the origin of CO thus bears implications on the planet formation and on the interactions with their environment.

While Bézard et al. (2002) and Lellouch et al. (2005) have proven the dual origin (internal and cometary) for CO in the atmospheres of Jupiter and Neptune, the question remained open for Saturn and Uranus.

Ground-based and Herschel observations

Combining JCMT observations at 345 GHz and 691 GHz (see Fig. 3.3 top) and coupling them with 1D vertical transport models, I have shown that CO in Saturn's stratosphere was probably delivered by a comet impact (Cavalié et al., 2009, 2010). While IDP models (with typical CO fluxes of 1.5-4×10^6 cm^{-2}·s^{-1}) cannot fit both lines simultaneously, an SL9-type comet depositing 3.5 ppm of CO above the 0.1 mbar level 220 years ago provides us with the best fit. VLT/CRIRES high spectral resolution observations in the 5 μm band currently analyzed by T. Fouchet (LESIA) provide us with the first unambiguous detection of internal CO in Saturn (see section 3.2 in chapter 2) and we have acquired follow-up data with IRTF/CSHELL in May 2018. In 2011, I have obtained an interferometric map of CO in Saturn's stratosphere with the Submillimeter Array (SMA). This map, which still needs to be fully calibrated by the observatory and that I still have to analyze, could shed light on the spatial distribution of CO and thus on its external source. Complementary clues could come from CO and HCN meridionally-resolved observations obtained by T. Fouchet with ALMA in July 2018.

I have used the Herschel Space Observatory, in the framework of my Open Time program, to detect the 822 GHz CO line in Uranus (see Fig. 3.3 bottom). This observations clearly points to an external source (Cavalié et al., 2014). Recent theoretical work of Moses and Poppe (2017) restrain the origin of external CO in Uranus to comet impacts and Edgeworth-Kuiper belt comet dust. There is yet no observational proof of an internal source of CO in Uranus, which may be reflective of the sluggish atmospheric overturning and lack of significant internal heat source (Pearl et al., 1990).

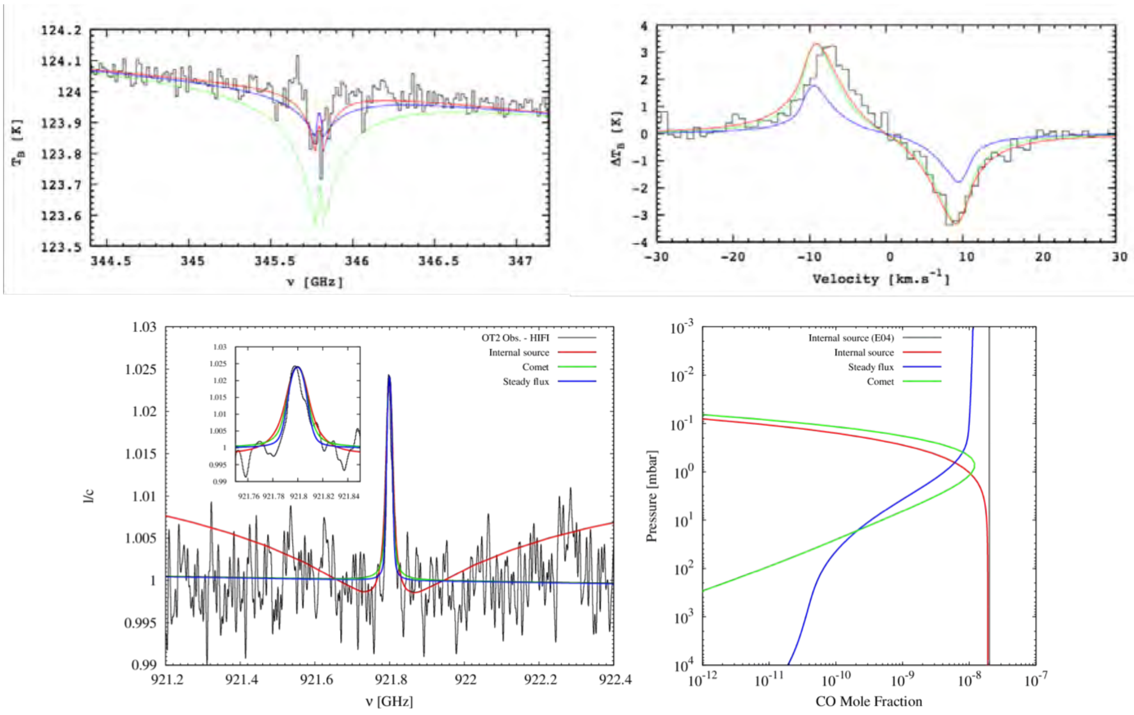

Figure 3.3: Observations of CO in the stratospheres of Saturn and Uranus. (Top) Combining JCMT observations of CO in Saturn at 345 and 691 GHz favors a cometary origin (red line) rather than an IDP-like steady source (blue and green line) (Cavalié et al., 2009, 2010). (Bottom) Observation of CO in Uranus with Herschel/HIFI and vertical profile models, proving that CO has an external source in Uranus (Cavalié et al., 2014). Figures adapted from Cavalié et al. (2010) and taken from Cavalié et al. (2014).

1.5 The origin of H_2O in Saturn's stratosphere

Introduction

Following the initial detection of H_2O in the stratosphere of Saturn by Feuchtgruber et al. (1997), photochemical modeling by Moses et al. (2000) and Ollivier et al. (2000) has shown that an oxygen influx with both H_2O and CO (or CO_2) compatible with cometary ice proportion is required. Temporal considerations (impact frequencies versus loss of H_2O by condensation) and compositional considerations (CO/H_2O ratio) make a comet impact an improbable scenario to explain Saturn's H_2O.

In 2006, Cassini detected plumes venting mostly H_2O in Saturn's system (Hansen et al., 2006; Porco et al., 2006; Waite et al., 2006), and a fraction of these emissions could end up raining into Saturn's atmosphere (Cassidy and Johnson, 2010; Moore et al., 2010). Ring rain caused by sputtering on icy ring grains could also produce H_2O that would be transported along magnetic field lines and precipitate into Saturn's atmosphere (Connerney, 1986; Prangé et al., 2006; Moore et al., 2015). More recently, Moses and Poppe (2017) have estimated the oxygen influx caused by interplanetary dust ablation. They have found that this source falls short by an order of magnitude at explaining the H_2O observations.

In the past 10 years, we have conducted a series of observations to constrain Saturn's external source of H_2O.

The Enceladus torus

The first Solar System observation performed by Herschel/HIFI in June 2009 was an observation of the 557 GHz H_2O line in Saturn (see Fig. 3.4). This HssO observation was puzzling at first, because it showed emission wings with an unexpected strong central absorption. Thanks to the very high spectral resolution and complementary observations at other frequencies, we could demonstrate in Hartogh et al. (2011) that we were observing a torus of cold H_2O, located at the orbital distance of Enceladus, that was absorbing Saturn's H_2O warmer line emission. The fact that it had not been observed before (Bergin et al., 2000) was due to a different observation geometry. The ring plane was close to its maximal inclination in 1999, while the line-of-sight was crossing Saturn's ring plane in 2009 (Saturn Equinox in 2009). This discovery was reminiscent of the detection of H_2O plumes at Enceladus (Hansen et al., 2006; Porco et al., 2006; Waite et al., 2006). We have therefore tested the 3D calculations of the evolution of the distribution of H_2O released by the plumes of Cassidy and Johnson (2010) and shown that such a torus model matched our data (Hartogh et al., 2011).

E. Lellouch (LESIA) has obtained Herschel Open Time and ALMA Cycle 2 follow up observations of Saturn and the Enceladus torus to constrain its composition and shape. The Herschel observations indicate a decrease of the torus absorption with increasing inclination of the ring plane (see Fig. 3.4), and he has obtained a first direct detection of H_2O in the torus. With ALMA, we have mapped the Saturn system at 88 GHz to try the detection of HCN in the torus. Once these data are fully analyzed, we will be able to better constrain the torus structure, kinematics and composition, and thus possibly the origin of the Enceladus plumes.

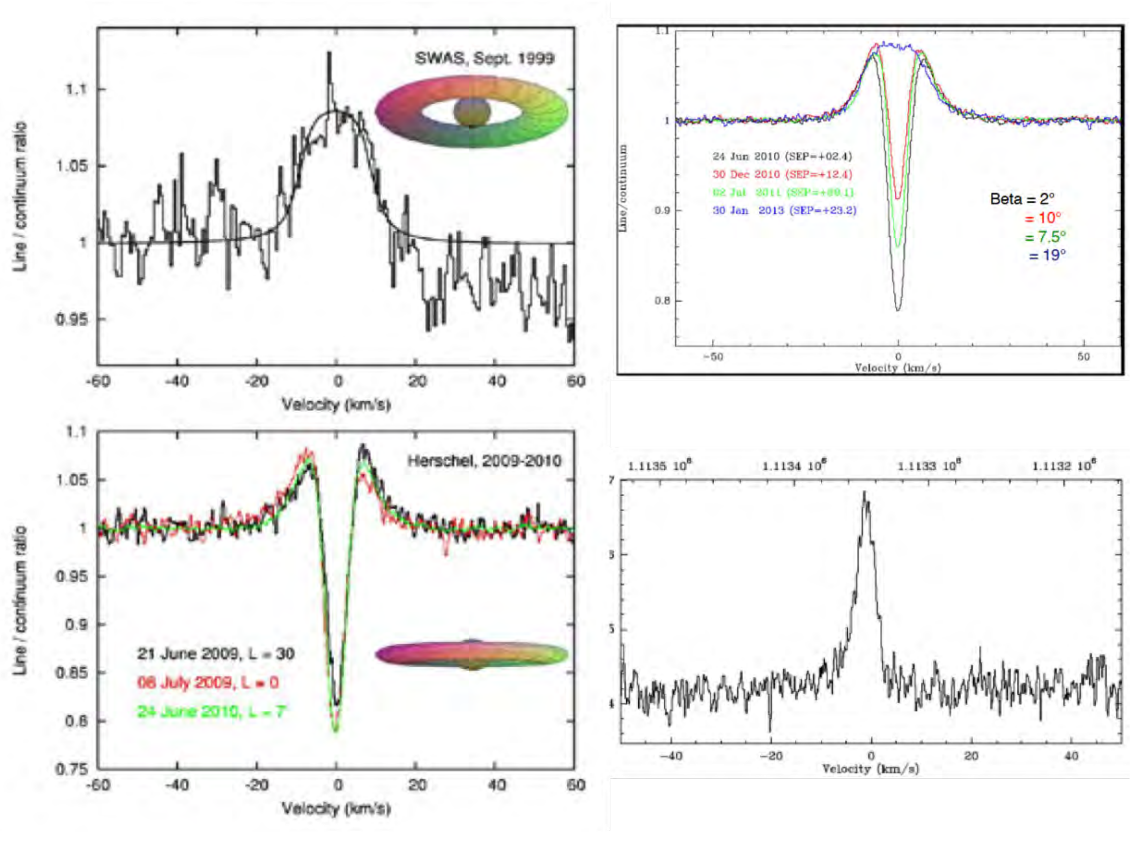

Figure 3.4: Observations of H_2O in the stratospheres of Saturn with SWAS in 1999 (top left), and Herschel in 2009 (bottom left). The central absorption seen in the 2009 data is caused by the Enceladus torus (Hartogh et al., 2011). Follow up Herschel Open Time observations led by E. Lellouch (LESIA) show the decrease of the torus absorption with increasing ring plane inclination (top right). He has also obtained the first direct detection of the torus (bottom right).

Mapping H_2O in Saturn's stratosphere with Herschel

With the detection of the Enceladus torus and the predictions of Cassidy and Johnson (2010), the missing piece of the puzzle was a direct observation of H_2O in Saturn's stratosphere (without torus absorption) that would show the signature of the Enceladus source. With the HssO program, I have recorded the first map of H_2O at 66 μm with PACS with a moderate spatial resolution of 9.4″. When accounting for the altitude-latitude temperature field at the time of observations (data taken from Fletcher et al. 2017) with the radiative transfer model described in section 1.3 of chapter 1, I find that only a meridional distribution of H_2O peaked around the equator can satisfactorily fit the data (Cavalié et al. in preparation). The gaussian solution presented in Fig. 3.5 is not unique and I am currently completing a full parameter space study. In any case, this seems to be direct proof that Enceladus is the ultimate source of H_2O of Saturn's stratosphere. From the obtained meridional distribution of H_2O, V. Hue (SwRI) and I will constrain the input fluxes to match the data, and we will then compare it with the Cassidy and Johnson (2010) predictions.

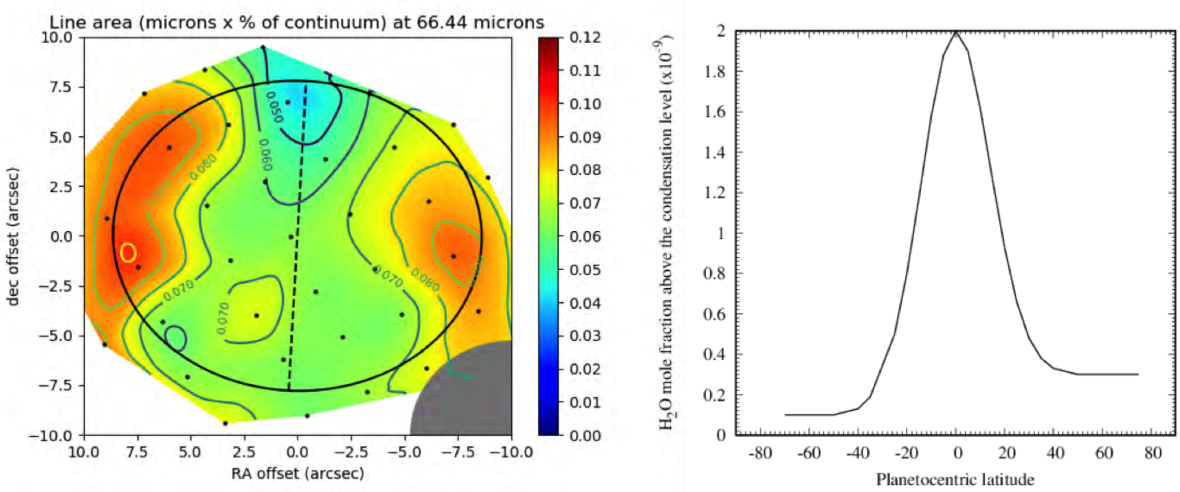

Figure 3.5: (Left) Map of H_2O in the stratosphere of Saturn as observed with Herschel/PACS at 66 μm. (Right) Example of meridional distribution of H_2O, in terms of constant mole fraction above the local condensation level, that fits the data. The distribution has a gaussian shape centered around the equator, which could be direct proof that Enceladus is the source of H_2O of Saturn's stratosphere. Figure extracted from Cavalié et al. (in preparation).

Conclusion et perspectives

I have contributed to a comprehensive observational and modeling work of H_2O in Saturn's stratosphere to constrain the origin of this species. We now have strong evidence pointing at Enceladus, its plumes and subsequent torus, as the main source. 2D photochemical modeling is underway to constrain the meridional shape and magnitude of the source to compare it with predictions of H_2O spreading from the Enceladus torus in the Saturn system.

In the frame of ALMA Cycle 5, I have obtained observation time for July 2018 to map H_2O at a spatial resolution that will improve over Herschel by a factor of 5. With this new map, I will be able to better constrain the meridional distribution of H_2O in Saturn's stratosphere. This will result in a better understanding of the processes that shape the Enceladus torus source.

The proximal orbits of Cassini's Grand Finale have revealed a rich molecular environment peaked around Saturn's equator (Waite, 2017). CO could be one of the molecules detected by INMS and could originate from Enceladus. New ALMA meridionally resolved maps of CO and HCN obtained by T. Fouchet in July 2018 will help confirm whether CO comes from a comet impact or from the Enceladus geysers.

1.6 Exogenic species: Conclusions and perspectives

In the past 10 years, I have conducted and participated in observations of oxygen, nitrogen and sulfur species in the stratospheres of the Giant Planets to constrain their external source(s). The general picture is now that CO seems to be produced by comet impacts in Giant Planet stratospheres (Bézard et al., 2002; Cavalié et al., 2010; Lellouch et al., 2005). This is backed-up at Jupiter and Neptune by observations of HCN and CS (Moreno et al., 2003, 2017). The case of Uranus remains unclear (Cavalié et al., 2014) and recent Cassini and ALMA observations could point to Enceladus as an additional source at Saturn. H_2O, on the other hand has a variety of sources: SL9 at Jupiter (Cavalié et al., 2013), Enceladus at Saturn (Cavalié in preparation), and most probably IDPs at Uranus and Neptune (Moses and Poppe, 2017). Fig. 3.6 summarizes the current picture.

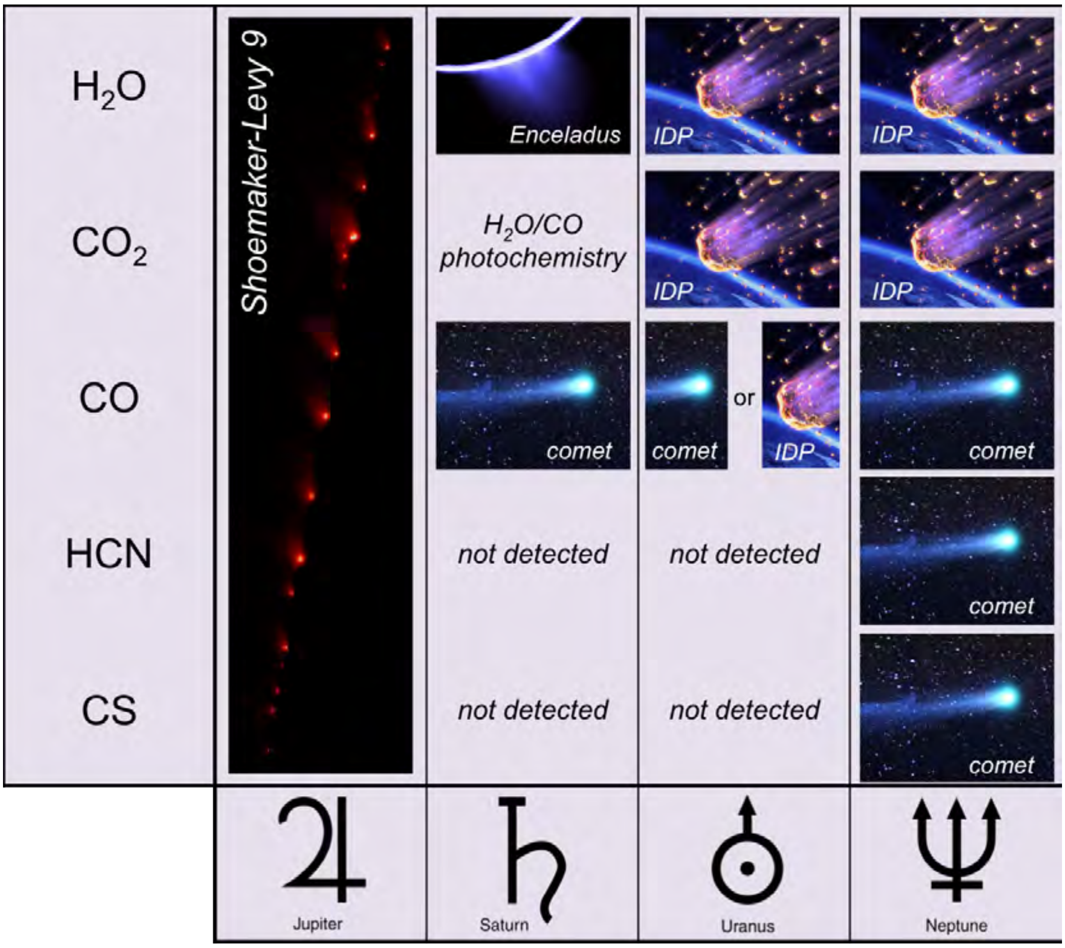

Figure 3.6: Table summarizing the current picture regarding the origin of exogenic species in the stratospheres of Giant Planets. References for Jupiter: Bézard et al. (2002), Lellouch et al. (2002), Moreno et al. (2003), and Cavalié et al. (2013) ; References for Saturn: Cavalié et al. (2010), Cavalié et al. (in preparation), and Moses and Poppe (2017) ; References for Uranus: Cavalié et al. (2014) and Moses and Poppe (2017) ; References for Neptune: Lellouch et al. (2005), Moses and Poppe (2017), Moreno et al. (2017).

However, a lot of work is still on the table, with many Herschel data not yet analyzed. In the next years, I will hopefully contribute to the retrieval of the H_2O vertical profile in the stratospheres of Uranus and Neptune from Herschel/HIFI high spectral resolution data. The same work has been underway for several years for Jupiter. Unfortunately, all have been put on hold by my german colleagues because of the development of the Submillimetre Wave Instrument (SWI). In the meantime, I will pursue the monitoring of H_2O in Jupiter with Odin and of other SL9-derived (CO, HCN and CS) species with

ALMA, in preparation for SWI observations, and support T. Fouchet (LESIA) in his analysis of ALMA maps of CO and HCN in Saturn.

2 Observations of Saturn's Great Storm of 2010-2011

2.1 Introduction

Saturn's slow seasonal cycle is disrupted by a planetary-scale storm every saturnian year (Sanchez-Lavega et al., 1991). In December 2010, the rise of a convective plume was the start of what would become to date, the longest ever witnessed storm in Saturn's atmosphere (Sánchez-Lavega et al., 2011, 2012, 2016). This tropospheric storm, located at 40°N, surprisingly and dramatically altered the stratospheric temperature and composition for months. Fletcher et al. (2011, 2012) observed the formation of two hot vortices, referred to as "beacons" (because of the rapid rotation of Saturn and of their appearance in the thermal infrared), that eventually merged to form a giant vortex in which the temperature increased by as much as 80 K at 1 mbar. Unexpectedly, acetylene and ethylene have seen their abundances increase significantly in the mbar region in the vortex (Fletcher et al., 2012; Hesman et al., 2012). So, the temperature and chemistry in the vortex was not understood.

2.2 Photochemical modeling

I have used the 1D time-dependent photochemical model presented in section 2.2 of chapter 1 to model the evolution of the composition in the stratospheric vortex, when accounting for the temperature evolution as measured by Fletcher et al. (2012). The modeling, published in Cavalié et al. (2015), shows that the dramatic temperature increase at the time of the beacon merger causes an increase of the ethylene abundance at the mbar level, but falls short by a factor of 5 to fit the observations. On the other hand, acetylene and ethane remain unchanged in the model, while observations show that the abundance of acetylene had increased by a factor of 3 at the mbar level and ethane was unaffected. In a complementary study, Moses et al. (2015) have shown that downwelling winds of $-10\,\mathrm{cm{\cdot}s^{-1}}$ near the 0.1 mbar are required in addition to the chemistry effect to reproduce the observed abundances.

2.3 Perspectives with Herschel and ALMA observations

The observation of abundance increases in several hydrocarbons has led me to wonder whether this was also the case for oxygen species. Actually, and given the magnitude of the storm, the question was even if tropospheric oxygen material could have been injected in the stratosphere during the outbreak of the storm. After an unexpected detection of the beacon in an HssO map at 67 μm, I have led two programs to map H_2O with Herschel and CO with ALMA in 2012-2013. With these programs, I also aim at monitoring the stratospheric temperature and oxygen chemistry in the 2 years that followed the beacon merger. As an example, the observations of H_2O and CO in January 2012 are displayed in Fig. 3.7. Once I will get the Saturn's H_2O distribution in quiescent conditions published (see section 1.5), I will use it with the 3D temperature field retrieved from Cassini/CIRS data by Fletcher et al. (2012) to constrain any variability of H_2O in the beacon. I will do a similar work with the CO map. Preliminary results (Cavalié et al., 2012b,c; Testi and Andreani, 2013) indicate that the increase seen in the CO emission in the beacon region could be explained by the sole increase of the stratospheric temperature, while the increase seen in the H_2O emission requires additional H_2O. The hypothesis I proposed in Cavalié et al. (2012b) is that the increase in temperature around the mbar level caused the partial or total sublimation of the thin stratospheric H_2O cloud around the 10 mbar level, releasing thus additional vapor. This seems to be expected from model simulations of Moses et al. (2015).

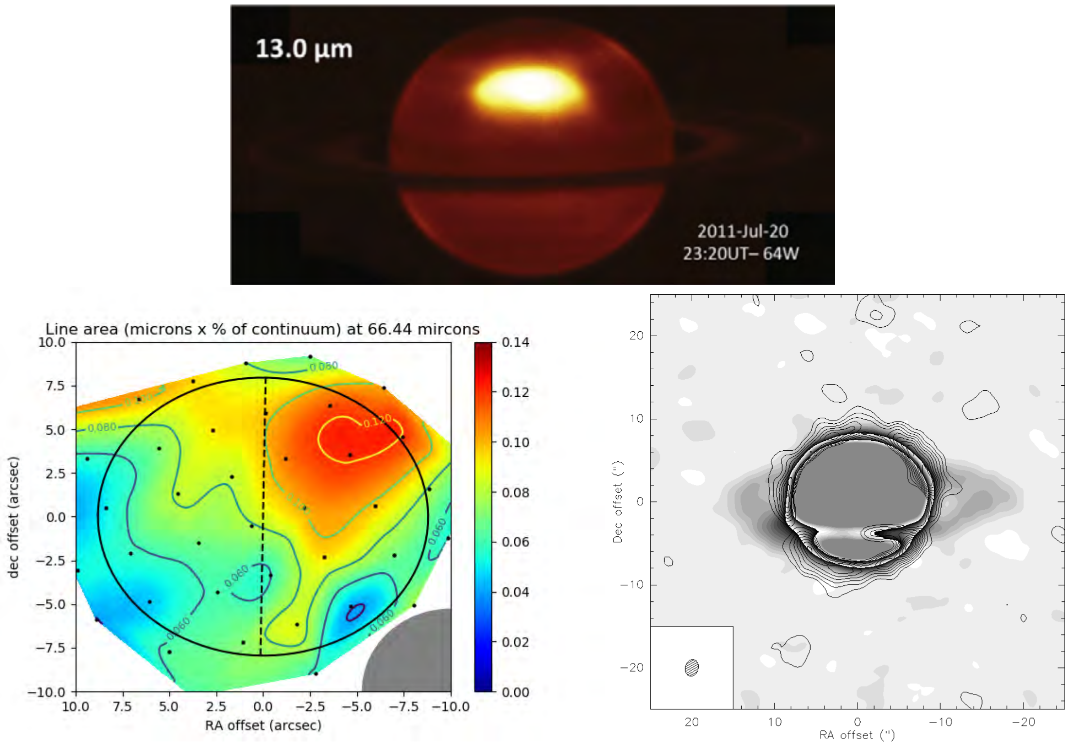

Figure 3.7: Observations of Saturn and its stratospheric beacon. (Top) VLT/VISIR observations of Fletcher et al. (2012) at 13 μm showing the beacon and associated the temperature increase in the vortex in July 2011. (Bottom left) Map of the H_2O emission obtained with Herschel, and (Bottom right) map of the CO emission (contours) and Saturn continuum (gray shades) recorded with ALMA, all in January 2012. The observations were set such that the beacon was located at the North-East limb to minimize longitudinal smearing caused by the rapid planet rotation during the exposures.

3 Dynamics of Jupiter's stratosphere

3.1 Introduction

It is possible to constrain vertical and meridional eddy mixing in Jupiter's stratosphere by modeling the distributions of the main hydrocarbons (Hue et al., 2018), and by observing the temporal evolution of the chemically stable SL9-derived species. The latter work has been initiated long ago by my colleagues of the Paris Observatory (e.g. Moreno et al. 2003, Griffith et al. 2004, Lellouch et al. 2006) and I have continued this work with a long-term monitoring of H_2O with the Odin space telescope (Cavalié et al., 2012a). This work continues at the time of writing and is presented in this part. In addition, I have obtained a map of SL9-derived species with ALMA in 2017. This high angular resolution map will be key in constraining long-term meridional mixing in the jovian stratosphere. At Saturn, Cassini/CIRS observations of the main hydrocarbons can be used to constrain vertical and meridional mixing (Guerlet et al., 2009, 2010; Hue et al., 2015).

For stratospheric wind measurements, the situation is more complex. While the tropospheres of the Giant Planets exhibit cloud features that can be tracked to derive their dynamics, the stratospheres lack such discrete and observable features. This is why, except wind field derivations from temperature field observations combined to application of the thermal wind equation (e.g. Flasar et al. 2004, Fouchet et al. 2008, Guerlet et al. 2011 and GCM modeling predictions (Medvedev et al., 2013), there is no clear view of what the stratospheric dynamics look like in the Giant Planets. (Sub)millimeter heterodyne spectroscopy will play a key role in the next years in assessing both the meridional and zonal components of stratospheric dynamics.

Thanks to the combination of high angular resolution and very high spectral resolution, ALMA data should now enable us to map zonal winds from direct Doppler shift measurements on the spectral lines. If so, these data will tell us if the tropospheric zonal wind patterns observed in Jupiter (Ingersoll et al., 2004) and Saturn (García-Melendo et al., 2011) extend to the stratosphere or if the stratospheric circulation regime is different. This technique of zonal wind mapping is going to be applied to Jupiter with my Cycle 4 data and to Saturn with the Cycle 5 data of T. Fouchet (LESIA). Such observations, to be also performed at Uranus and Neptune, will be provide us with unique constraints for the emerging GCMs (e.g. Guerlet et al. 2014) and pave the way for future space exploration. While stratospheric wind measurements are a secondary mission objectives for entry probes like the Hera, they will be the main goal of JUICE/SWI.

This section focuses more on current work and perspectives rather than on published results.

3.2 Temporal evolution of SL9 species in Jupiter's stratosphere

Following the SL9 impacts in Jupiter, Moreno et al. (2003) and Moreno and Marten (2006) have monitored the temporal evolution of the disk-averaged abundances of HCN, CO, and CS, with the IRAM-30m. Their observations show a slow but regular decrease of the various abundances by a factor of 5-15 in 10 years, and predict a slow vertical and meridional homogenization of the distributions. The timescale needed to homogenize these distributions is a key constraint on stratospheric vertical and meridional diffusion.

Lellouch et al. (2002) first studied the downward diffusion of H_2O deposited by SL9 and I have used subsequent SWAS and Odin observations to try and constrain the vertical eddy mixing (Cavalié et al., 2012a). Following these results, the monitoring of the H_2O emission at 557 GHz with Odin has continued ever since. K. Bermudez (Montpellier University), co-advised during his undergraduate internship by N. Biver (LESIA) and myself, has just completed the reduction of these data on the temporal evolution of the H_2O emissions. Subsequent modeling is now required to (in)validate the results presented in Cavalié et al. (2012a).

In parallel, Lellouch et al. (2006) have measured the meridional distribution of HCN and CO_2 with Cassini/CIRS in 2000. The HCN distribution was confirmed by Submillimeter Array (SMA) mapping (Moreno et al., 2007). The Cassini observations of HCN revealed a large south-north asymmetry, reminiscent of the SL9 impacts, and an abrupt decrease southwards of 45°S, indicative of a "dynamical barrier" isolating the southern polar region. On the other hand, CO_2 strongly peaked at the south pole. As CO_2 is a daughter molecule of the photochemistry of CO and H_2O, two species delivered by the SL9 impacts, it is difficult to understand how CO_2 and HCN could end up having so different meridional distributions. Either the two species are not located at the same altitudes, as proposed by Lellouch et al. (2006), or CO_2 has a strong (auroral?) source in the southern polar region.

With my ALMA Cycle 4 project and relevant 2D time-dependent photochemical modeling, I aim at constraining the long-term spatial variability of SL9 species and at understanding this discrepancy between the HCN and CO_2 meridional distributions. I will use HCN and CO maps at high angular resolution. Preliminary results (Cavalié et al., 2017a), shown in Fig. 3.8, indicate that (i) CO is rather uniformly mixed at all latitudes and present at altitudes for which $p<5$ mbar, (ii) HCN is rather uniformly mixed in the low-to-mid latitudes and located at the same altitude as CO, and (iii) HCN is only present at high altitude in the polar regions ($p<0.1$-0.2 mbar).

The fact that CO and HCN are present at the same altitude from the low-to-mid latitudes indicates that a different altitude location and different transport regimes are not the cause for the HCN/CO_2 distribution discrepancy seen by Lellouch et al. (2006). On the other hand, the lower stratospheric altitude cut in the HCN distribution at polar latitudes is surprising, as SL9-derived species should share the same vertical and horizontal distribution for chemically stable compounds. This means that HCN is removed in the polar region at pressures >0.1-0.2 mbar. Several processes can be invoked: (i) direct destruction by high energy electrons injected by the magnetosphere in the polar region (Gérard et al., 2014), or (ii) adsorption on aerosols and subsequent destruction by solid-state photochemistry as proposed on Titan (Anderson et al., 2016). Interestingly, the latitudinal extent of the aerosol distribution in the stratosphere of Jupiter is consistent with the latitudes where HCN is depleted (Zhang et al., 2013). A new ALMA H_2O map to be obtained in July 2018 and future JWST data to be obtained in the framework of the ERS project led by I. de Pater and T. Fouchet could help us to understand what processes are at play by providing us with additional contextual information on the distribution of oxygen species in Jupiter's polar regions.

In addition, a bright patch of HCN emission is colocated with the south polar auroral oval (see Fig. 3.9), indicating much higher temperatures in the oval for p<0.1-0.2 mbar, compared to other polar locations. Such a stratospheric auroral warming was identified in IRTF/TEXES data (Sinclair et al., 2017). Our data confirm this finding and will thus serve to link the auroral stratospheric temperatures with energy deposition by electrons in the auroral zone, as observed by Juno/UVS team and Hubble/STIS.

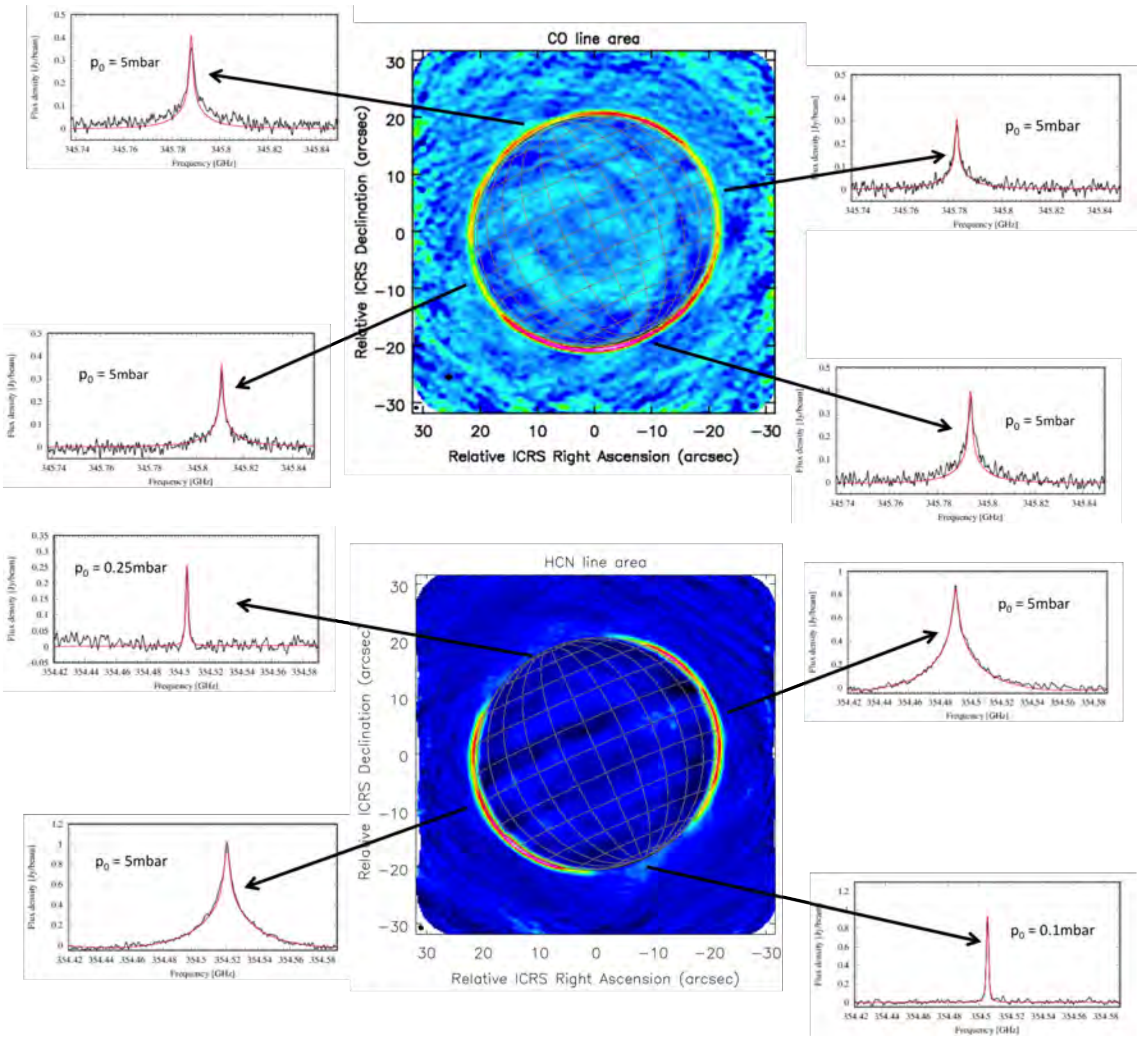

Figure 3.8: Observations of Jupiter (~40″) with ALMA in 2017. The angular resolution is 1″. (Top) CO line integrated map and spectra extracted from the E, W, N and S limbs. They essentially show that CO is meridionally well-mixed and present down to the 5 mbar level. (Bottom) Same plots for HCN, showing this species is meridionally well-mixed from low- to mid-latitudes and is also present down to the 5 mbar level. However, it is obvious that there is much less HCN in the polar regions and that HCN is located at much higher altitudes there (the lines are very narrow).

The measurement of the abundances of HCN and CO from the ALMA data of March 2017 will also enable me to refine prediction models of the HCN and CO abundances and spatial distributions for 2030, when we will observe these species with JUICE/SWI to measure stratospheric zonal winds of Jupiter.

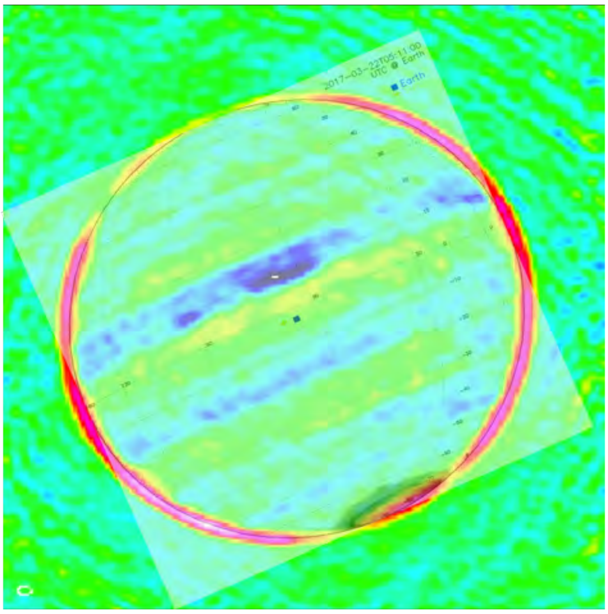

Figure 3.9: Superposition of UV aurora position prediction at the time of my ALMA Cycle 4 observations (gray map ; credits: V. Hue, Juno/UVS Team) and the HCN emission in the polar region (color map). I have selected the frequency bins in which the auroral emission is concentrated. As the HCN lines are very broad elsewhere on the limb, line wing emission causes the persisting low-to-mid latitude limb emissions on the map. The correlation between the southern auroral oval with the southern HCN emission peak is very good. This peak is caused by the auroral heating already observed by Sinclair et al. (2017).

3.3 Zonal winds in giant planet stratospheres

Atmospheric winds redistribute species that are not uniformly produced by (photo)chemistry in the stratospheres of the Giant Planets. It is thus essential to properly evaluate these winds. While upper tropospheric winds are measured with cloud tracking techniques, the stratospheres lack such dynamical tracers. Little is known about stratospheric winds, their magnitude, meridional variability, seasonal evolution, etc. It is thus not known yet whether tropospheric dynamics extend to the stratosphere.

Zonal winds can, in principle, be derived indirectly from the thermal structure through the thermal wind equation. Flasar et al. (2004) have deduced the presence of a strong tropical jet in the stratosphere of Jupiter. Orton et al. (1991) and Friedson (1999) have shown that the jovian tropical temperatures oscillate with a quasi-period of four years. The direction of the thermal wind should thus oscillate as well. This quasi-quadriennal oscillation (QQO) is thought to control the general circulation and chemical species distributions in the jovian tropics. Such oscillations exist in the Earth atmosphere (QBO) and in Saturn's stratosphere (SAO or QPO ; Orton et al. 2008; Fouchet et al. 2008). By analogy with the Earth, such oscillations seem to be resulting from interactions between atmospheric waves and the mean zonal flow (Li and Read, 2000; Baldwin et al., 2001).

The thermal wind equation technique however suffers from the following limitations: it cannot be applied at the equator and it requires a lower boundary condition. Direct stratospheric wind measurements are thus essential to constrain the mechanisms that create and maintain such oscillations, and more generally the stratospheric general circulation in the Giant Planets.

Heterodyne spectroscopy has proven that it is a useful tool to measure atmospheric winds directly from Doppler shifts of the spectral lines (Lellouch et al., 1991; Moreno et al., 2005, 2009; Cavalié et al., 2008b). However, there is a big challenge when trying to measure stratospheric winds in Giant Planets. Contrary to Mars and Venus, they are fast rotators and the measured Doppler shifts not only reflects wind velocities (few 10 to 100 $m{\cdot}s^{-1}$), but also the rotation of the planets (from 2.6 $km{\cdot}s^{-1}$ for Uranus to 12.6 $km{\cdot}s^{-1}$ for Jupiter). The equatorial rotation velocity of Jupiter and Saturn is about 2 orders of magnitude stronger than the anticipated winds. It is thus primordial to precisely locate the atmospheric limb in the observations to properly subtract the planet rotation and eventually measure the winds.

Even though measuring stratospheric winds with single dish antennas (e.g., IRAM-30m) and their low spatial resolution has always been extremely challenging, V. Hue (SwRI) and I are attempting to detect the equatorial jet in Jupiter's stratosphere (Flasar et al., 2004) with the IRAM-30m with data collected in January 2014. We have adopted the limb-switching technique on the HCN line at 265 GHz to cancel out baseline ripples caused by the strong planetary continuum, and we have used the highest sampling rate allowed by the system, with individual integration times of 125 ms, to avoid suffering from pointing instability. In such a short time and despite the 9″ resolution (with respect to a 45″ Jupiter), the pointing uncertainty is minimal (less than $0.1''$) and continuum is still very precisely measured allowing us to retrieve the pointing and remove the contribution of the planet rotation. We will then average all the individual spectra to try to reveal any strong stratospheric wind. Time (and work) will tell whether this attempt will be successful.

A great perspective with ALMA and its capabilities of extended mapping, high spatial resolution and high spectral resolution, is that of enabling the measurement of zonal winds in the stratospheres of the Giant Planets. The first obvious targets are Jupiter and Saturn, given their sizes. Mapping zonal winds in the stratospheres of these planets is one of the goals of two projects I am involved in. The first is the one I am leading for Jupiter and that is presented in the previous section. The second, led by T. Fouchet (LESIA), focuses on Saturn and data have been obtained in July 2018. In both cases, the main challenge remains the subtraction of the planet rotation. However, the high angular resolution combined to self-calibration should enable us to precisely retrieve the pointing from the continuum map and thus subtract the planet rotation component from the Doppler shifts.

All these observations will eventually be compared to the predictions of the LMD and MPS GCMs (Guerlet et al., 2014; Medvedev et al., 2013). In this sense, I want to reinforce the collaboration with the MPS team, by applying to the Bordeaux IdEx in 2019 to obtain funding for a PhD thesis or postdoc to be done in co-supervision with the MPS, as the University of Göttingen is a partner of the Bordeaux University in this program. The main goal would be to couple the chemistry expertise of the Bordeaux ASP Team with the GCM expertise of the MPS Microwave Team.

3.4 Perspectives

ALMA (and NOEMA in the northern hemisphere) is clearly the optimal observatory for the next ten years for stratospheric circulation characterization of the Giant Planets. In this sense, I will pursue my collaboration with the Planetology group at LESIA to monitor stratospheric winds in Jupiter and Saturn. On the longer term, an atmospheric entry probe, like the Hera ESA M5 mission unsuccessful candidate (Mousis et al., 2014, 2016), would enable us to measure (among other things) the vertical profile of the zonal wind at the latitude of entry. This would provide us with ground truth to be compared with the ALMA results.

Even though the angular resolution of ALMA is more limited for Uranus and Neptune, and even if there is a limited number of strong enough spectral lines in the stratosphere of Uranus, it should be possible to map zonal winds in the stratospheres of the Ice Giants and to compare the obtained wind pattern with tropospheric measurements (Hammel et al., 2005; Sromovsky et al., 2012; Fitzpatrick et al., 2014). The fact that the sub-Earth latitude of Uranus is constantly increasing since equinox in 2007 (and will reach 45° in the next few years) renders a detection more difficult, as the observable is the wind velocity times the cosine of this angle. However, it should not yet be seen as a limitation in the next years. In the (much) more distant future, Uranus and Neptune orbiter missions may be launched and embark atmospheric entry probes. A study report that emphasizes the improved science return of the combined orbiter/probe concept has recently been published for NASA by Hofstadter and colleagues[1]. In response to this work, the Hera team has published the science goals and an adapted version of its Hera Saturn

[1] https://www.lpi.usra.edu/icegiants/mission_study/Full-Report.pdf

probe concept to Uranus/Neptune (Mousis et al., 2018) in preparation of an NASA-ESA collaboration on such a mission. The timeframe the launch of such a mission is the late 2020s-early 2030s.

On the shorter term, the continuation of the analysis and interpretation of the Jupiter maps I have obtained with ALMA is the next natural step for me in trying to better understand the dynamics of the jovian stratosphere. From these data and adequate 2D photochemical modeling, I will be able to constrain meridional transport by fitting the observed distributions of HCN and CO. Fitting the temporal evolution of the abundances of these compounds will also be key in better understanding the chemistry of oxygen and nitrogen species in the jovian stratosphere. The spectral maps obtained with a very high spectral resolution will also enable me to produce the first complete map of stratospheric zonal winds. I will thus be able to determine whether or not the tropospheric wind pattern extends to the mid-stratosphere. If I detect stratospheric winds, I intend to apply for ALMA time every year over several years to better constrain the QQO. This work will come in preparation of the JUICE/SWI observation campaign, for which we aim at monitoring the jovian stratospheric circulation over the course of the mission.

4 Contributions to the JUICE mission and to SWI

4.1 Presentation of the JUICE mission

The JUICE mission is the first flagship mission of ESA and was selected in May 2012. It will explore Ganymede as a planetary object and possible habitat, Europa's recently active zone, and Callisto as a remnant of the early jovian system. JUICE will also study Jupiter and its system as an archetype for giant planets, by characterizing its atmosphere, magnetosphere, and satellite and ring system.

To fulfill these goals, ESA selected a payload of 10 instruments and a science investigation in February 2013: 3GM (radio science experiment), GALA (laser altimeter), JANUS (imaging system), J-MAG (magnetometer), MAJIS (visible-infrared hyperspectral imaging spectrometer), PEP (particle package), RIME (ice penetrating radar), RPWI (radio and plasma wave instrument), SWI (submillimetre wave instrument), UVS (ultraviolet imaging spectrometer), and PRIDE (VLBI experiment). JUICE is currently in its implementation phase at the spacecraft level by Airbus Defense and Space, and at the instrument level by the instrument consortia.

The mission launch is currently set for May 2022. After an Earth-Venus-Earth-Mars-Earth gravity assist, JUICE will reach Jupiter and proceed with Jovian Orbit Insertion (JOI) in October 2029. A 2.5 year Jupiter tour will then start. It is comprised of 5 phases:

- Phase 1 (Pre-JOI and first ellipse): characterized by large Jupiter distances (except during JOI),
- Phase 2 (Energy reduction phase): first Jupiter equatorial phase,
- Phase 3 (Europa flybys): short period that includes the 2 Europa flybys,
- Phase 4 (Inclined phase): the S/C uses Callisto flybys as a ladder to reach up to $\pm 30°$ sub-spacecraft latitude (and get a better view of Jupiter's polar regions), and then to go back to the equatorial plane,
- Phase 5 (Low energy phase): second Jupiter equatorial phase and approach to Ganymede.

Depending on the final trajectory, these phases include about 30 close flybys of Ganymede and Callisto, and the two Europa flybys. The Jupiter tour will be followed by a Ganymede Orbit Insertion (GOI) and a 9-month Ganymede orbital phase which comprises:

- GEO I: First Ganymede elliptic orbit phase,
- GCO5000: Ganymede circular orbit at 5000 km altitude,
- GEO II: Second Ganymede elliptic orbit phase,

- GCO500: Ganymede circular orbit at 500 km altitude.

This tour (see Fig. 3.10 for the Jupiter tour) is designed to ensure a variety of spatial resolutions and viewing geometries on all objects to be studied so that all mission science goals are fulfilled (refer to JUICE Red Book and Science Requirements document). After this nominal mission, and depending on delta-V, JUICE will either crash on the surface of Ganymede or complete an additional GCO200 phase.

The scientific coordination of the mission is under the responsibility of the Science Working Team (SWT), which is comprised of the Project Scientist, the instrument PIs, and the Interdisciplinary Scientists (IDS). The SWT is assisted by the Science Operation Center (SOC) and the Science Working Groups (WG).

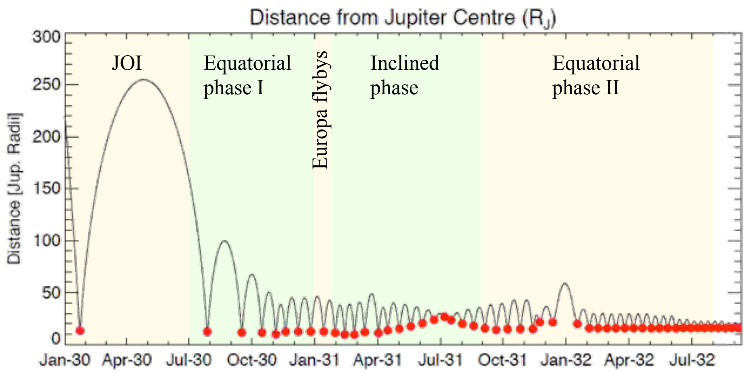

Figure 3.10: Example of a possible Jupiter tour for JUICE, in terms of distance to Jupiter. Red dots indicate perijoves.

4.2 The Submillimetre Wave Instrument (SWI)

One of the selected instruments of the JUICE payload is SWI. The PI is P. Hartogh (MPS). SWI is currently being implemented by a consortium of several institutes and companies (mostly european). I joined the SWI Science Team in 2009 when it was proposed for the model payload of what then was the Europa-Jupiter System Mission.

SWI is a 29-cm submillimeter telescope equipped with spectrometers/radiometers operating in two channels: 530 – 625 GHz (566 – 480 μm) and 1080 – 1275 GHz (277 – 235 μm). The suite of very high and high resolution spectrometers will ensure $R = 10^6$–10^7 (Chirp Transform Spectrometers – CTS, and Auto-Correlator Spectrometers – ACS, respectively). In addition two continuum detectors (CCH) will enable us to perform continuum radiometry. The instrument is further equipped with a scanning mechanism that will allow us to point $\pm 72^\circ$ along-track in the Jupiter phase (and cross-track in the Ganymede phase) and $\pm 4.3^\circ$ cross-track in the Jupiter phase (and along-track in the Ganymede phase) away from nadir. The scanning mechanism will allow us to map Jupiter and the Galilean moons from any point in the trajectory. The science goals of the instruments are the following:

- Characterize the composition and dynamics of Jupiter's stratosphere, and its coupling with the lower and upper atmosphere. Mapping observations of CH_4 and SL9-derived species lines with $R = 10^7$ and a very high signal-to-noise ratio will enable us to retrieve simultaneously the temperature, abundance and wind properties of the stratosphere as a function of latitude, longitude and time.

- Characterize the atmospheres of the Galilean satellites to determine their sources, sinks, and interactions with the jovian magnetosphere. Daily monitoring during the Jupiter phase (using the scanning mechanism), and very high spatial resolution mapping observations during flybys and

Ganymede phase, will enable us to constrain the H_2O atmospheres of Europa, Ganymede, and Callisto, and the SO/SO_2 atmosphere of Io. We will also assess the presence of other compounds.

- Determine isotopic ratios in the atmospheres of Jupiter and its satellites to constrain their origin, formation, and evolution. The SWI bands include the isotopic signatures of all main species that will be observed (H_2O, CO, HCN, CS, NH_3, SO, SO_2, etc.).
- Measure the surface and subsurface properties of the satellites to constrain their composition. Combined with atmospheric observations, we will be able to confirm the cryovolcanic activity hinted by the detection of H_2O plumes on Europa (Roth et al., 2014; Sparks et al., 2016), and further detect hot spots and cryovolcanic activity on Ganymede and Callisto.

The design of the instrument validated during the Instrument Preliminary Design Review (2017) is shown in Fig. 3.11.

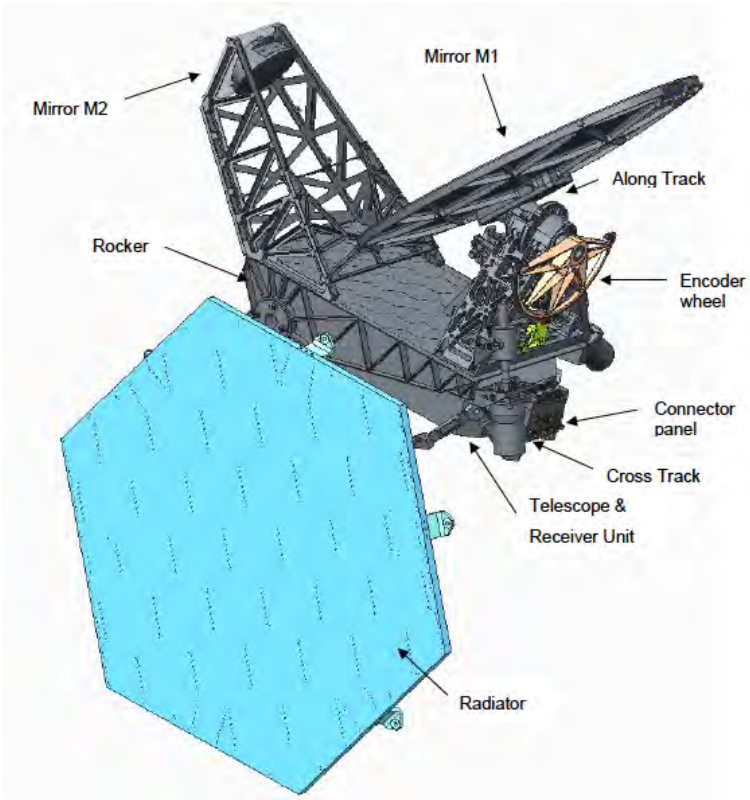

Figure 3.11: Design of SWI as of January 2018.

4.3 Preparation of the operations and scientific return of SWI and the JUICE mission

From science objectives to observation planning

The first task I have worked on after the selection of SWI was the translation of the science objectives into measurement requirements for Jupiter. I have then tried to list all the observations SWI needs to perform to fulfill its goals at Jupiter. With our radiative transfer models, we must then simulate these observations to estimate at best the required integration time. This simulation work has started and is underway in Bordeaux. In parallel and with inputs from the team, I have listed and detailed all the observation modes of SWI required to perform the observations in a so-called observation mode library (refer to publication list). I first delivered it to SOC in the Summer of 2015, and I am regularly providing the SOC with updates. We will use these observation modes in a plug-and-play fashion to put together our observation plan.

An Observation Planning Tool (OPT) for SWI is currently in development at LAB under my supervision. The idea is to render the choice of the observations to be executed (and thus the sequence of observation modes) as automatic as possible. This choice depends on several factors: the list of observations that remain to be performed, the orbital conditions (distance to the various targets, phase angle, etc.), and pre-established scheduling rules. The goal of the OPT is thus to semi-automatically produce a sequence of observations with appropriate parameters and time stamps. This sequence will eventually be uplinked to the instrument for execution, after cross-validation by the SWT with other instrument sequences. My aim is to have a first working version of the OPT in early 2019.

Preparation of SWI operations

At the time of operations, the Mission Operation Center (MOC) will collect the team inputs in terms of instrument commanding sequences. The low-level sequencing of observations will be organized at the Working Group level (see next section) to fix the timeline of operations and the attitude of the S/C, and to comply with S/C pointing and power resources. Instrument teams will then have to produce the detailed commanding sequence of their instrument and send it to MOC for implementation and uplink to the S/C.

MOC has issued limitations in terms of uplink data volume per instrument which are quite severe for SWI: 100 telecommands/day. Because SWI is a 1-pixel instrument, it requires a significant number of pointings to complete mapping observations, mirror movements for calibration, etc. So, if each of these individual operations would need to be translated into single telecommands, SWI would only be able to operate for a few minutes each day because it would exceed the telecommand limitation. This is why we had to agree with MOC on a different strategy for SWI. We decided to wrap individual instrument commands into instrument modes, which in turn would be used within observation modes (or observation templates). This means the Digital Processing Unit (DPU) of SWI has to be loaded with all the possible individual commands, instrument and observation modes. And the instrument and observation modes are scripts with appropriate parameters that enable the DPU to reconstruct the sequence of individual operations.

Since 2017, I have been coordinating a small team (E. Wirström, Chalmers University, and F. Herpin, LAB) on the definition and writing of these scripts, and I am the contact person on these matters for the DPU developers, SWI system engineer and project manager, and SOC/MOC. There are several tens of instrument modes and observation templates, as we must make sure we can operate the instrument in any possible instrument configuration (two receivers vs. one-receiver-only, CTS+CCH vs. CTS vs. ACS+CCH vs. ACS vs. CCH, position-switching vs. frequency-switching, etc.) and for any type of observation (stare, raster map, cross, etc.). After a first comprehensive delivery in December 2017, we aim at completing the script preparation task for the Summer of 2018 in view of the Engineering Model (EM) delivery to ESA. On the longer term, we need to validate the observation modes of the DPU with an instrument simulator. Such a simulator does not currently exist and will have to be developed.

Preparation of observation analysis

The first step in getting ready for data analysis is to validate all our radiative transfer and retrieval models.

There are several different radiative transfer models in the SWI Team, including LTE models for Jupiter and non-LTE models for the moons. I have coordinated this effort for the Jupiter codes. I have first put together a Jupiter atmosphere reference model and other model input parameters for everyone to compute a list of spectral lines under the same physical conditions. We have then cross-compared our codes for a list of representative spectral line observations, and I have written an internal report on this comparison and validation work (refer to publication list).

At this stage, I must recognize that one of the weaknesses of the french team is the lack retrieval model for Jupiter. Ideally, we should develop our own (and validate it versus the other ones) to be able to retrieve temperatures and winds from the measurements in a more automatic way.

All the activities that have to be performed from the definition of science objectives to the production of science results, and that I have described in the previous sections, are displayed in the flowchart of Fig. 3.12.

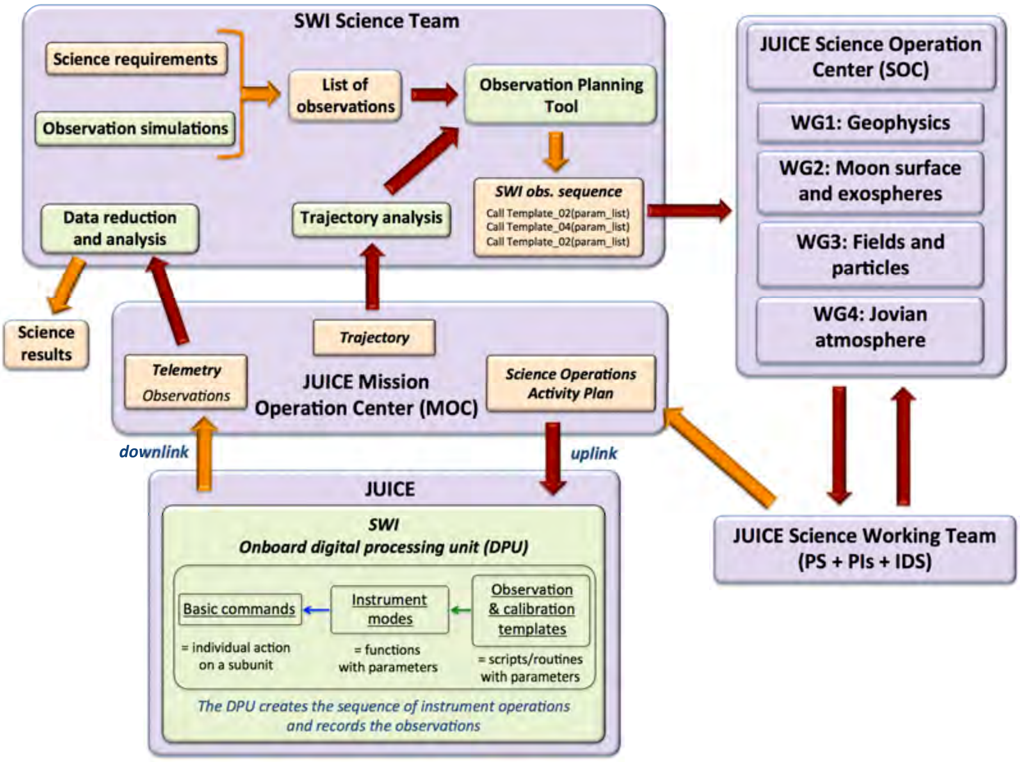

Figure 3.12: Flowchart describing the chain of events and interactions between the definition of the SWI science requirements and the production of science results. Mauve boxes stand for groups of people, green boxes for software operations, and orange boxes for data/information. Orange arrows indicate production of data and red arrows stand for information transfer.

Coordination of the "Working Group 4: Jupiter" of ESA and SWI

The Jupiter science Working Group (WG4) is one of four groups assembled to provide both scientific and operational support to the JUICE SWT. The science investigations covered by WG4 are those relevant to Jupiter's highly variable atmosphere from its upper troposphere to its lower thermosphere, nominally with the MAJIS, JANUS, SWI, UVS, and 3GM remote sensing instruments. They involve the long-term coverage of Jupiter's atmospheric key chemical and dynamical processes spanning timescales from hours to weeks, months and years. Since April 2015, WG4 is co-lead by L. Fletcher (Leicester University) and myself. It comprises more than 50 people, among which the PS, the PIs of all instruments, and experts from instrument teams in the fields relevant to our WG. The science and investigations covered by our WG have some overlap with WG2 ("Surfaces and near-surface exospheres of satellites, dust and rings") and WG3 ("Jovian magnetosphere and plasma environment").

Our primary goals are to (i) consolidate and update the Jupiter science goals/requirements for JUICE, (ii) prepare detailed observational strategies for each instrument, (iii) to assemble these strategies into sequences of observations during the jovian tour for MAPPS simulation by the SOC, (iv) to assess the science return from the tour as a whole, and (v) to understand opportunities for synergistic observations between instruments.

The first task of the WGs in 2015 consisted in simulating operations over GCO500, a Europa flyby, and a full Jupiter orbit (that included a Ganymede flyby), to assess the science return when considering S/C limitations in terms of power and downlink capabilities. WG4 was obviously only involved in the latter study. This work was delivered to the SWT at the end of 2015 and the SOC has used it to prepare the JUICE Science Requirement Review. The SWT then identified the need for an overall analysis of the tour to better assess the operational requirements to meet the science goals.

In early 2016, the SWT thus tasked the WGs perform a top-level science analysis of the global tour to identify priorities, dedicated campaigns as function of the mission phase. We have spent the following 2 years defining trajectory segments for Phases 2 to 5 of the Jupiter tour. Segments must be understood as periods where WG instruments require control of S/C pointing to acquire their observations. In this approach, detailed planning within a segment and power limitations were not considered. I have produced a software tool for the SWI Team to analyze and segment the trajectory using SPICE kernels[2] based on SWI observation requirements. After collecting inputs from all involved teams, we were able to define a limited set of generic segments for the Jupiter tour Phases 2 to 5 for WG4:

- Perijove segments: $\pm$50 hours (i.e., 10 Jupiter rotations) surrounding the closest approach to Jupiter (PJ), minus downlink windows, minus $\pm$12 hours surrounding primary satellite encounters, and minus short observations of distant satellites. These windows are our highest priority for high spatial resolution remote sensing. In some specific cases, these windows could be extended to $\pm$100 hours and/or downlink could be suspended to allow for intensive observation campaigns.

- Phase angle segments: where not included within the Perijove segments, 10 hours centered around (or as close as possibleto) 0°, 90° and 180° phase angle to study aerosol properties and lightning activity.

- Inclined segments: 20 hours around the maximum northern and southern inclinations, when the sub-S/C latitude exceeds $\pm$5°, to provide good coverage of the polar atmosphere and aurora.

- Monitoring segments: 10 hours every 2-3 days for regular remote sensing observations outside of the regular segments.

- Event-driven segments: windows for any unique/time-critical events outside of the segments defined above (e.g., occultations, Jupiter disk transits). Most of these segments are likely to fall within Perijove segments.

- Synergistic segments: windows of favorable observing to ensure all instruments work together to study a particular phenomenon (e.g., multi-spectral imaging of storm systems, lightning activity, auroral phenomena, cloud tracking, etc.). Most of these segments are likely to fall within Perijove segments.

I have provided WG4 with a simpler version of my segmentation tool to automatize the segmentation at the WG4 level, and an example of such segmentation for WG4 is displayed in Fig. 3.13.

The SOC has collected inputs from all WGs to identify conflicts and propose rules to solve them. These results have been implemented in an online tool that can generate automatically a segmentation for any new trajectory in the future, and thus facilitate higher level detailed planning (e.g. with the SWI

[2]SPICE is an "information system developed by NAIF to assist [...] scientists in planning and interpreting scientific observations from space-borne instruments, and to assist [...] engineers involved in modeling, planning and executing activities needed to conduct planetary exploration missions" (SPICE website: https://naif.jpl.nasa.gov/naif/spiceconcept.html).

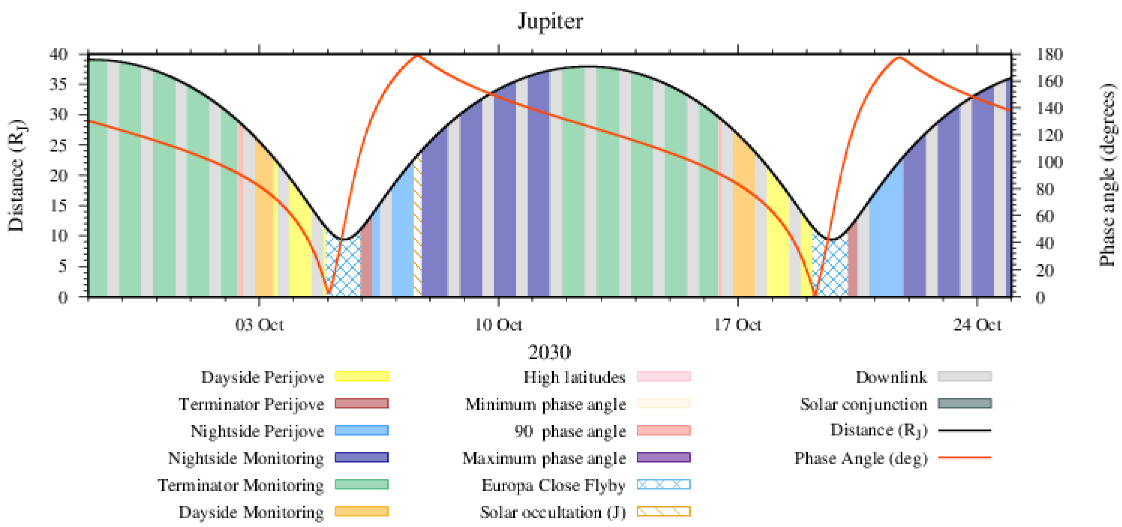

Figure 3.13: Example of the WG4 segmentation proposed for Phase 2 of the Jupiter tour. This is a simple example to keep it reader-friendly and still show the variety of Jupiter distance/illumination conditions.

OPT). The next steps will consist in applying the segmentation work to the Ganymede phase and then to assess resources within each WG segments to estimate feasibility of operations and produced data volume.

We have written several reports that summarize our work on these aspects: SWI and WG4 Jupiter-G5 report, SWI and WG4 Jupiter tour segmentation report.

4.4 Calibration activities

The Calibration Kick-off meeting for SWI and its subunits took place at MPS in November 2017. The list of calibration operations has been established by a team comprising scientists and engineers. The Calibration Team is coordinated by C. Jarchow (MPS) and includes four other scientists who all have experience from Herschel: R. Moreno (LESIA), F. Herpin (LAB), M. Rengel (MPS) and myself. As soon as subunits (and workforce!) become available for testing, or latest when the instrument is first assembled (end of 2018 - early 2019), we will proceed with calibration campaigns for:

- Spectral calibration: CCH passband shape, CTS and ACS frequency scale, channel response, and frequency drift vs. temperature
- Spatial response: beam characterization, pointing calibration
- Intensity calibration: sideband ratio, noise temperature, emissivities
- Stability: Allan variance
- Signal purity: spurs, standing waves

Similar activities will continue on a regular basis with inflight calibration campaign after launch.

4.5 Conclusion and perspectives

JUICE and its SWI instrument are going to revolutionize our understanding of Jupiter's middle atmosphere in terms of chemistry and dynamics. For instance, while ALMA will provide us with snapshots of the stratospheric wind structure, SWI will be the first instrument capable of directly measuring simultaneously the composition, temperature and stratospheric winds on a daily basis and over about 3 years. Following my recent ALMA observations of the jovian southern aurora oval, I am looking forward to synergistic science between SWI and UVS to better characterize the coupling between Jupiter's magnetosphere and its stratosphere (e.g., exogenic inputs of material and energy, ion-neutral chemistry).

We are halfway between the instrument selection (2013) and launch (2022 at best). There are still numerous milestones to pass at the instrument development level. The first fully assembled model of SWI should be available in the course of 2019. This will allow us to perform all necessary ground calibration measurements. In the meantime, we have to complete the development of the commanding of the instrument. Once inflight, we will take advantage of the long transfer time to Jupiter and of the Earth and Mars flybys to perform inflight calibration. This should bring us at the beginning of the 2030s, ready for data acquisition, analysis, interpretation... and so many discoveries!

5 Conclusion

In this chapter, I have first summarized the main results I have obtained regarding the chemistry and dynamics of the giant planet stratosphere, in an attempt to better understand how they work.

Using space-based telescopes (Odin and Herschel) and time-dependent photochemical modeling, I have shown that the bulk of Jupiter's stratospheric water originates from the SL9 impacts in 1994. I have also obtained the first submillimeter observations of CO in the stratospheres of Saturn and Uranus, from which I have shown that a cometary origin is the more likely scenario for Saturn, and that CO has an external source in Uranus. I have participated in the study that has enabled the first detection of the water torus produced by the geysers of Enceladus around Saturn. This torus is probably the ultimate source of H_2O of Saturn's stratosphere, according to Herschel data I am currently analyzing. With Herschel and ALMA, I have also obtained data that show the stratospheric counterpart of Saturn's Great Storm of 2010-2011, but these data remain to be analyzed.

I have then detailed the perspectives offered by observatories like ALMA to map the circulation in these stratospheres, from direct imaging of the Doppler shifts induced by winds on the spectral lines. On the longer term, I will take part in an extensive study of Jupiter's stratospheric chemistry and dynamics with the SWI instrument of the JUICE mission.

Conclusion

In this manuscript, I have presented my research work over the past 10 years in (sub)millimeter observation and modeling of the Giant Planets of the Solar System, in an attempt to better understand their formation and evolution. This work is primarily based on ground- and space-based observations and on the preparation of space missions with remote sensing and in situ instrumentation like JUICE and Hera. All observations require adapted models for interpretation, and I have contributed to the development of several atmospheric models.

In the first chapter, I have detailed the new models I have developed or contributed to, and that are adapted to very high spectral and spatial resolution observations I perform. My radiative transfer model in 3D ellipsoidal geometry is a continuous development project to keep it state-of-the-art. I use it almost on a daily basis either to analyze or prepare new observations. It is now also adapted to Titan, thanks to S. Cuzacq (Bordeaux University), and only a final validation is missing before it can be used by the ASP Team of LAB for observation proposals, data analysis and photochemical model testing against observational data. In parallel, I am pursuing my modeling effort by contributing to the development of thermochemical and photochemical models. We are currently working to parallelize our model solver, especially to be able to run 2D time-dependent photochemical simulations with full ion-neutral chemical networks rather than reduced ones. We are also updating the methanol block of our thermochemical network to better constrain the deep composition of Giant Planets. All these models have (or will have) exoplanetary applications (in the future).

In the second chapter, I have shown how remote sensing observations in the (sub)millimeter domain can help us to constrain the deep composition of Giant Planets and therefore their formation. We have achieved new measurements of the D/H ratio in all Giant Planets with Herschel and the publication of the Jupiter and Saturn values is the next step. We have performed observations of tropospheric CO and coupled the result with thermochemical modeling to estimate the deep oxygen abundance of Saturn, Uranus and Neptune. With the recent update of our thermochemical network, and by accounting for the inhibition of convection caused by the condensation of H_2O in the troposphere, we will establish refined deep oxygen abundances for all Giant Planets in the near future. In parallel, I am participating in an international effort to visit the Giant Planets with in situ atmospheric probes and obtain ground truth measurements of their composition. While our Saturn Hera mission proposal has recently been rejected by ESA, we have started adapting our concept to a mission to the Ice Giants as ESA will soon start a study to explore how it could best contribute to a NASA a flagship mission to these worlds. In the NASA latest study, an atmospheric probe to either planet is a very high priority, and ESA could contribute to such a mission by providing it. Discussions on the payload instrumentation had already started during the Hera proposal campaign, and I am managing an effort to get the electronics of the mass spectrometer, which could be embarked on an ESA probe, produced at LAB.

In the third chapter, I have presented the core of my work, which consists in characterizing the chemistry and dynamics of the Giant Planet stratospheres to better understand how they work. Most observations I have led and participated in the past years targeted exogenic species like H_2O and CO to constrain their external sources. These observations, obtained with observatories like Herschel and more recently ALMA, show that all types of sources (IDP, icy rings/satellites, and large comet impacts) seem to be at work in the Giant Planets, though in different proportions for each planet. While CO seems to be caused by comet impacts in all Giant Planets, H_2O seems to be originating from comet SL9 at Jupiter, the Enceladus geysers at Saturn, and IDP at Uranus and Neptune. With the dramatic increase of sensitivity and spatial resolution enabled by ALMA, submillimeter observations will now serve to directly measure Doppler winds in Giant Planet stratospheres to constrain their general circulation. In one decade form now, the JUICE mission with the SWI instrument will enable us to monitor Jupiter's stratospheric chemistry and circulation over the 3.5 years of the nominal mission.

The preparation of SWI both scientifically and technically, and of the JUICE mission at the Working Group level, is an investment for the future. I feel very lucky to participate in a mission from its start and hopefully until it is completed. I am currently devoting a significant part of my work time on the preparation of the JUICE mission, and I could not have done that without my permanent researcher status at CNRS. I hope young scientists will continue to have the chance of accessing such kind of positions and see other missions (like Uranus/Neptune orbiters/probes) from their proposal and development stages to the completion of their science programs.

At the time when we are discovering an ever increasing number of exoplanets, we must not forget that we have fantastic worlds within our reach and that the planets of our Solar System are so diverse that we can still learn a lot on planets in general by studying them with remote sensing and in situ techniques. In this sense, understanding how our own Solar System formed and how its works is complementary to exoplanet studies and cannot be disentangled from them.

Research program

The projects I work on aim at addressing the questions of the formation, evolution, chemistry and dynamics of the Giant Planets of the Solar System. The observation programs my work is articulated around are listed in Table 3.1 and my main collaborations are presented in Fig. 3.14. In what follows, I present my research program and development projects in a synthetic way and expected chronological order, with • for projects I am contributing to and ⋆ for projects I am leading. Most points are more explicitly detailed in chapters 1, 2 and 3.

Because of my move to LAB in September 2018, I have slightly adapted this program to better fit the LAB ASP Team science objectives.

Table 3.1: My current observation programs (either accepted or executed).

Title	Telescope	Type	Role
Constraining the internal and external sources of CO in Saturn's atmosphere	IRTF	Standard	Co-I
The Jupiter System	JWST	ERS	Science Team
Are the Enceladus geysers the source of Saturn's water ?	ALMA	Cycle 5	PI
Constraining Jupiter's atmospheric chemistry and dynamics from H_2O mapping in ALMA band 5	ALMA	Cycle 5	PI
The first direct measurement of Saturn's stratospheric winds	ALMA	Cycle 5	Co-I
Constraining Jupiter's atmospheric chemistry and dynamics from post-SL9 species mapping	ALMA	Cycle 4	PI
HCN emission: a diagnostic of Enceladus cryovolcanic activity and torus dynamics	ALMA	Cycle 2	Co-I
Probing the vertical structure of Saturn's storm with ALMA	ALMA	Cycle 0	PI
Water and related chemistry in the Solar System	Herschel	Guaranteed Time Key Program	Associate Scientist
Probing the temperature and chemistry of Saturn's storm with Herschel	Herschel	Open Time	PI
Probing the Enceladus torus with Herschel	Herschel	Open Time	Co-I
Variability in Ice Giant Stratospheres: Implications for Radiative, Chemical and Dynamical Processes	Herschel	Open Time	Co-I
The spatial distribution of CO in Saturn	SMA	Standard	PI
Observation of an equatorial jet in the atmosphere of Jupiter	IRAM-30m	Standard	PI
The origin of CO in Saturn's atmosphere	VLT	Short Program	Co-I
Jupiter's stratospheric HCN, hydrocarbon and temperature fields	SOFIA	Cycle 3	Co-I

Development projects for atmospheric models

Radiative transfer modeling

1. • Interface with an inversion model (e.g. optimal estimation method)
2. ⋆ Validation of the new Titan version of the model
3. ⋆ Account for vertical Doppler wind lineshifts in simulations

Photochemical modeling

1. ⋆ Parallelization of the model solver to account for more complex chemical networks (e.g. ion-neutral networks)
2. • Development of an ion-neutral chemical network for auroral chemistry
3. • Coupling of photochemical and general circulation models

Thermochemical modeling

1. • Update the CH_3OH block of the chemical network
2. • Extension of the chemical network to P (and S) species

Formation of the Giant Planets

Physico-chemical conditions of the formation of planetesimals

1. • Determination of the deuterium abundance in Jupiter and Saturn with Herschel
2. • Proposition of an atmospheric probe based on the Hera concept for a NASA-ESA Ice Giant flagship mission

Condensation processes of primordial ices

1. • Saturn's tropospheric CO with VLT/CRIRES and IRTF/CSHELL
2. ⋆ The deep oxygen abundance of Saturn
3. ⋆ Revision of the deep oxygen abundances of Uranus and Neptune

Seasonal chemistry in the stratospheres of the Giant Planets

Jupiter's stratospheric chemistry: temporal evolution of SL9-species

1. ⋆ Long-term evolution of the meridional distribution of SL9-species in Jupiter's stratosphere with ALMA
2. ⋆ Long-term evolution of the H_2O abundance in Jupiter's stratosphere with Odin
3. • Auroral chemistry with ALMA and JWST observations, and associated photochemical modeling
4. • Very long-term evolution of SL9-species with JUICE/SWI

The Saturn-Enceladus system

1. ⋆ Meridional distribution of H_2O in Saturn's stratosphere with Herschel and ALMA: is Enceladus the source?
2. • Physico-chemical characterization of the Enceladus torus with Herschel and ALMA
3. • Meridional distribution of CO and HCN in Saturn's stratosphere with ALMA
4. • The origin of exogenic species in Saturn's stratosphere: cometary and/or Enceladus?

Seasonal evolution of Saturn's stratosphere

1. ⋆ Physico-chemical evolution of Saturn's stratosphere during the Great Storm of 2010-2011 with Herschel and ALMA
2. • Saturn's stratospheric zonal winds with ALMA

Dynamics of the stratospheres of the Giant Planets

Jupiter's stratospheric dynamics from observations of SL9-species

1. ⋆ Vertical mixing in Jupiter's stratosphere: long-term monitoring of SL9 species
2. ⋆ Stratospheric zonal wind field with ALMA
3. • GCM modeling of Jupiter's stratosphere
4. • Seasonal mapping of zonal winds in Jupiter's stratosphere with JUICE/SWI

Saturn's stratospheric dynamics

1. • Stratospheric zonal wind field with ALMA
2. • GCM modeling of Saturn's stratosphere

Science themes	Observation programs			Models		Space missions	
	Telescope	Role	Collaborators	Type	Collaborators	Name	Collaborators
Formation of the giant planets 	VLT JWST IRTF	Co-I Science Team Co-I	T. Fouchet, E. Lellouch, B. Bézard, D. Bockelée (LESIA)	Thermochemistry Tropospheric thermal structure	O. Venot (LISA) R. Bounaceur (LRGP) J. Leconte, F. Hersant, F. Selsis (LAB)	Hera	O. Mousis (LAM) D. Atkinson (JPL) P. Wurz (Univ. Bern)
Spatio-temporal evolution of the atmospheres of giant planets 	ALMA JWST SOFIA Herschel SMA	PI Science Team Co-I PI, Co-I PI	R. Moreno, E. Lellouch, T. Fouchet, B. Bézard, N. Biver, T. Encrenaz, C. Leyrat (LESIA) T. Greathouse (SwRI) L. Fletcher (Univ. Leicester) J. Sinclair, G. Orton (JPL) M. Gurwell (Harvard CfA) F. Billebaud, M. Dobrijevic, E. Chapillon (LAB)	2D seasonal photochemistry (and climate)	V. Hue, T. Greathouse (SwRI) M. Dobrijevic, F. Hersant (LAB) J. C. Loison (ISM)	JWST Herschel Odin	P. Hartogh, C. Jarchow (MPS) R. Moreno, E. Lellouch, T. Fouchet, D. Bockelée, N. Biver (LESIA) F. Billebaud (LAB)
Atmospheric dynamics of the giant planets 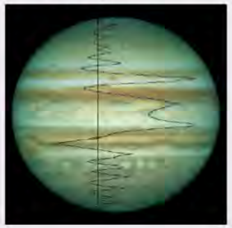	ALMA IRAM	PI, Co-I PI	R. Moreno, E. Lellouch, T. Fouchet (LESIA) T. Greathouse (SwRI) F. Billebaud, M. Dobrijevic, E. Chapillon (LAB)	2D seasonal photochemistry (General circulation)	V. Hue, T. Greathouse (SwRI) M. Dobrijevic, F. Hersant (LAB) A. Spiga, S. Guerlet (LMD) P. Hartogh, A. Medvedev (MPS)	JUICE	P. Hartogh, C. Jarchow, L. Rezac, N. Krupp (MPS) MPS hardware & software teams R. Moreno, E. Lellouch, T. Fouchet (LESIA) F. Billebaud, S. Lopez, F. Herpin (LAB) J.M. Krieg, A. Maestrini (LERMA) E. Wirström (Chalmers) H. Sagawa (Univ. Kyoto) O. Witasse, N. Altobelli, C. Vallat (ESA) L. Fletcher (Univ. Leicester) A. Masters (UCL)

Figure 3.14: Science themes and main collaborations.

Bibliography

Agúndez, M., Parmentier, V., Venot, O., Hersant, F., Selsis, F., 2014. Pseudo 2D chemical model of hot-Jupiter atmospheres: application to HD 209458b and HD 189733b. Astron. Astrophys. 564, A73.

Ali-Dib, M., Mousis, O., Petit, J.-M., Lunine, J. I., 2014. The Measured Compositions of Uranus and Neptune from their Formation on the CO Ice Line. Astrophys. J. 793, 9.

Altwegg, K., Balsiger, H., Bar-Nun, A., Berthelier, J. J., Bieler, A., Bochsler, P., Briois, C., Calmonte, U., Combi, M., De Keyser, J., Eberhardt, P., Fiethe, B., Fuselier, S., Gasc, S., Gombosi, T. I., Hansen, K. C., Hässig, M., Jäckel, A., Kopp, E., Korth, A., LeRoy, L., Mall, U., Marty, B., Mousis, O., Neefs, E., Owen, T., Rème, H., Rubin, M., Sémon, T., Tzou, C.-Y., Waite, H., Wurz, P., Jan. 2015. 67P/Churyumov-Gerasimenko, a Jupiter family comet with a high D/H ratio. Science 347 (27), 1261952.

Anderson, C. M., Samuelson, R. E., Yung, Y. L., McLain, J. L., Apr. 2016. Solid-state photochemistry as a formation mechanism for Titan's stratospheric C_4N_2 ice clouds. Geophys. Res. Lett. 43, 3088–3094.

Atreya, S. K., Wong, M. H., Owen, T. C., Mahaffy, P. R., Niemann, H. B., de Pater, I., Drossart, P., Encrenaz, T., 1999. A comparison of the atmospheres of Jupiter and Saturn: deep atmospheric composition, cloud structure, vertical mixing, and origin. Planet. Space Sci. 47, 1243–1262.

Atreya, S. K., Mahaffy, P. R., Niemann, H. B., Wong, M. H., Owen, T. C., Feb. 2003. Composition and origin of the atmosphere of Jupiter - an update, and implications for the extrasolar giant planets. Planet. Space Sci. 51, 105–112.

Baldwin, M. P., Gray, L. J., Dunkerton, T. J., Hamilton, K., Haynes, P. H., Randel, W. J., Holton, J. R., Alexander, M. J., Hirota, I., Horinouchi, T., Jones, D. B. A., Kinnersley, J. S., Marquardt, C., Sato, K., Takahashi, M., May 2001. The quasi-biennial oscillation. Reviews of Geophysics 39, 179–229.

Bar-Nun, A., Kleinfeld, I., Kochavi, E., 1988. Trapping of gas mixtures by amorphous water ice. Phys. Rev. B 38, 7749–7754.

Bergin, E. A., Lellouch, E., Harwit, M., Gurwell, M. A., Melnick, G. J., Ashby, M. L. N., Chin, G., Erickson, N. R., Goldsmith, P. F., Howe, J. E., Kleiner, S. C., Koch, D. G., Neufeld, D. A., Patten, B. M., Plume, R., Schieder, R., Snell, R. L., Stauffer, J. R., Tolls, V., Wang, Z., Winnewisser, G., Zhang, Y. F., Aug. 2000. Submillimeter Wave Astronomy Satellite Observations of Jupiter and Saturn:Detection of 557 GHZ Water Emission from the Upper Atmosphere. Astrophys. J. Lett. 539, L147–L150.

Bézard, B., Lellouch, E., Strobel, D., Maillard, J.-P., Drossart, P., 2002. Carbon Monoxide on Jupiter: Evidence for Both Internal and External Sources. Icarus 159, 95–111.

Bockelée-Morvan, D., Biver, N., Swinyard, B., de Val-Borro, M., Crovisier, J., Hartogh, P., Lis, D. C., Moreno, R., Szutowicz, S., Lellouch, E., Emprechtinger, M., Blake, G. A., Courtin, R., Jarchow, C., Kidger, M., Küppers, M., Rengel, M., Davis, G. R., Fulton, T., Naylor, D., Sidher, S., Walker, H., Aug. 2012. Herschel measurements of the D/H and $^{16}O/^{18}O$ ratios in water in the Oort-cloud comet C/2009 P1 (Garradd). Astron. Astrophys. 544, L15.

Bolton, S. J., Lunine, J., Stevenson, D., Connerney, J. E. P., Levin, S., Owen, T. C., Bagenal, F., Gautier, D., Ingersoll, A. P., Orton, G. S., Guillot, T., Hubbard, W., Bloxham, J., Coradini, A., Stephens, S. K., Mokashi, P., Thorne, R., Thorpe, R., Nov. 2017. The Juno Mission. Space Sci. Rev. 213, 5–37.

Boss, A. P., 1997. Giant planet formation by gravitational instability. Science 276, 1836–1839.

Boss, A. P., Sep. 2002. Formation of gas and ice giant planets. Earth and Planetary Science Letters 202, 513–523.

Boss, A. P., Wetherill, G. W., Haghighipour, N., Mar. 2002. NOTE: Rapid Formation of Ice Giant Planets. Icarus 156, 291–295.

Bourgalais, J., Spencer, M., Osborn, D. L., Goulay, F., Le Picard, S. D., 2016. Reactions of Atomic Carbon with Butene Isomers: Implications for Molecular Growth in Carbon-Rich Environments. J. Phys. Chem. A 120, 9138–9150.

Brown, P. D., Millar, T. J., Sep. 1989. Grain-surface formation of multi-deuterated molecules. Mon. Not. R. Astron. Soc. 240, 25P–29P.

Cassidy, T. A., Johnson, R. E., Oct. 2010. Collisional spreading of Enceladus' neutral cloud. Icarus 209, 696–703.

Cavalié, T., Billebaud, F., Fouchet, T., Lellouch, E., Brillet, J., Dobrijevic, M., 2008a. Observations of CO on Saturn and Uranus at millimeter wavelengths: new upper limit determinations. Astron. Astrophys. 484, 555–561.

Cavalié, T., Billebaud, F., Encrenaz, T., Dobrijevic, M., Brillet, J., Forget, F., Lellouch, E., 2008b. Vertical temperature profile and mesospheric winds retrieval on Mars from CO ;millimeter observations. Comparison with general circulation model predictions. Astron. Astrophys. 489, 795–809.

Cavalié, T., Billebaud, F., Biver, N., Dobrijevic, M., Lellouch, E., Brillet, J., Lecacheux, A., Hjalmarson, Å., Sandqvist, A., Frisk, U., Olberg, M., Bergin, E. A., The Odin Team, 2008c. Observation of water vapor in the stratosphere of Jupiter with the Odin space telescope. Planet. Space Sci. 56, 1573–1584.

Cavalié, T., Billebaud, F., Dobrijevic, M., Fouchet, T., Lellouch, E., Encrenaz, T., Brillet, J., Moriarty-Schieven, G. H., Wouterloot, J. G. A., Hartogh, P., 2009. First observation of CO at 345 GHz in the atmosphere of Saturn with the JCMT: New constraints on its origin. Icarus 203, 531–540.

Cavalié, T., Hartogh, P., Billebaud, F., Dobrijevic, M., Fouchet, T., Lellouch, E., Encrenaz, T., Brillet, J., Moriarty-Schieven, G. H., 2010. A cometary origin for CO in the stratosphere of Saturn? Astron. Astrophys. 510, A88.

Cavalié, T., Biver, N., Hartogh, P., Dobrijevic, M., Billebaud, F., Lellouch, E., Sandqvist, A., Brillet, J., Lecacheux, A., Hjalmarson, Å., Frisk, U., Olberg, M., Odin Team, Feb. 2012a. Odin space telescope monitoring of water vapor in the stratosphere of Jupiter. Planet. Space Sci. 61, 3–14.

Cavalié, T., Feuchtgruber, H., Hesman, B., Lellouch, E., Moreno, R., Fouchet, T., Achterberg, R., Moullet, A., Hartogh, P., Oct. 2012b. Herschel Temporal Monitoring Observations Of H_2O In Saturn's Hot Stratospheric Vortex Between 2011 And 2012. In: AAS/Division for Planetary Sciences Meeting Abstracts. Vol. 44 of AAS/Division for Planetary Sciences Meeting Abstracts. p. 403.07.

Cavalié, T., Hesman, B., Feuchtgruber, H., Lellouch, E., Moreno, R., Achterberg, R., Gueth, F., Fouchet, T., Hartogh, P., Moullet, A., 2012c. Temporal monitoring of Saturn's 2011 Great Storm and its aftermath in 2011-2012 with Herschel and ALMA. In: The First Year of ALMA Science.

Cavalié, T., Feuchtgruber, H., Lellouch, E., de Val-Borro, M., Jarchow, C., Moreno, R., Hartogh, P., Orton, G., Greathouse, T. K., Billebaud, F., Dobrijevic, M., Lara, L. M., González, A., Sagawa, H., May 2013. Spatial distribution of water in the stratosphere of Jupiter from Herschel HIFI and PACS observations. Astron. Astrophys. 553, A21.

Cavalié, T., Moreno, R., Lellouch, E., Hartogh, P., Venot, O., Orton, G. S., Jarchow, C., Encrenaz, T., Selsis, F., Hersant, F., Fletcher, L. N., 2014. The first submillimeter observation of CO in the stratosphere of Uranus. Astron. Astrophys. 562, A33.

Cavalié, T., Dobrijevic, M., Fletcher, L. N., Loison, J.-C., Hickson, K. M., Hue, V., Hartogh, P., Aug. 2015. Photochemical response to the variation of temperature in the 2011-2012 stratospheric vortex of Saturn. Astron. Astrophys. 580, A55.

Cavalié, T., Moreno, R., Lellouch, E., Fouchet, T., Hue, V., Greathouse, T. K., Dobrijevic, M., Hersant, F., Hartogh, P., Jarchow, C., Rezac, L., Bézard, B., Oct. 2017a. ALMA spectral imaging of SL9 species in Jupiter's stratosphere. In: AAS/Division for Planetary Sciences Meeting Abstracts #49. Vol. 49 of AAS/Division for Planetary Sciences Meeting Abstracts. p. 209.08.

Cavalié, T., Venot, O., Selsis, F., Hersant, F., Hartogh, P., Leconte, J., 2017b. Thermochemistry and vertical mixing in the tropospheres of Uranus and Neptune. How convection inhibition can affect the derivation of deep oxygen abundances. Icarus 291, 1–16.

Connerney, J. E. P., 1986. Magnetic connection for Saturn's rings and atmosphere. Geophysical Research Letters 13, 773–776.

Coustenis, A., Salama, A., Lellouch, E., Encrenaz, T., Bjoraker, G. L., Samuelson, R. E., de Graauw, T., Feuchtgruber, H., Kessler, M. F., Aug. 1998. Evidence for water vapor in Titan's atmosphere from ISO/SWS data. Astron. Astrophys. 336, L85–L89.

Cunha de Miranda, B., Romanzin, C.a dn Chefdeville, S., Vuitton, V., Žabka, J., Polášek, M., Alcaraz, C., 2015. Reactions of State-Selected Atomic Oxygen Ions $O^+(^4S, ^2D, ^2P)$ with Methane. J. Phys. Chem. A 119, 6082–6098.

de Graauw, T., Feuchtgruber, H., Bezard, B., Drossart, P., Encrenaz, T., Beintema, D. A., Griffin, M., Heras, A., Kessler, M., Leech, K., Lellouch, E., Morris, P., Roelfsema, P. R., Roos-Serote, M., Salama, A., Vandenbussche, B., Valentijn, E. A., Davis, G. R., Naylor, D. A., May 1997. First results of ISO-SWS observations of Saturn: detection of CO_2, CH_3C_2H, C_4H_2 and tropospheric H_2O. Astron. Astrophys. 321, L13–L16.

de Graauw, T., Helmich, F. P., Phillips, T. G., Stutzki, J., Caux, E., Whyborn, N. D., Dieleman, P., Roelfsema, P. R., Aarts, H., Assendorp, R., Bachiller, R., Baechtold, W., Barcia, A., Beintema, D. A., Belitsky, V., Benz, A. O., Bieber, R., Boogert, A., Borys, C., Bumble, B., Caïs, P., Caris, M., Cerulli-Irelli, P., Chattopadhyay, G., Cherednichenko, S., Ciechanowicz, M., Coeur-Joly, O., Comito, C., Cros, A., de Jonge, A., de Lange, G., Delforges, B., Delorme, Y., den Boggende, T., Desbat, J.-M., Diez-González, C., di Giorgio, A. M., Dubbeldam, L., Edwards, K., Eggens, M., Erickson, N., Evers, J., Fich, M., Finn, T., Franke, B., Gaier, T., Gal, C., Gao, J. R., Gallego, J.-D., Gauffre, S., Gill, J. J., Glenz, S., Golstein, H., Goulooze, H., Gunsing, T., Güsten, R., Hartogh, P., Hatch, W. A., Higgins, R., Honingh, E. C., Huisman, R., Jackson, B. D., Jacobs, H., Jacobs, K., Jarchow, C., Javadi, H., Jellema, W., Justen, M., Karpov, A., Kasemann, C., Kawamura, J., Keizer, G., Kester, D., Klapwijk, T. M., Klein, T., Kollberg, E., Kooi, J., Kooiman, P.-P., Kopf, B., Krause, M., Krieg, J.-M., Kramer, C., Kruizenga, B., Kuhn, T., Laauwen, W., Lai, R., Larsson, B., Leduc, H. G., Leinz, C., Lin, R. H., Liseau, R., Liu, G. S., Loose, A., López-Fernandez, I., Lord, S., Luinge, W., Marston, A., Martín-Pintado, J., Maestrini, A., Maiwald, F. W., McCoey, C., Mehdi, I., Megej, A., Melchior, M., Meinsma, L., Merkel, H., Michalska, M., Monstein, C., Moratschke, D., Morris, P., Muller, H., Murphy, J. A., Naber, A., Natale, E., Nowosielski, W., Nuzzolo, F., Olberg, M., Olbrich, M., Orfei, R., Orleanski, P., Ossenkopf, V., Peacock, T., Pearson, J. C., Peron, I., Phillip-May, S., Piazzo, L., Planesas, P., Rataj, M., Ravera, L., Risacher, C., Salez, M., Samoska, L. A., Saraceno, P., Schieder, R., Schlecht, E., Schlöder, F., Schmülling, F., Schultz, M., Schuster, K., Siebertz, O., Smit, H., Szczerba, R., Shipman, R., Steinmetz, E., Stern, J. A., Stokroos, M., Teipen, R., Teyssier, D., Tils, T., Trappe, N., van Baaren, C., van Leeuwen, B.-J., van de Stadt, H., Visser, H., Wildeman, K. J., Wafelbakker, C. K., Ward, J. S., Wesselius, P., Wild, W., Wulff, S., Wunsch, H.-J., Tielens, X., Zaal, P., Zirath, H., Zmuidzinas, J., Zwart, F., Jul. 2010. The Herschel-Heterodyne Instrument for the Far-Infrared (HIFI). Astron. Astrophys. 518, L6.

de Pater, I., Richmond, M., Jul. 1989. Neptune's microwave spectrum from 1 MM to 20 CM. Icarus 80, 1–13.

de Pater, I., Romani, P. N., Atreya, S. K., 1991. Possible microwave absorption by H2S gas in Uranus' and Neptune's atmospheres. Icarus 91, 220–233.

Dobrijevic, M., Parisot, J. P., Dutour, I., Feb. 1995. A study of chemical systems using signal flow graph theory: application to Neptune. Planet. Space Sci. 43, 15–24.

Dobrijevic, M., Parisot, J. P., May 1998. Effect of chemical kinetics uncertainties on hydrocarbon production in the stratosphere of Neptune. Planet. Space Sci. 46, 491–505.

Dobrijevic, M., Ollivier, J. L., Billebaud, F., Brillet, J., Parisot, J. P., Jan. 2003. Effect of chemical kinetic uncertainties on photochemical modeling results: Application to Saturn's atmosphere. Astron. Astrophys. 398, 335–344.

Dobrijevic, M., Cavalié, T., Hébrard, E., Billebaud, F., Hersant, F., Selsis, F., Oct. 2010. Key reactions in the photochemistry of hydrocarbons in Neptune's stratosphere. Planet. Space Sci. 58, 1555–1566.

Dobrijevic, M., Cavalié, T., Billebaud, F., Jul. 2011. A methodology to construct a reduced chemical scheme for 2D-3D photochemical models: Application to Saturn. Icarus 214, 275–285.

Dobrijevic, M., Hébrard, E., Loison, J. C., Hickson, K. M., Jan. 2014. Coupling of oxygen, nitrogen, and hydrocarbon species in the photochemistry of Titan's atmosphere. Icarus 228, 324–346.

Encrenaz, T., Lellouch, E., Drossart, P., Feuchtgruber, H., Orton, G. S., Atreya, S. K., Jan. 2004. First detection of CO in Uranus. Astron. Astrophys. 413, L5–L9.

Fegley, B., Prinn, R. G., 1988. Chemical constraints on the water and total oxygen abundances in the deep atmosphere of Jupiter. The Astrophysical Journal 324, 621–625.

Feuchtgruber, H., Lellouch, E., de Graauw, T., Bézard, B., Encrenaz, T., Griffin, M., Sep. 1997. External supply of oxygen to the atmospheres of the giant planets. Nature 389, 159–162.

Feuchtgruber, H., Lellouch, E., Bézard, B., Encrenaz, T., de Graauw, T., Davis, G. R., Jan. 1999. Detection of HD in the atmospheres of Uranus and Neptune: a new determination of the D/H ratio. Astron. Astrophys. 341, L17–L21.

Feuchtgruber, H., Lellouch, E., Orton, G., de Graauw, T., Vandenbussche, B., Swinyard, B., Moreno, R., Jarchow, C., Billebaud, F., Cavalié, T., Sidher, S., Hartogh, P., 2013. The D/H ratio in the atmospheres of Uranus and Neptune from Herschel-PACS observations. Astron. Astrophys. 551, A126.

Fitzpatrick, P. J., de Pater, I., Luszcz-Cook, S., Wong, M. H., Hammel, H. B., Mar. 2014. Dispersion in Neptune's zonal wind velocities from NIR Keck AO observations in July 2009. Astrophys. Space Sci.350, 65–88.

Flandes, A., Spilker, L., Morishima, R., Pilorz, S., Leyrat, C., Altobelli, N., Brooks, S., Edgington, S. G., Nov. 2010. Brightness of Saturn's rings with decreasing solar elevation. Planet. Space Sci. 58, 1758–1765.

Flasar, F. M., Kunde, V. G., Achterberg, R. K., Conrath, B. J., Simon-Miller, A. A., Nixon, C. A., Gierasch, P. J., Romani, P. N., Bézard, B., Irwin, P., Bjoraker, G. L., Brasunas, J. C., Jennings, D. E., Pearl, J. C., Smith, M. D., Orton, G. S., Spilker, L. J., Carlson, R., Calcutt, S. B., Read, P. L., Taylor, F. W., Parrish, P., Barucci, A., Courtin, R., Coustenis, A., Gautier, D., Lellouch, E., Marten, A., Prangé, R., Biraud, Y., Fouchet, T., Ferrari, C., Owen, T. C., Abbas, M. M., Samuelson, R. E., Raulin, F., Ade, P., Césarsky, C. J., Grossman, K. U., Coradini, A., Jan. 2004. An intense stratospheric jet on Jupiter. Nature 427, 132–135.

Fletcher, L. N., Hesman, B. E., Irwin, P. G. J., Baines, K. H., Momary, T. W., Sanchez-Lavega, A., Flasar, F. M., Read, P. L., Orton, G. S., Simon-Miller, A., Hueso, R., Bjoraker, G. L., Mamoutkine, A., del Rio-Gaztelurrutia, T., Gomez, J. M., Buratti, B., Clark, R. N., Nicholson, P. D., Sotin, C., Jun. 2011. Thermal Structure and Dynamics of Saturn's Northern Springtime Disturbance. Science 332, 1413.

Fletcher, L. N., Swinyard, B., Salji, C., Polehampton, E., Fulton, T., Sidher, S., Lellouch, E., Moreno, R., Orton, G., Cavalié, T., Courtin, R., Rengel, M., Sagawa, H., Davis, G. R., Hartogh, P., Naylor, D., Walker, H., Lim, T., 2012. Sub-millimetre spectroscopy of Saturn's trace gases from Herschel/SPIRE. Astron. Astrophys. 539, A44.

Fletcher, L. N., Guerlet, S., Orton, G. S., Cosentino, R. G., Fouchet, T., Irwin, P. G. J., Li, L., Flasar, F. M., Gorius, N., Morales-Juberías, R., Nov. 2017. Disruption of Saturn's quasi-periodic equatorial oscillation by the great northern storm. Nature Astronomy 1, 765–770.

Fouchet, T., Guerlet, S., Strobel, D. F., Simon-Miller, A. A., Bézard, B., Flasar, F. M., May 2008. An equatorial oscillation in Saturn's middle atmosphere. Nature 453, 200–202.

Fouchet, T., Lellouch, E., Cavalié, T., Bézard, B., Oct. 2017. First determination of the tropospheric CO abundance in Saturn. In: AAS/Division for Planetary Sciences Meeting Abstracts. Vol. 49 of AAS/Division for Planetary Sciences Meeting Abstracts. p. 209.05.

Friedson, A. J., Jan. 1999. New Observations and Modelling of a QBO-Like Oscillation in Jupiter's Stratosphere. Icarus 137, 34–55.

Friedson, A. J., Moses, J. I., Apr. 2012. General circulation and transport in Saturn's upper troposphere and stratosphere. Icarus 218, 861–875.

García-Melendo, E., Pérez-Hoyos, S., Sánchez-Lavega, A., Hueso, R., Sep. 2011. Saturn's zonal wind profile in 2004-2009 from Cassini ISS images and its long-term variability. Icarus 215, 62–74.

Gautier, D., Hersant, F., Mousis, O., Lunine, J. I., 2001. Enrichments in Volatiles in Jupiter: A New Interpretation of the Galileo Measurements. Astrophys. J. Lett. 550, L227–L230.

Gautier, D., Hersant, F., 2005. Formation and Composition of Planetesimals. Space Sci. Rev. 116, 25–52.

Gérard, J.-C., Bonfond, B., Grodent, D., Radioti, A., Clarke, J. T., Gladstone, G. R., Waite, J. H., Bisikalo, D., Shematovich, V. I., Nov. 2014. Mapping the electron energy in Jupiter's aurora: Hubble spectral observations. Journal of Geophysical Research (Space Physics) 119, 9072–9088.

Greathouse, T. K., Lacy, J. H., Bézard, B., Moses, J. I., Griffith, C. A., Richter, M. J., Sep. 2005. Meridional variations of temperature, C_2H_2 and C_2H_6 abundances in Saturn's stratosphere at southern summer solstice. Icarus 177, 18–31.

Greathouse, T. K., Strong, S. B., Moses, J. I., Dowling, T. E., Sep. 2008. A Radiative Seasonal Climate Model Applied to Saturn. In: AAS/Division for Planetary Sciences Meeting Abstracts #40. Vol. 40 of Bulletin of the American Astronomical Society. p. 472.

Griffin, M. J., Abergel, A., Abreu, A., Ade, P. A. R., André, P., Augueres, J.-L., Babbedge, T., Bae, Y., Baillie, T., Baluteau, J.-P., Barlow, M. J., Bendo, G., Benielli, D., Bock, J. J., Bonhomme, P., Brisbin, D., Brockley-Blatt, C., Caldwell, M., Cara, C., Castro-Rodriguez, N., Cerulli, R., Chanial, P., Chen, S., Clark, E., Clements, D. L., Clerc, L., Coker, J., Communal, D., Conversi, L., Cox, P., Crumb, D., Cunningham, C., Daly, F., Davis, G. R., de Antoni, P., Delderfield, J., Devin, N., di Giorgio, A., Didschuns, I., Dohlen, K., Donati, M., Dowell, A., Dowell, C. D., Duband, L., Dumaye, L., Emery, R. J., Ferlet, M., Ferrand, D., Fontignie, J., Fox, M., Franceschini, A., Frerking, M., Fulton, T., Garcia, J., Gastaud, R., Gear, W. K., Glenn, J., Goizel, A., Griffin, D. K., Grundy, T., Guest, S., Guillemet, L., Hargrave, P. C., Harwit, M., Hastings, P., Hatziminaoglou, E., Herman, M., Hinde, B., Hristov, V., Huang, M., Imhof, P., Isaak, K. J., Israelsson, U., Ivison, R. J., Jennings, D., Kiernan, B., King, K. J., Lange, A. E., Latter, W., Laurent, G., Laurent, P., Leeks, S. J., Lellouch, E., Levenson, L., Li, B., Li, J., Lilienthal, J., Lim, T., Liu, S. J., Lu, N., Madden, S., Mainetti, G., Marliani, P., McKay, D., Mercier, K., Molinari, S., Morris, H., Moseley, H., Mulder, J., Mur, M., Naylor, D. A., Nguyen, H., O'Halloran, B., Oliver, S., Olofsson, G., Olofsson, H.-G., Orfei, R., Page, M. J., Pain, I., Panuzzo, P., Papageorgiou, A., Parks, G., Parr-Burman, P., Pearce, A., Pearson, C., Pérez-Fournon, I., Pinsard, F., Pisano, G., Podosek, J., Pohlen, M., Polehampton, E. T., Pouliquen, D., Rigopoulou, D., Rizzo, D., Roseboom, I. G., Roussel, H., Rowan-Robinson, M., Rownd, B., Saraceno, P., Sauvage, M., Savage, R., Savini, G., Sawyer, E., Scharmberg, C., Schmitt, D., Schneider, N., Schulz, B., Schwartz, A., Shafer, R., Shupe, D. L., Sibthorpe, B., Sidher, S., Smith, A., Smith, A. J., Smith, D., Spencer, L., Stobie, B., Sudiwala, R., Sukhatme, K., Surace, C., Stevens, J. A., Swinyard, B. M., Trichas, M., Tourette, T., Triou, H., Tseng, S., Tucker, C., Turner, A., Vaccari, M., Valtchanov, I., Vigroux, L., Virique, E., Voellmer, G., Walker, H., Ward, R., Waskett, T., Weilert, M., Wesson, R., White, G. J., Whitehouse, N., Wilson, C. D., Winter, B., Woodcraft, A. L., Wright, G. S., Xu, C. K., Zavagno, A., Zemcov, M., Zhang, L., Zonca, E., Jul. 2010. The Herschel-SPIRE instrument and its in-flight performance. Astron. Astrophys. 518, L3.

Griffith, C. A., Bézard, B., Greathouse, T., Lellouch, E., Lacy, J., Kelly, D., Richter, M. J., Jul. 2004. Meridional transport of HCN from SL9 impacts on Jupiter. Icarus 170, 58–69.

Guerlet, S., Fouchet, T., Bézard, B., Simon-Miller, A. A., Michael Flasar, F., Sep. 2009. Vertical and meridional distribution of ethane, acetylene and propane in Saturn's stratosphere from CIRS/Cassini limb observations. Icarus 203, 214–232.

Guerlet, S., Fouchet, T., Bézard, B., Moses, J. I., Fletcher, L. N., Simon-Miller, A. A., Michael Flasar, F., Oct. 2010. Meridional distribution of CH_3C_2H and C_4H_2 in Saturn's stratosphere from CIRS/Cassini limb and nadir observations. Icarus 209, 682–695.

Guerlet, S., Fouchet, T., Bézard, B., Flasar, F. M., Simon-Miller, A. A., May 2011. Evolution of the equatorial oscillation in Saturn's stratosphere between 2005 and 2010 from Cassini/CIRS limb data analysis. Geophys. Res. Lett. 38, L09201.

Guerlet, S., Spiga, A., Sylvestre, M., Indurain, M., Fouchet, T., Leconte, J., Millour, E., Wordsworth, R., Capderou, M., Bézard, B., Forget, F., Aug. 2014. Global climate modeling of Saturn's atmosphere. Part I: Evaluation of the radiative transfer model. Icarus 238, 110–124.

Guillot, T., Hueso, R., Mar. 2006. The composition of Jupiter: sign of a (relatively) late formation in a chemically evolved protosolar disc. Mon. Not. R. Astron. Soc. 367, L47–L51.

Hammel, H. B., de Pater, I., Gibbard, S., Lockwood, G. W., Rages, K., Jun. 2005. Uranus in 2003: Zonal winds, banded structure, and discrete features. Icarus 175, 534–545.

Hansen, C. J., Esposito, L., Stewart, A. I. F., Colwell, J., Hendrix, A., Pryor, W., Shemansky, D., West, R., Mar. 2006. Enceladus' Water Vapor Plume. Science 311, 1422–1425.

Hartogh, P., Lellouch, E., Crovisier, J., Banaszkiewicz, M., Bensch, F., Bergin, E. A., Billebaud, F., Biver, N., Blake, G. A., Blecka, M. I., Blommaert, J., Bockelée-Morvan, D., Cavalié, T., Cernicharo, J., Courtin, R., Davis, G., Decin, L., Encrenaz, P., Encrenaz, T., González, A., de Graauw, T., Hutsemékers, D., Jarchow, C., Jehin, E., Kidger, M., Küppers, M., de Lange, A., Lara, L.-M., Lis, D. C., Lorente, R., Manfroid, J., Medvedev, A. S., Moreno, R., Naylor, D. A., Orton, G., Portyankina, G., Rengel, M., Sagawa, H., Sánchez-Portal, M., Schieder, R., Sidher, S., Stam, D., Swinyard, B., Szutowicz, S., Thomas, N., Thornhill, G., Vandenbussche, B., Verdugo, E., Waelkens, C., Walker, H., 2009. Water and related chemistry in the solar system. A guaranteed time key programme for Herschel. Planet. Space Sci. 57, 1596–1606.

Hartogh, P., Błecka, M. I., Jarchow, C., Sagawa, H., Lellouch, E., de Val-Borro, M., Rengel, M., Medvedev, A. S., Swinyard, B. M., Moreno, R., Cavalié, T., Lis, D. C., Banaszkiewicz, M., Bockelée-Morvan, D., Crovisier, J., Encrenaz, T., Küppers, M., Lara, L.-M., Szutowicz, S., Vandenbussche, B., Bensch, F., Bergin, E. A., Billebaud, F., Biver, N., Blake, G. A., Blommaert, J. A. D. L., Cernicharo, J., Decin, L., Encrenaz, P., Feuchtgruber, H., Fulton, T., de Graauw, T., Jehin, E., Kidger, M., Lorente, R., Naylor, D. A., Portyankina, G., Sánchez-Portal, M., Schieder, R., Sidher, S., Thomas, N., Verdugo, E., Waelkens, C., Lorenzani, A., Tofani, G., Natale, E., Pearson, J., Klein, T., Leinz, C., Güsten, R., Kramer, C., Oct. 2010a. First results on Martian carbon monoxide from Herschel/HIFI observations. Astron. Astrophys. 521, L48.

Hartogh, P., Crovisier, J., de Val-Borro, M., Bockelée-Morvan, D., Biver, N., Lis, D. C., Moreno, R., Jarchow, C., Rengel, M., Emprechtinger, M., Szutowicz, S., Banaszkiewicz, M., Bensch, F., Blecka, M. I., Cavalié, T., Encrenaz, T., Jehin, E., Küppers, M., Lara, L.-M., Lellouch, E., Swinyard, B. M., Vandenbussche, B., Bergin, E. A., Blake, G. A., Blommaert, J. A. D. L., Cernicharo, J., Decin, L., Encrenaz, P., de Graauw, T., Hutsemekers, D., Kidger, M., Manfroid, J., Medvedev, A. S., Naylor, D. A., Schieder, R., Thomas, N., Waelkens, C., Roelfsema, P. R., Dieleman, P., Güsten, R., Klein, T., Kasemann, C., Caris, M., Olberg, M., Benz, A. O., Jul. 2010b. HIFI observations of water in the atmosphere of comet C/2008 Q3 (Garradd). Astron. Astrophys. 518, L150.

Hartogh, P., Jarchow, C., Lellouch, E., de Val-Borro, M., Rengel, M., Moreno, R., Medvedev, A. S., Sagawa, H., Swinyard, B. M., Cavalié, T., Lis, D. C., Błęcka, M. I., Banaszkiewicz, M., Bockelée-Morvan, D., Crovisier, J., Encrenaz, T., Küppers, M., Lara, L.-M., Szutowicz, S., Vandenbussche, B., Bensch, F., Bergin, E. A., Billebaud, F., Biver, N., Blake, G. A., Blommaert, J. A. D. L., Cernicharo, J., Decin, L., Encrenaz, P., Feuchtgruber, H., Fulton, T., de Graauw, T., Jehin, E., Kidger, M., Lorente, R., Naylor, D. A., Portyankina, G., Sánchez-Portal, M., Schieder, R., Sidher, S., Thomas, N., Verdugo, E., Waelkens, C., Whyborn, N., Teyssier, D., Helmich, F., Roelfsema, P., Stutzki, J., Leduc, H. G., Stern, J. A., Oct. 2010c. Herschel/HIFI observations of Mars: First detection of O_2 at submillimetre wavelengths and upper limits on HCl and H_2O_2. Astron. Astrophys. 521, L49.

Hartogh, P., Lellouch, E., Moreno, R., Bockelée-Morvan, D., Biver, N., Cassidy, T., Rengel, M., Jarchow, C., Cavalié, T., Crovisier, J., Helmich, F. P., Kidger, M., Aug. 2011. Direct detection of the Enceladus water torus with Herschel. Astron. Astrophys. 532, L2.

Hébrard, E., Dobrijevic, M., Loison, J. C., Bergeat, A., Hickson, K. M., Caralp, F., Apr. 2013. Photochemistry of C_3H_p hydrocarbons in Titan's stratosphere revisited. Astron. Astrophys. 552, A132.

Hébrard, E., Dobrijevic, M., Pernot, P., Carrasco, N., Bergeat, A., Hickson, K. M., Canosa, A., Le Picard, S. D., Sims, I. R., Sep. 2009. How Measurements of Rate Coefficients at Low Temperature Increase the Predictivity of Photochemical Models of Titan's Atmosphere. Journal of Physical Chemistry A 113, 11227–11237.

Helled, R., Anderson, J. D., Podolak, M., Schubert, G., 2011. Interior Models of Uranus and Neptune. Astrophys. J. 726, 15.

Helled, R., Lunine, J., 2014. Measuring Jupiter's water abundance by Juno: the link between interior and formation models. Mon. Not. R. Astron. Soc. 441, 2273–2279.

Helled, R., Guillot, T., May 2017. Internal Structure of Giant and Icy Planets: Importance of Heavy Elements and Mixing. ArXiv e-prints.

Hersant, F., Gautier, D., Huré, J.-M., 2001. A Two-dimensional Model for the Primordial Nebula Constrained by D/H Measurements in the Solar System: Implications for the Formation of Giant Planets. Astrophys. J. 554, 391–407.

Hersant, F., Gautier, D., Lunine, J. I., 2004. Enrichment in volatiles in the giant planets of the Solar System. Planet. Space Sci. 52, 623–641.

Hesman, B. E., Bjoraker, G. L., Sada, P. V., Achterberg, R. K., Jennings, D. E., Romani, P. N., Lunsford, A. W., Fletcher, L. N., Boyle, R. J., Simon-Miller, A. A., Nixon, C. A., Irwin, P. G. J., Nov. 2012. Elusive Ethylene Detected in Saturn's Northern Storm Region. Astrophys. J. 760, 24.

Homayoon, Z., Bowman, J. M., Balucani, N., Casavecchia, P., 2014. Quasiclassical Trajectory Calculations of the N(^{2}D) + H_2O Reaction Elucidating the Formation Mechanism of HNO and HON Seen in Molecular Beam Experiments. J. Phys. Chem. Lett. 5, 3508–3513.

Hue, V., Cavalié, T., Dobrijevic, M., Hersant, F., Greathouse, T. K., Sep. 2015. 2D photochemical modeling of Saturn's stratosphere. Part I: Seasonal variation of atmospheric composition without meridional transport. Icarus 257, 163–184.

Hue, V., Greathouse, T. K., Cavalié, T., Dobrijevic, M., Hersant, F., Mar. 2016. 2D photochemical modeling of Saturn's stratosphere. Part II: Feedback between composition and temperature. Icarus 267, 334–343.

Hue, V., Hersant, F., Cavalié, T., Dobrijevic, M., Sinclair, J. A., Jun. 2018. Photochemistry, mixing and transport in Jupiter's stratosphere constrained by Cassini. Icarus 307, 106–123.

Ingersoll, A. P., Dowling, T. E., Gierasch, P. J., Orton, G. S., Read, P. L., Sánchez-Lavega, A., Showman, A. P., Simon-Miller, A. A., Vasavada, A. R., 2004. Dynamics of Jupiter's atmosphere. In: Bagenal, F., Dowling, T. E., McKinnon, W. B. (Eds.), Jupiter. The Planet, Satellites and Magnetosphere. pp. 105–128.

Janssen, M. A., Hofstadter, M. D., Gulkis, S., Ingersoll, A. P., Allison, M., Bolton, S. J., Levin, S. M., Kamp, L. W., Feb. 2005. Microwave remote sensing of Jupiter's atmosphere from an orbiting spacecraft. Icarus 173, 447–453.

Janssen, M. A., Oswald, J. E., Brown, S. T., Gulkis, S., Levin, S. M., Bolton, S. J., Allison, M. D., Atreya, S. K., Gautier, D., Ingersoll, A. P., Lunine, J. I., Orton, G. S., Owen, T. C., Steffes, P. G., Adumitroaie, V., Bellotti, A., Jewell, L. A., Li, C., Li, L., Misra, S., Oyafuso, F. A., Santos-Costa, D., Sarkissian, E., Williamson, R., Arballo, J. K., Kitiyakara, A., Ulloa-Severino, A., Chen, J. C., Maiwald, F. W., Sahakian, A. S., Pingree, P. J., Lee, K. A., Mazer, A. S., Redick, R., Hodges, R. E., Hughes, R. C., Bedrosian, G., Dawson, D. E., Hatch, W. A., Russell, D. S., Chamberlain, N. F., Zawadski, M. S., Khayatian, B., Franklin, B. R., Conley, H. A., Kempenaar, J. G., Loo, M. S., Sunada, E. T., Vorperion, V., Wang, C. C., Nov. 2017. MWR: Microwave Radiometer for the Juno Mission to Jupiter. Space Sci. Rev. 213, 139–185.

Karpowicz, B. M., Steffes, P. G., Mar. 2013. Investigating the H_2-He-H_2O-CH_4 equation of state in the deep troposphere of Jupiter. Icarus 223, 277–297.

Kidger, M. R., Sep. 2003. Dust production and coma morphology of 67P/Churyumov-Gerasimenko during the 2002-2003 apparition. Astron. Astrophys. 408, 767–774.

Kiefer, F., Lecavelier des Etangs, A., Augereau, J.-C., Vidal-Madjar, A., Lagrange, A.-M., Beust, H., Jan. 2014a. Exocomets in the circumstellar gas disk of HD 172555. Astron. Astrophys. 561, L10.

Kiefer, F., Lecavelier des Etangs, A., Boissier, J., Vidal-Madjar, A., Beust, H., Lagrange, A.-M., Hébrard, G., Ferlet, R., Oct. 2014b. Two families of exocomets in the β Pictoris system. Nature 514, 462–464.

Landgraf, M., Liou, J.-C., Zook, H. A., Grün, E., May 2002. Origins of Solar System Dust beyond Jupiter. Astron. J. 123, 2857–2861.

Larson, H. P., Fink, U., Treffers, R., Gautier, III, T. N., 1975. Detection of water vapor on Jupiter. Astrophys. J. 197, L137–L140.

Leconte, J., Selsis, F., Hersant, F., Guillot, T., Feb. 2017. Condensation-inhibited convection in hydrogen-rich atmospheres . Stability against double-diffusive processes and thermal profiles for Jupiter, Saturn, Uranus, and Neptune. Astron. Astrophys. 598, A98.

Lellouch, E., Rosenqvist, J., Goldstein, J. J., Bougher, S. W., Paubert, G., Dec. 1991. First absolute wind measurements in the middle atmosphere of Mars. Astrophys. J. 383, 401–406.

Lellouch, E., Paubert, G., Moreno, R., Festou, M. C., Bezard, B., Bockelee-Morvan, D., Colom, P., Crovisier, J., Encrenaz, T., Gautier, D., Marten, A., Despois, D., Strobel, D. F., Sievers, A., 1995. Chemical and Thermal Response of Jupiter's Atmosphere Following the Impact of Comet Shoemaker-Levy-9. Nature 373, 592–595.

Lellouch, E., Bézard, B., Fouchet, T., Feuchtgruber, H., Encrenaz, T., de Graauw, T., 2001. The deuterium abundance in Jupiter and Saturn from ISO-SWS observations. Astron. Astrophys. 370, 610–622.

Lellouch, E., Bézard, B., Moses, J. I., Davis, G. R., Drossart, P., Feuchtgruber, H., Bergin, E. A., Moreno, R., Encrenaz, T., Sep. 2002. The Origin of Water Vapor and Carbon Dioxide in Jupiter's Stratosphere. Icarus 159, 112–131.

Lellouch, E., Moreno, R., Paubert, G., 2005. A dual origin for Neptune's carbon monoxide? Astron. Astrophys. 430, L37–L40.

Lellouch, E., Bézard, B., Strobel, D. F., Bjoraker, G. L., Flasar, F. M., Romani, P. N., Oct. 2006. On the HCN and CO_2 abundance and distribution in Jupiter's stratosphere. Icarus 184, 478–497.

Lellouch, E., Hartogh, P., Feuchtgruber, H., Vandenbussche, B., de Graauw, T., Moreno, R., Jarchow, C., Cavalié, T., Orton, G., Banaszkiewicz, M., Blecka, M. I., Bockelée-Morvan, D., Crovisier, J., Encrenaz, T., Fulton, T., Küppers, M., Lara, L. M., Lis, D. C., Medvedev, A. S., Rengel, M., Sagawa, H., Swinyard, B., Szutowicz, S., Bensch, F., Bergin, E., Billebaud, F., Biver, N., Blake, G. A., Blommaert, J. A. D. L., Cernicharo, J., Courtin, R., Davis, G. R., Decin, L., Encrenaz, P., Gonzalez, A., Jehin, E., Kidger, M., Naylor, D., Portyankina, G., Schieder, R., Sidher, S., Thomas, N., de Val-Borro, M., Verdugo, E., Waelkens, C., Walker, H., Aarts, H., Comito, C., Kawamura, J. H., Maestrini, A., Peacocke, T., Teipen, R., Tils, T., Wildeman, K., 2010. First results of Herschel-PACS observations of Neptune. Astron. Astrophys. 518, L152.

Leonori, F., Balucani, N., Capozza, G., Segoloni, E., Volpia, G. G., Casavecchia, P., 2014. Dynamics of the $O(^3P) + C_2H_2$ reaction from crossed molecular beam experiments with soft electron ionization detection. Phys. Chem. Chem. Phys. 16, 10008–10022.

Li, X., Read, P. L., Jun. 2000. A mechanistic model of the quasi-quadrennial oscillation in Jupiter's stratosphere. Planet. Space Sci. 48, 637–669.

Lis, D. C., Biver, N., Bockelée-Morvan, D., Hartogh, P., Bergin, E. A., Blake, G. A., Crovisier, J., de Val-Borro, M., Jehin, E., Küppers, M., Manfroid, J., Moreno, R., Rengel, M., Szutowicz, S., Sep. 2013. A Herschel Study of D/H in Water in the Jupiter-family Comet 45P/Honda-Mrkos-Pajdušáková and Prospects for D/H Measurements with CCAT. Astrophys. J. Lett. 774, L3.

Lodders, K., Fegley, Jr., B., 1994. The origin of carbon monoxide in Neptunes's atmosphere. Icarus 112, 368–375.

Loison, J. C., Hébrard, E., Dobrijevic, M., Hickson, K. M., Caralp, F., Hue, V., Gronoff, G., Venot, O., Bénilan, Y., Feb. 2015. The neutral photochemistry of nitriles, amines and imines in the atmosphere of Titan. Icarus 247, 218–247.

Lunine, J. I., Stevenson, D. J., 1985. Thermodynamics of clathrate hydrate at low and high pressures with application to the outer solar system. Astrophys. J. Suppl. 58, 493–531.

Luszcz-Cook, S. H., de Pater, I., 2013. Constraining the origins of Neptune's carbon monoxide abundance with CARMA millimeter-wave observations. Icarus 222, 379–400.

Mahaffy, P. R., Niemann, H. B., Alpert, A., Atreya, S. K., Demick, J., Donahue, T. M., Harpold, D. N., Owen, T. C., 2000. Noble gas abundance and isotope ratios in the atmosphere of Jupiter from the Galileo Probe Mass Spectrometer. J. Geophys. Res. 105, 15061–15072.

Marten, A., Gautier, D., Owen, T., Sanders, D. B., Matthews, H. E., Atreya, S. K., Tilanus, R. P. J., Deane, J. R., 1993. First observations of CO and HCN on Neptune and Uranus at millimeter wavelengths and the implications for atmospheric chemistry. Astrophys. J. 406, 285–297.

Matousek, S., 2007. The Juno New Frontiers mission. Acta Astronautica 61, 932–939.

Medvedev, A. S., Sethunadh, J., Hartogh, P., Jul. 2013. From cold to warm gas giants: A three-dimensional atmospheric general circulation modeling. Icarus 225, 228–235.

Mizuno, H., Aug. 1980. Formation of the Giant Planets. Progress of Theoretical Physics 64, 544–557.

Moore, L., Mueller-Wodarg, I., Galand, M., Kliore, A., Mendillo, M., Nov. 2010. Latitudinal variations in Saturn's ionosphere: Cassini measurements and model comparisons. Journal of Geophysical Research (Space Physics) 115 (A14), A11317.

Moore, L., O'Donoghue, J., Müller-Wodarg, I., Galand, M., Mendillo, M., Jan. 2015. Saturn ring rain: Model estimates of water influx into Saturn's atmosphere. Icarus 245, 355–366.

Moreno, R., Marten, A., Matthews, H. E., Biraud, Y., 2003. Long-term evolution of CO, CS and HCN in Jupiter after the impacts of comet Shoemaker-Levy 9. Planet. Space Sci. 51, 591–611.

Moreno, R., Marten, A., Hidayat, T., Jul. 2005. Interferometric measurements of zonal winds on Titan. Astron. Astrophys. 437, 319–328.

Moreno, R., Marten, A., Sep. 2006. Mass Losses Of CO, CS And HCN On Jupiter/SL9. In: AAS/Division for Planetary Sciences Meeting Abstracts #38. Vol. 38 of Bulletin of the American Astronomical Society. p. 497.

Moreno, R., Gurwell, M., Marten, A., Lellouch, E., Oct. 2007. Jupiter's Interferometric Mapping of HCN(3-2) with the SMA. In: AAS/Division for Planetary Sciences Meeting Abstracts #39. Vol. 39 of Bulletin of the American Astronomical Society. p. 423.

Moreno, R., Lellouch, E., Forget, F., Encrenaz, T., Guilloteau, S., Millour, E., Jun. 2009. Wind measurements in Mars' middle atmosphere: IRAM Plateau de Bure interferometric CO observations. Icarus 201, 549–563.

Moreno, R., Lellouch, E., Courtin, R., Swinyard, B., Fulton, T., Orton, G., Hartogh, P., Jarchow, C., Cavalié, T., Feuchtgruber, H., Team, T. H., 2011. Observations of CO and HCN on Neptune with Herschel SPIRE. In: Geophysical Research Abstracts. Vol. 13 of Geophysical Research Abstracts. pp. EGU2011–8299.

Moreno, R., Lellouch, E., Cavalié, T., Moullet, A., Dec. 2017. Detection of CS in Neptune's atmosphere from ALMA observations. Astron. Astrophys. 608, L5.

Moses, J. I., Lellouch, E., Bézard, B., Gladstone, G. R., Feuchtgruber, H., Allen, M., May 2000. Photochemistry of Saturn's Atmosphere. II. Effects of an Influx of External Oxygen. Icarus 145, 166–202.

Moses, J. I., Visscher, C., Fortney, J. J., Showman, A. P., Lewis, N. K., Griffith, C. A., Klippenstein, S. J., Shabram, M., Friedson, A. J., Marley, M. S., Freedman, R. S., 2011. Disequilibrium Carbon, Oxygen, and Nitrogen Chemistry in the Atmospheres of HD 189733b and HD 209458b. Astrophys. J. 737, 15.

Moses, J. I., Mar. 2014. Chemical kinetics on extrasolar planets. Philosophical Transactions of the Royal Society of London Series A 372, 20130073–20130073.

Moses, J. I., Armstrong, E. S., Fletcher, L. N., Friedson, A. J., Irwin, P. G. J., Sinclair, J. A., Hesman, B. E., Nov. 2015. Evolution of stratospheric chemistry in the Saturn storm beacon region. Icarus 261, 149–168.

Moses, J. I., Poppe, A. R., Nov. 2017. Dust ablation on the giant planets: Consequences for stratospheric photochemistry. Icarus 297, 33–58.

Mousis, O., Fletcher, L. N., Lebreton, J.-P., Wurz, P., Cavalié, T., Coustenis, A., Courtin, R., Gautier, D., Helled, R., Irwin, P. G. J., Morse, A. D., Nettelmann, N., Marty, B., Rousselot, P., Venot, O., Atkinson, D. H., Waite, J. H., Reh, K. R., Simon, A. A., Atreya, S., André, N., Blanc, M., Daglis, I. A., Fischer, G., Geppert, W. D., Guillot, T., Hedman, M. M., Hueso, R., Lellouch, E., Lunine, J. I., Murray, C. D., O'Donoghue, J., Rengel, M., Sánchez-Lavega, A., Schmider, F.-X., Spiga, A., Spilker, T., Petit, J.-M., Tiscareno, M. S., Ali-Dib, M., Altwegg, K., Bolton, S. J., Bouquet, A., Briois, C., Fouchet, T., Guerlet, S., Kostiuk, T., Lebleu, D., Moreno, R., Orton, G. S., Poncy, J., Dec. 2014. Scientific rationale for Saturn's in situ exploration. Planet. Space Sci. 104, 29–47.

Mousis, O., Atkinson, D. H., Spilker, T., Venkatapathy, E., Poncy, J., Frampton, R., Coustenis, A., Reh, K., Lebreton, J.-P., Fletcher, L. N., Hueso, R., Amato, M. J., Colaprete, A., Ferri, F., Stam, D., Wurz, P., Atreya, S., Aslam, S., Banfield, D. J., Calcutt, S., Fischer, G., Holland, A., Keller, C., Kessler, E., Leese, M., Levacher, P., Morse, A., Muñoz, O., Renard, J.-B., Sheridan, S., Schmider, F.-X., Snik, F., Waite, J. H., Bird, M., Cavalié, T., Deleuil, M., Fortney, J., Gautier, D., Guillot, T., Lunine, J. I., Marty, B., Nixon, C., Orton, G. S., Sánchez-Lavega, A., Oct. 2016. The Hera Saturn entry probe mission. Planet. Space Sci. 130, 80–103.

Mousis, O., Atkinson, D. H., Cavalié, T., Fletcher, L. N., Amato, M. J., Aslam, S., Ferri, F., Renard, J.-B., Spilker, T., Venkatapathy, E., Wurz, P., Aplin, K., Coustenis, A., Deleuil, M., Dobrijevic, M., Fouchet, T., Guillot, T., Hartogh, P., Hewagama, T., Hofstadter, M. D., Hue, V., Hueso, R., Lebreton, J.-P., Lellouch, E., Moses, J., Orton, G. S., Pearl, J. C., Sánchez-Lavega, A., Simon, A., Venot, O., Waite, J. H., Achterberg, R. K., Atreya, S., Billebaud, F., Blanc, M., Borget, F., Brugger, B., Charnoz, S., Chiavassa, T., Cottini, V., d'Hendecourt, L., Danger, G., Encrenaz, T., Gorius, N. J. P., Jorda, L., Marty, B., Moreno, R., Morse, A., Nixon, C., Reh, K., Ronnet, T., Schmider, F.-X., Sheridan, S., Sotin, C., Vernazza, P., Villanueva, G. L., Jun. 2018. Scientific rationale for Uranus and Neptune in situ explorations. Planet. Space Sci. 155, 12–40.

Nettelmann, N., Helled, R., Fortney, J. J., Redmer, R., 2013. New indication for a dichotomy in the interior structure of Uranus and Neptune from the application of modified shape and rotation data. Planet. Space Sci. 77, 143–151.

Niemann, H. B., Atreya, S. K., Carignan, G. R., Donahue, T. M., Haberman, J. A., Harpold, D. N., Hartle, R. E., Hunten, D. M., Kasprzak, W. T., Mahaffy, P. R., Owen, T. C., Way, S. H., 1998. The composition of the Jovian atmosphere as determined by the Galileo probe mass spectrometer. J. Geophys. Res. 103, 22831–22846.

Nixon, C. A., Achterberg, R. K., Conrath, B. J., Irwin, P. G. J., Teanby, N. A., Fouchet, T., Parrish, P. D., Romani, P. N., Abbas, M., LeClair, A., Strobel, D., Simon-Miller, A. A., Jennings, D. J., Flasar, F. M., Kunde, V. G., May 2007. Meridional variations of C_2H_2 and C_2H_6 in Jupiter's atmosphere from Cassini CIRS infrared spectra. Icarus 188, 47–71.

Nixon, C. A., Achterberg, R. K., Romani, P. N., Allen, M., Zhang, X., Teanby, N. A., Irwin, P. G. J., Flasar, F. M., Nov. 2010. Abundances of Jupiter's trace hydrocarbons from Voyager and Cassini. Planet. Space Sci. 58, 1667–1680.

Noll, K. S., Knacke, R. F., Geballe, T. R., Tokunaga, A. T., 1986. Detection of carbon monoxide in Saturn. Astrophys. J. Lett. 309, L91–L94.

Noll, K. S., Larson, H. P., Jan. 1991. The spectrum of Saturn from 1990 to 2230/cm - Abundances of AsH3, CH3D, CO, GeH4, NH3, and PH3. Icarus 89, 168–189.

Ollivier, J. L., Dobrijévic, M., Parisot, J. P., Jun. 2000. New photochemical model of Saturn's atmosphere. Planet. Space Sci. 48, 699–716.

Orton, G. S., Friedson, A. J., Caldwell, J., Hammel, H. B., Baines, K. H., Bergstralh, J. T., Martin, T. Z., Malcom, M. E., West, R. A., Golisch, W. F., Griep, D. M., Kaminski, C. D., Tokunaga, A. T., Baron, R., Shure, M., Apr. 1991. Thermal maps of Jupiter - Spatial organization and time dependence of stratospheric temperatures, 1980 to 1990. Science 252, 537–542.

Orton, G. S., Yanamandra-Fisher, P. A., Fisher, B. M., Friedson, A. J., Parrish, P. D., Nelson, J. F., Bauermeister, A. S., Fletcher, L., Gezari, D. Y., Varosi, F., Tokunaga, A. T., Caldwell, J., Baines, K. H., Hora, J. L., Ressler, M. E., Fujiyoshi, T., Fuse, T., Hagopian, H., Martin, T. Z., Bergstralh, J. T., Howett, C., Hoffmann, W. F., Deutsch, L. K., van Cleve, J. E., Noe, E., Adams, J. D., Kassis, M., Tollestrup, E., May 2008. Semi-annual oscillations in Saturn's low-latitude stratospheric temperatures. Nature 453, 196–199.

Orton, G. S., Fletcher, L. N., Moses, J. I., Mainzer, A. K., Hines, D., Hammel, H. B., Martin-Torres, F. J., Burgdorf, M., Merlet, C., Line, M. R., Nov. 2014a. Mid-infrared spectroscopy of Uranus from the Spitzer Infrared Spectrometer: 1. Determination of the mean temperature structure of the upper troposphere and stratosphere. Icarus 243, 494–513.

Orton, G. S., Moses, J. I., Fletcher, L. N., Mainzer, A. K., Hines, D., Hammel, H. B., Martin-Torres, J., Burgdorf, M., Merlet, C., Line, M. R., Nov. 2014b. Mid-infrared spectroscopy of Uranus from the Spitzer infrared spectrometer: 2. Determination of the mean composition of the upper troposphere and stratosphere. Icarus 243, 471–493.

Owen, T., Mahaffy, P., Niemann, H. B., Atreya, S., Donahue, T., Bar-Nun, A., de Pater, I., 1999. A low-temperature origin for the planetesimals that formed Jupiter. Nature 402, 269–270.

Owen, T., Encrenaz, T., 2003. Element Abundances and Isotope Ratios in the Giant Planets and Titan. Space Sci. Rev. 106, 121–138.

Pearl, J. C., Conrath, B. J., Hanel, R. A., Pirraglia, J. A., 1990. The albedo, effective temperature, and energy balance of Uranus, as determined from Voyager IRIS data. Icarus 84, 12–28.

Pierel, J. D. R., Nixon, C. A., Lellouch, E., Fletcher, L. N., Bjoraker, G. L., Achterberg, R. K., Bézard, B., Hesman, B. E., Irwin, P. G. J., Flasar, F. M., Nov. 2017. D/H Ratios on Saturn and Jupiter from Cassini CIRS. Astron. J. 154, 178.

Pilbratt, G. L., Riedinger, J. R., Passvogel, T., Crone, G., Doyle, D., Gageur, U., Heras, A. M., Jewell, C., Metcalfe, L., Ott, S., Schmidt, M., Jul. 2010. Herschel Space Observatory. An ESA facility for far-infrared and submillimetre astronomy. Astron. Astrophys. 518, L1.

Poglitsch, A., Waelkens, C., Geis, N., Feuchtgruber, H., Vandenbussche, B., Rodriguez, L., Krause, O., Renotte, E., van Hoof, C., Saraceno, P., Cepa, J., Kerschbaum, F., Agnèse, P., Ali, B., Altieri, B., Andreani, P., Augueres, J.-L., Balog, Z., Barl, L., Bauer, O. H., Belbachir, N., Benedettini, M., Billot, N., Boulade, O., Bischof, H., Blommaert, J., Callut, E., Cara, C., Cerulli, R., Cesarsky, D., Contursi, A., Creten, Y., De Meester, W., Doublier, V., Doumayrou, E., Duband, L., Exter, K., Genzel, R., Gillis, J.-M., Grözinger, U., Henning, T., Herreros, J., Huygen, R., Inguscio, M., Jakob, G., Jamar, C., Jean, C., de Jong, J., Katterloher, R., Kiss, C., Klaas, U., Lemke, D., Lutz, D., Madden, S., Marquet, B., Martignac, J., Mazy, A., Merken, P., Montfort, F., Morbidelli, L., Müller, T., Nielbock, M., Okumura, K., Orfei, R., Ottensamer, R., Pezzuto, S., Popesso, P., Putzeys, J., Regibo, S., Reveret, V., Royer, P., Sauvage, M., Schreiber, J., Stegmaier, J., Schmitt, D., Schubert, J., Sturm, E., Thiel, M., Tofani, G., Vavrek, R., Wetzstein, M., Wieprecht, E., Wiezorrek, E., Jul. 2010. The Photodetector Array Camera and Spectrometer (PACS) on the Herschel Space Observatory. Astron. Astrophys. 518, L2.

Pollack, J. B., Hubickyj, O., Bodenheimer, P., Lissauer, J. J., Podolak, M., Greenzweig, Y., 1996. Formation of the Giant Planets by Concurrent Accretion of Solids and Gas. Icarus 124, 62–85.

Poppe, A. R., Jan. 2016. An improved model for interplanetary dust fluxes in the outer Solar System. Icarus 264, 369–386.

Porco, C. C., Helfenstein, P., Thomas, P. C., Ingersoll, A. P., Wisdom, J., West, R., Neukum, G., Denk, T., Wagner, R., Roatsch, T., Kieffer, S., Turtle, E., McEwen, A., Johnson, T. V., Rathbun, J., Veverka, J., Wilson, D., Perry, J., Spitale, J., Brahic, A., Burns, J. A., Del Genio, A. D., Dones, L., Murray, C. D., Squyres, S., Mar. 2006. Cassini Observes the Active South Pole of Enceladus. Science 311, 1393–1401.

Prangé, R., Fouchet, T., Courtin, R., Connerney, J. E. P., McConnell, J. C., Feb. 2006. Latitudinal variation of Saturn photochemistry deduced from spatially-resolved ultraviolet spectra. Icarus 180, 379–392.

Prather, M. J., Logan, J. A., McElroy, M. B., Aug. 1978. Carbon monoxide in Jupiter's upper atmosphere - an extraplanetary source. Astrophys. J. 223, 1072–1081.

Rengel, M., Hartogh, P., Jarchow, C., Aug. 2008. Mesospheric vertical thermal structure and winds on Venus from HHSMT CO spectral-line observations. Planet. Space Sci. 56, 1368–1384.

Rezac, L., de Val-Borro, M., Hartogh, P., Cavalié, T., Jarchow, C., Rengel, M., Dobrijevic, M., Mar. 2014. New determination of the HCN profile in the stratosphere of Neptune from millimeter-wave spectroscopy. Astron. Astrophys. 563, A4.

Roelfsema, P. R., Helmich, F. P., Teyssier, D., Ossenkopf, V., Morris, P., Olberg, M., Shipman, R., Risacher, C., Akyilmaz, M., Assendorp, R., Avruch, I. M., Beintema, D., Biver, N., Boogert, A., Borys, C., Braine, J., Caris, M., Caux, E., Cernicharo, J., Coeur-Joly, O., Comito, C., de Lange, G., Delforge, B., Dieleman, P., Dubbeldam, L., de Graauw, T., Edwards, K., Fich, M., Flederus, F., Gal, C., di Giorgio, A., Herpin, F., Higgins, D. R., Hoac, A., Huisman, R., Jarchow, C., Jellema, W., de Jonge, A., Kester, D., Klein, T., Kooi, J., Kramer, C., Laauwen, W., Larsson, B., Leinz, C., Lord, S., Lorenzani, A., Luinge, W., Marston, A., Martín-Pintado, J., McCoey, C., Melchior, M., Michalska, M., Moreno, R., Müller, H., Nowosielski, W., Okada, Y., Orleański, P., Phillips, T. G., Pearson, J., Rabois, D., Ravera, L., Rector, J., Rengel, M., Sagawa, H., Salomons, W., Sánchez-Suárez, E., Schieder, R., Schlöder, F., Schmülling, F., Soldati, M., Stutzki, J., Thomas, B., Tielens, A. G. G. M., Vastel, C., Wildeman, K., Xie, Q., Xilouris, M., Wafelbakker, C., Whyborn, N., Zaal, P., Bell, T., Bjerkeli, P., De Beck, E., Cavalié, T., Crockett, N. R., Hily-Blant, P., Kama, M., Kaminski, T., Leflóch, B., Lombaert, R., de Luca, M., Makai, Z., Marseille, M., Nagy, Z., Pacheco, S., van der Wiel, M. H. D., Wang, S., Yıldız, U., Jan. 2012. In-orbit performance of Herschel-HIFI. Astron. Astrophys. 537, A17.

Roth, L., Saur, J., Retherford, K. D., Strobel, D. F., Feldman, P. D., McGrath, M. A., Nimmo, F., Jan. 2014. Transient Water Vapor at Europa's South Pole. Science 343, 171–174.

Sagawa, H., Hartogh, P., Rengel, M., de Lange, A., Cavalié, T., Nov. 2010. Preparation for the solar system observations with Herschel: Simulation of Jupiter observations with PACS. Planet. Space Sci. 58, 1692–1698.

Sanchez-Lavega, A., Colas, F., Lecacheux, J., Laques, P., Parker, D., Miyazaki, I., Oct. 1991. The Great White SPOT and disturbances in Saturn's equatorial atmosphere during 1990. Nature 353, 397–401.

Sánchez-Lavega, A., del Río-Gaztelurrutia, T., Hueso, R., Gómez-Forrellad, J. M., Sanz-Requena, J. F., Legarreta, J., García-Melendo, E., Colas, F., Lecacheux, J., Fletcher, L. N., Barrado y Navascués, D., Parker, D., International Outer Planet Watch Team, Akutsu, T., Barry, T., Beltran, J., Buda, S., Combs, B., Carvalho, F., Casquinha, P., Delcroix, M., Ghomizadeh, S., Go, C., Hotershall, J., Ikemura, T., Jolly, G., Kazemoto, A., Kumamori, T., Lecompte, M., Maxson, P., Melillo, F. J., Milika, D. P., Morales, E., Peach, D., Phillips, J., Poupeau, J. J., Sussenbach, J., Walker, G., Walker, S., Tranter, T., Wesley, A., Wilson, T., Yunoki, K., Jul. 2011. Deep winds beneath Saturn's upper clouds from a seasonal long-lived planetary-scale storm. Nature 475, 71–74.

Sánchez-Lavega, A., del Río-Gaztelurrutia, T., Delcroix, M., Legarreta, J. J., Gómez-Forrellad, J. M., Hueso, R., García-Melendo, E., Pérez-Hoyos, S., Barrado-Navascués, D., Lillo, J., International Outer Planet Watch Team IOPW-PVOL, Aug. 2012. Ground-based observations of the long-term evolution and death of Saturn's 2010 Great White Spot. Icarus 220, 561–576.

Sánchez-Lavega, A., Fischer, G., Fletcher, L. N., García-Melendo, E., Hesman, B., Pérez-Hoyos, S., Sayanagi, K. M., Sromovsky, L. A., Nov. 2016. The Great Saturn Storm of 2010-2011. ArXiv e-prints.

Sinclair, J. A., Orton, G. S., Greathouse, T. K., Fletcher, L. N., Tao, C., Gladstone, G. R., Adriani, A., Dunn, W., Moses, J. I., Hue, V., Irwin, P. G. J., Melin, H., Giles, R. S., Jun. 2017. Independent evolution of stratospheric temperatures in Jupiter's northern and southern auroral regions from 2014 to 2016. Geophys. Res. Lett. 44, 5345–5354.

Sleiman, C., González, S., Klippenstein, S. J., Talbi, D., El Diba, G., Canosa, A., 2016. Pressure dependent low temperature kinetics for CN + CH_3CN: competition between chemical reaction and van der Waals complex formation. Phys. Chem. Chem. Phys. 18, 15118.

Sparks, W. B., Hand, K. P., McGrath, M. A., Bergeron, E., Cracraft, M., Deustua, S. E., Oct. 2016. Probing for Evidence of Plumes on Europa with HST/STIS. Astrophys. J. 829, 121.

Spilker, L., Ferrari, C., Cuzzi, J. N., Showalter, M., Pearl, J., Wallis, B., Dec. 2003. Saturn's rings in the thermal infrared. Planet. Space Sci. 51, 929–935.

Spilker, L. J., Pilorz, S. H., Edgington, S. G., Wallis, B. D., Brooks, S. M., Pearl, J. C., Flasar, F. M., Jun. 2005. Cassini CIRS Observations of a Roll-Off in Saturn Ring Spectra at Submillimeter Wavelengths. Earth Moon and Planets 96, 149–163.

Sromovsky, L. A., Fry, P. M., Hammel, H. B., de Pater, I., Rages, K. A., Aug. 2012. Post-equinox dynamics and polar cloud structure on Uranus. Icarus 220, 694–712.

Strobel, D. F., Yung, Y. L., 1979. The Galilean satellites as a source of CO in the Jovian upper atmosphere. Icarus 37, 256–263.

Swinyard, B. M., Hartogh, P., Sidher, S., Fulton, T., Lellouch, E., Jarchow, C., Griffin, M. J., Moreno, R., Sagawa, H., Portyankina, G., Blecka, M., Banaszkiewicz, M., Bockelee-Morvan, D., Crovisier, J., Encrenaz, T., Kueppers, M., Lara, L., Lis, D., Medvedev, A., Rengel, M., Szutowicz, S., Vandenbussche, B., Bensch, F., Bergin, E., Billebaud, F., Biver, N., Blake, G., Blommaert, J., de Val-Borro, M., Cernicharo, J., Cavalie, T., Courtin, R., Davis, G., Decin, L., Encrenaz, P., de Graauw, T., Jehin, E., Kidger, M., Leeks, S., Orton, G., Naylor, D., Schieder, R., Stam, D., Thomas, N., Verdugo, E., Waelkens, C., Walker, H., Jul. 2010. The Herschel-SPIRE submillimetre spectrum of Mars. Astron. Astrophys. 518, L151.

Teanby, N. A., Irwin, P. G. J., 2013. An external origin for carbon monoxide on uranus from herschel/spire? Astrophys. J. Lett. 775 (2), L49.

Testi, L., Andreani, P., Mar. 2013. Report on the Conference "The First Year of ALMA Science". The Messenger 151, 50–54.

Toublanc, D., Parisot, J. P., Brillet, J., Gautier, D., Raulin, F., McKay, C. P., Jan. 1995. Photochemical Modeling of Titan's Atmosphere. Icarus 113, 2–26.

Venot, O., Hébrard, E., Agúndez, M., Dobrijevic, M., Selsis, F., Hersant, F., Iro, N., Bounaceur, R., 2012. A chemical model for the atmosphere of hot Jupiters. Astron. Astrophys. 546, A43.

Visscher, C., Fegley, Jr., B., 2005. Chemical Constraints on the Water and Total Oxygen Abundances in the Deep Atmosphere of Saturn. Astrophys. J. 623, 1221–1227.

Visscher, C., Moses, J. I., Saslow, S. A., 2010. The deep water abundance on Jupiter: New constraints from thermochemical kinetics and diffusion modeling. Icarus 209, 602–615.

von Zahn, U., Hunten, D. M., Lehmacher, G., 1998. Helium in Jupiter's atmosphere: Results from the Galileo probe helium interferometer experiment. J. Geophys. Res. 103, 22815–22830.

Waite, J. H., Combi, M. R., Ip, W.-H., Cravens, T. E., McNutt, R. L., Kasprzak, W., Yelle, R., Luhmann, J., Niemann, H., Gell, D., Magee, B., Fletcher, G., Lunine, J., Tseng, W.-L., Mar. 2006. Cassini Ion and Neutral Mass Spectrometer: Enceladus Plume Composition and Structure. Science 311, 1419–1422.

Waite, J. H., Sep. 2017. Cassini INMS Measurements of Saturn's Atmosphere. European Planetary Science Congress 11, EPSC2017–736.

Watson, W. D., Feb. 1974. Ion-Molecule Reactions, Molecule Formation, and Hydrogen-Isotope Exchange in Dense Interstellar Clouds. Astrophys. J. 188, 35–42.

Wong, M. H., Mahaffy, P. R., Atreya, S. K., Niemann, H. B., Owen, T. C., 2004. Updated Galileo probe mass spectrometer measurements of carbon, oxygen, nitrogen, and sulfur on Jupiter. Icarus 171, 153–170.

Zahnle, K., Schenk, P., Levison, H., Dones, L., Jun. 2003. Cratering rates in the outer Solar System. Icarus 163, 263–289.

Zhang, X., West, R. A., Banfield, D., Yung, Y. L., Sep. 2013. Stratospheric aerosols on Jupiter from Cassini observations. Icarus 226, 159–171.

Appendix A

Publication list

Refereed publications

1. Mousis, O., Atkinson, D., Cavalié, T., Fletcher, L., Amato, M. J., Ferri, F., Renard, J.-B., Spilker, T., Venkatapathy, E., Wurz, P, Aplin, K., Coustenis, A., Deleuil, M., Dobrijevic, M., Fouchet, T., Guiloot, T., Hartogh, P., Hueso, R., Hewagama, T., Hofstadter, M. D., Hue, V., Lebreton, J.-P., Lellouch, E., Moses, J., Orton, G. S., Pearl, J. C., Sánchez-Lavega, A., Simon, A., Venot, O., Waite, J. H., Atreya, S., Billebaud, F., Brugger, B., Achterberg, R., Blanc, M., Charnoz, S., Cottini, V., Encrenaz, T., Gorius, N. J. P., Marty, B., Moreno, R., Morse, A., Nixon, C., Reh, K., Schmider, F.-X., Sheridan, S., Sotin, C., Vernazza, P., Villanueva, G. L., 2017. Scientific rationale for Uranus and Neptune in situ explorations. Planetary and Space Science 155, 12-40.

2. Hue, V., Hersant, F., Cavalié, T., Dobrijevic, M., Sinclair, J., 2017. Photochemistry, mixing and transport in Jupiter's stratosphere constrained by Cassini. Icarus 307, 106-123.

3. Moreno, R., Lellouch, E., Cavalié, T., Moullet, A., 2017. Detection of CS in Neptune's atmosphere from ALMA observations. Astronomy and Astrophysics 608, L5.

4. Cavalié, T., Venot, O., Selsis, F., Hersant, F., Hartogh, P., Leconte, J., 2017. Thermochemistry and vertical mixing in the tropospheres of Uranus and Neptune. How convection inhibition can affect the derivation of deep oxygen abundances. Icarus 291, 1-16.

5. Mousis, O., Atkinson, D. H., Spilker, T., Venkatapathy, E., Poncy, J., Frampton, R., Coustenis, A., Reh, K., Lebreton, J.-P., Fletcher, L. N., Hueso, R., Amato, M. J., Colaprete, A., Ferri, F., Stam, D., Wurz, P., Atreya, S., Aslam, S., Banfield, D. J., Calcutt, S., Fischer, G., Holland, A., Keller, C., Kessler, E., Leese, M., Levacher, P., Morse, A., Muoz, O., Renard, J.-B., Sheridan, S., Schmider, F.-X., Snik, F., Waite, J. H., Bird, M., Cavalié, T., Deleuil, M., Fortney, J., Gautier, D., Guillot, T., Lunine, J. I., Marty, B., Nixon, C., Orton, G. S., Sánchez-Lavega, A., 2016. The Hera Saturn entry probe mission. Planetary and Space Science 130, 80-103.

6. Hue, V., Greathouse, T. K., Cavalié, T., Dobrijevic, M., Hersant, F., 2016. 2D photochemical modeling of Saturn's stratosphere. Part II: Feedback between composition and temperature. Icarus 267, 334-343.

7. Norwood, J., Moses, J., Fletcher, L. N., Orton, G., Irwin, P. G. J., Atreya, S., Rages, K., Cavalié, T., Sánchez-Lavega, A., Hueso, R., Chanover, N., 2016. Giant Planet Observations with the James Webb Space Telescope. Publications of the Astronomical Society of Pacific 128, 018005.

8. Mandt, K. E., Mousis, O., Marty, B., Cavalié, T., Harris, W., Hartogh, P., Willacy, K., 2015. Constraints from Comets on the Formation and Volatile Acquisition of the Planets and Satellites. Space Science Reviews 197, 297-342.

9. Hue, V., Cavalié, T., Dobrijevic, M., Hersant, F., Greathouse, T. K., 2015. 2D photochemical modelling of Saturn's stratosphere. Part I: Seasonal variation of atmospheric composition. Icarus 257, 163-184.

10. Cavalié, T., Dobrijevic, M, Fletcher, L. N., Loison, J. C., Hickson, K. M., Hue, V., Hartogh, P., 2015. The photochemical response to the variation of temperature in Saturn's 2011-2012 stratospheric vortex. Astronomy and Astrophysics 580, A55.

11. Lellouch, E., Moreno, R., Orton, G. S., Feuchtgruber, H., Cavalié, T., Moses, J. I., Hartogh, P., Jarchow, C., Sagawa, H., 2015. New constraints on the CH4 vertical profile in Uranus and Neptune from Herschel observations. Astronomy and Astrophysics 579, A121.

12. Mousis, O., Fletcher, L. N., Lebreton, J.-P., Wurz, P., Cavalié, T., Coustenis, A., Courtin, R., Gautier, D., Helled, R., Irwin, P. G. J., Morse, A. D., Nettelman, N., Marty, B., Rousselot, P., Venot, O., Atkinson, D. H., Waite, J. H., Reh, K., Simon-Miller, A., Atreya, S., André, N., Blanc, M., Daglis, I. A., Fischer, G., Geppert, W. D., Guillot, T., Hedman, M. M., Hueso, R., Lellouch, E., Lunine, J. I., Murray, C. D., O'Donoghue, J., Rengel, M., Sánchez-Lavega, A., Schmider, F.-X., Spiga, A., Spilker, T., Petit, J.-M., Tiscanero, M. S., Ali-Dib, M., Altwegg, K., Bouquet, A., Briois, C., Fouchet, T., Guerlet, S., Kostiuk, T., Lebleu, D., Moreno, R., Orton, G. S., Poncy, J., 2014. Scientific rationale of Saturn's in situ exploration. Planetary and Space Science 104, 29-47.

13. Arridge, C., Agnor, C., Ambrosini, R. M., André, N., Banfield, D., Bocanegra-Bahamon, T., Bonfond, B., Bracken, C., Briand, C., Brooks, S. M., Briois, C., Castillo-Rogez, J. C., Cavalié, T., Dirkx, D., Fletcher, L. N., Gerth, I., Grassi, D., Hedman, M. M., Hillier, J., Hospodarsky, G., Jackman, C. M., Khalisi, E., Konstantinidis, K., Krüger, H., Labrianidis, C., Lamy, L. L., Laneuville, M., Luntzer, A., MacArthur, J., McKenna-Lawlor, S., Maier, A., Melin, H., Moragas-Klostermeyer, G., Morschhauser, A., Milillo, A., Mousis, O., Neubauer, F. M., Nordheim, T. A., Peron, R., Postberg, F., Retherford, K. D., Russell, C. T., Rymer, A. M., Sallantin, R., Spahn, F., Sitja, M. C., Srama, R., Tiscareno, M., Tobie, G., Tosi, F., Turrini, D., Turtle, E., Wilson, R. J., 2014. The science case for an orbital mission to Uranus: Exploring the origins and evolution of ice giant planets. Planetary and Space Science 104, 122-140.

14. Hickson, K. M., Loison, J. C., Cavalié, T., Hébrard, É., Dobrijevic, M., 2014. The evolution of infalling sulfur species in Titan's atmosphere. Astronomy and Astrophysics 572, A58.

15. Rezac, L., de Val-Borro, M., Hartogh, P., Cavalié, T., Jarchow, C., Rengel, M., Dobrijevic, M., 2014. New determination of the HCN profile in the stratosphere of Neptune from millimeter-wave spectroscopy. Astronomy and Astrophysics 563, A4.

16. Cavalié, T., Moreno, R., Lellouch, E., Hartogh, P., Venot, O., Orton, G., Jarchow, C., Encrenaz, T., Selsis, F., Hersant, F., Fletcher, L., 2014. First submillimeter observation of CO in the stratosphere of Uranus. Astronomy and Astrophysics 562, A33.

17. Cavalié, T., Feuchtgruber, H., Lellouch, E., de Val-Borro, Jarchow, C., M., Moreno, R., Hartogh, P., Orton, G., Greathouse T., Billebaud, F., Dobrijevic, M., Lara, L. M., Gonzalez, A., Sagawa, H., 2013. The spatial distribution of water in the stratosphere of Jupiter from Herschel–HIFI and –PACS observations. Astronomy and Astrophysics 553, A21.

18. Feuchtgruber, H., Lellouch, E., Orton, G., de Graauw, T., Vandenbussche, B., Swinyard, B., Moreno, R., Jarchow, C., Billebaud, F., Cavalié, T., Hartogh, P., 2013. The D/H ratio in the atmospheres of Uranus and Neptune from Herschel PACS observations. Astronomy and Astrophysics 551, A126.

19. Fletcher, L. N., Swinyard, B., Salji, C., Polehampton, E., Fulton, T., Sidher, S., Lellouch, E., Moreno, R., Orton, G., Cavalié, T., Courtin, R., Rengel, M., Sagawa, H., Davis, G. R., Hartogh, P., Naylor, D., Walker, H., Lim, T., 2012. Sub-millimetre spectroscopy of Saturn's trace gases from Herschel/SPIRE. Astronomy and Astrophysics 539, A44.

20. Cavalié, T., Biver, N., Hartogh, P., Dobrijevic, M., Billebaud, F., Lellouch, E., Sandqvist, Aa, Brillet, J., Lecacheux, A., Hjalmarson, Å, Frisk, U., Olberg, M., The Odin Team, 2012. Odin Space Telescope monitoring of water vapor in the stratosphere of Jupiter. Planetary and Space Science 537, A17.

21. Roelfsema, P. R., Helmich, F. P., Teyssier, D., Ossenkopf, V., Morris, P., Olberg, M., Shipman, R., Risacher, C., Akyilmaz, M., Assendorp, R., Avruch, I .A., Beintema, D., Biver, N., Boogert, A., Borys, C., Braine, J., Caris, M., Caux, E., Cernicharo, J., Coeur-Joly, O., Comito, C., de Lange, G., Delforge, B., Dieleman, P., Dubbeldam, L., de Graauw, Th., Edwards, K., Fich, M., Flederus, F., Gal, C., DiGiorgio, A., Herpin, F., Higgins, D. R., Hoac, A., Huisman, R., Jarchow, C., Jellema, W., de Jonge, A., Kester, D., Klein, T., Kooi, J., Kramer, C., Laauwen, W., Larsson, B., Leinz, C., Lord, S., Lorenzani, A., Luinge, W., Marston, A., Martn-Pintado, J., McCoey, C., Melchior, M., Michalska, M., Moreno, R., Müller, H., Nowosielski, W., Okada, Y., Orleánski, P., Phillips, T. G., Pearson, J., Rabois, D., Ravera, L., Rector, J., Rengel, M., Sagawa, H., Salomons, W., Sánchez-Suárez, E., Schieder, R., Schlöder, F., Schmülling, F., Soldati, M., Stutzki, J., Thomas, B. Tielens, A. G. G. M., Vastel, C., Wildeman, K., Xie, Q., Xilouris, M., Wafelbakker, C., Whyborn, N., and Zaal, P., Bell, T., Bjerkelli, P., de Beck, E., Cavalié, T., Crockett, N. R., Hily-Blant, P., Kama, M., Kaminski, T., Leflóch, B., Lombaert, R., De Luca, M., Makai, Z., Marseille, M., Nagy, Z., Pacheco, S., van der Weil, M. H. D., Wang, S., Yıldız, U, 2012. In-orbit performance of Herschel-HIFI. Astronomy and Astrophysics 537, A17.

22. Hartogh, P., Lellouch, E., Moreno, R., Bockelée-Morvan, D., Biver, N., Cassidy, T., Rengel, M., Jarchow, C., Cavalié, T., Crovisier, J., Helmich, F. P., 2011. Direct detection of the Enceladus H_2O torus with Herschel. Astronomy and Astrophysics 532, L2.

23. Dobrijevic, M., Cavalié, T., Billebaud, F., 2011. A methodology to construct a reduced chemical scheme for 2D-3D photochemical models: Application to Saturn. Icarus 214, 275-285.

24. Sagawa, H., Hartogh, P., Rengel, M., de Lange, A., Cavalié, T., 2010. Preparation for the Solar system observations with Herschel: Simulation of Jupiter observations with PACS. Planetary and Space Science 58, 1692-1698.

25. Dobrijevic, M., Cavalié, T., Hébrard, É., Billebaud, F., Hersant, F., Selsis, F., 2010. Key reactions in the photochemistry of hydrocarbon in Neptune's stratosphere. Planetary and Space Science 58, 1555-1566.

26. Hartogh, P., Jarchow, C., Lellouch, E., de Val-Borro, M., Rengel, M., Moreno, R., Medvedev, A.S., Sagawa, H., Swinyard, B. M., Cavalié, T., Lis, D. C., Błęcka, M. I., Banaszkiewicz, M., Bockelée-Morvan, D., Crovisier, J., Encrenaz, T., Küppers, M., Lara, L.-M., Szutowicz, S., Vandenbussche, B., Bensch, F., Bergin, E. A., Billebaud, F., Biver, N., Blake, G. A., Blommaert, J. A. D. L., Cernicharo, J., Decin, L., Encrenaz, P., Feuchtgruber, H., Fulton, T., de Graauw, T., Jehin, E., Kidger, M., Lorente, R., Naylor, D. A., Portyankina, G., Sánchez-Portal, M., Schieder, R., Sidher, S., Thomas, N., Verdugo, E., Waelkens, C., Whyborn, N., Teyssier, D., Helmich, F., Roelfsema, P., Stutzki, J., Leduc, H. G., Stern, J. A., 2010c. Herschel/HIFI observations of Mars: First detection of O2 at submillimetre wavelengths and upper limits on HCl and H_2O_2. Astronomy and Astrophysics 521, L49.

27. Hartogh, P., Błęcka, M. I., Jarchow, C., Sagawa, H., Lellouch, E., de Val-Borro, M., Rengel, M., Medvedev, A.S., Swinyard, B. M., Moreno, R., Cavalié, T., Lis, D. C., Banaszkiewicz, M., Bockelée-Morvan, D., Crovisier, J., Encrenaz, T., Küppers, M., Lara, L.-M., Szutowicz, S., Vandenbussche, B., Bensch, F., Bergin, E. A., Billebaud, F., Biver, N., Blake, G. A., Blommaert, J. A. D. L., Cernicharo, J., Decin, L., Encrenaz, P., Feuchtgruber, H., Fulton, T., de Graauw, T., Jehin, E., Kidger, M., Lorente, R., Naylor, D. A., Portyankina, G., Sánchez-Portal, M., Schieder, R., Sidher, S., Thomas, N., Verdugo, E., Waelkens, C., Lorenzani, A., Tofani, G., Natale, E., Pearson, J., Klein, T., Leinz, C., Güsten, R., Kramer, C., 2010b. First results on martian carbon monoxide from Herschel/HIFI observations. Astronomy and Astrophysics 521, L48.

28. Lellouch, E., Hartogh, P., Feuchtgruber, H., Vandenbussche, B., de Graauw, T., Moreno, R., Jarchow, C., Cavalié, T., Orton, G., Banaszkiewicz, M., Błęcka, M., Bockelée-Morvan, D., Crovisier, J., Encrenaz, T., Fulton, T., Küppers, M., Lara, L.-M., Lis, D. C., Medvedev, A., Rengel, M., Sagawa, H., Swinyard, B., Szutowicz, S., Bensch, F., Bergin, E., Billebaud, F., Biver, N., Blake, G. A., Blommaert, J., Cernicharo, J., Courtin, R., Davis, G. R., Decin, L., Encrenaz, P., Gonzalez, A., Jehin, E., Kidger, M., Naylor, D., Portyankina, G., Schieder, R., Sidher, S., Thomas, N., de Val-Borro, M., Verdugo, E., Waelkens, C., Walker, H., Aarts, H., Comito, C., Kawamura, J. H., Maestrini, A., Peacoke, T., Teipen, R., Tils, T., Wildeman, K., 2010. First results of Herschel / PACS observations of Neptune. Astronomy and Astrophysics 518, L152.

29. Swinyard, B. M., Hartogh, P., Sidher, S., Fulton, T., Lellouch, E., Jarchow, C., Griffin, M. J., Moreno, R., Sagawa, H., Portyankina, G., Błęcka, M., Banaszkiewicz, M., Bockelée-Morvan, D., Crovisier, J., Encrenaz, T., Kueppers, M., Lara, L., Lis, D., Medvedev, A., Rengel, M., Szutowicz, S., Vandenbussche, B., Bensch, F., Bergin, E., Billebaud, F., Biver, N., Blake, G., Blommaert, J., de Val-Borro, M., Cernicharo, J., Cavalié, T., Courtin, R., Davis, G., Decin, L., Encrenaz, P., de Graauw, T., Jehin, E., Kidger, M., Leeks, S., Orton, G., Naylor, D., Schieder, R., Stam, D., Thomas, N., Verdugo, E., Waelkens, C., Walker, H., 2010. The Herschel-SPIRE submillimetre spectrum of Mars. Astronomy and Astrophysics 518, L151.

30. Hartogh, P., Crovisier, J., de Val-Borro, M., Bockelée-Morvan, D., Biver, N., Lis, D. C., Moreno, R., Jarchow, C., Rengel, M., Emprechtinger, M., Szutowicz, S., Banaszkiewicz, M., Bensch, F., Błęcka, M. I., Cavalié, T., Encrenaz, T., Jehin, E., Küppers, M., Lara, L.-M., Lellouch, E., Swinyard, B. M., Vandenbussche, B., Bergin, E. A., Blake, G. A., Blommaert, J. A. D. L., Cernicharo, J., Decin, L., Encrenaz, P., de Graauw, T., Hutsemekers, D., Kidger, M., Manfroid, J., Medvedev, A. S., Naylor, D. A., Schieder, R., Thomas, N., Waelkens, C., Roelfsema, P. R., Dieleman, P., Güsten, R., Klein, T., Kasemann, C., Caris, M., Olberg, M., Benz, A. O., 2010a. HIFI Observations of Water in the Atmosphere of Comet C/2008 Q3 (Garradd). Astronomy and Astrophysics 518, L150.

31. Cavalié, T., Hartogh, P., Billebaud, F., Dobrijevic, M., Fouchet, T., Lellouch, E., Encrenaz, T., Brillet, J., Moriarty-Schieven, G. H., 2010. A cometary origin for CO in the stratosphere of Saturn? Astronomy and Astrophysics 510, A88.

32. Hartogh, P., Lellouch, E., Crovisier, J., Banaszkiewicz, M., Bensch, F., Bergin, E. A., Billebaud, F., Biver, N., Blake, G. A., Błęcka, M. I., Blommaert, J., Bockelée-Morvan, D., Cavalié, T., Cernicharo, J., Courtin, R., Davis, G., Decin, L., Encrenaz, P., Encrenaz, T., González, A., de Graauw, T., Hutsemékers, D., Jarchow, C., Jehin, E., Kidger, M., Küppers, M., de Lang, A., Lara, L.-M., Lis, D. C., Lorent, R., Manfroid, J., Medvedev, A. S., Moreno, R., Naylor, D. A., Orton, G., Portyankina, G., Rengel, M., Sagawa, H., Sánchez-Portal, M., Schieder, R., Sidher, S., Stam, D., Swinyard, B., Szutowicz, S., Thomas, N., Thornhill, G. Vandenbussche, B., Verdugo, E., Waelkens, C., Walker, H., 2009. Water and related chemistry in the Solar System. A guaranteed Time Key Program for Hershel. Planetary and Space Science 57, 1596-1606.

33. Cavalié, T., Billebaud, F., Dobrijevic, M., Fouchet, T., Lellouch, E., Encrenaz, T., Brillet, J., Moriarty-Schieven, G. H., Wouterloot, J. G. A., Hartogh, P., 2009. First observation of CO at 345 GHz in the atmosphere of Saturn with the JCMT. New constraints on its origin. Icarus 203, 531-540.

34. Cavalié, T., Billebaud, F., Biver, N., Dobrijevic, M., Lellouch, E., Brillet, J., Lecacheux, A., Hjalmarson, Å, Sandqvist, Aa, Frisk, U., Olberg, M., Bergin, E. A., The Odin Team, 2008c. Observation of water vapor in the stratosphere of Jupiter with the Odin Space Telescope. Planetary and Space Science 56, 1573-1584.

35. Cavalié, T., Billebaud, F., Encrenaz, T., Brillet, J., Forget, F., Dobrijevic, M., 2008b. Vertical temperature profile and mesospheric winds retrieval on Mars from millimeter observations. Comparison with General Circulation Model predictions. Astronomy and Astrophysics 489, 795-809.

36. Cavalié, T., Billebaud, F., Fouchet, T., Lellouch, E., Brillet, J., Dobrijevic, M., 2008a. Observations of CO on Saturn and Uranus at millimeter wavelengths: New upper limit determinations. Astronomy and Astrophysics 484, 555-561.

Unrefereed publications - Minor Planet Center Circulars

1. Ludwig, F., Stecklum, B. Bacci, P., Maestripieri, M., Grazia, M. D., Tesi, L., Fagioli, G., Buzzi, L., Pettarin, E., Schwartz, M., Holvorcem, P. R., Thinius, B., Bulger, J., Lowe, T., Schultz, A., Willman, M., Chambers, K., Chastel, S., Denneau, L., Flewelling, H., Huber, M., Lilly, E., Magnier, E., Wainscoat, R., Waters, C., Weryk, R., Holmes, R., Foglia, S., Linder, T., Leonard, G. J., Matheny, R. G., Christensen, E. J., Fuls, D. C., Gibbs, A. R., Grauer, A. D., Johnson, J. A., Kowalski, R. A., Larson, S. M., Seaman, R. L., Shelly, F. C., Losse, F., Cavalié, T., Birtwhistle, P., Bacci, R., Heinze, A., Weiland, H., Tonry, J., Stalder, B. 2017 VN15. Minor Planet Electronic Circ., No. 2017-W68 (2017).

2. Ludwig, F., Stecklum, B., Bacci, P., Maestripieri, M., Tesi, L., Fagioli, G., Jaeger, M., Prosperi, E., Vollmann, W., Buzzi, L., Gilmore, A. C., Kilmartin, P. M., Bittesini, L., Bressan, F., Pettarin, E., Kowalski, R. A., Christensen, E. J., Fuls, D. C., Gibbs, A. R., Grauer, A. D., Johnson, J. A., Larson, S. M., Leonard, G. J., Matheny, R. G., Seaman, R. L., Shelly, F. C., Schwartz, M., Holvorcem, P. R., Holmes, R., Foglia, S., Linder, T., Losse, F., Cavalié, T., Birtwhistle, P., Favero, G., Campestrin, M., Bacci, R., Denneau, L., Heinze, A., Weiland, H., Tonry, J., Flewelling, H., Stalder, B. 2017 WP. Minor Planet Electronic Circ., No. 2017-W69 (2017).

3. Bacci, P., Maestripieri, M., Grazia, M. D., Tesi, L., Fagioli, G., Schwartz, M., Holvorcem, P. R., Grauer, A. D., Christensen, E. J., Fuls, D. C., Gibbs, A. R., Johnson, J. A., Kowalski, R. A., Larson, S. M., Leonard, G. J., Matheny, R. G., Seaman, R. L., Shelly, F. C., Holmes, R., Foglia, S., Buzzi, L., Linder, T., Losse, F., Cavalié, T., Ruiz, P., Knoefel, A., Koschny, D., Busch, M., Micheli, M., Schwab, E. 2017 WR. Minor Planet Electronic Circ., No. 2017-W70 (2017).

4. Schwartz, M., Holvorcem, P. R., Grauer, A. D., Christensen, E. J., Fuls, D. C., Gibbs, A. R., Johnson, J. A., Kowalski, R. A., Larson, S. M., Leonard, G. J., Matheny, R. G., Seaman, R. L., Shelly, F. C., Ryan, W. H., Ryan, E. V., Holmes, R., Foglia, S., Buzzi, L., Linder, T., Losse, F., Cavalié, T. 2017 WV. Minor Planet Electronic Circ., No. 2017-W71 (2017).

5. Schwartz, M., Holvorcem, P. R., Bulger, J., Lowe, T., Schultz, A., Willman, M., Chambers, K., Chastel, S., Denneau, L., Flewelling, H., Huber, M., Lilly, E., Magnier, E., Wainscoat, R., Waters, C., Weryk, R., Grauer, A. D., Christensen, E. J., Fuls, D. C., Gibbs, A. R., Johnson, J. A., Kowalski, R. A., Larson, S. M., Leonard, G. J., Matheny, R. G., Seaman, R. L., Shelly, F. C., Ryan, W. H.,

Ryan, E. V., Holmes, R., Foglia, S., Buzzi, L., Linder, T., Losse, F., Cavalié, T., Bacci, R. 2017 WW. Minor Planet Electronic Circ., No. 2017-W72 (2017).

6. Ludwig, F., Stecklum, B., Bacci, P., Maestripieri, M., Grazia, M. D., Tesi, L., Fagioli, G., Jaeger, M., Prosperi, E., Vollmann, W., Foglia, S., Galli, G., Fuls, D. C., Christensen, E. J., Gibbs, A. R., Grauer, A. D., Johnson, J. A., Kowalski, R. A., Larson, S. M., Leonard, G. J., Matheny, R. G., Seaman, R. L., Shelly, F. C., Schwartz, M., Holvorcem, P. R., Bulger, J., Lowe, T., Schultz, A., Willman, M., Chambers, K., Chastel, S., Denneau, L., Flewelling, H., Huber, M., Lilly, E., Magnier, E., Wainscoat, R., Waters, C., Weryk, R., Losse, F., Cavalié, T., Favero, G., Campestrin, M., Pascoli Observatory, G., Bacci, R. 2017WN1. Minor Planet Electronic Circ., No. 2017-W84 (2017).

7. Boattini, A., Christensen, E. J., Gibbs, A. R., Grauer, A. D., Hill, R. E., Johnson, J. A., Kowalski, R. A., Larson, S. M., McNaught, R. H., Shelly, F. C., Fratev, F., Minkov, M., Hume, C., Twer, A., Klein, M., Mantero, A., Holmes, R., Foglia, S., Buzzi, L., Devore, H., Kostin, A., Linder, T., Lister, T., Vorobjov, T., Hug, G., Losse, F., Cavalié, T., D'Anna, W., Birtwhistle, P. 2013 QF11. Minor Planet Electronic Circ., 2013-Q50 (2013).

Conference papers

Invited talks

1. Cavalié, T., Moreno, R., Lellouch, E., Fouchet, T., Hue, V., Greathouse, T., Sinclair, J., Dobrijevic, M., Hersant, F., Hartogh, P., Jarchow, C., Rezac, L., Bézard, B., Gladstone, R., Lamy, L., Chapillon, E. SL9 species imaging in Jupiter's auroral regions with ALMA. Asia Oceania Geosciences Society, Honolulu, USA, 4-8 Juin 2018.

2. Cavalié, T., Lellouch, E., Moreno, R., Fouchet, T., Hartogh, P., Hesman, B., Feuchtgruber, H., Achterberg, R., Gueth, F., Moullet, A. Évolution temporelle de la Tempte de Saturne de 2011 avec Herschel et ALMA. SF2A, Toulouse, 1–5 June 2015.

3. Cavalié, T., Feuchtgruber, H., Hesman, B., Dobrijevic, M., Fletcher, L., Hartogh, P., Jarchow, C., Lellouch, E., Moreno, R., Gueth, F., Fouchet, T., Achterberg, R., Moullet, A. Saturn's 2010 Great Storm and its stratospheric aftermath: temporal monitoring with Herschel and ALMA in 2011-2013 and photochemical modeling. Asia Oceania Geosciences Society, Brisbane, Australia, 24-28 June 2013.

4. Cavalié, T., Hesman, B., Fouchet, T., Lellouch, E., Moreno, R., Achterberg, R., Moullet, A., Hartogh, P., Feuchtgruber, H., Gueth, F. Probing Saturn's 2011 Storm with Herschel and ALMA. ALMA Community Days 2012: Early Science in Cycle 1. Garching, Germany, 25-27 June 2012.

Conference proceedings

1. Cavalié, T., Lellouch, E., Hartogh, P., Moreno, R., Billebaud, F., Bockelée-Morvan, D., Biver, N., Cassidy, T., Courtin, R., Crovisier, J., Dobrijevic, M., Feuchtgruber, H., Gonzalez, A., Greathouse, T., Jarchow, C., Kidger, M., Lara, L., Rengel, M., Orton, G., Sagawa, H., de Val-Borro, M. The origin of external oxygen in Jupiter and Saturn's environments. Proceedings of the annual meeting of the French Society of Astronomy & Astrophysics (SF2A), Paris, 3-6 June 2014, 173.

2. Cavalié, T., Billebaud, F., Biver, N., Dobrijevic, M., Fouchet, T., Lellouch, E., Brillet, J., Encrenaz, T., Moriarty-Schieven, G., Wouterloot, J. CO in the atmospheres of Saturn and Uranus. Observations at millimeter and submillimeter wavelengths. Proceedings of the annual meeting of the French Society of Astronomy & Astrophysics (SF2A), Paris, France, 30 June – 4 July 2008.

3. Cavalié, T., Billebaud, F., Biver, N., Dobrijevic, M., Lellouch, E., Brillet, J., Lecacheux, A., Hjalmarson, Å., Sandqvist, Aa., Frisk, U., Olberg, M. and The Odin Team. Contribution of the Odin space telescope to the understanding of the origin of water vapor in the atmosphere of Jupiter. Proceedings of the annual meeting of the French Society of Astronomy & Astrophysics (SF2A), Grenoble, France, 2-6 Juillet 2007.

4. Encrenaz, T., Lellouch, E., Paubert, G., Cavalié, T., Billebaud, F., Moreno, R., Fouchet, T. Millimeter observations of Mars with the IRAM 30-m antenna: constraints on CO, T(p), and zonal winds. Mars Atmosphere Modelling and Observations, Grenada, Spain, 27 Februar - 3 March 2006. Mars Atmosphere Modelling and Observations, 517-518.

Other conference communications

- Oral communications in international conferences: 23
- Oral communications in national conferences: 5
- Poster communications in international conferences: 8
- Posters in national conferences: 1

ESA technical documents

1. SWI observation mode library. Cavalié, 2018.
2. SWI instrument modes. Cavalié, 2018.
3. Reference model of Jupiter's atmosphere for SWI radiative transfer simulations and radiative transfer model intercomparison. Cavalié, 2018.
4. Report on SWI observation simulations: CTS vs. ACS. Cavalié, 2018.
5. WG4 segmentation plan report – Phases 2, 3, 4, and 5. Cavalié, Fletcher & WG4, 2016-2018.
6. SWI instrument operation and concept document. Cavalié, 2017.
7. WG4 Jupiter orbit – G5 flyby report. Cavalié, Fletcher & WG4, 2015.
8. SWI typical observation scenarios. Cavalié, 2015.

Appendix B

Copy of my 5 most significant papers

I have selected the following 5 publications as my most significant results. They are listed from the most recent one to the oldest one:

- Cavalié, T., Venot, O., Selsis, F., Hersant, F., Hartogh, P., Leconte, J., 2017. Thermochemistry and vertical mixing in the tropospheres of Uranus and Neptune. How convection inhibition can affect the derivation of deep oxygen abundances. Icarus 291, 1-16.
- Hue, V., Cavalié, T., Dobrijevic, M., Hersant, F., Greathouse, T. K., 2015. 2D photochemical modelling of Saturn's stratosphere. Part I: Seasonal variation of atmospheric composition. Icarus 257, 163-184.
- Cavalié, T., Moreno, R., Lellouch, E., Hartogh, P., Venot, O., Orton, G., Jarchow, C., Encrenaz, T., Selsis, F., Hersant, F., Fletcher, L., 2014. First submillimeter observation of CO in the stratosphere of Uranus. Astronomy and Astrophysics 562, A33.
- Cavalié, T., Feuchtgruber, H., Lellouch, E., de Val-Borro, Jarchow, C., M., Moreno, R., Hartogh, P., Orton, G., Greathouse T., Billebaud, F., Dobrijevic, M., Lara, L. M., Gonzalez, A., Sagawa, H., 2013. The spatial distribution of water in the stratosphere of Jupiter from Herschel–HIFI and –PACS observations. Astronomy and Astrophysics 553, A21.
- Cavalié, T., Hartogh, P., Billebaud, F., Dobrijevic, M., Fouchet, T., Lellouch, E., Encrenaz, T., Brillet, J., Moriarty-Schieven, G. H., 2010. A cometary origin for CO in the stratosphere of Saturn? Astronomy and Astrophysics 510, A88.

In the final pages of this documents, these publications are copied in extenso.

Icarus 291 (2017) 1–16

Contents lists available at ScienceDirect

Icarus

journal homepage: www.elsevier.com/locate/icarus

Thermochemistry and vertical mixing in the tropospheres of Uranus and Neptune: How convection inhibition can affect the derivation of deep oxygen abundances

T. Cavalié[a,*], O. Venot[b,c], F. Selsis[d], F. Hersant[d], P. Hartogh[e], J. Leconte[d]

[a] LESIA, Observatoire de Paris, PSL Research University, CNRS, Sorbonne Universités, UPMC Univ. Paris 06, Univ. Paris Diderot, Sorbonne Paris Cité, F-92195 Meudon, France
[b] Instituut voor Sterrenkunde, Katholieke Universiteit Leuven, Leuven, Belgium
[c] Laboratoire Interuniversitaire des Systèmes Atmosphériques (LISA), CNRS UMR 7583, Université Paris-Est Créteil, Université Paris Diderot, 61 avenue du Général de Gaulle, 94010 Créteil Cedex, France
[d] Laboratoire d'Astrophysique de Bordeaux, Univ. Bordeaux, CNRS, B18N, allée Geoffroy Saint-Hilaire, 33615 Pessac, France
[e] Max-Planck-Institut für Sonnensystemforschung, 37077 Göttingen, Germany

ARTICLE INFO

Article history:
Received 9 December 2016
Revised 3 March 2017
Accepted 10 March 2017
Available online 18 March 2017

Keywords:
Abundances
Atmospheres
Abundances
Interior
Uranus
Neptune

ABSTRACT

Thermochemical models have been used in the past to constrain the deep oxygen abundance in the gas and ice giant planets from tropospheric CO spectroscopic measurements. Knowing the oxygen abundance of these planets is a key to better understand their formation. These models have widely used dry and/or moist adiabats to extrapolate temperatures from the measured values in the upper troposphere down to the level where the thermochemical equilibrium between H_2O and CO is established. The mean molecular mass gradient produced by the condensation of H_2O stabilizes the atmosphere against convection and results in a vertical thermal profile and H_2O distribution that departs significantly from previous estimates. We revisit O/H estimates using an atmospheric structure that accounts for the inhibition of the convection by condensation. We use a thermochemical network and the latest observations of CO in Uranus and Neptune to calculate the internal oxygen enrichment required to satisfy both these new estimates of the thermal profile and the observations. We also present the current limitations of such modeling.

1. Introduction

One of the great mysteries in the Solar System is how the gas and ice giant planets formed from the protoplanetary disk 4.5 billion years ago. This question is even more relevant regarding ice giants after the discovery of the commonality of Neptune-class planets among the exoplanets detected by Kepler (Batalha et al., 2013; Fressin et al., 2013). Two scenarios have been proposed regarding the formation of giant planets: disk gravitational instability (Boss, 1997) and core accretion (Pollack et al., 1996). These scenarios differ not only in the time required to form planets (a few hundred years vs. several million years, respectively), but also in the final composition of the planets' interiors. While gravitational instability should result in ~solar abundances of heavy elements (except if a significant external source of heavy elements is incorporated after the planet formation), core accretion formation should lead to an enrichment in heavy elements increasing with heliocentric distance. The level of enrichment then would depend on how the ices of the planetesimal that formed the cores of these planets condensed. Here again, several competing scenarios exist: condensation in amorphous ices (Bar-Nun et al., 1988; Owen et al., 1999) and clathration (Lunine and Stevenson, 1985; Gautier et al., 2001; Hersant et al., 2004; Gautier and Hersant, 2005).

While measuring the D/H ratio in the giant planets (Lellouch et al., 2001; Feuchtgruber et al., 2013) gives us an insight on the origin and condensation temperature of the protoplanetary ices in the outer Solar System (Hersant et al., 2001), measuring the heavy element abundances can help constraining the ice condensation processes. Enrichment in heavy elements has been observed by the Galileo probe in Jupiter's troposphere, with an average enrichment factor of $\sim 4 \pm 2$ in C, N, S, Ar, Kr and Xe, except for O which was found depleted (Niemann et al., 1998; Atreya et al., 1999; Mahaffy et al., 2000; Wong et al., 2004; Owen and Encrenaz, 2006). The O measurement may only be a lower limit because the Galileo probe most likely entered a dry zone of Jupiter and did not reach the levels where H_2O is well-mixed (Wong et al., 2004), though alternative scenarios explaining an oxygen depletion exist

* Corresponding author.
E-mail address: thibault.cavalie@obspm.fr (T. Cavalié).

http://dx.doi.org/10.1016/j.icarus.2017.03.015
0019-1035/© 2017 Published by Elsevier Inc.

(Lodders, 1994; Mousis et al., 2012). The global enrichment in heavy elements reported by Galileo favors the core accretion scenario for Jupiter. This formation model, if applied to the other giant planets, predicts enrichment factors that increase with increasing heliocentric distance: ~7, 30 and 50 for Saturn, Uranus, and Neptune, respectively (Owen and Encrenaz, 2003). At Saturn, the C, N, P and S abundances have been measured (Fletcher et al., 2009; Hersant et al., 2008; Mandt et al., 2015) and are also found enriched compared to the solar value. At Uranus and Neptune, the information is more sparse, with only the C abundance has constraints (Baines et al., 1995; Sromovsky and Fry, 2008; Karkoschka and Tomasko, 2009).

The key measurement that would enable differentiating the condensation processes of the planetesimal ices and hence how other heavy elements were trapped is the deep water abundance. Indeed, the clathration scenario needs a larger amount of water at the time of the condensation of the planetesimal ices than the amorphous ice scenario (Owen, 2007), especially if the efficiency of the clathration process was lower than 100%. While Galileo probably failed to measure the Jovian deep water abundance below the water cloud (Niemann et al., 1998) because it entered a dry hot spot and probably did not reach the base of the water cloud, Juno (Matousek, 2007) should shed light on this long lasting question. However, there is no such mission planned in the near future to measure the deep water abundance in the other giant planets. A few mission concepts are being developed for Saturn (Mousis et al., 2012, 2014; Atkinson et al., 2016) and the ice giants (Arridge et al., 2012, 2014; Masters et al., 2014), but these challenging missions require probes that would have to survive high pressures to reach below the water cloud (up to ~100 bars in the ice giants). In principle, cm-waves can probe down to several tens of bars and could probe below the water cloud (de Pater et al., 1991; Hofstadter and Butler, 2003; Klein and Hofstadter, 2006). However, the opacity at these levels can also be caused by NH_3 and H_2S and the degeneracy is difficult to waive (e.g., de Pater et al., 2005). Therefore, it is important to find other ways to constrain the deep water abundance. One interesting way is to take advantage of the chemical quenching of species like CO. The observed abundance of CO is in chemical disequilibrium and is inherited from deeper layer, where its abundance is in thermochemical equilibrium with water, through the combination of fast vertical mixing and slow chemical kinetics.

Following the first detection of CO in the atmosphere of Jupiter by Beer (1975), a simple model was proposed to constrain the deep water abundance in Jupiter by studying the tropospheric thermochemistry and vertical transport, and in particular the following thermochemical equilibrium reaction:

$$H_2O + CH_4 = CO + 3H_2. \tag{1}$$

This model, first developed by Fegley and Prinn (1988) is based on the approximation that the tropospheric mole fraction of CO is fixed at a so-called "quench" level, where the chemical timescale of the conversion of CO into H_2O becomes longer than the timescale for its vertical transport by convection. This kind of model relies on the determination of the rate-limiting reaction of the conversion scheme. Therefore, assuming the kinetics of this rate-limiting reaction is known, the kinetics of the whole conversion scheme is constrained and the measured upper tropospheric mole fraction of CO can be linked to the deep water abundance. Prinn and Barshay (1977) initially proposed this reaction to be $H_2CO + H_2 \rightarrow CH_3 + OH$. Later, Yung et al. (1988) proposed a two-step reaction scheme in which the rate-limiting reaction was $H + H_2CO + M \rightarrow CH_3O + M$. This "quench-level" approximation model was then used by Lodders and Fegley (1994) to constrain the atmospheric O/H ratio in all giant planets. However, Smith (1998) showed that the assumptions of these modelers on diffusion timescales were incorrect. His work was then applied by Bézard et al. (2002) to Jupiter, by Visscher and Fegley (2005) and Cavalié et al. (2009) to Saturn, and by Luszcz-Cook and de Pater (2013) to Neptune using either the Prinn and Barshay (1977) or Yung et al. (1988) limiting reactions, which renders any comparison between these results hazardous.

Visscher et al. (2010) first applied a comprehensive thermochemical and diffusive transport model to the troposphere of Jupiter. They have evaluated the Jovian deep water mole fraction to be $(0.25–6.0)\times10^{-3}$, corresponding to an enrichment of 0.3–7.3 times the protosolar abundance (9.61×10^{-4}). Similar thermochemical models have been applied ever since to investigate the thermochemistry in exoplanets (Visscher and Moses, 2011; Moses et al., 2011; 2013; Venot et al., 2012; 2014; 2015) and in Solar System giants (Cavalié et al., 2014; Mousis et al., 2014; Wang et al., 2016). While all these models improve on the modeling of deep tropospheric chemistry compared to the "quench-level" approximation studies, they still have to rely on assumptions made on tropospheric vertical mixing and temperatures. Interestingly, recent theoretical work enables progress in the determination of these quantities:

- Vertical mixing: vertical mixing in the troposphere of giant planets is caused by convection, and it is usually modeled by an eddy diffusion coefficient. It is estimated within an order of magnitude from the mixing length theory (Stone, 1976). Following rotating tank experiments, a recent paper by Wang et al. (2015) proposes a new formulation to estimate this coefficient with a narrower error bar. The authors even show that this vertical mixing is latitude-dependent, with a stronger magnitude at low latitudes.
- Tropospheric temperatures extrapolation: Until now, dry and/or moist adiabats have been used to extrapolate the thermal profiles of Solar System giant planets from observations around 1-bar to deeper levels (e.g., Luszcz-Cook and de Pater, 2013). In a new paper, Leconte et al. (2016) propose a new criterion to compute the thermal gradient in the giant planet tropospheres. It takes into account not only dry and moist processes, but also the effect of the mean molecular weight gradient associated with the condensation of H_2O and can produce a jump in temperature at the H_2O condensation level that is caused by a thin radiative layer.

Both are composition-dependent and remain therefore quite uncertain. In addition, the possible radiative gradient at the H_2O condensation level is poorly constrained and the CH_4 tropospheric abundance is only known within a factor of two in Uranus and Neptune (Baines et al., 1995; Sromovsky and Fry, 2008; Karkoschka and Tomasko, 2009). We have therefore chosen to study the parameter space – which consists of the following four parameters: O/H, C/H, temperature, K_{zz} – with a thermochemical and diffusion model of Uranus and Neptune to better evaluate the parameter space that is compliant with observations of CO in their upper tropospheres.

In this paper, we apply to the Solar System Ice Giants the thermochemical and diffusion model of Venot et al. (2012) along with the prescriptions of Leconte et al. (2016) to compute tropospheric thermal profiles. We present our models in Section 2, and review the various observational constraints on composition and temperature in Section 3. We detail the results of the 4D parameter space simulations and our nominal case in Section 4. We discuss our results in Section 5, and detail other sources of uncertainties that currently limit these kind of models in Section 6. We give our conclusions in Section 7.

2. Models

We have adapted the thermochemical and diffusion model of Venot et al. (2012), initially developed for the atmospheres of warm exoplanet atmospheres, to the giant planet tropospheres to constrain their deep oxygen abundance from CO observations. Obtaining the tropospheric composition from thermochemical and diffusion calculations requires some knowledge on the troposphere temperature, composition, and vertical mixing. In the following sections, we illustrate how we have run sequentially various steps to eventually link the observed tropospheric CO abundances to the deep oxygen abundances in Uranus and Neptune. These steps include:

1. temperature profile extrapolation to deep levels where thermochemistry prevails, assuming a given composition of the main compounds (H_2, He, CH_4 and H_2O)
2. thermochemical equilibrium calculation using the temperature profile and a given elemental composition, to derive an initial composition state for the next round of computations
3. thermochemistry and diffusion calculations using the temperature profile and initial composition state of step 1 and step 2 and assuming a given vertical mixing K_{zz}, to obtain the steady state tropospheric composition
4. K_{zz} assumption cross-check with theoretical estimates

To run the thermochemistry and diffusion model, we need at minimum to set as initial conditions the internal elemental abundances of H, He, C, N, and O, a thermal profile, and an eddy diffusion coefficient. The case of N will not be discussed any further as nitrogen chemistry has no significant impact on carbon and oxygen chemistries (Cavalié et al., 2014), the deep oxygen abundance is an assumption of the model, and other elemental abundances can be estimated a priori.

2.1. Step 0 - estimating the internal composition by neglecting chemistry

As will be shown in what follows, the computation of the thermal profile needs a priori knowledge of the deep composition in terms of H_2, He, CH_4 and H_2O. To estimate these molecular abundances as well as the elemental abundances of H, He and C, we start from the upper tropospheric abundances of H_2, He, CH_4, and an initial condition on the deep O abundance. Assuming that chemistry and the abundance of compounds other than H_2, He, CH_4, and H_2O, can be neglected, and that the upper tropospheric abundance of H_2O is negligible (because of condensation), we can derive a set of equations to link the upper tropospheric and deep tropospheric composition:

$$X_{\mathrm{He}} = y^{\mathrm{top}}_{He} / (y^{\mathrm{top}}_{\mathrm{H_2}} + 2y^{\mathrm{top}}_{\mathrm{CH_4}}) \times (X_{\mathrm{H}} - 2X_{\mathrm{O}})/2, \tag{2}$$

$$X_{\mathrm{C}} = X_{\mathrm{He}} \times y^{\mathrm{top}}_{\mathrm{CH_4}} / y^{\mathrm{top}}_{\mathrm{He}}, \tag{3}$$

$$y^{\mathrm{bottom}}_{\mathrm{H_2O}} = X_{\mathrm{O}} / (X_{\mathrm{H}}/2 + X_{\mathrm{He}} - X_{\mathrm{C}}), \tag{4}$$

where X_i is the abundance of element i, y^{top}_i is the mole fraction of compound i in the upper of the troposphere (but below the CH_4 cloud), and y^{bottom}_i is the mole fraction of compound i in the deep troposphere. By convention, $X_{\mathrm{H}} = 10^{12}$.

In practice, we have measurements from which we can determine $y^{\mathrm{top}}_{\mathrm{He}}$, $y^{\mathrm{top}}_{\mathrm{CH_4}}$, and $y^{\mathrm{top}}_{\mathrm{H_2}}$ (see Section 3), and we assume a deep oxygen abundance X_{O}. We can thus derive an estimate of X_{He}, X_{C}, and $y^{\mathrm{bottom}}_{\mathrm{H_2O}}$, which are needed for the preparation of the thermochemistry and diffusion computations, by using sequentially Eqs. (2)–(4). We control the validity of these assumptions on X_{He} and X_{C} a posteriori, by checking that the final upper tropospheric abundances of He and CH_4 fit the observations.

2.2. Step 1 - extrapolating tropospheric temperatures

Formation models of the giant planets of the Solar System predict enrichment factors for heavy elements that increase together with heliocentric distance. The precise values for the O enrichment factor depend on the ice condensation scenario (amorphous ices vs. clathration). But even in the case where the O enrichment should be the lowest, i.e., in the scenario where ices condense and trap volatiles in amorphous form, the expected enrichment factors are 4, 7, 30, and 50 (respectively) for Jupiter, Saturn, Uranus, and Neptune (respectively), according to Owen and Encrenaz (2003). The high abundance of tropospheric CO in Neptune could even indicate that O is enriched by a factor >100 (Lodders and Fegley, 1994; Luszcz-Cook and de Pater, 2013). Actually, above an enrichment factor of $\sim$100–150 in Uranus and Neptune, we expect to see the abundance of O exceeding the abundance of He. Given the molecular mass of the main O carrier (i.e., water) compared to the molecular mass of the main atmospheric constituents (i.e., H_2 and He), a significant mean molecular mass gradient ∇_μ is expected around the layers where water condenses. Consequently, the Ledoux stability criterion (Ledoux, 1947; Sakashita and Hayashi, 1959) must be used instead of the Schwarzschild stability criterion in the computations of the temperature gradient ∇_{T}, as double diffusive processes may appear. The temperature gradient can be significantly affected, as shown by Guillot (1995) in the case of the condensation of methane.

Hereafter, we will especially consider the cases of Uranus and Neptune, as these planets are the most "symptomatic" cases of mean molecular weight discontinuities around the water condensation level, because of the expected large oxygen enrichments.

2.2.1. Methodology

The thermochemistry and diffusion computations require a thermal profile for the troposphere down to the region where thermochemistry prevails over vertical diffusion, i.e. below the CO quench-level in our case.

Previous studies of the Solar System giant planets thermochemistry have used a variety of dry and/or moist adiabats, based on the application of the Schwarzschild and Härm (1958) stability criterion, to compute the tropospheric thermal structures (e.g., Lodders and Fegley, 1994; Luszcz-Cook and de Pater, 2013). In a new paper, Leconte et al. (2016) show that, in hydrogen-rich atmospheres, the mean molecular weight gradient around the cloud base (of a species heavier than H_2) can be strong enough to stabilize the atmosphere against convection (i.e. inhibit moist convection) in this region. Although it shares some similarities with the processes described by Ledoux that work for non condensable species (Ledoux, 1947; Sakashita and Hayashi, 1959), this mechanism can suppress moist convection when the enrichment in the condensable species is higher than a critical threshold. Because the interior still needs to release its energy, a stable radiative layer with a steep temperature gradient develops. Guillot (1995) has already shown that such an effect can be produced by CH_4 in Uranus and Neptune. We can expect this effect to happen with H_2O too in Uranus and Neptune, in the transition zone between the H_2O-rich region (deep troposphere) and the H_2O-poor region (upper troposphere), and we have therefore implemented their stability criterion when extrapolating thermal profiles. We will refer to "3-layer profiles" for thermal profiles extrapolated using the prescription of Leconte et al. (2016).

In the computations we present in this paper, we start from the temperature measured at the 2-bar level (see Table 1). We will explore various cases for extrapolating deep tropospheric thermal profiles: (i) dry processes leading to a dry adiabat, (ii) latent heat effects leading to a moist adiabat, (iii) latent heat and mean molecular weight effects leading to what we will refer to as "3-layer pro-

Table 1
Summary of observational data.

Planet	Jupiter	Saturn	Uranus	Neptune
$y_{He}^{(1)}$	0.1359 ± 0.0027	0.118 ± 0.025	0.152 ± 0.033	$0.149^{+0.017}_{-0.022}$
$y_{CH4}^{(2)}$	(2.04 ± 0.50)×10^{-3}	(4.7 ± 0.2)×10^{-3}	0.01-0.05	0.01-0.05
$y_{CO}^{(3)}$	(1.0 ± 0.2)×10^{-9}	< 10^{-9}	< 2.1×10^{-9}	(0.20 ± 0.05)×10^{-6}
$T^{(4)}$	207.1	132.9	102.9	93.1
$F^{(5)}$	5.44 ± 0.43	2.01 ± 0.14	0.042 ± 0.047	0.433 ± 0.046
$T_{int}^{(6)}$	99.0	77.2	29.3	52.6

Notes: y_i are mole fractions, and F is the internal heat flux in W· m^{-2}, temperatures are in K. References: $^{(1)}$ von Zahn et al. (1998) and Niemann et al. (1998) for Jupiter, Conrath and Gautier (2000) for Saturn, Conrath et al. (1987) for Uranus, and Burgdorf et al. (2003) for Neptune. $^{(2)}$ Wong et al. (2004) for Jupiter, Fletcher et al. (2009); 2012) for Saturn, Lindal et al. (1987); Baines et al. (1995); Karkoschka and Tomasko (2009); Sromovsky et al. (2014) for Uranus, and Lindal et al. (1990); Baines et al. (1995); Karkoschka and Tomasko (2011) for Neptune. The range for Uranus and Neptune represents the observed latitudinal variability. $^{(3)}$ Bézard et al. (2002) for Jupiter, Cavalié et al. (2009) for Saturn, Teanby and Irwin (2013) for Uranus, and Luszcz-Cook and de Pater (2013) and Moreno (1998) for Neptune. $^{(4)}$ Galileo measurement of Seiff et al. (1998) for Jupiter, equatorial average at 1 bar obtained with Cassini/CIRS by Fletcher et al. (2016) for Saturn, Spitzer measurements from Orton et al. (2014) for Uranus, Voyager 2 occultation observations from Lindal (1992) for Neptune. Temperatures at 2 bar, except for Saturn (1 bar). $^{(5)}$ Voyager 2 measurements from Hanel et al. (1981) for Jupiter, Hanel et al. (1983) for Saturn, Pearl et al. (1990) for Uranus, and Pearl and Conrath (1991) for Neptune. $^{(6)}$ T_{int} is computed from $F = \sigma T_{int}^4$.

files". Finally, because magnitude of the temperature jump in the radiative layer of the 3-layer profiles is quite uncertain, we derive an extreme case (iv) from the Leconte et al. (2016) formulations in which the temperature jump of the radiative layer is limited by the deep water abundance.

2.2.2. Dry adiabat

Starting from the 2-bar level temperature, we extrapolate to deeper levels using the Schwarzschild and Härm (1958) criterion, which translates into the following:

$$T_{i+1} = T_i \times \exp\left(\nabla_{\rm dry} \frac{\ln(p_{i+1})}{\ln(p_i)}\right) \tag{5}$$

and

$$\nabla_{\rm dry} = \frac{R}{\mu c_{\rm p}}, \tag{6}$$

where μ is the mean molecular weight, and R is the ideal gas constant. We use the temperature-dependent expressions given by the NIST for the specific heat capacities of He, CH_4 and H_2O. For H_2, we use the temperature- and pressure-dependent data from the Cryogenic Data Handbook[1]. We assume equilibrium hydrogen, in agreement with observations of Baines et al. (1995) of the upper tropospheres of Uranus and Neptune. Because we start from the 2-bar level in both Uranus and Neptune, the lowest temperatures we consider are sufficiently high so that we do not have to consider the effects of CH_4 condensation (Guillot, 1995). We then compute the next levels with very small steps in $\ln(p)$ ($\sim 10^{-4}$), with p in Pa.

This kind of profile is obviously the least realistic given the expected high abundance of H_2O in the interiors of Uranus and Neptune.

2.2.3. Moist adiabat

In the region where H_2O condenses, latent heat is released and the gas is heated. Convection is thus reinforced. Adding this effect to the previous stability criterion results in replacing $\nabla_{\rm dry}$ in Eq. (5) by the expression given in Leconte et al. (2013):

$$\nabla_{\rm moist} = \frac{p}{p - p_{\rm v}} \frac{(1-q_{\rm v})R_{\rm a} + \frac{q_{\rm v}L_{\rm v}}{T}}{q_{\rm v}c_{\rm p,v} + q_{\rm a}c_{\rm p,a} + q_{\rm c}c_{\rm p,c} + q_{\rm v}\frac{L_{\rm v}}{T}\frac{p}{p-p_{\rm v}}\frac{\mathrm{d}\ln p_{\rm s}}{\mathrm{d}\ln T}}, \tag{7}$$

where subscripts i = a,v,c refer to non-condensable gas, condensable gas, and condensed material (solid or liquid), respectively. p_i is the partial pressure, M_i the molar mass, q_i is the mass mixing ratio and is the ratio of the mass of component i over the mass of the gas, $c_{\rm p,\,i}$ the mass heat capacity, and $R_i = R/M_i$. p_s is the saturation vapor pressure (which is equal to $p_{\rm v}$ in our case). For H_2O, we use the Tetens formula. $L_{\rm v}$ is the latent heat of vaporization. We assume here that all the condensed material falls into deeper layers. As a consequence, the term $q_{\rm c}c_{\rm p,\,c}$ disappears and the process can no longer be considered as strictly adiabatic (hence the term *pseudo-adiabat* sometimes used). We note that below the H_2O cloud, $\nabla_{\rm moist} = \nabla_{\rm dry}$.

2.2.4. 3-layer profiles

Condensation of H_2O can result in a significant gradient in molecular weight when high oxygen enrichments are considered. The increase of molecular weight with pressure introduces a stabilizing effect. Leconte et al. (2016) derived a new stability criterion that applies in this situation. When

$$\varpi q_{\rm v} \frac{\mathrm{d}\ln p_{\rm s}}{\mathrm{d}\ln T} > 1, \tag{8}$$

where $\varpi \equiv (\mu_v - \mu_a)/\mu_v$ and $q_{\rm v} \equiv q_{H_2O}$, convection is inhibited and a radiative layer is formed. This layer is stable against double-diffusive processes in 1D, as demonstrated by Leconte et al. (2016). The thermal gradient from (7) must then be replaced by a radiative gradient

$$\nabla_{\rm r} = \frac{3}{16}\frac{\kappa p T_{\rm int}^4}{g T^4}, \tag{9}$$

where κ is the Rosseland mean opacity, g the gravity and $T_{\rm int}$ the temperature associated with the internal heat flux (see Table 1). For the Rosseland mean opacities, we use the parameterization from Valencia et al. (2013). This parameterization requires a metallicity, which we compute by accounting for the elemental abundances of oxygen and carbon.

Thus, if q_{H_2O} exceeds a given threshold (see Eq. (17) in Leconte et al., 2016), a positive feedback appears in the condensation region. As the mean molecular weight gradient, that manifests itself as an increase of q_{H_2O} in Eq. (8), stabilizes the layer, the thermal gradient can increase and exceed the moist gradient owing to (9). As a consequence, more H_2O is vaporized and the H_2O mole fraction at the level $i+1$ increases, resulting in an increase of the

[1] https://www.bnl.gov/magnets/staff/gupta/cryogenic-data-handbook/Section3.pdf .

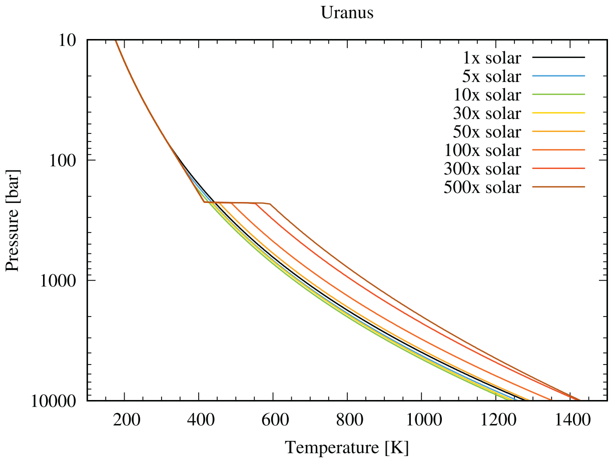

Fig. 1. "3-layer" thermal profiles computed for Uranus, assuming an O enrichment factor over the solar value ranging from 1 to 500. The case for which there is no water (not shown) would correspond to a dry adiabat, while low enrichment factors result in a wet adiabat. When the O abundance exceeds a threshold (O/H$\sim$ 20 times the solar value ; valid for both Uranus and Neptune), a significant jump in mean molecular weight translates into a significant jump in temperature in the layers where water condenses. In this thin layer ($\Delta z \sim 1$ km, whatever the O/H beyond the threshold), the convective temperature gradient is too high and the atmosphere is radiative. Refer to the online version for the color plot.

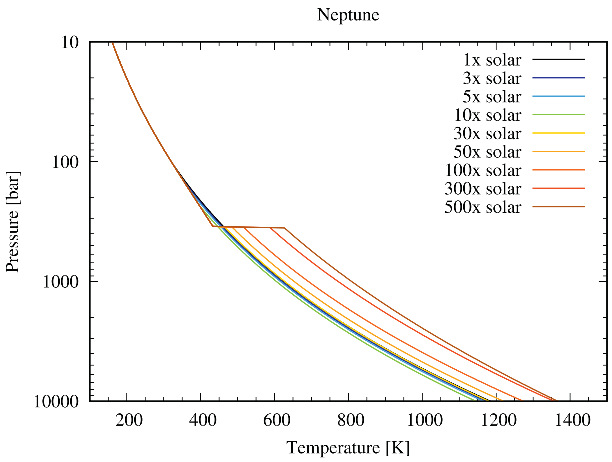

Fig. 2. Same as Fig. 1 for Neptune.

mean molecular weight gradient. For high enough oxygen elemental abundances, this creates a very localized radiative region ($\Delta z \sim 1$ km, whatever the O/H beyond the threshold) that separates the water-poor and water-rich regions. This interface is associated with a jump in temperature due to inefficient heat transport, as demonstrated by Leconte et al. (2016). Profiles for various oxygen enrichments are displayed in Figs. 1 and 2 for Uranus and Neptune.

2.2.5. Extreme case and sampling range

The magnitude of the temperature jump in the 3-layer profiles is controlled by the magnitude of the Rosseland opacities. Those are not well-constrained for heterogeneously enriched mixtures (Valencia et al., 2013). Moreover, any possible opacity of the condensate itself has been neglected with the formulation we have used. Because the jump in temperature at the transition zone between a water-rich and a water-poor region may be governed by these opacities, we may overestimate or underestimate this jump.

For illustration, let us take the example of Neptune around the nominal case that will be presented later in Section 4. Even if we divide the Rosseland opacities by a factor of 10, the upper tropospheric mole fraction of CO is unnoticeably altered. On the other hand, if the opacities are increased by a factor of 5, y_{CO}^{top} is already multiplied by a factor of 10. At Uranus, the effect is less prominent, because of the smaller temperature jump implied by the lower nominal O/H: an increase of the opacities by a factor of 10 increases y_{CO}^{top} by 25%. It is thus important to see if we can set limits to this source of uncertainty.

Interestingly, the formulation of Leconte et al. (2016) implies that the temperature jump cannot exceed a limit. This means that even if the opacities are significantly underestimated, the temperature jump cannot grow infinitely. This limit is given by the following f_μ factor:

$$f_\mu = \frac{1}{1 + (\mu_a / M_{H_2O} - 1) y_{H_2O}^{mass}} \tag{10}$$

and f_μ is a multiplicative factor that is applied to the temperature of a moist profile at the H_2O condensation level. In the previous expression, μ_a is the mean molecular weight of the dry air and

$$y_{H_2O}^{mass} = \frac{M_{H_2O}}{\mu} y_{H_2O}^{bottom} \tag{11}$$

is the mass fraction of H_2O. Indeed, if we assume that a zone, in which dry convection would occur despite the presence of H_2O, can exist, then the virtual potential temperature of Eq. (8) in Leconte et al. (2016) should be approximately constant. If we now consider that the mole fraction of H_2O is negligible in the upper troposphere, the deep temperature cannot exceed the temperature given by the virtual potential temperature of the upper troposphere. This gives the limiting factor of Eq. (10). In practice, the temperature at the bottom of the atmosphere should be always lower than this limit, because of diffusive phenomena and moist convection that transport energy in the form of latent heat. We will explore the range of allowed thermal profiles by sampling the allowed profiles between the coldest one, which is given by the moist adiabat, and the warmest one, which is given by a moist adiabat in which the temperature at the H_2O condensation layer is multiplied by f_μ. We emphasize that the 3-layer profiles always fall inside this range of profiles. In practice in this study, we compute 20 profiles from the coldest to the warmest, for each set of O/H, $y_{CH_4}^{top}$ and K_{zz}.

2.3. Step 2 - calculating the thermochemical equilibrium

Once the internal elemental composition is estimated and the thermal profile derived, we can compute the atmospheric composition as a function of altitude assuming thermochemical equilibrium, i.e. in the absence of vertical mixing. This thermochemical equilibrium state is calculated by minimizing the Gibbs energy and these calculations are based on the algorithm of Gordon and McBride (1994). This equilibrium code has been developed by Agúndez et al. (2014) and adapted for our purposes. The results of this code are then used as initial conditions of the thermochemical and diffusion model. This step enables us to speed up the latter computations by feeding the model with a non-empty atmosphere.

2.4. Step 3 - calculating the thermochemistry and diffusion steady state

We use the thermochemical and diffusion model of Venot et al. (2012) adapted to the giant planet tropospheres to compute the steady state composition of the troposphere. This model has the advantage to be based on a chemical scheme that has been validated intensively by the combustion industry (Bounaceur et al., 2007). A full description of the model and its chemical scheme can be found in Venot et al. (2012) and can be retrieved from the KIDA database (Wakelam et al., 2012).

We start from an initial condition assuming chemical equilibrium as detailed in the previous section, assume a value for K_{zz}, and integrate the continuity equation over $\sim 10^8$ s usually. This enables reaching a steady state in all cases. As CO has also an external source in Uranus and Neptune (Cavalié et al., 2014; Lellouch et al., 2005), we have made sure that any reasonable change in the magnitude of the CO external source had no significant effect on the tropospheric CO mole fraction that is usually implicitly assimilated to an internal source. In Neptune, the external source is probably a relatively recent comet (Lellouch et al., 2005; Luszcz-Cook and de Pater, 2013) that should therefore not have had enough time to contaminate the upper tropospheric CO profile. In Uranus, the nature of the external source is still uncertain (Cavalié et al., 2014). However, the fact that the vertical mixing time through the stratosphere is more than two orders of magnitude higher than the integration time we need in our computations makes the tropospheric CO more sensitive to the internal source than to the external source. As a consequence, we can constrain the deep oxygen abundance with our model by fitting the observed upper tropospheric CO.

2.5. Step 4 - tropospheric vertical mixing estimation and validation

In 1D thermochemical models, convective mixing is usually approximated by a vertical eddy diffusion coefficient K_{zz}. A thermochemical reaction can be quenched when the vertical diffusion timescale becomes shorter than the chemical timescale. Therefore, constraining the level at which the quenching of CO happens requires an estimate of vertical transport timescales in the tropospheres of giant planets.

As shown in previous studies, it appears that the final CO tropospheric mole fraction is sensitive to the K_{zz} at the CO quench-level only. This quench-level remains typically around the same temperature level (i.e. $\sim$900 K). So, we need to use a value relevant for this temperature level, and will assume uniform K_{zz} coefficients. The validity of the latter assumption is further discussed in Section 6.1.

Following the free-convection and mixing-length theories (MLT) of Stone (1976) and Gierasch and Conrath (1985); Visscher et al. (2010) give a generic form for K_{zz}:

$$K_{zz} \simeq \left(\frac{k_B F}{\rho m c_p}\right)^{1/3} \times H. \tag{12}$$

This formulation, in which k_B is the Boltzmann constant, requires the knowledge of the planet's internal heat flux F, the atmospheric mean mass density ρ, the atmospheric mean molecular mass m, the atmospheric mass specific heat at constant pressure c_p, and the atmospheric scale height H. The value of F has been measured by Voyager 2 (see Table 1). This formulation is supposed to provide estimates valid within an order of magnitude.

The aforementioned formulation based on MLT thus depends on the composition (via ρ, m, c_p, and H) and on the thermal structure (via H and c_p). The thermal structure in our models also depends on composition (via mean molecular weight effects and, to a lesser extent, c_p). Therefore, we cannot compute K_{zz} a priori and we will investigate a broad range of value (typically 5–6 orders of magnitude) in our thermochemical computations. Only after obtaining the thermal and composition results are we able to establish the validity range for K_{zz} using the MLT formulation.

More recently, Wang et al. (2015) have used laboratory studies of turbulent rotating convection to derive a new formulation of K_{zz} that provides estimates with a relative uncertainty of $\sim$25% only. We note that their formulation for low latitudes is similar to Eq. (12), only corrected by a scaling factor. So, again, their formulation exhibits a dependence on temperature and composition.

3. Observational constraints

3.1. Tropospheric abundances observed in giant planets

The thermochemical and diffusion model is initiated by specifying the deep abundances of the following elements : H, He, C, N, and O. We thus have to adjust the elemental abundances to ensure fitting the abundances of the main species in the upper troposphere, where their abundances have been measured. We have reviewed the abundances of species relevant to our model in all the Solar System giant planets and listed the values in Table 1.

The tropospheric CO mole fractions come from recent interferometric and space-based observations for Uranus and Neptune. On Uranus, Teanby and Irwin (2013) have obtained an upper limit of 2.1×10^{-9}, which is an improvement over Cavalié et al. (2008b) by almost an order of magnitude. The observations of Luszcz-Cook and de Pater (2013) that we use for Neptune have quite significantly revised the previously accepted value of 1.0×10^{-6} (Rosenqvist et al., 1992; Marten et al., 1993; 2005; Lellouch et al., 2005; 2010; Fletcher et al., 2010), and their result is confirmed (and the error bar is narrowed) by the recent IRAM-30m and Herschel/SPIRE observations (R. Moreno, priv. com.) that we use here as our nominal value: 0.2×10^{-6}.

The helium mole fraction we use for Uranus and Neptune come from the Voyager 2 measurement of Conrath et al. (1987) and from Infrared Space Observatory observations (Burgdorf et al., 2003). Both indicate that there is 15% of helium in both atmospheres.

Contrary to Jupiter and Saturn, Uranus and Neptune have cold enough tropopauses for CH_4 to condense and sharply decrease from their tropospheres to their stratospheres (Lellouch et al., 2015). Karkoschka and Tomasko (2009) and Sromovsky et al. (2011); 2014) for Uranus, and Karkoschka and Tomasko (2011) for Neptune, have recently shown that the tropospheric CH_4 abundance is not uniform with latitude. The widely accepted measurements of Baines et al. (1995) ($\sim$2% in both planets) seems to be representative of high latitudes, while the CH_4 equatorial tropospheric mole fraction is around 4%. We will take this latter value as our nominal abundance for CH_4.

3.2. Upper tropospheric temperatures and internal heat fluxes

As a starting point for the temperature extrapolation in the troposphere, we take the temperature at 2 bar in Uranus and Neptune, as measured by Orton et al. (2014), and Lindal (1992), respectively.

The computation of K_{zz} requires the knowledge of the internal heat flux. We take the Voyager 2 measurements from Pearl et al. (1990) and Pearl and Conrath (1991) for Uranus and Neptune.

4. Results

Hereafter, we present the results of our exploration of a 4D parameter space (O/H, C/H, temperature, K_{zz}) in thermochemical and diffusion computations in an attempt to constrain the deep oxygen abundance of Uranus and Neptune by fitting the observed upper tropospheric CO mole fraction. From this set of results, we also show how the O/H ratios derived from a thermochemical model that considers "3-layer" thermal profiles as nominal compare to previously published results in which dry or wet adiabats had been assumed. We want to keep the reader aware of the fact that the "3-layer" thermal profiles have been shown to be stable in 1D (Leconte et al., 2016), but may not be in a 3D treatment. The model is affected by sources of uncertainties other than those investigated in this 4D study and they are described in Section 6. So, in the following sections, we present the results of our 4D grid computations, and we provide the reader with the deep O/H obtained for Uranus and Neptune with our model, when assuming our nominal input parameters.

In the text that follows, the O/H and C/H ratios will be presented as a function of the O and C solar abundances, i.e. 8.73 dex for O and 8.39 dex, as reported by Lodders (2010).

4.1. K_{zz} *a posteriori validation*

The estimation of the deep composition at step 0 and the calculation of the thermal profile at step 1 of our modeling enables us to compute estimates of K_{zz} using the MLT or the Wang et al. (2015) formulation. For simplicity, we take the MLT formulation. The results presented below include an a posteriori consistency check between the estimated K_{zz} and the value assumed in the thermochemical modeling (step 3). This is the step 4 of our analysis. For Uranus and Neptune, we find $K_{zz} \simeq 10^8$ $cm^2 \cdot s^{-1}$.

4.2. *Exploring the 4D parameter space*

4.2.1. *Methodology*

The y_{CO}^{top} we obtain from our computations depends on the following quantities: the deep O abundance, $y_{CH_4}^{top}$ (as it controls X_C), the deep tropospheric temperature, and K_{zz}. To properly explore this 4D parameter space, we have run our models detailed in steps 0–3 of Section 2 in a loop format, by varying these quantities.

For the deep oxygen abundance we go from 10 to 300$\odot$ for Uranus and from 10 to 600$\odot$ for Neptune, and for the $y_{CH_4}^{top}$ mole fraction we go from 1.5% to 4.5%. The temperature profiles are computed once these quantities are fixed.

The link between the upper tropospheric CO mole fraction and the deep O abundance depends on the level at which the quenching of CO occurs, i.e. the level at which the chemical lifetime of CO, which is mainly governed by temperature, equals its diffusion timescale given by K_{zz}. This level is usually located below the H_2O cloud base, i.e. in a region where a dry adiabat prevails in any case. Because the behavior of the thermal profile remains poorly constrained around the H_2O condensation level, and because the thermal profile should follow a simple dry adiabat below this level, we can explore the various possible deep thermal profiles by starting a dry adiabatic extrapolation from below the H_2O cloud base. The starting temperature range from the temperature given by the moist adiabat, i.e. the coldest case, and the extreme case derived from Leconte et al. (2016). The 3-layer profiles fall, by definition, in this range. When computing the extreme thermal profiles, we apply the f_μ factor from Eq. (10) to the temperature at the level where the temperature jump occurs in the 3-layer profiles. We thus have the possibility to limit the range of possible temperature jumps, from a situation in which the opacities would be so low that no jump would be formed and the temperature profile would finally follow the moist adiabat to a situation in which the opacities would be high enough so that the temperature jump would reach its allowed limit. We sample this range with 20 profiles.

Finally, we vary the values of K_{zz} over 5–6 orders of magnitude around the value that provides a fit to y_{CO}^{top} in the "3-layer" case.

4.2.2. *Effect of* K_{zz}

This case is obvious as the deep O abundance required to fit the upper tropospheric CO decreases with increasing K_{zz}. The relationships for Uranus and Neptune are presented in Figs. 3 and 4. They show the range of values for (K_{zz}, O/H) that are compliant with observations. We remind the reader that the observations at Uranus have only enabled setting an upper limit on y_{CO}^{top}, and all values of

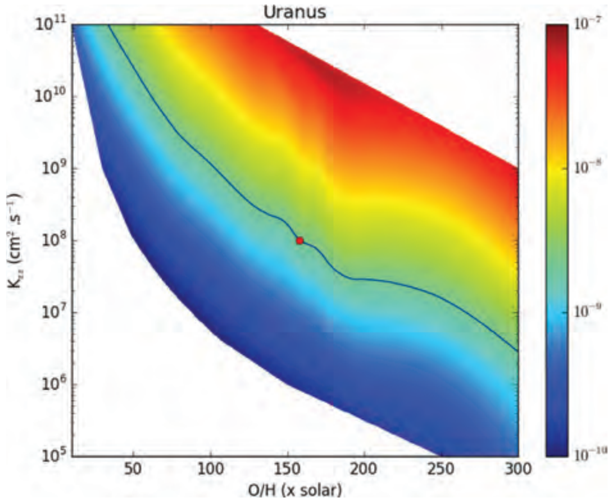

Fig. 3. Relationship between the magnitude of K_{zz} in the troposphere, the deep O abundance (expressed in solar abundances), and the resulting upper tropospheric CO for Uranus. In these simulations, we use "3-layer" thermal profiles and $y_{CH_4}^{top}$ is set to 0.04. The black curve represents the values of K_{zz} and O/H that fit the observations of y_{CO}^{top}. The red dot is the nominal case ($y_{CH_4}^{top}$ =0.04, $K_{zz} = 10^8$ $cm^2 \cdot s^{-1}$, "3-layer" profile). At Uranus, this curve is an upper limit for O/H. We refer the reader to the online version of the paper for the color scale. (For interpretation of the references to color in this figure legend, the reader is referred to the web version of this article.)

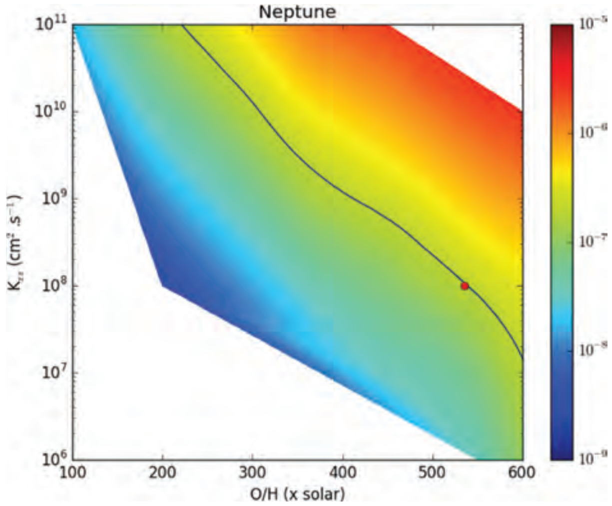

Fig. 4. Same as Fig. 3 for Neptune. (For interpretation of the references to color in this figure legend, the reader is referred to the web version of this article.)

O/H below the black curve shown in the figure are thus not ruled out.

4.2.3. *Effect of* $y_{CH_4}^{top}$

Cavalié et al. (2014) investigated the effect of the tropospheric CH_4 mole fraction on the deep O abundance in Uranus. They found that an increase of the CH_4 abundance implied a decrease of the required O abundance to fit the tropospheric CO, essentially because increasing the C abundance implies an increase C atoms available to form CO. However, they used strictly similar thermal profiles for their two cases and neglected the influence of CH_4 on the thermal profile.

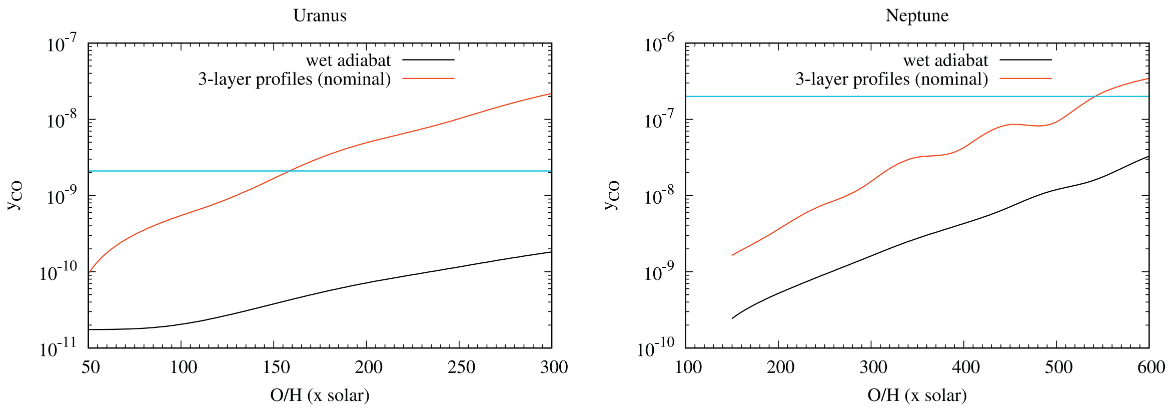

Fig. 5. Comparison between the upper tropospheric CO mole fraction produced with wet adiabats and nominal 3-layer profiles as a function of the deep O/H ratio, for Uranus and Neptune. The latter produce significantly more CO for a given O/H ratio. We use the nominal values for $y_{CH_4}^{top}$ (0.04) and K_{zz} (10^8 cm$^2 \cdot$ s^{-1}). The y_{CO} upper limit for Uranus and measurement in Neptune are indicated with a thin blue line. (For interpretation of the references to color in this figure legend, the reader is referred to the web version of this article.)

In this work, we take into account the influence of the mean molecular weight μ and of the c_p of CH_4 and H_2O when computing the thermal profile. Increasing the C abundance now also implies increasing μ_a in Eq. (8) and thus having a temperature jump located deeper in the troposphere. Moreover, the thermal gradient is lower because of a higher μc_p. Consequently, the deep tropospheric temperatures are colder when $y_{CH_4}^{top}$ increases, if other quantities are kept constant. However, the increase of available C atoms to form CO remains the dominant effect when $y_{CH_4}^{top}$ (and thus X_C) increases. So, if $y_{CH_4}^{top}$ (and thus the deep C abundance) increases, a lower deep O abundance is needed to fit the tropospheric CO.

4.2.4. Effect of the temperature jump magnitude in the H_2O condensation region

We have investigated 20 profiles for each set of O/H, C/H and K_{zz} that range from the coldest possible profile, i.e. a wet adiabat, to the warmest one, i.e. a wet adiabat in which the multiplication factor f_μ is applied to the temperature in the layer where H_2O condenses. The latter is the extreme profile of the "3-layer" case and the multiplication factor is given by Eq. (10). The nominal 3-layer profiles always fall within this range.

The results are quite difficult to present, in the sense that each individual O/H results in a different f_μ factor. A first indication can be obtained by comparing the results obtained with wet adiabats and nominal 3-layer profiles. Fig. 5 essentially shows that the 3-layer profiles require significantly lower O/H ratios to produce a given upper tropospheric CO mole fraction. To illustrate the full range of 3-layer profiles that are allowed and their impact on the results, we choose to normalize the results with respect to the maximal magnitude of multiplication factor for each O/H, noted f_μ^{max}. We thus compute the curves for $f_\mu - 1/f_\mu^{max} - 1$ as a function of O/H. The values range from the wet adiabat, for which $f_\mu = 1$ and $f_\mu - 1/f_\mu^{max} - 1$=0, to the maximum amplitude temperature jump, for which $f_\mu = f_\mu^{max}$ and $f_\mu - 1/f_\mu^{max} - 1$=1. Figs. 6 and 7 display the results for both planets. In this case, K_{zz} is fixed to 10^8 cm$^2 \cdot$ s^{-1}. The downside is that the absolute magnitude of f_μ is not directly accessible to the reader. It essentially shows that a much higher O/H would be needed to fit the data if a pure wet adiabat was used in Uranus, and that even the warmest profile cannot produce enough CO in the upper troposphere if the deep O abundance is lower than ~80 times solar. However, the tropospheric CO value is an upper limit in Uranus and this constraint is therefore useless. In Neptune, the fraction of the maximal multiplication factor sufficient to produce enough CO in the troposphere decreases quickly with increasing O/H, as this multiplication factor is already huge for O/H of several hundreds and a small fraction of it produces a big temperature jump in the zone where H_2O condenses. The results also show that a minimum of O/H~190 times solar seems to be a lower limit in Neptune with our model.

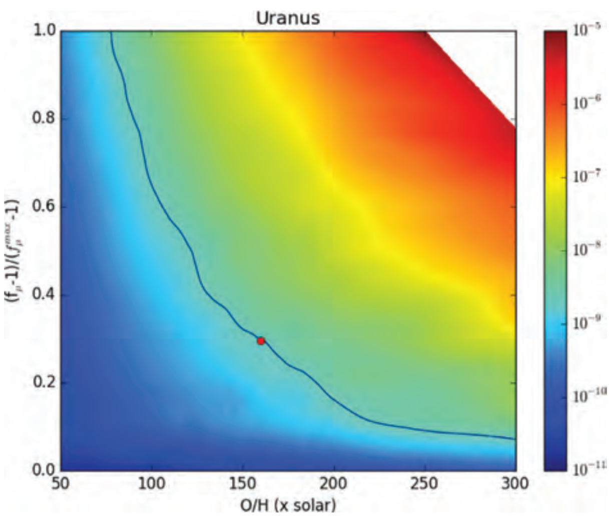

Fig. 6. Relationship between the multiplication factor applied to the temperature at the condensation level of H_2O (normalized to its maximal allowed value, see Eq. (10)), the deep O abundance, and the resulting upper tropospheric CO for Uranus. We use the nominal values for $y_{CH_4}^{top}$ (0.04) and K_{zz} (10^8 cm$^2 \cdot$ s^{-1}). The black curve represents the values that fit the observations of y_{CO}^{top}. The red dot is the nominal case ($y_{CH_4}^{top}$ =0.04, $K_{zz} = 10^8$ cm$^2 \cdot$ s^{-1}, "3-layer" profile). At Uranus, this curve is an upper limit for O/H. We refer the reader to the online version of the paper for the color scale. (For interpretation of the references to color in this figure legend, the reader is referred to the web version of this article.)

4.3. Uranus nominal case

"3-layer" thermal profiles of Uranus present a less spectacular transition zone than in Neptune, but still modify significantly the upper limit on the O/H ratio when compared to cases in which we would use dry or wet adiabats. We find that reproducing the observed upper limit of 2.1×10^{-9} of CO and the reported He and

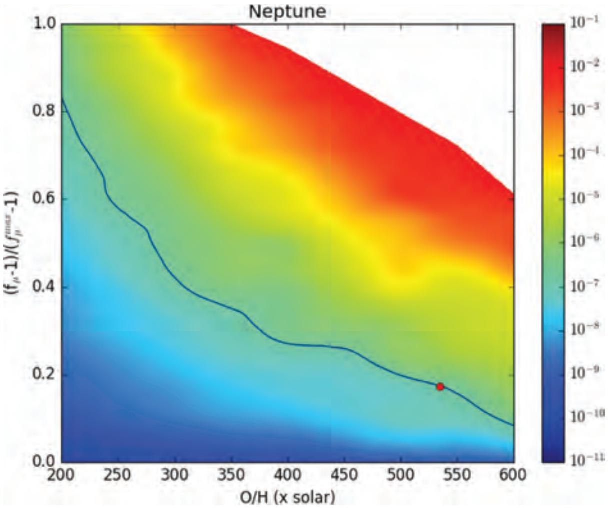

Fig. 7. Same as Fig. 6 for Neptune. (For interpretation of the references to color in this figure legend, the reader is referred to the web version of this article.)

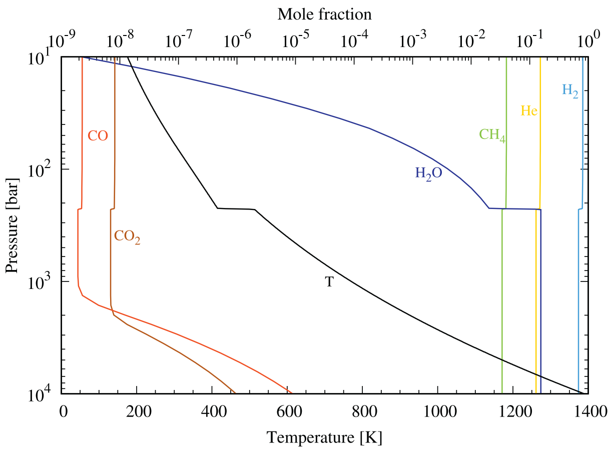

Fig. 8. Molar fraction profiles in the troposphere of Uranus obtained with the thermochemical and diffusion model, targeting the upper limit of 2.1×10^{-9} upper tropospheric CO mole fraction, as determined by Teanby and Irwin (2013). The deep O/H ratio is 160 times the solar value. We use the nominal values for $y_{CH_4}^{top}$ (0.04) and K_{zz} (10^8 cm^2 · s^{-1}). The "3-layer" temperature profile in the troposphere corresponding to this O abundance and with which these abundance profiles have been obtained is shown with a black solid line. CO is quenched between 1 and 2 kbar, at T = 900–1000 K.

CH_4 abundances (see Table 1) requires C/H and O/H ratios of 75, and 160 times the solar value. The resulting abundance profiles are displayed in Fig. 8. As in the Neptune case, using dry or wet adiabats would lead to much lower amounts of CO when starting from the same elementary abundances.

4.4. Neptune nominal case

As stated above, Neptune is expected to be the most "symptomatic" case demonstrating the impact of the mean molecular weight gradient in the transition zone from the water-rich to the water-poor region in its troposphere. It leads to a "3-layer" thermal profile with a significant departure from the purely dry or wet adiabats that had been used previously in the literature (e.g., Lodders and Fegley, 1994; Luszcz-Cook and de Pater, 2013). To fit the nominal 0.2×10^{-6} of tropospheric CO (see Table 1), we had to set the

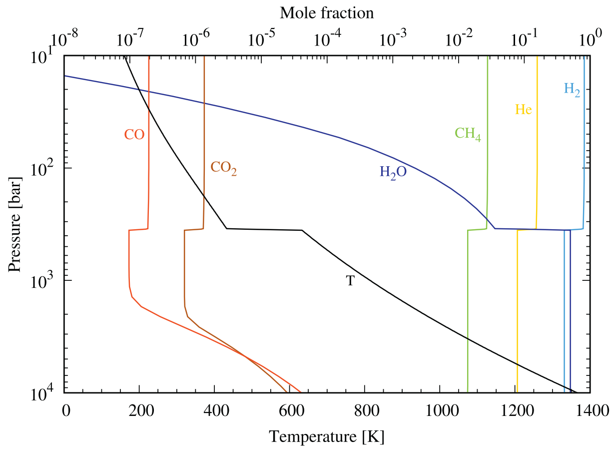

Fig. 9. Molar fraction profiles in the troposphere of Neptune obtained with the thermochemical and diffusion model, targeting a 0.2×10^{-6} upper tropospheric CO mole fraction. The deep O/H ratio is 480 times the solar value. We use nominal the values for $y_{CH_4}^{top}$ (0.04) and K_{zz} (10^8 cm^2 · s^{-1}). The "3-layer" temperature profile in the troposphere corresponding to this O abundance and with which these abundance profiles have been obtained is shown with a black solid line. CO is quenched between 1 and 2 kbar, at T = 800–900 K. The increase in mole fraction of compounds other than H_2O between 300 and 400 bar is caused by the condensation of H_2O.

O/H ratio to ~540 times the solar value. The corresponding "3-layer" thermal profile is displayed in Fig. 9. The nominal C/H ratio is 40 times the solar value. This value is rather low, if compared to a value that would simply be deduced from the upper atmospheric abundances of CH_4. The difference is caused by the high internal abundance of O and thus the high deep H_2O abundance. Indeed, we find in this calculation that H_2O is more abundant than H_2 in Neptune's interior.

5. Discussion

This section will be divided in two parts. In the first one, we will discuss the results of the nominal model, as presented in Section 4. In the second part, we will discuss the microwave spectral counterpart of our model results to further constrain their validity.

5.1. Nominal results

We find nominally that Uranus has a C/H ratio of 75 times the solar value and a O/H ratio below 160 times the solar value. For Neptune, we get a C/H 40 times the solar value and a O/H 540 times the solar value.

5.1.1. A deep compositional difference between Uranus and Neptune?

One of the striking compositional differences in Uranus and Neptune atmospheres is their CO abundances, while their He and CH_4 abundances and D/H ratios are relatively similar (Baines et al., 1995; Karkoschka and Tomasko, 2009; 2011; Sromovsky et al., 2011; 2014; Feuchtgruber et al., 2013). Indeed, they differ by at least two orders of magnitude in the troposphere (Teanby and Irwin, 2013; Luszcz-Cook and de Pater, 2013). However, previous evaluations of the O/H ratios in these bodies using the quench-level approximation and dry/wet adiabats never differed by more than a factor of two (Lodders and Fegley, 1994; Luszcz-Cook and de Pater, 2013; Cavalié et al., 2014). Accounting for the stability criterion of Leconte et al. (2016) in the water condensation layers has a significant effect on the planets thermal profile and hence

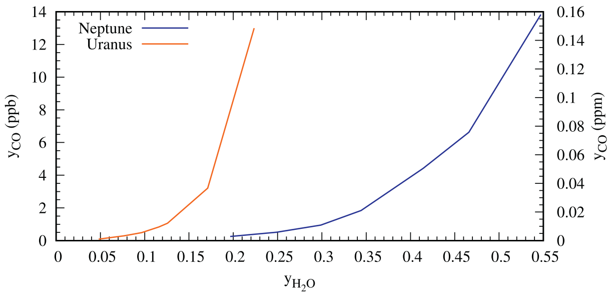

Fig. 10. Relationship between the deep H_2O abundance and the CO abundance at the quench level in Uranus and Neptune, taking nominal conditions for K_{zz} and $y^{top}_{CH_4}$. CO increases non-linearly with respect to H_2O, to compensate for the decrease of H_2 which has a stoichiometric coefficient of 3 in the equilibrium reaction.

on the derived O/H values. Our nominal values show that O/H< 160 and O/H = 540 times the solar value for Uranus and Neptune, respectively. So, there is a factor of ≥3.3 difference between these two values. The two-order of magnitude difference between the upper tropospheric CO mole fraction on Uranus and Neptune is still caused by a much smaller difference between their deep H_2O abundances. This can be understood from the equilibrium Eq. (1). An increase on H_2O implies a linear decrease of H_2. As the power on H_2 is 3 (and the CH_4 abundance is relatively constant), CO has to increase non-linearly to equilibrate the reaction. This effect is shown for both planets on Fig. 10, where we plot the relationship between the CO and H2O abundances at the quench level for our nominal cases for K_{zz} and $y^{top}_{CH_4}$. Another interesting feature of our results is that a similar CH_4 abundance in Uranus and Neptune does not reflect in a similar C/H ratio. This can be understood from Eqs. (2) and (3). Indeed, the very high O/H ratio of Neptune implies a lower C/H ratio than in Uranus to reproduce both the CO and CH_4 abundances in the upper troposphere. In Uranus, the deep H_2O abundance is comparable to the He abundance, while the deep H_2O abundance even exceeds the H_2 abundance in Neptune.

We confirm that a large difference in terms of CO abundance (two orders of magnitude) does not imply such a large difference in terms of O/H ratios in the two planets in our nominal model. This rather small difference seen in their O/H ratios, compared to their CO abundances, is then mostly caused by the 10 K difference at 2 bar, where we initiate our thermal profiles.

5.1.2. Consistency with interior and formation models

While the tropospheric mole fractions of CO are very different in Uranus and Neptune, their D/H ratios are quite similar, according to Feuchtgruber et al. (2013). One of the possible explanations presented by these authors, based on the interior models of Helled et al. (2011) and Nettelmann et al. (2013), is that the cores of the planets may be more rocky than icy, with rock fraction of 68–86%, for their D/H to be still representative of the one seen in Oort cloud comets. The O/H in core ices implied in such cases ranges from 79 to 172 times the solar value for Uranus and from 68 to 148 times the solar value for Neptune (Feuchtgruber et al., 2013). These numbers, relevant only if the planets went through complete mixing at least once in their histories, are compatible with the O/H in the outer envelope of Uranus but seem nevertheless too low for Neptune's core ices to result in a sufficiently high outer envelope O/H ratio compared to our nominal results.

A scenario has been proposed recently to reconcile the D/H measurements at Uranus and Neptune with the Oort cloud comet value by Ali-Dib et al. (2014). They propose that Uranus and Neptune formed on the CO snowline and that their ices were mostly composed of CO ices rather than H_2O ices. Therefore, the present day atmospheric D/H would be representative of the dilution of the small fraction of D-enriched Oort-comet-like H_2O ices in the H_2O coming from the thermochemical conversion of the more abundant primordial CO. This scenario then predicts that oxygen should be enriched in a similar way as carbon in both planets. Our simulation results show that this is probably neither the case for Uranus nor for Neptune and seem to contradict the model of Ali-Dib et al. (2014). We find C/O ratios of >0.21 and ~0.03, respectively, for the two planets. In Neptune, the C/O ratio could be brought back to one if CO tropospheric mole fraction was several orders of magnitude below its measured value, i.e., at the lower end of the measurement range of Luszcz-Cook and de Pater, 2013). However, recent Herschel-SPIRE and IRAM-30m observations show that the CO tropospheric mole fraction is rather in the upper part of the measurement range of Luszcz-Cook and de Pater (2013), with a measured value of y_{CO} of 0.20 ± 0.05 ppm (R. Moreno, priv. com.). In any case, the model of Ali-Dib et al. (2014) seems not to be compatible with the Nice model (Gomes et al., 2005; Morbidelli et al., 2005; Tsiganis et al., 2005) and it would anyway need to be improved by accounting for the protoplanetary disk temporal evolution as well as ice and core formation kinetics to better constrain the validity of their assumption that core formation on the CO snowline is possible.

Our results can further be used for direct comparison with formation model predictions. For instance, Hersant et al. (2004) predicted the O/H enrichment in Uranus and Neptune by exploring the range of possible C/H values when assuming that heavy elements were trapped by clathration. For instance, if C was carried by only CO during the formation of planetesimals, then 5.75 H_2O molecules were required to trap CO in clathrates. Then, the resulting C/O ratio is $1/(1 + 5.75) = 0.15$. However, their prediction is less extreme and is as follows: for C/H ratios of 40, 60, and 80 times the solar value, the O/H ratio should be 87, 130, and 176 times the solar value (based on solar abundances of Anders and Grevesse, 1989). In this case, half of the carbon comes from clathrated CO and half from pure CO_2 ice, and the resulting C/O ratio is $1/(2 \times 1/2 + 5.75 \times 1/2 + 1/2) = 1/4.375 = 0.23$. For reference, the solar C/O ratio is 0.46, according to Lodders (2010). The lower limit we obtain on the C/O ratio of Uranus is at the limit of compatibility with the case in which carbon equally comes from clathrated CO and CO_2 ice. On the other hand, the Neptune C/O ratio we derive would become compatible with the case in which all carbon comes from clathrated CO, as long as the efficiency of clathration was about 20%.

The rather large difference in terms of C/O ratio in Uranus and Neptune seems to imply different condensation environments, which may be difficult to explain. The question then is, whether the Uranus upper tropospheric CO value is representative for the CO quench level value? Actually, convection could be much less efficient than assumed in our computations. We have indeed based our computations of the tropospheric K_{zz} of Uranus on the nominal value of F reported in Pearl et al. (1990). However, the error bars on F are such that even a zero value is compatible with the Voyager observations. A lower F implies a lower K_{zz}, as $K_{zz} \propto F^{1/3}$ (see Eq. (12)). We can then reversely use our model to constrain K_{zz} to bring the O/H of Uranus to an O/H compatible with the clathration scenario of Hersant et al. (2004). If the O/H of Uranus is set to ~450 times the solar value, so that C/O~0.15, then C/H is ~50 times solar and $K_{zz} \sim 10^5$ cm$^2 \cdot$ s^{-1}. Bringing the Uranus O/H further up to the Neptune nominal value implies K_{zz} also $\lesssim 10^5$ cm$^2 \cdot$ s^{-1}. It is thus possible that Uranus and Neptune are more similar regarding their oxygen reservoir than their tropospheric CO seem to tell us, provided that convection is strongly inhibited in the interior of Uranus. This seems to be supported by recent internal structure and evolution modeling. Nettelmann et al. (2016) attempt to fit both the low luminosity of Uranus and its gravitational data with an internal structure and evolution model. Achieving this requires a thermal boundary around 0.1 Mbar that breaks the adiabat. They also find that fitting J_4 for Uranus requires an O/H of less than 30, while C/H is about 80. However, they do not consider C/O > 1 to be a good assumption for the core, implying that deep stratification is the cause for a lower O abundance at observable levels.

We can also compute the outer envelope heavy element mass fraction from the deep abundances of the species accounted for in the model and check whether they are in agreement with the internal structures inferred by Nettelmann et al. (2013). For Uranus and Neptune, we find $Z_1 < 55\%$ and $= 80\%$, respectively. The Neptune value is above the limit of ~65% allowed by their model (see Fig. 3 in Nettelmann et al., 2013). Only if we consider the most extreme case of temperature jump in our simulations, in which the O/H of Neptune cannot be lower than 190 times solar, can we get within the limit of Nettelmann et al. (2013), with Z_1 equal to 58%. Our Uranus O/H value, being an upper limit higher than the range of values allowed by their model, is not constraining. Fig. 3 of Nettelmann et al. (2013) indicates an upper limit for Z_1 in Uranus of ~10%, which in turn would imply an O/H ratio much lower than our upper limit. Carbon which is mainly carried by CH_4 already represents a mass fraction ≥10% in the outer envelope, and a lower O/H would result in a higher C/H and C mass fraction. Thus, it seems difficult to reconcile the model of Nettelmann et al. (2013) of Uranus with upper tropospheric measurements and their implication on deep tropospheric elemental composition. The case of Uranus thus remains puzzling, and more generally, the formation of Uranus and Neptune is difficult to explain (Helled and Lunine, 2014). It thus underlines the need for new data. In this sense, dedicated orbital missions with atmospheric descent probes are highly desirable (Arridge et al., 2012; 2014; Masters et al., 2014; Turrini et al., 2014).

Finally and as will be discussed in Section 6.2, our model may underestimate the production of CO. In this case, the model would require lower O abundances and bring the results closer to an agreement with the predictions from Nettelmann et al. (2013) for both planets.

5.2. Radio spectrum of Uranus and Neptune

To further constrain the validity of the results of this paper, we present radiative transfer simulations in the microwave range with the temperature and abundance profiles of our thermochemical computations. It is indeed worth checking whether the temperature jump implied for high deep O abundances and the sharp composition transition in the H_2O condensation zone translate into spectra that are in agreement with observations in the mm-cm range (e.g. de Pater et al., 1991).

We thus take our results in terms of temperature profiles and corresponding abundance profiles. We use the radiative transfer model already described in Cavalié et al. (2008a, 2013) to compute synthetic spectra of Uranus and Neptune in the mm-cm range. We extend our tropospheric thermal profiles of Uranus and Neptune from 2 bar to 10 mbar with the data from Orton et al. (2014) and from the Herschel Science Centre “ESA5” model[2] profiles for Uranus and Neptune, respectively. We add profiles of H_2S and NH_3 based on DeBoer and Steffes (1994) to account for their respective opacities, in addition to the microwave opacity of the H_2O line at 22 GHz. The NH_3 mole fraction between the NH_4SH and NH_3 clouds is set to 6×10^{-6} and 1×10^{-5} in Uranus and Neptune (Moreno, 1998 and “ESA5” model, resp.). Below the NH_4SH cloud, the NH_3 mole fraction is set to 1×10^{-4} and the deep H_2S mole fraction is set such that all H_2S is consumed to form the NH_4SH cloud. We use Bellotti et al. (2016) for the H_2O microwave opacity, Moreno (1998) for the NH_3 microwave opacity, Liebe and Dillon (1969) for H_2- and He-broadening and temperature dependence parameters for the 22 GHz line of H_2O, Fletcher et al. (2007) for the H_2-broadening and temperature dependence parameters of NH_3 lines, DeBoer and Steffes (1994) for the H_2S microwave opacity and broadening parameters, and de Pater et al. (1991) and Fray and Schmitt (2009) for H_2S condensation laws. Other spectral line parameters come from the JPL Molecular Spectroscopy Database (Pickett et al., 1998). The collision-induced absorption caused by H_2-H_2, H_2-He, and H_2-CH_4 pairs is computed following Borysow et al. (1985, 1988) and Borysow and Frommhold (1986).

The resulting spectra for Uranus and Neptune in the centimeter wavelength range, when considering the nominal cases of Section 4, are displayed in Fig. 11. Even though we make no particular attempt to improve the fit to the data (especially around 1 cm) by modifying the NH_3 and/or H_2S abundances, the obtained spectra are in good agreement with observations presented in Gulkis et al. (1978); Cunningham et al. (1981); Muhleman and Berge (1991); Griffin and Orton (1993); Greve et al. (1994); Klein and Hofstadter (2006), and Weiland et al. (2011), for Uranus, and Orton et al. (1986); Romani et al. (1989); de Pater and Richmond (1989); de Pater et al. (1991); Muhleman and Berge (1991); Griffin and Orton (1993); Hofstadter (1993); Greve et al. (1994), and Weiland et al. (2011), for Neptune. Even the extreme cases, in which the O abundance is lower but compensated by the biggest temperature jump allowed by the model (see Section 4.2.4), the cm-wave spectrum of both planets remains in agreement with observations. This comes from the fact that the region where the jump in temperature and H_2O abundance occur, i.e. the radiative layer, is only marginally probed by the H_2O absorption at 20 cm wavelength, as shown in DeBoer and Steffes (1996).

6. Limitations and other questions

In this section, we will detail the limitations of our model and stress the data that are desirable for increasing the predictability of such models.

6.1. The radiative layer as an insulation layer?

One of the novel aspects of our work is the inclusion of the stability criterion of Leconte et al. (2016) when extrapolating measured tropospheric temperatures to deeper levels where the atmosphere is in thermochemical equilibrium. Accounting for the mean molecular weight gradient when extending thermal profiles from observed levels in the upper troposphere to deeper levels implies the formation of a thin radiative layer ($\Delta z \sim 1$ km) in Uranus and Neptune at the levels where H_2O condenses. If such a stable layer exists, it should act as an insulation layer for the both the transport of heat and the chemical mixing, making our assumption of a vertically uniform K_{zz} profile questionable. There is no estimate for chemical mixing under such conditions, but within this layer K_{zz} could, in principle, be as low as that of molecular diffusivity D, resulting in a gradient for CO, a species that has a non-zero flux at the boundaries of the model. According to our model, molecular diffusivity is in the range of 10^{-2}-10^{-3} cm$^2 \cdot$ s^{-1}, where the radiative layer in both planets resides. We estimate the variation in the CO mole fraction between the two limits of the radiative layer using $\phi_{CO} = -nD\frac{dy_{CO}}{dt}$, where ϕ_{CO} is the flux of CO at the upper boundary of the model (i.e., the top of the troposphere) and n is the total number density. As CO is relatively stable in the stratospheres of Uranus and Neptune, a good approximation for ϕ_{CO}

[2] http://archives.esac.esa.int/hsa/legacy/ADP/PlanetaryModels/ .

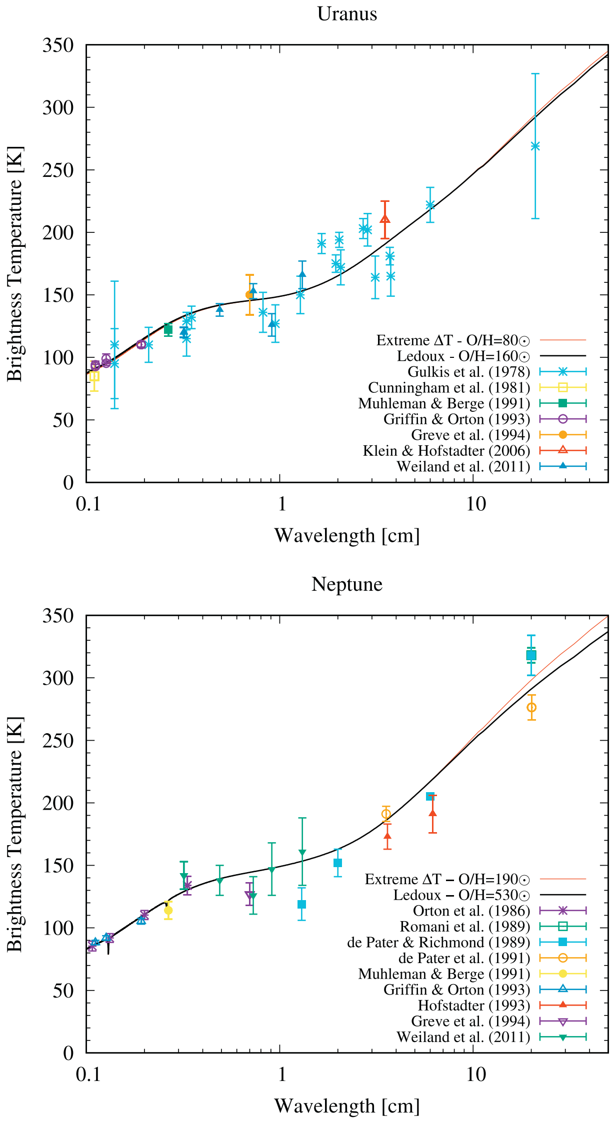

Fig. 11. Brightness temperature spectra of Uranus and Neptune in the centimeter wavelength range. We account for the opacities of NH_3, H_2S, CO, and H_2O, on top of the collision-induced absorption spectrum of H_2-H_2, H_2-He, and H_2-CH_4. The two millimetric absorption lines in the Neptune spectrum are caused by CO. The spectral resolution is 1 GHz.

is given by the input fluxes caused by external sources, and we take 10^5 and 10^8 $cm^{-2}.s^{-1}$ respectively (Cavalié et al., 2014; Lellouch et al., 2005). We confirm such values running test cases in the stratosphere with the photochemical model of Dobrijevic et al. (2010). In this case only, the variation in the CO mole fraction between the two limits of the radiative layer would be of the order of magnitude of the observed y_{CO}^{top}. This means that the tropospheric CO could be partly caused by the external source because of the transport boundary caused by the radiative zone. Then, it would be impossible to constrain the deep oxygen abundance from the sole observation of y_{CO}^{top} and thermochemical modeling, as presented in this paper. A full model accounting for thermochemistry in the troposphere, photochemistry in the stratosphere and external sources would be required to do so. This potentially is a significant limitation that should be kept in mind, although it only applies in the case where K_{zz} is as low as D in the radiative layer and the flux of CO from the stratosphere is as strong as the external source of CO. As long as $K_{zz} \geq 10^{-1}$, the gradient disappears and y_{CO}^{top} can be taken as a probe to the deep oxygen abundance. In 3D, overshooting across the 1 km radiative layer is plausible and would help in this sense.

6.2. Chemical scheme

Moses (2014) compared her chemical scheme with the one we have adopted in this work (from Venot et al., 2012) for studying the composition of HD189733b, a hot Jupiter. In her chemical scheme, she used the reaction rates updated by Moses et al. (2011), based on *ab initio* calculations. She found that the main difference between the two schemes resided in the reaction rate used for $CH_3OH + H = CH_3 + H_2O$. Moses et al. (2011) then proceeded with a much slower reaction than Venot et al. (2012). The difference between these two reaction rates, when used in the Venot et al. (2012) model has been shown for Jupiter and Saturn by Wang et al. (2016). The scheme we use nominally in this study produces 10–30 times less CO than the same scheme with the Moses et al. (2011) rate for the $CH_3OH + H = CH_3 + H_2O$ reaction (see also their Figs. 4 and 5).

If we proceed as Wang et al. (2016) and alter in the Venot et al. (2012) scheme the reaction rate for $CH_3OH + H = CH_3 + H_2O$ by using the value of Moses et al. (2011), and still use "3-layer" thermal profiles, we find that the (O/H,C/H) ratios in Uranus and Neptune become ~(<55,85) and ~(280,65) times solar, respectively. These values are significantly lower than with our nominal chemical scheme, as expected. However, we emphasize that these values are just presented for the sake of comparison. While the *ab initio* calculations of Moses et al. (2011) are correct, including this rate in the scheme of Venot et al. (2012) as prescribed by Moses (2014) in the chemical scheme does not enable reproducing of the experimental data of different combustion studies (Cathonnet et al., 1982; Hidaka et al., 1989; Held and Dryer, 1998) (R. Bounaceur, priv. comm. June 2016). Using such a reaction rate is thus not validated in the frame of our chemical scheme. In any case, it certainly underlines the urgent need for a better understanding of the kinetics of CH_3OH at high temperatures and pressures.

6.3. Tropospheric equation of state

In this work, we have implicitly used the ideal gas law. Significant water abundances at high pressures obviously render such a choice questionable. Nettelmann et al. (2008) proposed a new equation of state for H_2-He-H_2O mixtures, but for a higher pressure/temperature regime than investigated in this paper. More recently, Karpowicz and Steffes (2013) have proposed a tropospheric equation of state for Jupiter's troposphere. The effect on pressure and temperature seems rather limited (2% decrease of T, compared to the ideal gas law, at their lower boundary of 200 bars), when compared to the temperature increases caused by the mean molecular weight gradient effect shown in this paper. Nevertheless, it remains to be seen what the effect of applying such equation of state to Uranus and Neptune would be, as they have presumably much more H_2O in their deep tropospheres than Jupiter. Unfortunately, the authors underline that their "equation of state will likely have decreased accuracy under jovian conditions for pressures exceeding much beyond 100 bars, and may be invalid at pressures exceeding 2500 bars". New laboratory experiments and theoretical simulations are thus needed to enable applying reliable equations of state for H_2-H_2O-He in the pressure/temperature range we are interested in (see Baraffe et al., 2014 for a review). However, even if we had a robust non-ideal equation of state relevant for our conditions, our chemical model would need to be updated. Indeed, though we explicitly assume an ideal gas law in many calculations of our models, we also implicitly assume it in the kinetic rates.

6.4. Latent heat release by other condensates

In this work, we do not account for the release of latent heat caused by the formation of various clouds besides the H_2O clouds. Other expected clouds, from the deep troposphere to the upper troposphere, are supposedly composed of NH_4SH, NH_3 or H_2S (depending on which one is the most abundant in the deep troposphere and “survives” the formation of the NH_4SH cloud), and CH_4. Our choice to start our thermal profiles below the CH_4 cloud deck is meant so as not to have to account for the CH_4 cloud formation, related latent heat release, and even possible mean molecular weight gradient effect (Guillot, 1995).

7. Conclusion

In this paper, we have modeled the thermochemistry in the tropospheres of Uranus and Neptune, in an attempt to constrain their deep oxygen abundance from upper tropospheric observations of CO. The derivation of the deep O/H ratio in Giant Planet tropospheres from thermochemical computations requires precise measurements of upper tropospheric CO and CH_4, knowledge of oxygen species kinetics, as well as a good knowledge of tropospheric temperatures and vertical mixing.

We have shown that the transition between a water-rich and a water-poor region in giant planet tropospheres results in a significant gradient of mean molecular weight that impacts, in turn, the shape of the thermal profile. Accounting for this gradient in the condensation zone of H_2O by applying the stability criterion of Leconte et al. (2016) implies a significant departure of temperature from the dry/wet adiabats that have been used so far in previous papers. Our results show that large oxygen enrichments can produce a thin radiative layer ($\Delta z \sim 1$ km) where H_2O condenses. The thermal gradient, stabilized by the downward increasing mean molecular weight, gets very strong and becomes radiative in this zone. This results in higher temperatures in deep levels compared to dry/wet adiabats.

While the mean molecular weight gradient effects are beginning to be applied to internal and formation models of giant planets (Leconte and Chabrier, 2012; Vazan et al., 2015), our model shows for the first time the importance of accounting for these effects already at upper tropospheric levels for oxygen-rich giant planets (Leconte et al., 2016). Our results show that these new profiles lower the required oxygen abundances to reproduce the CO observations. However, our estimates are affected by the current limitations of the model, like the lack of Rosseland opacities for the considered mixtures. Another source of uncertainty is related to the high pressures at the quench level which would require non ideal equation of states and modified kinetics. While a better equation of state can be expected soon and is rather simple to implement, its impact on the kinetics might be extremely difficult to derive. Finally, it is noticeable that if (but only if) vertical mixing is as low as molecular diffusivity in the ~1 km thin radiative layer, then it is much more complicated to constrain the deep oxygen abundance in Uranus and Neptune because the CO external source then needs to be precisely characterized as well.

While using such temperature models should lead to lower O/H ratios than when using dry/wet adiabats, our nominal value for Neptune's O/H ratio is close to the value derived by Luszcz-Cook and de Pater (2013) (they have used wet adiabats). This is caused by differences in oxygen chemistry. This certainly underlines the need for improved knowledge of the oxygen species thermochemistry. For instance, with kinetics that reduce significantly the destruction of CH_3OH, as proposed by Moses et al. (2011) and applied by Wang et al. (2016), then the O/H required to fit the upper tropospheric observations of CO significantly decreases. However, using such different kinetics first require validation within a complete scheme over the temperature/pressure range relevant to such studies. We believe this is the main strength of the chemical scheme we are using, but we do not underestimate the work that still needs to be done to improve our knowledge of CH_3OH kinetics.

In our nominal model, in which we fix the temperature, the CH_4 abundance, and the tropospheric mixing to our best estimates, the O/H in Uranus and Neptune are < 160 and 540 times the solar value, respectively. While Uranus' and Neptune's ices formation and heavy element enrichment could result from clathration, this scenario would imply different mixtures of CO/CO_2 at the time of planetesimal condensation. The difference seen in their C/O ratios (> 0.23 for Uranus and ~0.03 for Neptune) is actually rather puzzling and may therefore be an indication that convection is strongly inhibited in the troposphere of Uranus. Indeed, this appealing explanation could enable reconciling formation models for the two planets with observations of their tropospheric composition. Among other things, the inconsistency between Uranus' and Neptune's O/H remains puzzling for now, and new data from dedicated orbiters with atmospheric descent probes are highly desirable to study these mysterious worlds (Arridge et al., 2012; 2014; Masters et al., 2014; Turrini et al., 2014). In the meantime, *James Webb Space Telescope* observations will enable measurements that will better constrain the deep abundances of several heavy elements, like Ge, As, and P (Norwood et al., 2016b; 2016a).

Strong uncertainties remain in Uranus and Neptune on the upper tropospheric CH_4 mole fraction, on the tropospheric mixing and on the tropospheric temperature profile. Because these are central to such thermochemical modeling, we have explored this whole parameter space with a chemical model that uses a scheme validated in the temperature/pressure range of interest here. When more precise measurements of temperature, mixing and CH_4 abundance are obtained, our results can be used to find the corresponding O/H required to fit the tropospheric CO in both planets.

In the case of the gas giants, the lower oxygen enrichments that are expected should result in a much less significant mean molecular weight gradient in the condensation region of H_2O and thus a less spectacular effect on the thermal profile and on the derivation of their deep O/H ratio. In this sense, it will be interesting to compare our thermochemical model results with the measurements that will be provided by Juno (Matousek, 2007; Helled and Lunine, 2014), which successfully performed its Jupiter orbit insertion on July 4, 2016. At Saturn, a descent probe has recently been proposed for an ESA M5 mission (Mousis et al., 2014; 2016). While this probe may not be able to reach the well-mixed region of H_2O and thus measure Saturn's O/H, it would provide ground truth as to the abundances of other heavy elements and disequilibrium species and shed light on the formation processes of Saturn.

Acknowledgements

T. Cavalié thanks the CNRS/INSU Programme National de Planétologie (PNP) for funding support. O. Venot acknowledges support from the KU Leuven IDO project IDO/10/2013, from the FWO Postdoctoral Fellowship program, and from the Centre National d'Études Spatiales (CNES). T. Cavalié and O.Venot thank R. Bounaceur (LRPG, Nancy, France) for useful discussions on the kinetics of CH_3OH. T. Cavalié thanks I. de Pater (Univ. of California, Berkeley, USA) for providing her H_2S condensation laws. We thank Dr. Dong Wang and an anonymous reviewer for they constructive comments that help us improve our paper.

References

Agúndez, M., Parmentier, V., Venot, O., Hersant, F., Selsis, F., 2014. Pseudo 2D chemical model of hot-Jupiter atmospheres: application to HD 209458b and HD 189733b. Astron. Astrophys. 564, A73.

Ali-Dib, M., Mousis, O., Petit, J.-M., Lunine, J.I., 2014. The measured compositions of Uranus and Neptune from their formation on the CO ice line. Astrophys. J. 793, 9.

Anders, E., Grevesse, N., 1989. Abundances of the elements - meteoritic and solar. Geochim. Cosmochim. Acta 53, 197–214.

Arridge, C.S., Achilleos, N., Agarwal, J., Agnor, C.B., Ambrosi, R., André, N., Badman, S.V., Baines, K., Banfield, D., Barthélémy, M., Bisi, M.M., Blum, J., Bocanegra-Bahamon, T., Bonfond, B., Bracken, C., Brandt, P., Briand, C., Briois, C., Brooks, S., Castillo-Rogez, J., Cavalié, T., Christophe, B., Coates, A.J., Collinson, G., Cooper, J.F., Costa-Sitja, M., Courtin, R., Daglis, I.A., de Pater, I., Desai, M., Dirkx, D., Dougherty, M.K., Ebert, R.W., Filacchione, G., Fletcher, L.N., Fortney, J., Gerth, I., Grassi, D., Grodent, D., Grün, E., Gustin, J., Hedman, M., Helled, R., Henri, P., Hess, S., Hillier, J.K., Hofstadter, M.H., Holme, R., Horanyi, M., Hospodarsky, G., Hsu, S., Irwin, P., Jackman, C.M., Karatekin, O., Kempf, S., Khalisi, E., Konstantinidis, K., Krüger, H., Kurth, W.S., Labrianidis, C., Lainey, V., Lamy, L.L., Laneuville, M., Lucchesi, D., Luntzer, A., MacArthur, J., Maier, A., Masters, A., McKenna-Lawlor, S., Melin, H., Milillo, A., Moragas-Klostermeyer, G., Morschhauser, A., Moses, J.I., Mousis, O., Nettelmann, N., Neubauer, F.M., Nordheim, T., Noyelles, B., Orton, G.S., Owens, M., Peron, R., Plainaki, C., Postberg, F., Rambaux, N., Retherford, K., Reynaud, S., Roussos, E., Russell, C.T., Rymer, A.M., Sallantin, R., Sánchez-Lavega, A., Santolik, O., Saur, J., Sayanagi, K.M., Schenk, P., Schubert, J., Sergis, N., Sittler, E.C., Smith, A., Spahn, F., Srama, R., Stallard, T., Sterken, V., Sternovsky, Z., Tiscareno, M., Tobie, G., Tosi, F., Trieloff, M., Turrini, D., Turtle, E.P., Vinatier, S., Wilson, R., Zarka, P., 2014. The science case for an orbital mission to Uranus: exploring the origins and evolution of ice giant planets. Planet. Space Sci. 104, 122–140.

Arridge, C.S., Agnor, C.B., André, N., Baines, K.H., Fletcher, L.N., Gautier, D., Hofstadter, M.D., Jones, G.H., Lamy, L., Langevin, Y., Mousis, O., Nettelmann, N., Russell, C.T., Stallard, T., Tiscareno, M.S., Tobie, G., Bacon, A., Chaloner, C., Guest, M., Kemble, S., Peacocke, L., Achilleos, N., Andert, T.P., Banfield, D., Barabash, S., Barthelemy, M., Bertucci, C., Brandt, P., Cecconi, B., Chakrabarti, S., Cheng, A.F., Christensen, U., Christou, A., Coates, A.J., Collinson, G., Cooper, J.F., Courtin, R., Dougherty, M.K., Ebert, R.W., Entradas, M., Fazakerley, A.N., Fortney, J.J., Galand, M., Gustin, J., Hedman, M., Helled, R., Henri, P., Hess, S., Holme, R., Karatekin, O., Krupp, N., Leisner, J., Martin-Torres, J., Masters, A., Melin, H., Miller, S., Müller-Wodarg, I., Noyelles, B., Paranicas, C., de Pater, I., Pätzold, M., Prangé, R., Quémerais, E., Roussos, E., Rymer, A.M., Sánchez-Lavega, A., Saur, J., Sayanagi, K.M., Schenk, P., Schubert, G., Sergis, N., Sohl, F., Sittler, E.C., Teanby, N.A., Tellmann, S., Turtle, E.P., Vinatier, S., Wahlund, J.-E., Zarka, P., 2012. Uranus Pathfinder: exploring the origins and evolution of ice giant planets. Exp Astron. 33, 753–791.

Atkinson, D.H., Simon, A.A., Banfield, D., Atreya, S.K., Blacksberg, J., Brinckerhoff, W., Colaprete, A., Coustenis, A., Fletcher, L., Guillot, T., Hofstadter, M., Lunine, J.I., Mahaffy, P., Marley, M.S., Mousis, O., Spilker, T.R., Trainer, M.G., Webster, C., 2016. Exploring Saturn - the Saturn PRobe Interior and aTmosphere Explorer (SPRITE) mission. AAS/Division for Planetary Sciences Meeting Abstracts. Vol. 48 of AAS/Division for Planetary Sciences Meeting Abstracts. #123.29

Atreya, S.K., Wong, M.H., Owen, T.C., Mahaffy, P.R., Niemann, H.B., de Pater, I., Drossart, P., Encrenaz, T., 1999. A comparison of the atmospheres of Jupiter and Saturn: deep atmospheric composition, cloud structure, vertical mixing, and origin. Planet. Space Sci. 47, 1243–1262.

Baines, K.H., Mickelson, M.E., Larson, L.E., Ferguson, D.W., 1995. The abundances of methane and ortho/para hydrogen on Uranus and Neptune: implications of new laboratory 4-0 H2 quadrupole line parameters. Icarus 114, 328–340.

Bar-Nun, A., Kleinfeld, I., Kochavi, E., 1988. Trapping of gas mixtures by amorphous water ice. Phys. Rev. B 38, 7749–7754.

Baraffe, I., Chabrier, G., Fortney, J., Sotin, C., 2014. Planetary internal structures. ArXiv e-prints.

Batalha, N.M., Rowe, J.F., Bryson, S.T., Barclay, T., Burke, C.J., Caldwell, D.A., Christiansen, J.L., Mullally, F., Thompson, S.E., Brown, T.M., Dupree, A.K., Fabrycky, D.C., Ford, E.B., Fortney, J.J., Gilliland, R.L., Isaacson, H., Latham, D.W., Marcy, G.W., Quinn, S.N., Ragozzine, D., Shporer, A., Borucki, W.J., Ciardi, D.R., Gautier III, T.N., Haas, M.R., Jenkins, J.M., Koch, D.G., Lissauer, J.J., Rapin, W., Basri, G.S., Boss, A.P., Buchhave, L.A., Carter, J.A., Charbonneau, D., Christensen–Dalsgaard, J., Clarke, B.D., Cochran, W.D., Demory, B.-O., Desert, J.-M., Devore, E., Doyle, L.R., Esquerdo, G.A., Everett, M., Fressin, F., Geary, J.C., Girouard, F.R., Gould, A., Hall, J.R., Holman, M.J., Howard, A.W., Howell, S.B., Ibrahim, K.A., Kinemuchi, K., Kjeldsen, H., Klaus, T.C., Li, J., Lucas, P.W., Meibom, S., Morris, R.L., Prša, A., Quintana, E., Sanderfer, D.T., Sasselov, D., Seader, S.E., Smith, J.C., Steffen, J.H., Still, M., Stumpe, M.C., Tarter, J.C., Tenenbaum, P., Torres, G., Twicken, J.D., Uddin, K., Van Cleve, J., Walkowicz, L., Welsh, W.F., 2013. Planetary candidates observed by Kepler. III. Analysis of the first 16 months of data. Astrophys. J. Suppl. 204, 24.

Beer, R., 1975. Detection of carbon monoxide in Jupiter. Astrophys. J. Lett. 200, L167–L169.

Bellotti, A., Steffes, P.G., Chinsomboom, G., 2016. Laboratory measurements of the 5–20 cm wavelength opacity of ammonia, water vapor, and methane under simulated conditions for the deep Jovian atmosphere. Icarus 280, 255–267.

Bézard, B., Lellouch, E., Strobel, D., Maillard, J.-P., Drossart, P., 2002. Carbon monoxide on Jupiter: evidence for both internal and external sources. Icarus 159, 95–111.

Borysow, A., Frommhold, L., 1986. Theoretical collision-induced rototranslational absorption spectra for the outer planets - H_2-CH_4 pairs. Astrophys. J. 304, 849–865.

Borysow, J., Frommhold, L., Birnbaum, G., 1988. Collison-induced rototranslational absorption spectra of H_2-He pairs at temperatures from 40 to 3000 K. Astrophys. J. 326, 509–515.

Borysow, J., Trafton, L., Frommhold, L., Birnbaum, G., 1985. Modeling of pressure-induced far-infrared absorption spectra molecular hydrogen pairs. Astrophys. J. 296, 644–654.

Boss, A.P., 1997. Giant planet formation by gravitational instability. Science 276, 1836–1839.

Bounaceur, R., Glaude, P.A., Fournet, R., Battin-Leclerc, F., Jay, S., Pires Da Cruz, A., 2007. Kinetic modelling of a surrogate diesel fuel applied to 3D auto-ignition in HCCI engines. Int. J. Vehicle Des. 44, 124–142.

Burgdorf, M., Orton, G.S., Davis, G.R., Sidher, S.D., Feuchtgruber, H., Griffin, M.J., Swinyard, B.M., 2003. Neptune's far-infrared spectrum from the ISO long-wavelength and short-wavelength spectrometers. Icarus 164, 244–253.

Cathonnet, M., Boettner, J.C., James, H., 1982. Study of methanol oxidation and self ignition in the temperature-range 500–600-degrees-C. Journal de Chimie Physique Et De Physico-Chimie Biologique 79, 475–478.

Cavalié, T., Billebaud, F., Biver, N., Dobrijevic, M., Lellouch, E., Brillet, J., Lecacheux, A., Hjalmarson, A., Sandqvist, A., Frisk, U., Olberg, M., Bergin, E.A., The Odin Team, 2008. Observation of water vapor in the stratosphere of Jupiter with the Odin space telescope. Planet. Space Sci. 56, 1573–1584.

Cavalié, T., Billebaud, F., Dobrijevic, M., Fouchet, T., Lellouch, E., Encrenaz, T., Brillet, J., Moriarty-Schieven, G.H., Wouterloot, J.G.A., Hartogh, P., 2009. First observation of CO at 345 GHz in the atmosphere of Saturn with the JCMT: new constraints on its origin. Icarus 203, 531–540.

Cavalié, T., Billebaud, F., Fouchet, T., Lellouch, E., Brillet, J., Dobrijevic, M., 2008. Observations of CO on Saturn and Uranus at millimeter wavelengths: new upper limit determinations. Astron. Astrophys. 484, 555–561.

Cavalié, T., Feuchtgruber, H., Lellouch, E., de Val-Borro, M., Jarchow, C., Moreno, R., Hartogh, P., Orton, G., Greathouse, T.K., Billebaud, F., Dobrijevic, M., Lara, L.M., González, A., Sagawa, H., 2013. Spatial distribution of water in the stratosphere of Jupiter from Herschel HIFI and PACS observations. Astron. Astrophys. 553, A21.

Cavalié, T., Moreno, R., Lellouch, E., Hartogh, P., Venot, O., Orton, G.S., Jarchow, C., Encrenaz, T., Selsis, F., Hersant, F., Fletcher, L.N., 2014. The first submillimeter observation of CO in the stratosphere of Uranus. Astron. Astrophys. 562, A33.

Conrath, B., Hanel, R., Gautier, D., Marten, A., Lindal, G., 1987. The helium abundance of Uranus from Voyager measurements. J. Geophys. Res. 92, 15003–15010.

Conrath, B.J., Gautier, D., 2000. Saturn helium abundance: a reanalysis of Voyager measurements. Icarus 144, 124–134.

Cunningham, C.T., Ade, P.A.R., Robson, E.I., Nolt, I.G., Radostitz, J.V., 1981. The submillimeter spectra of the planets - narrow-band photometry. Icarus 48, 127–139.

DeBoer, D.R., Steffes, P.G., 1994. Laboratory measurements of the microwave properties of H2S under simulated Jovian conditions with an application to Neptune. Icarus 109, 352–366.

DeBoer, D.R., Steffes, P.G., 1996. Estimates of the tropospheric vertical structure of Neptune based on microwave radiative transfer studies. Icarus 123, 324–335.

Dobrijevic, M., Cavalié, T., Hébrard, E., Billebaud, F., Hersant, F., Selsis, F., 2010. Key reactions in the photochemistry of hydrocarbons in Neptune's stratosphere. Planet. Space Sci. 58, 1555–1566.

Fegley, B., Prinn, R.G., 1988. Chemical constraints on the water and total oxygen abundances in the deep atmosphere of Jupiter. Astrophys. J. 324, 621–625.

Feuchtgruber, H., Lellouch, E., Orton, G., de Graauw, T., Vandenbussche, B., Swinyard, B., Moreno, R., Jarchow, C., Billebaud, F., Cavalié, T., Sidher, S., Hartogh, P., 2013. The D/H ratio in the atmospheres of Uranus and Neptune from Herschel–PACS observations. Astron. Astrophys. 551, A126.

Fletcher, L.N., Drossart, P., Burgdorf, M., Orton, G.S., Encrenaz, T., 2010. Neptune's atmospheric composition from AKARI infrared spectroscopy. Astron. Astrophys. 514, A17.

Fletcher, L.N., Irwin, P.G.J., Achterberg, R.K., Orton, G.S., Flasar, F.M., 2016. Seasonal variability of Saturn's tropospheric temperatures, winds and para-H_2 from Cassini far-IR spectroscopy. Icarus 264, 137–159.

Fletcher, L.N., Irwin, P.G.J., Teanby, N.A., Orton, G.S., Parrish, P.D., Calcutt, S.B., Bowles, N., de Kok, R., Howett, C., Taylor, F.W., 2007. The meridional phosphine distribution in Saturn's upper troposphere from Cassini/CIRS observations. Icarus 188, 72–88.

Fletcher, L.N., Orton, G.S., Teanby, N.A., Irwin, P.G.J., Bjoraker, G.L., 2009. Methane and its isotopologues on Saturn from Cassini/CIRS observations. Icarus 199, 351–367.

Fletcher, L.N., Swinyard, B., Salji, C., Polehampton, E., Fulton, T., Sidher, S., Lellouch, E., Moreno, R., Orton, G., Cavalié, T., Courtin, R., Rengel, M., Sagawa, H., Davis, G.R., Hartogh, P., Naylor, D., Walker, H., Lim, T., 2012. Sub-millimetre spectroscopy of Saturn's trace gases from Herschel/SPIRE. Astron. Astrophys. 539, A44.

Fray, N., Schmitt, B., 2009. Sublimation of ices of astrophysical interest: abibliographic review. Planet. Space Sci. 57, 2053–2080.

Fressin, F., Torres, G., Charbonneau, D., Bryson, S.T., Christiansen, J., Dressing, C.D., Jenkins, J.M., Walkowicz, L.M., Batalha, N.M., 2013. The false positive rate of Kepler and the occurrence of planets. Astrophys. J. 766, 81.

Gautier, D., Hersant, F., 2005. Formation and composition of planetesimals. Space Sci. Rev. 116, 25–52.

Gautier, D., Hersant, F., Mousis, O., Lunine, J.I., 2001. Enrichments in volatiles in Jupiter: a new interpretation of the Galileo measurements. Astrophys. J. Lett. 550, L227–L230.

Gierasch, P.J., Conrath, B.J., 1985. Energy conversion processes in the outer planets. Recent Adv. Planet. Meteorol. 121–146.

Gomes, R., Levison, H.F., Tsiganis, K., Morbidelli, A., 2005. Origin of the cataclysmic Late Heavy Bombardment period of the terrestrial planets. Nature 435, 466–469.

Gordon, S., McBride, B.J., 1994. Computer program for calculation of complex chemical equilibrium compositions and applications. Part 1: analysis. NASA Reference Publication 1311.

Greve, A., Steppe, H., Graham, D., Schalinski, C.J., 1994. Disk brightness temperature of the planets at 43 GHz (and 43 GHz flux densities of some continuum sources). Astron. Astrophys. 286, 654–658.

Griffin, M.J., Orton, G.S., 1993. The near-millimeter brightness temperature spectra of Uranus and Neptune. Icarus 105, 537.

Guillot, T., 1995. Condensation of methane, ammonia, and water and the inhibition of convection in giant planets. Science 269, 1697–1699.

Gulkis, S., Janssen, M.A., Olsen, E.T., 1978. Evidence for the depletion of ammonia in the Uranus atmosphere. Icarus 34, 10–19.

Hanel, R., Conrath, B., Herath, L., Kunde, V., Pirraglia, J., 1981. Albedo, internal heat, and energy balance of Jupiter - preliminary results of the Voyager infrared investigation. J. Geophys. Res. 86, 8705–8712.

Hanel, R.A., Conrath, B.J., Kunde, V.G., Pearl, J.C., Pirraglia, J.A., 1983. Albedo, internal heat flux, and energy balance of Saturn. Icarus 53, 262–285.

Held, T.J., Dryer, F.L., 1998. A comprehensive mechanism for methanol oxidation. Int. J. Chem. Kinet. 30, 805–830.

Helled, R., Anderson, J.D., Podolak, M., Schubert, G., 2011. Interior models of Uranus and Neptune. Astrophys. J. 726, 15.

Helled, R., Lunine, J., 2014. Measuring Jupiter's water abundance by Juno: the link between interior and formation models. Mon. Not. R. Astron. Soc. 441, 2273–2279.

Hersant, F., Gautier, D., Huré, J.-M., 2001. A two-dimensional model for the primordial nebula constrained by D/H measurements in the solar system: implications for the formation of giant planets. Astrophys. J. 554, 391–407.

Hersant, F., Gautier, D., Lunine, J.I., 2004. Enrichment in volatiles in the giant planets of the solar system. Planet. Space Sci. 52, 623–641.

Hersant, F., Gautier, D., Tobie, G., Lunine, J.I., 2008. Interpretation of the carbon abundance in Saturn measured by Cassini. Planet. Space Sci. 56, 1103–1111.

Hidaka, Y., Oki, T., Kawano, H., Higashihara, T., 1989. Thermal decomposition of methanol in shock waves. J. Chem. Phys. 93, 7134–7139.

Hofstadter, M.D., 1993. Microwave imaging of Neptune's troposphere. In: AAS/Division for Planetary Sciences Meeting Abstracts #25. Vol. 25 of Bulletin of the American Astronomical Society, p. 1077.

Hofstadter, M.D., Butler, B.J., 2003. Seasonal change in the deep atmosphere of Uranus. Icarus 165, 168–180.

Karkoschka, E., Tomasko, M., 2009. The haze and methane distributions on Uranus from HST-STIS spectroscopy. Icarus 202, 287–309.

Karkoschka, E., Tomasko, M.G., 2011. The haze and methane distributions on Neptune from HST-STIS spectroscopy. Icarus 211, 780–797.

Karpowicz, B.M., Steffes, P.G., 2013. Investigating the H_2-He-H_2O-CH_4 equation of state in the deep troposphere of Jupiter. Icarus 223, 277–297.

Klein, M.J., Hofstadter, M.D., 2006. Long-term variations in the microwave brightness temperature of the Uranus atmosphere. Icarus 184, 170–180.

Leconte, J., Chabrier, G., 2012. A new vision of giant planet interiors: impact of double diffusive convection. Astron. Astrophys. 540, A20.

Leconte, J., Forget, F., Charnay, B., Wordsworth, R., Pottier, A., 2013. Increased insolation threshold for runaway greenhouse processes on Earth-like planets. Nature 504, 268–271.

Leconte, J., Selsis, F., Hersant, F., Guillot, T., 2016. Condensation-inhibited convection in hydrogen-rich atmospheres. Stability against double-diffusive processes and thermal profiles for Jupiter, Saturn, Uranus, and Neptune. Astron. Astrophys. 598, A98.

Ledoux, P., 1947. Stellar models with convection and with discontinuity of the mean molecular weight. Astrophys. J. 105, 305.

Lellouch, E., Bézard, B., Fouchet, T., Feuchtgruber, H., Encrenaz, T., de Graauw, T., 2001. The deuterium abundance in Jupiter and Saturn from ISO-SWS observations. Astron. Astrophys. 370, 610–622.

Lellouch, E., Hartogh, P., Feuchtgruber, H., Vandenbussche, B., de Graauw, T., Moreno, R., Jarchow, C., Cavalié, T., Orton, G., Banaszkiewicz, M., Blecka, M.I., Bockelée-Morvan, D., Crovisier, J., Encrenaz, T., Fulton, T., Küppers, M., Lara, L.M., Lis, D.C., Medvedev, A.S., Rengel, M., Sagawa, H., Swinyard, B., Szutowicz, S., Bensch, F., Bergin, E., Billebaud, F., Biver, N., Blake, G.A., Blommaert, J.A.D.L., Cernicharo, J., Courtin, R., Davis, G.R., Decin, L., Encrenaz, P., Gonzalez, A., Jehin, E., Kidger, M., Naylor, D., Portyankina, G., Schieder, R., Sidher, S., Thomas, N., de Val-Borro, M., Verdugo, E., Waelkens, C., Walker, H., Aarts, H., Comito, C., Kawamura, J.H., Maestrini, A., Peacocke, T., Teipen, R., Tils, T., Wildeman, K., 2010. First results of Herschel-PACS observations of Neptune. Astron. Astrophys. 518, L152.

Lellouch, E., Moreno, R., Orton, G.S., Feuchtgruber, H., Cavalié, T., Moses, J.I., Hartogh, P., Jarchow, C., Sagawa, H., 2015. New constraints on the CH_4 vertical profile in Uranus and Neptune from Herschel observations. Astron. Astrophys. 579, A121.

Lellouch, E., Moreno, R., Paubert, G., 2005. A dual origin for Neptune's carbon monoxide? Astron. Astrophys. 430, L37–L40.

Liebe, H.J., Dillon, T.A., 1969. Accurate foreign-gas-broadening parameters of the 22-GHz H2O line from refraction spectroscopy. J. Chem. Phys. 50, 727–732.

Lindal, G.F., 1992. The atmosphere of Neptune - an analysis of radio occultation data acquired with Voyager 2. Astron. J. 103, 967–982.

Lindal, G.F., Lyons, J.R., Sweetnam, D.N., Eshleman, V.R., Hinson, D.P., 1987. The atmosphere of Uranus - results of radio occultation measurements with Voyager 2. J. Geophys. Res. 92, 14987–15001.

Lindal, G.F., Lyons, J.R., Sweetnam, D.N., Eshleman, V.R., Hinson, D.P., 1990. The atmosphere of Neptune - results of radio occultation measurements with the Voyager 2 spacecraft. Geophys. Res. Lett. 17, 1733–1736.

Lodders, K., 1994. Jupiter formed with more tar than ice. Astrophys. J. 611, 587–597.

Lodders, K., 2010. Solar System Abundances of the Elements. Principles Perspect. Cosmochem. 379.

Lodders, K., Fegley Jr., B., 1994. The origin of carbon monoxide in Neptune's atmosphere. Icarus 112, 368–375.

Lunine, J.I., Stevenson, D.J., 1985. Thermodynamics of clathrate hydrate at low and high pressures with application to the outer solar system. Astrophys. J. Suppl. 58, 493–531.

Luszcz-Cook, S.H., de Pater, I., 2013. Constraining the origins of Neptune's carbon monoxide abundance with CARMA millimeter-wave observations. Icarus 222, 379–400.

Mahaffy, P.R., Niemann, H.B., Alpert, A., Atreya, S.K., Demick, J., Donahue, T.M., Harpold, D.N., Owen, T.C., 2000. Noble gas abundance and isotope ratios in the atmosphere of Jupiter from the Galileo probe mass spectrometer. J. Geophys. Res. 105, 15061–15072.

Mandt, K.E., Mousis, O., Marty, B., Cavalié, T., Harris, W., Hartogh, P., Willacy, K., 2015. Constraints from comets on the formation and volatile acquisition of the planets and satellites. Space Sci. Rev. 197, 297–342.

Marten, A., Gautier, D., Owen, T., Sanders, D.B., Matthews, H.E., Atreya, S.K., Tilanus, R.P.J., Deane, J.R., 1993. First observations of CO and HCN on Neptune and Uranus at millimeter wavelengths and the implications for atmospheric chemistry. Astrophys. J. 406, 285–297.

Marten, A., Matthews, H.E., Owen, T., Moreno, R., Hidayat, T., Biraud, Y., 2005. Improved constraints on Neptune's atmosphere from submillimetre-wavelength observations. Astron. Astrophys. 429, 1097–1105.

Masters, A., Achilleos, N., Agnor, C.B., Campagnola, S., Charnoz, S., Christophe, B., Coates, A.J., Fletcher, L.N., Jones, G.H., Lamy, L., Marzari, F., Nettelmann, N., Ruiz, J., Ambrosi, R., Andre, N., Bhardwaj, A., Fortney, J.J., Hansen, C.J., Helled, R., Moragas-Klostermeyer, G., Orton, G., Ray, L., Reynaud, S., Sergis, N., Srama, R., Volwerk, M., 2014. Neptune and Triton: essential pieces of the Solar System puzzle. Planet. Space Sci. 104, 108–121.

Matousek, S., 2007. The Juno New Frontiers mission. Acta Astronautica 61, 932–939.

Morbidelli, A., Levison, H.F., Tsiganis, K., Gomes, R., 2005. Chaotic capture of Jupiter's Trojan asteroids in the early solar system. Nature 435, 462–465.

Moreno, R.M., 1998. Observations millimétriques et submillimétriques des planètes géantes. Étude de Jupiter après la chute de la comète SL9. Université Paris VI Ph.d. thesis.

Moses, J.I., 2014. Chemical kinetics on extrasolar planets. Philos. Trans. R. Soc.London Ser. A 372. 20130073-20130073

Moses, J.I., Madhusudhan, N., Visscher, C., Freedman, R.S., 2013. Chemical consequences of the C/O ratio on hot Jupiters: examples from WASP-12b, CoRoT-2b, XO-1b, and HD 189733b. Astrophys. J. 763, 25.

Moses, J.I., Visscher, C., Fortney, J.J., Showman, A.P., Lewis, N.K., Griffith, C.A., Klippenstein, S.J., Shabram, M., Friedson, A.J., Marley, M.S., Freedman, R.S., 2011. Disequilibrium carbon, oxygen, and nitrogen chemistry in the atmospheres of HD 189733b and HD 209458b. Astrophys. J. 737, 15.

Mousis, O., Atkinson, D.H., Spilker, T., Venkatapathy, E., Poncy, J., Frampton, R., Coustenis, A., Reh, K., Lebreton, J.-P., Fletcher, L.N., Hueso, R., Amato, M.J., Colaprete, A., Ferri, F., Stam, D., Wurz, P., Atreya, S., Aslam, S., Banfield, D.J., Calcutt, S., Fischer, G., Holland, A., Keller, C., Kessler, E., Leese, M., Levacher, P., Morse, A., Muñoz, O., Renard, J.-B., Sheridan, S., Schmider, F.-X., Snik, F., Waite, J.H., Bird, M., Cavalié, T., Deleuil, M., Fortney, J., Gautier, D., Guillot, T., Lunine, J.I., Marty, B., Nixon, C., Orton, G.S., Sánchez-Lavega, A., 2016. The Hera Saturn entry probe mission. Planet. Space Sci. 130, 80–103.

Mousis, O., Fletcher, L.N., Lebreton, J.-P., Wurz, P., Cavalié, T., Coustenis, A., Courtin, R., Gautier, D., Helled, R., Irwin, P.G.J., Morse, A.D., Nettelmann, N., Marty, B., Rousselot, P., Venot, O., Atkinson, D.H., Waite, J.H., Reh, K.R., Simon, A.A., Atreya, S., André, N., Blanc, M., Daglis, I.A., Fischer, G., Geppert, W.D., Guillot, T., Hedman, M.M., Hueso, R., Lellouch, E., Lunine, J.I., Murray, C.D., O'Donoghue, J., Rengel, M., Sánchez-Lavega, A., Schmider, F.-X., Spiga, A., Spilker, T., Petit, J.-M., Tiscareno, M.S., Ali-Dib, M., Altwegg, K., Bolton, S.J., Bouquet, A., Briois, C., Fouchet, T., Guerlet, S., Kostiuk, T., Lebleu, D., Moreno, R., Orton, G.S., Poncy, J., 2014. Scientific rationale for Saturn's in situ exploration. Planet. Space Sci. 104, 29–47.

Mousis, O., Lunine, J.I., Madhusudhan, N., Johnson, T.V., 2012. Nebular water depletion as the cause of Jupiter's low oxygen abundance. Astrophys. J. Lett. 751, L7.

Muhleman, D.O., Berge, G.L., 1991. Observations of Mars, Uranus, Neptune, Io, Europa, Ganymede, and Callisto at a wavelength of 2.66 MM. Icarus 92, 263–272.

Nettelmann, N., Helled, R., Fortney, J.J., Redmer, R., 2013. New indication for a dichotomy in the interior structure of Uranus and Neptune from the application of modified shape and rotation data. Planet. Space Sci. 77, 143–151.

Nettelmann, N., Holst, B., Kietzmann, A., French, M., Redmer, R., Blaschke, D., 2008. Ab initio equation of state data for hydrogen, helium, and water and the internal structure of Jupiter. Astrophys. J. 683, 1217–1228.

Nettelmann, N., Wang, K., Fortney, J.J., Hamel, S., Yellamilli, S., Bethkenhagen, M., Redmer, R., 2016. Uranus evolution models with simple thermal boundary layers. Icarus 275, 107–116.

Niemann, H.B., Atreya, S.K., Carignan, G.R., Donahue, T.M., Haberman, J.A., Harpold, D.N., Hartle, R.E., Hunten, D.M., Kasprzak, W.T., Mahaffy, P.R., Owen, T.C., Way, S.H., 1998. The composition of the Jovian atmosphere as determined by the Galileo probe mass spectrometer. J. Geophys. Res. 103, 22831–22846.

Norwood, J., Hammel, H., Milam, S., Stansberry, J., Lunine, J., Chanover, N., Hines, D., Sonneborn, G., Tiscareno, M., Brown, M., Ferruit, P., 2016. Solar system observations with the James Webb Space Telescope. Publ. Astron. Soc. Pac. 128 (2), 025004.

Norwood, J., Moses, J., Fletcher, L.N., Orton, G., Irwin, P.G.J., Atreya, S., Rages, K., Cavalié, T., Sánchez-Lavega, A., Hueso, R., Chanover, N., 2016. Giant planet observations with the James Webb Space Telescope. Publ. Astron. Soc. Pac. 128 (1), 018005.

Orton, G.S., Fletcher, L.N., Moses, J.I., Mainzer, A.K., Hines, D., Hammel, H.B., Martin–Torres, F.J., Burgdorf, M., Merlet, C., Line, M.R., 2014. Mid-infrared spectroscopy of Uranus from the Spitzer Infrared Spectrometer: 1. Determination of the mean temperature structure of the upper troposphere and stratosphere. Icarus 243, 494–513.

Orton, G.S., Griffin, M.J., Ade, P.A.R., Nolt, I.G., Radostitz, J.V., 1986. Submillimeter and millimeter observations of Uranus and Neptune. Icarus 67, 289–304.

Owen, T., Encrenaz, T., 2003. Element abundances and isotope ratios in the giant planets and Titan. Space Sci. Rev. 106, 121–138.

Owen, T., Encrenaz, T., 2006. Compositional constraints on giant planet formation. Planet. Space Sci. 54, 1188–1196.

Owen, T., Mahaffy, P., Niemann, H.B., Atreya, S., Donahue, T., Bar-Nun, A., de Pater, I., 1999. A low-temperature origin for the planetesimals that formed Jupiter. Nature 402, 269–270.

Owen, T.C., 2007. Planetary atmospheres. Space Sci. Rev. 130, 97–104.

de Pater, I., DeBoer, D., Marley, M., Freedman, R., Young, R., 2005. Retrieval of water in Jupiter's deep atmosphere using microwave spectra of its brightness temperature. Icarus 173, 425–438.

de Pater, I., Richmond, M., 1989. Neptune's microwave spectrum from 1 MM to 20 CM. Icarus 80, 1–13.

de Pater, I., Romani, P.N., Atreya, S.K., 1991. Possible microwave absorption by H2S gas in Uranus' and Neptune's atmospheres. Icarus 91, 220–233.

Pearl, J.C., Conrath, B.J., 1991. The albedo, effective temperature, and energy balance of Neptune, as determined from Voyager data. J. Geophys. Res. 96, 18921.

Pearl, J.C., Conrath, B.J., Hanel, R.A., Pirraglia, J.A., 1990. The albedo, effective temperature, and energy balance of Uranus, as determined from Voyager IRIS data. Icarus 84, 12–28.

Pickett, H.M., Poynter, R.L., Cohen, E.A., Delitsky, M.L., Pearson, J.C., Müller, H.S.P., 1998. Submillimeter, millimeter and microwave spectral line catalog. J. Quant. Spectrosc. Radiat. Transfer 60, 883–890.

Pollack, J.B., Hubickyj, O., Bodenheimer, P., Lissauer, J.J., Podolak, M., Greenzweig, Y., 1996. Formation of the giant planets by concurrent accretion of solids and gas. Icarus 124, 62–85.

Prinn, R.G., Barshay, S.S., 1977. Carbon monoxide on Jupiter and implications for atmospheric convection. Science 198, 1031–1034.

Romani, P.N., de Pater, I., Atreya, S.K., 1989. Neptune's deep atmosphere revealed. Geophys. Res. Lett. 16, 933–936.

Rosenqvist, J., Lellouch, E., Romani, P.N., Paubert, G., Encrenaz, T., 1992. Millimeter-wave observations of Saturn, Uranus, and Neptune - CO and HCN on Neptune. Astrophys. J. Lett. 392, L99–L102.

Sakashita, S., Hayashi, C., 1959. Internal structure and evolution of very massive stars. Prog. Theor. Phys. 22, 830–834.

Schwarzschild, M., Härm, R., 1958. Evolution of very massive stars. Astrophys. J. 128, 348.

Seiff, A., Kirk, D.B., Knight, T.C.D., Young, R.E., Mihalov, J.D., Young, L.A., Milos, F.S., Schubert, G., Blanchard, R.C., Atkinson, D., 1998. Thermal structure of Jupiter's atmosphere near the edge of a 5-μm hot spot in the north equatorial belt. J. Geophys. Res. 103, 22857–22890.

Smith, M.D., 1998. Estimation of a length scale to use with the quench level approximation for obtaining chemical abundances. Icarus 132, 176–184.

Sromovsky, L.A., Fry, P.M., 2008. The methane abundance and structure of Uranus' cloud bands inferred from spatially resolved 2006 Keck grism spectra. Icarus 193, 252–266.

Sromovsky, L.A., Fry, P.M., Kim, J.H., 2011. Methane on Uranus: the case for a compact CH $_4$ cloud layer at low latitudes and a severe CH $_4$ depletion at high--latitudes based on re-analysis of Voyager occultation measurements and STIS spectroscopy. Icarus 215, 292–312.

Sromovsky, L.A., Karkoschka, E., Fry, P.M., Hammel, H.B., de Pater, I., Rages, K., 2014. Methane depletion in both polar regions of Uranus inferred from HST/STIS and Keck/NIRC2 observations. Icarus 238, 137–155.

Stone, P.H., 1976. The meteorology of the Jovian atmosphere. In: Gehrels, T. (Ed.), IAU Colloq. 30: Jupiter: Studies of the Interior, Atmosp here, Magnetosphere and Satellites, pp. 586–618.

Teanby, N.A., Irwin, P.G.J., 2013. An external origin for carbon monoxide on Uranus from Herschel/SPIRE? Astrophys. J. Lett. 775 (2), L49.

Tsiganis, K., Gomes, R., Morbidelli, A., Levison, H.F., 2005. Origin of the orbital architecture of the giant planets of the Solar System. Nature 435, 459–461.

Turrini, D., Politi, R., Peron, R., Grassi, D., Plainaki, C., Barbieri, M., Lucchesi, D.M., Magni, G., Altieri, F., Cottini, V., Gorius, N., Gaulme, P., Schmider, F.-X., Adriani, A., Piccioni, G., 2014. The comparative exploration of the ice giant planets with twin spacecraft: unveiling the history of our Solar System. Planet. Space Sci. 104, 93–107.

Valencia, D., Guillot, T., Parmentier, V., Freedman, R.S., 2013. Bulk composition of GJ 1214b and other sub-Neptune exoplanets. Astrophys. J. 775, 10.

Vazan, A., Helled, R., Kovetz, A., Podolak, M., 2015. Convection and mixing in giant planet evolution. Astrophys. J. 803, 32.

Venot, O., Agúndez, M., Selsis, F., Tessenyi, M., Iro, N., 2014. The atmospheric chemistry of the warm Neptune GJ 3470b: influence of metallicity and temperature on the CH_4/CO ratio. Astron. Astrophys. 562, A51.

Venot, O., Hébrard, E., Agúndez, M., Decin, L., Bounaceur, R., 2015. New chemical scheme for studying carbon-rich exoplanet atmospheres. Astron. Astrophys. 577, A33.

Venot, O., Hébrard, E., Agúndez, M., Dobrijevic, M., Selsis, F., Hersant, F., Iro, N., Bounaceur, R., 2012. A chemical model for the atmosphere of hot Jupiters. Astron. Astrophys. 546, A43.

Visscher, C., Fegley Jr., B., 2005. Chemical constraints on the water and total oxygen abundances in the deep atmosphere of Saturn. Astrophys. J. 623, 1221–1227.

Visscher, C., Moses, J.I., 2011. Quenching of carbon monoxide and methane in the atmospheres of cool brown dwarfs and hot Jupiters. Astrophys. J. 738, 72.

Visscher, C., Moses, J.I., Saslow, S.A., 2010. The deep water abundance on Jupiter: new constraints from thermochemical kinetics and diffusion modeling. Icarus 209, 602–615.

Wakelam, V., Herbst, E., Loison, J.-C., Smith, I.W.M., Chandrasekaran, V., Pavone, B., Adams, N.G., Bacchus-Montabonel, M.-C., Bergeat, A., Béroff, K., Bierbaum, V.M., Chabot, M., Dalgarno, A., van Dishoeck, E.F., Faure, A., Geppert, W.D., Gerlich, D., Galli, D., Hébrard, E., Hersant, F., Hickson, K.M., Honvault, P., Klippenstein, S.J., Le Picard, S., Nyman, G., Pernot, P., Schlemmer, S., Selsis, F., Sims, I.R., Talbi, D., Tennyson, J., Troe, J., Wester, R., Wiesenfeld, L., 2012. A KInetic Database for Astrochemistry (KIDA). Astrophys. J. Suppl. 199, 21.

Wang, D., Gierasch, P.J., Lunine, J.I., Mousis, O., 2015. New insights on Jupiter's deep water abundance from disequilibrium species. Icarus 250, 154–164.

Wang, D., Lunine, J.I., Mousis, O., 2016. Modeling the disequilibrium species for Jupiter and Saturn: implications for Juno and Saturn entry probe. Icarus 276, 21–38.

Weiland, J.L., Odegard, N., Hill, R.S., Wollack, E., Hinshaw, G., Greason, M.R., Jarosik, N., Page, L., Bennett, C.L., Dunkley, J., Gold, B., Halpern, M., Kogut, A., Komatsu, E., Larson, D., Limon, M., Meyer, S.S., Nolta, M.R., Smith, K.M., Spergel, D.N., Tucker, G.S., Wright, E.L., 2011. Seven-year Wilkinson Microwave Anisotropy Probe (WMAP) observations: planets and celestial calibration sources. Astrophys. J. Suppl. 192, 19.

Wong, M.H., Mahaffy, P.R., Atreya, S.K., Niemann, H.B., Owen, T.C., 2004. Updated Galileo probe mass spectrometer measurements of carbon, oxygen, nitrogen, and sulfur on Jupiter. Icarus 171, 153–170.

Yung, Y.L., Drew, W.A., Pinto, J.P., Friedl, R.R., 1988. Estimation of the reaction rate for the formation of CH3O from H + H2CO – implications for chemistry in the solar system. Icarus 73, 516–526.

von Zahn, U., Hunten, D.M., Lehmacher, G., 1998. Helium in Jupiter's atmosphere: results from the Galileo probe helium interferometer experiment. J. Geophys. Res. 103, 22815–22830.

Icarus 257 (2015) 163–184

Contents lists available at ScienceDirect

Icarus

journal homepage: www.elsevier.com/locate/icarus

2D photochemical modeling of Saturn's stratosphere. Part I: Seasonal variation of atmospheric composition without meridional transport

V. Hue [a,b,*], T. Cavalié [c], M. Dobrijevic [a,b], F. Hersant [a,b], T.K. Greathouse [d]

[a] Université de Bordeaux, Laboratoire d'Astrophysique de Bordeaux, UMR 5804, F-33270 Floirac, France
[b] CNRS, Laboratoire d'Astrophysique de Bordeaux, UMR 5804, F-33270 Floirac, France
[c] Max Planck Institute for Solar System Research, Justus-von-Liebig-Weg 3, 37077, Göttingen, Germany
[d] Southwest Research Institute, San Antonio, TX 78228, United States

ARTICLE INFO

Article history:
Received 12 November 2014
Revised 31 March 2015
Accepted 1 April 2015
Available online 14 May 2015

Keywords:
Photochemistry
Saturn
Atmospheres, evolution

ABSTRACT

Saturn's axial tilt of 26.7° produces seasons in a similar way as on Earth. Both the stratospheric temperature and composition are affected by this latitudinally varying insolation along Saturn's orbital path. A new time-dependent 2D photochemical model is presented to study the seasonal evolution of Saturn's stratospheric composition. This study focuses on the impact of the seasonally variable thermal field on the main stratospheric C2-hydrocarbon chemistry (C_2H_2 and C_2H_6) using a realistic radiative climate model. Meridional mixing and advective processes are implemented in the model but turned off in the present study for the sake of simplicity. The results are compared to a simple study case where a latitudinally and temporally steady thermal field is assumed. Our simulations suggest that, when the seasonally variable thermal field is accounted for, the downward diffusion of the seasonally produced hydrocarbons is faster due to the seasonal compression of the atmospheric column during winter. This effect increases with increasing latitudes which experience the most important thermal changes in the course of the seasons. The seasonal variability of C_2H_2 and C_2H_6 therefore persists at higher-pressure levels with a seasonally-variable thermal field. Cassini limb-observations of C_2H_2 and C_2H_6 (Guerlet, S. et al. [2009]. Icarus 203, 214–232) are reasonably well-reproduced from the equator to 40° in both hemispheres in the 0.1–1 mbar pressure range. At lower pressure levels, the models only fit the Cassini observations in the northern hemisphere, from the equator to 40°N. Beyond 40° in both hemispheres, deviations from the pure photochemical predictions, mostly in the southern hemisphere, suggest the presence of large-scale stratospheric dynamics.

1. Introduction

Observations of Saturn in the infrared and millimetric range, performed by ISO or ground-based facilities gave us access to its disk-averaged stratospheric composition (see the review of Fouchet et al. (2009) for a complete list of observations), for which 1D photochemical models have done a fairly good job reproducing it (Moses et al., 2000a,b). Close-up observations, performed by the Voyager missions as well as recent ground-based observations, have unveiled variations with latitude of the temperature and the stratospheric composition (Ollivier et al., 2000a; Greathouse et al., 2005; Sinclair et al., 2014). The Cassini probe has now mapped (as a function of altitude and latitude) and monitored for almost 10 years, i.e., 1.5 Saturn season, the temperature and the main hydrocarbon emissions in Saturn's stratosphere (Howett et al., 2007; Fouchet et al., 2008; Hesman et al., 2009; Guerlet et al., 2009, 2010; Li et al., 2010; Fletcher et al., 2010; Sinclair et al., 2013, 2014).

We now have an impressive amount of data for which 1D photochemical models (e.g., Moses et al., 2000a,b, 2005; Ollivier et al., 2000b) have become insufficient in predicting the 3D properties of Saturn's stratosphere, especially in terms of dynamics (diffusion and advection). On the other hand, general circulation models (GCM) are being developed for Jupiter (Medvedev et al., 2013) and Saturn (Dowling et al., 2006, 2010; Friedson and Moses, 2012; Guerlet et al., 2014). Such models usually focus on dynamics and therefore are restricted in their description of the atmospheric chemistry as they are limited to only a few reactions, if any at all. Liang et al. (2005) and Moses and Greathouse (2005) made the first attempts to construct latitude-altitude photochemical models for the giant planets, followed by Moses et al. (2007) who built a

* Corresponding author at: Université de Bordeaux, Laboratoire d'Astrophysique de Bordeaux, UMR 5804, F-33270 Floirac, France. Tel.: +33 5 5777 6164.
E-mail address: Vincent.Hue@obs.u-bordeaux1.fr (V. Hue).

http://dx.doi.org/10.1016/j.icarus.2015.04.001
0019-1035/

2D-photochemical model for Saturn and who accounted for simple Hadley-type circulation cells as well as meridional diffusive transport. The quasi-two-dimensional model developed by Liang et al. (2005) does not fully account for the latitudinal transport as a diffusive correction is added at the end of the one-dimensional calculations. This model also does not account for evolution of the orbital parameters. Due to its very low obliquity, the seasonal effects on Jupiter should be mainly caused by its eccentricity and might be non negligible. On the other hand, the model developed by Moses and Greathouse (2005) accounts for the seasonal evolution of the orbital parameters as well as the variations in solar conditions. They have shown that, for Saturn, the seasonal effects on atmospheric composition are important, as Saturn's obliquity is slightly larger than the Earth's. Their model consists of a sum of 1D-photochemical model runs at different solar declinations and conditions. It does not include meridional transport processes nor the calculation of the actinic fluxes in 2D/3D. Saturn's high obliquity similarly impacts the stratospheric temperatures (Fletcher et al., 2010). This effect was accounted for by Moses and Greathouse (2005) in their photochemical model as part of a sensitivity case study, by locally warming their nominal temperature profile at two latitudes, according to the observations of Greathouse et al. (2005). In this sense, the photochemical model in Guerlet et al. (2010) represents an improvement from the previous model of Moses and Greathouse (2005) as it includes the latitudinal thermal gradient observed both by Fletcher et al. (2007) and Guerlet et al. (2009), but held constant with seasons. Finally, Moses et al. (2007) accounted for the meridional transport in a 2D-photochemical model, but similarly neglected the seasonal evolution of the stratospheric temperature. They were unable to reproduce the ground-based hydrocarbon observations prior to Cassini mission (Greathouse et al., 2005). After 10 years of Cassini measurements, data has shown that Saturn's stratospheric thermal structure is complex, with a 40 K pole-to-pole gradient after solstice (Fletcher et al., 2010), and thermal oscillations in the equatorial zone (Orton et al., 2008; Fouchet et al., 2008; Guerlet et al., 2011).

For the moment, there is no 2D photochemical model that simultaneously accounts for seasonal forcing, meridional transport and the evolution of the stratospheric temperature. In this paper, we present a new step toward this model, applied to Saturn. These latitudinally and seasonally variable 1D models, coupled by a 3D-radiative transfer model, can be seen as an intermediate class of model between the 1D photochemical models that have the most complete chemistries and the GCMs that are focused on 3D dynamics. In this paper, we present a restricted version of our full-2D model. The goal of this preliminary study is to evaluate the atmospheric chemical response to seasonal forcing in terms of solar radiation and atmospheric temperatures. The meridional transport is therefore set to zero for this study in order to focus on photochemical effects. In forthcoming papers we will focus on the effect of 2D advective and diffusive transport on the predicted abundances.

In the first part of this paper, we present in detail how the seasonally variable parameters are accounted for in the model, including Saturn's orbital parameters and the thermal field. Then, we describe the photochemical model, the chemical scheme used in that model and the 3D radiative transfer model used to calculate the attenuation of the UV radiation in the atmosphere. We afterwards describe the seasonal evolution of the chemical composition, first by assuming that the thermal field does not evolve with time and latitude, to compare with previous findings, then by considering a more realistic thermal field with spatio-temporal variations. We underline the effect of such thermal field variations on the chemical composition. Finally, we will compare our results with the Cassini/CIRS observations.

2. Seasonal modeling of the photochemistry

2.1. Introduction

The amount of solar radiation striking the top of the atmosphere at a given latitude varies with seasons because of Saturn's obliquity and eccentricity. Atmospheric heating occurs through methane near-IR absorption of this radiation. Cooling is preponderant in the mid-IR range, mainly through emissions from acetylene, ethane, and, to a lesser extent, methane (Yelle et al., 2001). These IR-emissions increase with increasing atmospheric temperatures and/or abundances of these compounds. Therefore, the temperature field, as a function of altitude and latitude, mostly depends on the seasonal distribution of these species and on their response to the seasonally varying insolation.

Methane, which is generally assumed to be well-mixed in Saturn's atmosphere (see e.g., Fletcher et al., 2009) and optically thick in its IR bands, can be used as a thermometer to constrain the thermal field (Greathouse et al., 2005). Asymmetries in Saturn's atmospheric temperatures have been observed as a function of season, from Voyager (Pirraglia et al., 1981; Hanel et al., 1981, 1982; Conrath and Pirraglia, 1983; Courtin et al., 1984) and ground-based observations (e.g., Gillett and Orton, 1975; Rieke, 1975; Tokunaga et al., 1978; Gezari et al., 1989; Ollivier et al., 2000a; Greathouse et al., 2005). These observations have been reproduced in an approximate sense by radiative transfer model predictions (Cess and Caldwell, 1979; Bézard et al., 1984; Bézard and Gautier, 1985).

The Cassini spacecraft arrived in Saturn's system in July 2004, shortly after its northern winter solstice (see Fig. 1). It has provided full-coverage of the temperatures for the upper troposphere and stratosphere ever since. It has given us the opportunity to observe seasonal changes in the temperature field for over 10 years. For instance, the North/South thermal asymmetry at the northern winter solstice has been observed: the southern hemisphere was experiencing summer and was found warmer than the northern one (Flasar et al., 2005; Howett et al., 2007; Fletcher et al., 2007). Subsequently, Cassini observed how the winter hemisphere evolves when emerging from the shadow of the rings and how the summer hemisphere cools down when approaching equinox (Fletcher et al., 2010; Sinclair et al., 2013).

The main driver for atmospheric chemistry comes from solar UV radiation. This radiation initiates a complex chemistry through methane photolysis leading to the production of highly reactive chemical radicals. The kinetics of the chemical reactions triggered by photolysis generally have a thermal dependence that can impact the overall production/loss rates of atmospheric constituents over the course of Saturn's long seasons.

Since we want to evaluate the atmospheric chemical response to seasonal forcing in terms of solar radiation and atmospheric temperatures, we thus compare the results of our model obtained in two different cases:

- The temperature field consists of a single profile applied to all latitudes and seasons in a similar way to previous 1D studies. This study case will be denoted (U)
- The temperature field is vertically, latitudinally and seasonally variable. This study case will be denoted (S)

We stress again that the latitudes are not connected in the following study, i.e., the meridional transport is set to zero, so as to better quantify the effects of a seasonally variable temperature field on the distribution of chemical species. We defer the study of meridional transport to a forthcoming paper.

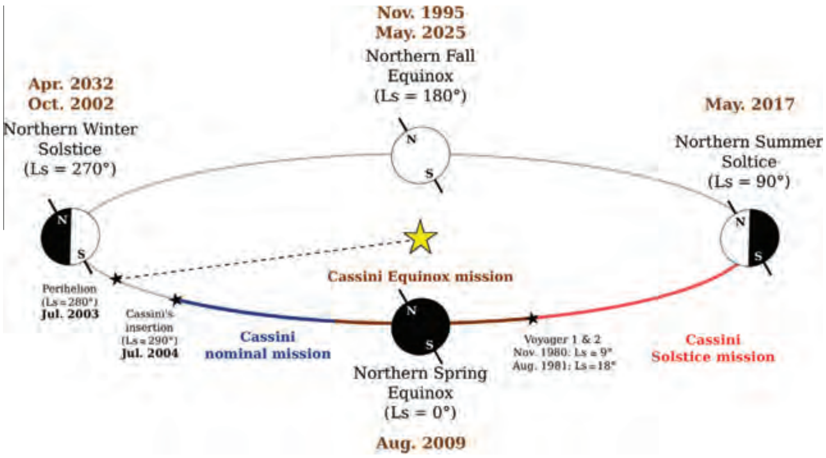

Fig. 1. Overview of Saturn's seasons. The position of Saturn on its orbit is defined by its heliocentric longitude (L_s). $L_s = 0°, L_s = 90°, L_s = 180°$ and $L_s = 270°$ correspond to Saturn's northern vernal equinox, summer solstice, autumnal equinox and winter solstice, respectively. The Cassini orbital insertion around Saturn occurred on July 1, 2004, shortly after the northern winter solstice (October 2002) and Saturn's perihelion (July 2003). Cassini's nominal, equinox and solstice missions are indicated. Voyager missions 1 and 2 flew by Saturn system on November 12, 1980 and on August 26, 1981, respectively, for their closest encounters.

2.2. Accounting for Saturn's eccentric orbit

Due to Kepler's second law, Saturn's southern summer is shorter and hotter than the northern one, as Saturn reaches its perihelion shortly after the southern summer solstice (see Fig. 2). In the present model, Saturn's elliptic orbit is sampled using a regularly spaced heliocentric longitude grid of 10°. From one orbital point to the next one, the integration time of the photochemical model is computed from the Kepler equation and Saturn's true anomaly. The true anomaly and heliocentric longitude are similar quantities, only differing by their relative origin, the former one being Saturn's perihelion whereas the latter being the Vernal equinox. The offset position in heliocentric longitude of Saturn's perihelion was set at 280.077° (Guerlet et al., 2014), a value based on J2000 parameters. Similarly to Moses and Greathouse (2005), integration over several orbits was needed for the simulations to converge down to the 100 mbar pressure level. Although the eddy diffusion coefficient profile as a function pressure was identical in every simulation, differences were found in the number of orbits required for convergence in the simulations depending on the thermal field. We will explain the reasons for these differences in Section 4.2.

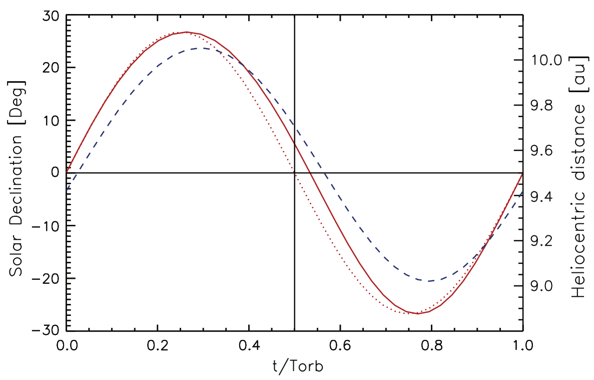

Fig. 2. Variation of solar declination (left scale) as a function of the orbital fraction, assuming Saturn's eccentricity (red solid line) and null eccentricity (red dotted line). The origin of the orbital fraction is taken at the northern spring equinox. The corresponding variation of the heliocentric distance (dashed line, right scale) is also plotted. Saturn's perihelion occurs shortly after the northern winter solstice. The solid vertical line at $t/T_{orb} = 0.5$ denotes the moment when the planet has spent half of its orbital period. At this point the subsolar point is still on the northern hemisphere, due to Saturn eccentricity. (For interpretation of the references to color in this figure legend, the reader is referred to the web version of this article.)

The variation of the solar declination as a function of the orbital fraction, starting from vernal equinox, is displayed in Fig. 2. As Saturn's perihelion occurs shortly after the southern summer solstice, the orbital fraction during which the subsolar point is on the northern hemisphere is longer than the opposite one. This is shown by the solid curve being shifted to the right, at orbital fraction of 0.5, with respect to the circular case (dotted line).

2.3. Temperature field

2.3.1. Spatially uniform thermal profile

In our first study case, the temperatures over the planet only vary with altitude and are constant with time and latitude, consistent with Moses and Greathouse (2005). We have taken the thermal profile that was used to obtain the reduced chemical scheme (Dobrijevic et al., 2011) we employ in our model. The temperatures below the 10^{-5} mbar pressure level come from a retrieval performed by Fouchet et al. (2008) on Cassini/CIRS data observed at a planetographic latitude of 20°S. Extrapolation to the upper stratosphere has been made using data from Smith et al. (1983) (see Fig. 4). This thermal profile is presented in Fig. 4. In what follows, we will refer to this case as the "spatially uniform" (U) temperature field case.

2.3.2. Seasonally variable thermal field

The second temperature field we considered comes from the seasonal radiative climate model of Greathouse et al. (2008), which has already been compared to Cassini/CIRS observations (Fletcher et al., 2010). This radiative transfer model takes into account heating and cooling from Saturn's major atmospheric compounds, i.e., CH_4, C_2H_2, and C_2H_6, as well as seasonal variation of Saturn's orbital parameters, i.e., solar declination, heliocentric distance and eccentricity. It also includes ring shadowing and accounts for Saturn's oblate shape. In this second study case, the temperature varies with altitude, latitude and time. This case will be referred to as the "seasonal" (S) temperature field case.

The seasonal thermal field used in this paper is shown in Fig. 3 as a function of planetocentric latitudes and heliocentric longitudes, and is presented for two pressure levels: 0.1 mbar and 10 mbar. Hereafter, all quoted latitudes are planetocentric, if not otherwise specified. The North–South asymmetry during the summer is caused by Saturn's eccentricity. The effects of ring shadowing are clearly observed at 0.1 mbar, around the solstices between 0° and 40° planetocentric latitude in the winter hemispheres. Time-lag between temperatures and seasons, due to the atmospheric thermal-inertia, can be seen at 10 mbar by the difference in temperature profile at 0.1 and 10 mbar. The thermal field has been computed by taking, as a first guess, the CH_4, C_2H_2 and C_2H_6 vertical distributions observed by Cassini (Guerlet et al., 2009) at planetographic latitude of 45°S and held fixed with time.

The temperature map predicted from the radiative climate model is calculated within the pressure range from 500 mbar to 10^{-6} mbar (Fletcher et al., 2010; Greathouse et al., 2008). Although the seasonal model of Greathouse et al. (2008) extends down to 500 mbar, temperatures are only accurate to 10 mbar as this model was created primarily to model the stratosphere. At lower altitudes, the model lacks aerosol absorption and scattering and convective adjustment. Due to this lack of aerosols, the tropospheric temperatures are lower by 5–15 K than measured by Cassini. We note this discrepancy, but are focused on understanding effect of temperature on stratospheric photochemistry occur at altitudes above the 10 mbar level where the physics are self consistent. Below the 500 mbar level we extrapolate the temperature assuming a dry adiabatic lapse rate, using a specific heat of c_p = 10,658 J kg^{-1} K^{-1} (Irwin, 2006) and a latitude-dependent gravity field (see Supplementary Materials of Guerlet et al., 2014). Above 10^{-3} mbar, where non-LTE effects dominate, the temperature was held constant, and no thermosphere is assumed above the stratosphere in this model. The lowest pressure level in our grid is set in order to ensure that each monochromatic optical depth is smaller than 1 in the UV at the top of the atmosphere. Fig. 4 displays the resulting temperature profiles at 4 latitudes: 80°S (upper-left panel), 60°S (upper-right panel), 40°S (lower left panel) and the equator (lower right panel). The colored solid lines represent the atmospheric temperatures inferred from the radiative climate model at solstices and equinoxes and the reconstruction procedure described above.

2.3.3. Thermal evolution

The first case studied in this paper, namely the spatially uniform thermal field does not require special care on how the pressure–altitude background is treated, as it remains constant all along the year. However, when the temperature changes, i.e., in the case of a seasonally variable thermal field, the pressure–altitude background also changes and has to be handled carefully.

Two ways of dealing with changes in the atmospheric pressure–temperature background in photochemical modeling exist. Either the altitude grid is held constant and the pressure varies with temperature, or the pressure grid is held constant and the altitude grid is free to contract or expand (e.g., Agúndez et al., 2014). Since the two approaches are self-consistent, we have chosen to hold the altitude grid constant and let the pressure grid vary with temperature.

This choice has been made to allow two latitudinally-contiguous numerical cells to exchange material through their common boundary, for future 2D-modeling including circulation and meridional advection.

The altitude-temperature grid at all latitudes and heliocentric longitudes is built assuming hydrostatic equilibrium. Variations in scale height due to Saturn's latitudinally and altitudinally-dependent gravity field and variations in the mean molecular mass in the upper atmosphere due to molecular diffusion are included when solving the hydrostatic equilibrium equation. The latitudinal-dependency adopted here follows the prescription of Guerlet et al. (2014). We have made sure that the pressure–temperature background using this prescription is consistent with the latitudinally dependent gravitational field published by Lindal et al. (1985) and combined with the Voyager 2 zonal wind measurements (Smith et al., 1982; Ingersoll and Pollard, 1982).

The effect on the pressure–altitude grid can be large as shown in Fig. 5, which presents this grid for 80°N at the equinoxes and solstices. Solid and dashed lines respectively represent this grid when the latitudinally-dependent gravity is included and when considering a constant surface gravity, set to the equatorial one. The pressure–altitude grid of the uniform model (see Section 2.3.1) is also shown (black solid line) for comparison. Differential surface gravity due to Saturn's high rotation rate results in more contracted atmospheric columns at polar latitudes. Hence, at the same altitude level, the pressure is lower at the poles relative to the equator when considering variable surface gravity. At a given latitude, the column also expands or contracts with temperature as shown in Fig. 5. This example at 80°N is extreme as the amplitude of the temperature variation with season is maximum at polar latitudes. The seasonal variation of the pressure–altitude grid is damped toward the equator, as the seasonal thermal gradient is reduced in this region.

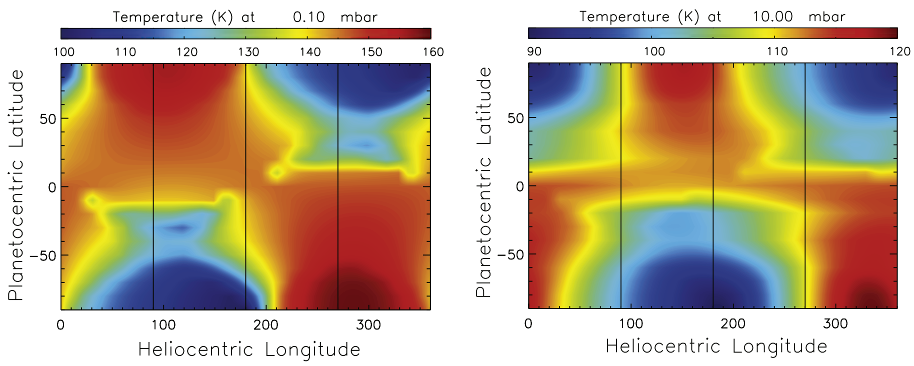

Fig. 3. Seasonal temperature field inferred from the radiative climate model of Greathouse et al. (2008) as a function of planetocentric latitude and heliocentric longitude. The temperature variation at 0.1 mbar is twice as large as that at 10 mbar due to the increase in thermal inertia with depth in the atmosphere (note the color range is stretched differently for the two plots). Left panel: Temperatures at 0.1 mbar. Right panel: Temperatures at 10 mbar. (For interpretation of the references to color in this figure legend, the reader is referred to the web version of this article.)

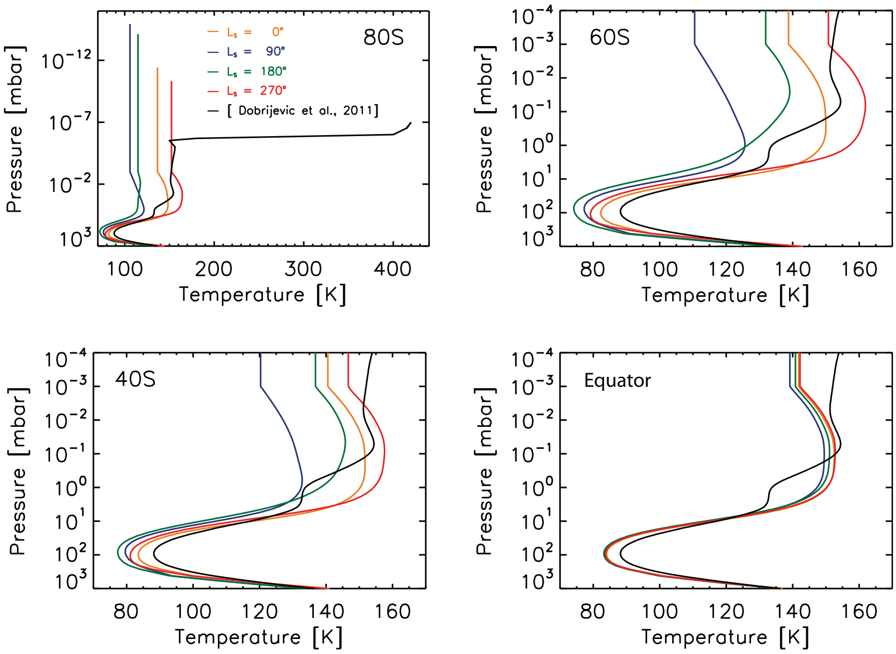

Fig. 4. Temperature profiles used in this work as a function of pressure. The colored lines depict the seasonally variable thermal field (S) predicted from the radiative climate model at the solstices and equinoxes, for 4 latitudes: 80°S (upper-left panel), 60°S (upper-right panel), 40°S (lower left panel) and the equator (lower left panel). $L_s = 0°$, 90°, 180° and 270° correspond to northern fall equinox, summer solstice, spring equinox and winter solstice, respectively (see Fig. 1). The black solid lines display the spatially uniform thermal field (U) we consider in this work. This profile comes from Cassini/CIRS observations (Fouchet et al., 2008) and Voyager 2 observations (Smith et al., 1983) (see text for details). (For interpretation of the references to color in this figure legend, the reader is referred to the web version of this article.)

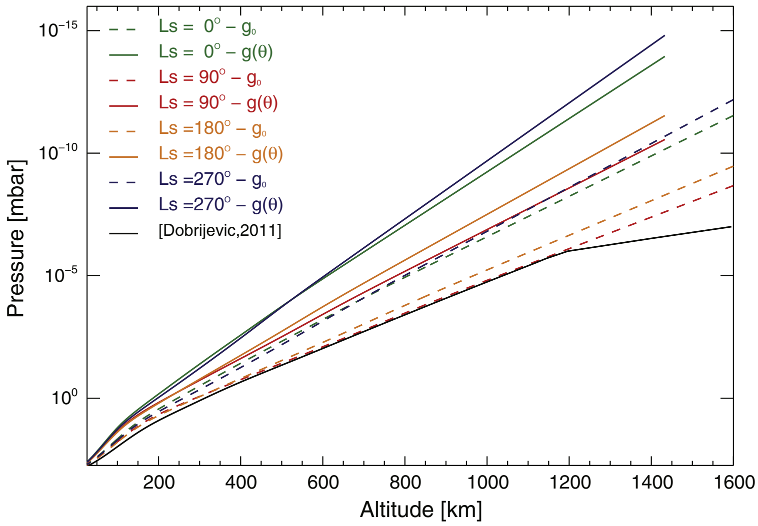

Fig. 5. Pressure–altitude grid at 80°N for the solstices and equinoxes, assuming a constant surface gravity (dashed colored lines) and a latitudinally-variable surface gravity (solid colored lines). $L_s = 0°$, 90°, 180° and 270° correspond to northern fall equinox, summer solstice, spring equinox and winter solstice, respectively (see Fig. 1). 0 km is equal to the 1 bar level. The black solid line represents the pressure–altitude grid of the uniform temperature profile. (For interpretation of the references to color in this figure legend, the reader is referred to the web version of this article.)

In the present paper, we have chosen to work with a common altitude grid for all latitudes and seasons that start at a common origin ($z = 0$ km and $P = 1$ bar). Above that origin, the pressure grid expands or contracts according to temperature changes. The mole fraction vertical profiles of the model species are expressed as a function of pressure and thus follow the same contraction/expansion as the pressure grid. Therefore, each time the temperature/pressure grid changes, the mole fraction profiles are interpolated onto the new pressure grid.

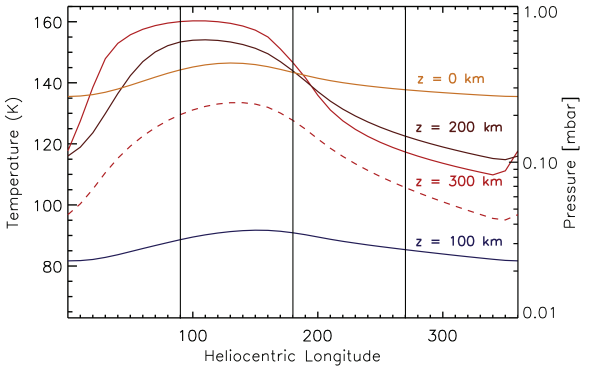

Fig. 6. Seasonal evolution of temperature (left scale, solid lines) and pressure (right scale, dashed line) at altitudes of 300 km (red lines), 200 km (brown), 100 km (blue) and 0 km (orange). The quantities are presented for a planetocentric latitude of 80°N, where the variations are most noticeable. The black solid lines indicate the position of the solstices and equinoxes (see Fig. 1). (For interpretation of the references to color in this figure legend, the reader is referred to the web version of this article.)

It is instructive to represent the seasonal evolution of the temperature and pressure at a given latitude for a few altitude levels (see Fig. 6 for an illustration at 80°N). When the temperature rises, the atmospheric column expands, and the associated pressure at the same altitude increases. It should be noted that temperature and pressure are not totally in phase, as the pressure at a given altitude depends on the thermodynamical conditions of the altitude levels underneath. Therefore the temperature at a few altitude levels below the considered altitude are presented on the same figure. We note that the increase in the pressure at 300 km is in phase with the temperature changes at altitude levels below that level.

3. Latitudinally and seasonally variable 1D models

3.1. General description

In an atmosphere, the spatio-temporal distribution of each species' number density is governed by the continuity-transport equation, that is:

$$\frac{\partial n_i}{\partial t} = P_i - n_i L_i - \nabla \cdot (\Phi_i) \tag{1}$$

where n_i ($\mathrm{cm^{-3}}$) is the number density, P_i ($\mathrm{cm^{-3}\,s^{-1}}$) the (photo) chemical production rate, L_i ($\mathrm{s^{-1}}$) the (photo) chemical loss rate and Φ_i ($\mathrm{cm^{-2}\,s^{-1}}$) is the particle flux due to transport. Longitudinal mixing timescales appear to be relatively short in Jupiter's atmosphere (e.g., Banfield et al., 1996) and deviations from the mean zonal temperatures are limited (Flasar et al., 2004). We assume the situation is similar at Saturn and we thus do not consider longitudinal variability in this study. The continuity equation is then solved on a 2D altitude-latitude spherical grid. We use a 13 km altitude grid resolution, in order to have at least 3 altitudinal numerical cells per scale height at all times throughout the year. The planet radius considered here is Saturn's mean radius, R = 58,210 km (Guillot, 2005), which corresponds to the altitude level z = 0 km. The flux Φ_i includes transport processes in the vertical and the meridional directions.

Taking these mixing processes into account at all scales and in detail would require a full hydrodynamical model, which is beyond the scope of this work. In our model, the physical processes that are accounted for through the vertical flux Φ_i^z, are eddy diffusion, molecular diffusion and vertical advection. This flux is expressed as:

$$\Phi_i^z = -D_i n_i \left(\frac{1}{y_i}\frac{\partial y_i}{\partial z} + \frac{1}{H_i} - \frac{1}{H}\right) - K_{zz} n_i \left(\frac{1}{y_i}\frac{\partial y_i}{\partial z}\right) + v_i^z n_i \tag{2}$$

where y_i is the mole fraction of species i, defined as the ratio between the number density of i over the total number density. H_i and H (cm) are respectively the specific and the mean density scale height, D_i ($\mathrm{cm^2\,s^{-1}}$) the molecular diffusion coefficient, K_{zz} ($\mathrm{cm^2\,s^{-1}}$) the vertical eddy diffusion coefficient and v_i^z ($\mathrm{cm\,s^{-1}}$) the vertical wind. The numerical scheme used in this study is similar to the one used by Agúndez et al. (2014) in their pseudo-2D photochemical model except that we use an upwind scheme to treat the advective part of the molecular diffusion (Godunov, 1959). The meridional flux Φ_i^θ is set to zero for the current study.

The vertical eddy diffusion coefficient K_{zz} is a free parameter in the model to account for mixing processes caused by dynamics occurring at every scale. This parameter may vary with altitude and latitude, but our knowledge for giant planet stratospheres is very limited (see for instance Moreno et al., 2003 and Liang et al., 2005). This coefficient is related to the small-scale waves and is therefore expected to be influenced by the atmospheric number density (Lindzen, 1971, 1981). Consequently, 2D/3D models will probably have to account for its latitudinal and longitudinal variability. In this study, we consider that K_{zz} is fixed with respect to the pressure coordinate. Due to the lack of constraint on that parameter, we consider this does not vary with latitude. The reduced chemical scheme we use has been obtained using the K_{zz} profile of Dobrijevic et al. (2011). Therefore, we consistently take their K_{zz}. The molecular diffusion coefficient we adopt is based on experimental measurements of binary gas diffusion coefficients (Fuller et al., 1966, 1969). As a first step in this study, we set K_{yy}, v^z and v^θ to zero. These parameters will be studied in a forthcoming paper, either by trying to fit them from the observations or by testing outputs of the yet-to-be-finalized GCM of Guerlet et al. (2014).

At the lower boundary of the model (i.e., 1 bar), the H_2 and He mole fractions are set to 0.8773 and 0.118, respectively (Conrath and Gautier, 2000). The methane mole fraction was set to 4.7×10^{-3} according to recent Cassini/CIRS observations (Fletcher et al., 2009). At this boundary, all other compounds diffuse down to the lower troposphere at their maximum diffusion velocity, i.e., $v = -K_{zz}(0)/H(0)$. At the upper boundary of the model, all fluxes are set to zero except for atomic hydrogen. Following Moses et al. (2005), we set its influx to $\Phi_H = 1.0 \times 10^8\ \mathrm{cm^{-2}\,s^{-1}}$ at all latitudes.

3.2. Chemical scheme

In typical 1D photochemical models, the chemical schemes contain as many reactions as possible, i.e., usually hundreds, and numerous species. This makes it extremely difficult for current computers to solve Eq. (1) in a reasonable time when extending such models to 2D or 3D. Dobrijevic et al. (2011) have developed an objective methodology to reproduce the chemical processes for a subset of compounds of interest (usually observed compounds) with a limited number of reactions. These are extracted from a more complete chemical scheme by running a 1D photochemical model and applying propagation of uncertainties on chemical rates and a global sensitivity analysis.

Uncertainties in the chemical rate constants are a critical source of uncertainty in photochemical model predictions (Dobrijevic and Parisot, 1998), as chemical schemes generally include tens to hundreds of chemical compounds, non-linearly coupled in even more reactions. Propagating uncertainties on each chemical reaction, using a Monte Carlo procedure for instance, can lead to several orders of magnitude in uncertainty (Dobrijevic et al., 2003). By computing correlations between reaction rate uncertainties and photochemical model predictions, Dobrijevic et al. (2010a,b)

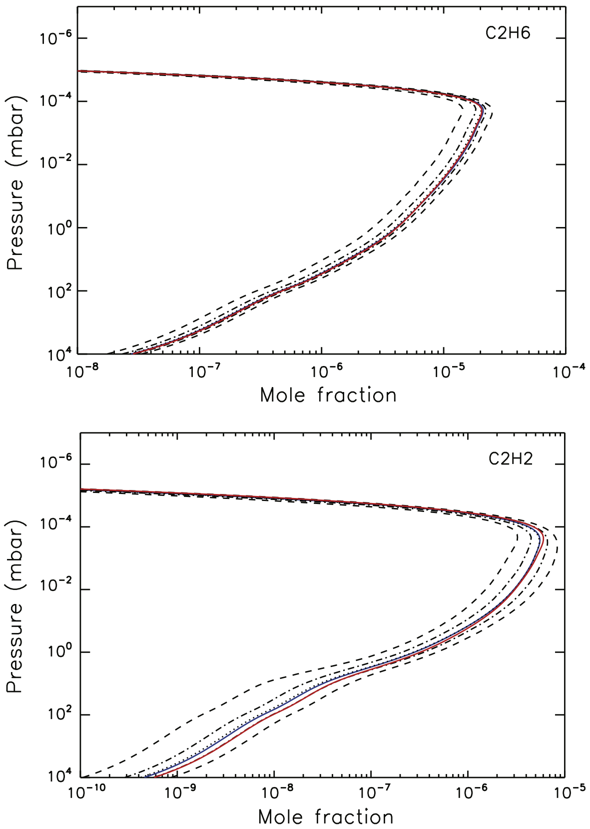

Fig. 7. Red solid line: C_2H_6 (top panel) and C_2H_2 (botom panel) vertical profile with the reduced chemical scheme. Blue line: nominal vertical profile obtained using the initial chemical scheme. Black dotted line: median profile of the full-scheme distribution. Black dashed-dotted lines: 5th and 15th 20-quantiles of the full-scheme distribution. Black dashed lines: 1st and 19th 20-quantiles of the full-scheme distribution. (For interpretation of the references to color in this figure legend, the reader is referred to the web version of this article.)

Table 1
List of the 22 chemical compounds included in the scheme.

He; H; H_2
CH; C; $^1CH_2$; $^3CH_2$; CH_3; CH_4
C_2H; C_2H_2; C_2H_3; C_2H_4; C_2H_5; C_2H_6
O^3P; O^1D; OH; H_2O
CO; CO_2; H_2CO

developed a global sensitivity analysis methodology to identify key reactions in chemical schemes. These reactions have a major impact on the results, either because their uncertainty is intrinsically high, or because they significantly contribute in the production/loss terms of the compound of interest (or one of the compounds related to it).

A reaction that has a low degree of significance means that changing its rate constant (within its uncertainty range) does not significantly change the results of the model, or well inside the model error bars. Building a reduced network then consists in removing reactions, and thus compounds once they are no longer linked by reactions, that have a very low degree of significance. The results stay very close to the median profile of the full chemical scheme for the remaining compounds.

A reduced chemical scheme is valid when it agrees with the full chemical scheme, given the uncertainties of each chemical compound profile. The initial scheme we consider includes 124 compounds, 1141 reactions and 172 photodissociation processes and comes from Loison et al. (2015). The compounds we have selected to build the reduced chemical scheme are the ones monitored by Cassini/CIRS and most relevant regarding stratospheric heating and cooling: CH_4, C_2H_2, and C_2H_6 (Guerlet et al., 2009; Sinclair et al., 2013). We based our reduction scheme on the model validation performed for Saturn's hydrocarbons by Cavalié et al. (2015). C_2H_2, and C_2H_6 vertical profiles using the reduced chemical scheme are in good agreement with the full chemical scheme results (Fig. 7). The reduced scheme produces vertical profiles that are within the 5th and 15th of the full-scheme 20-quantiles distribution for C_2H_6 at all pressure levels and for C_2H_2 above 10 mbar. Below 10 mbar, the C_2H_2 vertical profile is almost superimposed to the 15th 20-quantiles of the distribution.

Three main oxygen compounds have also been added to the reduced scheme which are present in Saturn's stratosphere (H_2O, CO, and CO_2) as ground work for a forthcoming paper on the spatial distribution of H_2O, following observations by Herschel (Hartogh et al., 2009, 2011). The oxygen species will not be used in the present study and will not be presented nor discussed any further. In the end, the reduced scheme used in the present study includes 22 compounds, 33 reactions, and 24 photodissociations, listed in Table 1. Such a reduced chemical scheme enables extending photochemical computations to 2D/3D. The chemical reaction rates and the photochemical reactions of the reduced chemical network are respectively listed in Table 2 and Table 3.

3.3. Actinic flux

The knowledge of the solar UV flux at any latitude/altitude/season is required to properly compute photodissociation coefficients. We use a full-3D spherical line-by-line radiative transfer model, improved over the model initially developed by Brillet et al. (1996), to account for the attenuation of solar UV in the atmosphere. It now accounts for the full 3D distribution of absorbers instead of assuming vertically homogeneous distributions in latitude and longitude as in Brillet et al. (1996). However, as stated previously, we consider here a zonally mixed atmosphere and limit variability to altitude and latitude. Absorption is formally calculated by the exact computation of the optical path. Rayleigh diffusion is also accounted for using single photon ray tracing in a Monte Carlo procedure. The wavelengths considered here range from 10 nm to 250 nm, because the hydrocarbons considered in this study do not substantially absorb beyond these limits. The radiative transfer procedure uses the altitude-latitude absorption and diffusion coefficients, extrapolated onto a 3D atmosphere assuming zonal homogeneity. Correspondence between subsolar and planetocentric coordinates is then made assuming Saturn's orbital parameters at the moment of the Kronian year, i.e., when the altitude-latitude-longitude actinic flux needs to be computed. Saturn's ellipsoidal shape is not taken into account, while the elliptical orbit is. The elliptical orbit causes a peak in actinic flux during southern summer.

The daily-averaged actinic flux (W m^{-2}) at the top of the atmosphere is shown in Fig. 8. Actinic flux, unlike solar insolation, does not refer to any specifically oriented collecting surface. This is a fundamental quantity for photochemistry, since we consider that molecules do not preferentially absorb radiation with respect to any particular orientation in space. This quantity is therefore not corrected by the cosine of the incident angle, unlike insolation. From this 3D actinic flux, the daily-averaged insolation is computed. As a comparison with Figs. 8 and 9 presents the daily-averaged solar insolation (W m^{-2}) received by a horizontal unit surface in Saturn's atmosphere. Following Moses and Greathouse (2005), we use a solar constant of 14.97 W m^{-2} for

Table 2
List of reactions of the reduced network (references can be found in Loison et al. (2015)). $k(T) = \alpha \times (T/300)^{\beta} \times \exp(-\gamma/T)$ in cm^3 molecule^{-1} s^{-1} or cm^6 molecule^{-1} s^{-1}. $k_{adduct} = (k_0[\mathrm{M}]F + k_r)k_\infty / k_0[\mathrm{M}] + k_\infty$ with $\log(F) = \log(F_c)/1 + [\log(k_0[\mathrm{M}] + k_{capture})/N]^2$, $F_c = 0.60$ and $N = 1$. Please refer to Hébrard et al. (2013) for details about the semi-empirical model.

	Reactions		Rate coefficients
R1	$H + CH$	$\rightarrow C + H_2$	$1.24 \times 10^{-10} \times (T/300)^{0.26}$
R2	$H + {}^3CH_2$	$\rightarrow CH + H_2$	$2.2 \times 10^{-10} \times (T/300)^{0.32}$
R3	$H + {}^3CH_2$	$\rightarrow CH_3$	$k_0 = 3.1 \times 10^{-30} \times \exp(457/T)$
			$k_\infty = 1.5 \times 10^{-10}$
			$k_r = 0$
R4	$H + CH_3$	$\rightarrow CH_4$	$k_0 = 8.9 \times 10^{-29} \times (T/300)^{-1.8} \times \exp(-31.8/T)$
			$k_\infty = 3.2 \times 10^{-10} \times (T/300)^{0.133} \times \exp(-2.54/T)$
			$k_r = 1.31 \times 10^{-16} \times (T/300)^{-1.29} \times \exp(19.6/T)$
R5	$H + C_2H_2$	$\rightarrow C_2H_3$	$k_0 = 2.0 \times 10^{-30} \times (T/300)^{-1.07} \times \exp(-83.8/T)$
			$k_\infty = 1.17 \times 10^{-13} \times (T/300)^{8.41} \times \exp(-359/T)$
			$k_r = 0$
R6	$H + C_2H_3$	$\rightarrow C_2H_2 + H_2$	6.0×10^{-11}
R7	$H + C_2H_3$	$\rightarrow C_2H_4$	$k_0 = 3.47 \times 10^{-27} \times (T/300)^{-1.3}$
			$k_\infty = 1.0 \times 10^{-10}$
			$k_r = 0$
R8	$H + C_2H_4$	$\rightarrow C_2H_5$	$k_0 = 1.0 \times 10^{-29} \times (T/300)^{-1.51} \times \exp(-72.9/T)$
			$k_\infty = 6.07 \times 10^{-13} \times (T/300)^{-5.31} \times \exp(174/T)$
			$k_r = 0$
R9	$H + C_2H_5$	$\rightarrow C_2H_6$	$k_0 = 2.0 \times 10^{-28} \times (T/300)^{-1.5}$
			$k_\infty = 1.07 \times 10^{-10}$
			$k_r = 0$
R10	$H + C_2H_5$	$\rightarrow CH_3 + CH_3$	$k_0 = k_\infty - k_{adduct}$
R11	$C + H_2$	$\rightarrow {}^3CH_2$	$k_0 = 7.0 \times 10^{-32} \times (T/300)^{-1.5}$
			$k_\infty = 2.06 \times 10^{-11} \times \exp(-57/T)$
			$k_r = 0$
R12	$CH + H_2$	$\rightarrow CH_3$	$k_0 = 6.2 \times 10^{-30} \times (T/300)^{-1.6}$
			$k_\infty = 1.6 \times 10^{-10} \times (T/300)^{-0.08}$
			$k_r = 0$
R13	$CH + CH_4$	$\rightarrow C_2H_4 + H$	$1.05 \times 10^{-10} \times (T/300)^{-1.04} \times \exp(-36.1/T)$
R14	${}^1CH_2 + H_2$	$\rightarrow {}^3CH_2 + H_2$	$1.6 \times 10^{-11} \times (T/300)^{-0.9}$
R15	${}^1CH_2 + H_2$	$\rightarrow CH_3 + H$	$8.8 \times 10^{-11} \times (T/300)^{0.35}$
R16	${}^3CH_2 + H_2$	$\rightarrow CH_3 + H$	$8.0 \times 10^{-12} \times \exp(-4500/T)$
R17	${}^3CH_2 + CH_3$	$\rightarrow C_2H_4 + H$	1.0×10^{-10}
R18	${}^3CH_2 + C_2H_3$	$\rightarrow C_2H_2 + CH_3$	3.0×10^{-11}
R19	${}^3CH_2 + C_2H_5$	$\rightarrow C_2H_4 + CH_3$	3.0×10^{-11}
R20	$CH_3 + CH_3$	$\rightarrow C_2H_6$	$k_0 = 1.8 \times 10^{-26} \times (T/300)^{-3.77} \times \exp(-61.6/T)$
			$k_\infty = 6.8 \times 10^{-11} \times (T/300)^{-0.359} \times \exp(-30.2/T)$
			$k_r = 0$
R21	$C_2H + H_2$	$\rightarrow C_2H_2 + H$	$1.2 \times 10^{-11} \times \exp(-998/T)$
R22	$C_2H + CH_4$	$\rightarrow C_2H_2 + CH_3$	$1.2 \times 10^{-11} \times \exp(-491/T)$
R23	$C_2H_3 + H_2$	$\rightarrow C_2H_4 + H$	$3.45 \times 10^{-14} \times (T/300)^{2.56} \times \exp(-2530/T)$
R24	$C_2H_3 + CH_4$	$\rightarrow C_2H_4 + CH_3$	$2.13 \times 10^{-14} \times (T/300)^{4.02} \times \exp(-2750/T)$
R25	$O(^3P) + CH_3$	$\rightarrow CO + H_2 + H$	2.9×10^{-11}
R26	$O(^3P) + CH_3$	$\rightarrow H_2CO + H$	1.1×10^{-10}
R27	$O(^3P) + C_2H_5$	$\rightarrow OH + C_2H_4$	3.0×10^{-11}
R28	$O(^1D) + H_2$	$\rightarrow OH + H$	1.1×10^{-10}
R29	$OH + H_2$	$\rightarrow H_2O + H$	$2.8 \times 10^{-12} \times \exp(-1800/T)$
R30	$OH + CH_3$	$\rightarrow H_2O + {}^1CH_2$	3.2×10^{-11}
R31	$OH + CH_3$	$\rightarrow H_2CO + H_2$	8.0×10^{-12}
R32	$OH + CO$	$\rightarrow CO_2 + H$	1.3×10^{-13}
R33	$H_2CO + C$	$\rightarrow CO + {}^3CH_2$	4.0×10^{-10}

these calculations. In both figures, the effect of Saturn's elliptical orbit is obvious. Since Saturn reaches its perihelion shortly after the summer solstice, the amount of solar flux is more important at this time. The dark blue areas in the winter hemispheres indicate polar nights.

Ring shadowing effects due to the A–B–C rings and to the Cassini division are also included. Brinkman and McGregor (1979) and Bézard (1986) have first calculated ring shadowing in atmospheric models, however we adopt the prescription of Guerlet et al. (2014), which is more suited for implementation in our photochemical model. This method calculates whether or not a point on the planet at a given latitude and longitude is under the shadow of the rings. If this is the case, the solar flux at this point is reduced by the ring opacity. We adopt the normal opacity profile of the rings from Guerlet et al. (2014), which is based on more than 100 stellar occultations measured by the UVIS instrument aboard Cassini (Colwell et al., 2010). Finally, these normal opacities are corrected to account for the incidence angle of radiation over the rings. Diffusion effects from the ring are not included. We account for the latitudinal extent of the numerical cells in our calculations. Here we present results from simulations that use 10°-wide latitudinal cells. Therefore, the ring occultation is averaged over these 10°-wide cells. Each of

Table 3
Photodissocation processes (references can be found in Loison et al., 2015).

	Photodissociations	
R34	$OH + h\nu$	$\rightarrow O(^1D) + H$
R35	$H_2O + h\nu$	$\rightarrow H + OH$
R36		$\rightarrow H_2 + O(^1D)$
R37		$\rightarrow H + H + O(^3P)$
R38	$CO + h\nu$	$\rightarrow C + O(^3P)$
R39	$CO_2 + h\nu$	$\rightarrow C + O(^1D)$
R40		$\rightarrow CO + O(^3P)$
R41	$H_2 + h\nu$	$\rightarrow H + H$
R42	$CH_4 + h\nu$	$\rightarrow CH_3 + H$
R43		$\rightarrow {}^1CH_2 + H + H$
R44		$\rightarrow {}^1CH_2 + H2$
R45		$\rightarrow {}^3CH_2 + H + H$
R46		$\rightarrow CH + H_2 + H$
R47	$CH_3 + h\nu$	$\rightarrow {}^1CH_2 + H$
R48	$C_2H_2 + h\nu$	$\rightarrow C_2H + H$
R49	$C_2H_3 + h\nu$	$\rightarrow C_2H_2 + H$
R50	$C_2H_4 + h\nu$	$\rightarrow C_2H_2 + H_2$
R51		$\rightarrow C_2H_2 + H + H$
R52		$\rightarrow C_2H_3 + H$
R53	$C_2H_6 + h\nu$	$\rightarrow C_2H_4 + H_2$
R54		$\rightarrow C_2H_4 + H + H$
R55		$\rightarrow C_2H_2 + H_2 + H_2$
R56		$\rightarrow CH_4 + H_2 + H_2$
R57		$\rightarrow CH_3 + CH_3$

the 10°-wide cells have been sampled over 0.1°-wide sub-cell. The effect of ring shadowing can be seen at mid latitudes in the winter hemispheres in Figs. 8 and 9.

4. Results

In this section, we first present results from our photochemical model using the spatially uniform thermal field (U) described in Section 2.3.1 in order to compare with existing models (Moses and Greathouse, 2005). We detail the variability in hydrocarbon abundances as a function of altitude/latitude/time only due to the variation of the heliocentric distance of Saturn and of the latitude of the sub-solar point. Then, we give a brief overview of the influence of the rings on chemistry. Finally, we present the effect induced by the seasonal temperature field (S) and compare the results with the spatially uniform case. The interest here lies in the fact that we first present photochemical results using a simple test-case, i.e., a spatio-temporally uniform case previously studied (Moses and Greathouse, 2005), before adding more complexity by considering a more realistic thermal field.

4.1. Seasonal variability with the spatially uniform thermal field

We present here the results from seasonal simulations using the spatially uniform (U) temperature field, with an emphasis on

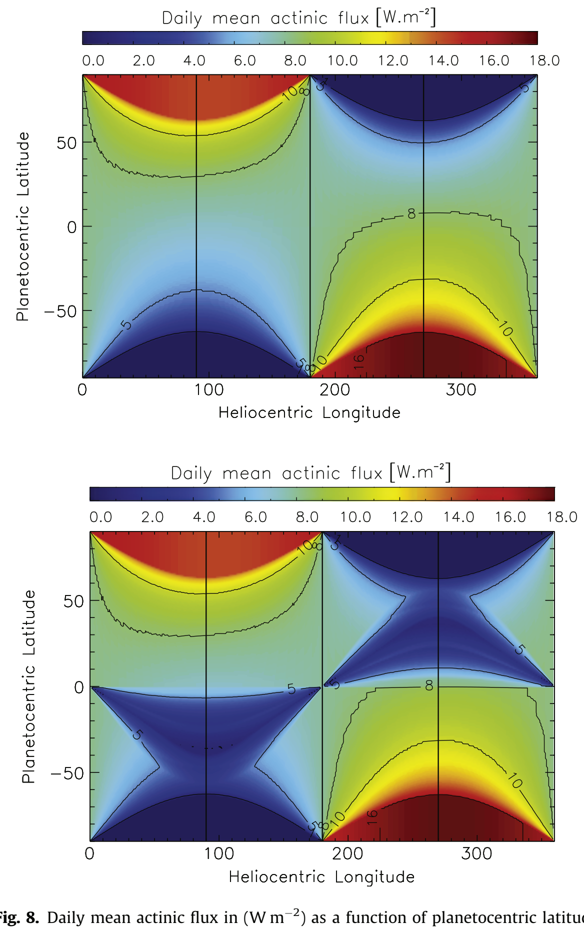

Fig. 8. Daily mean actinic flux in ($W\,m^{-2}$) as a function of planetocentric latitude and heliocentric longitude. Ring shadowing is included in the lower panel. The black solid lines indicate the position of the solstices and equinoxes (see Fig. 1). (For interpretation of the references to color in this figure legend, the reader is referred to the web version of this article.)

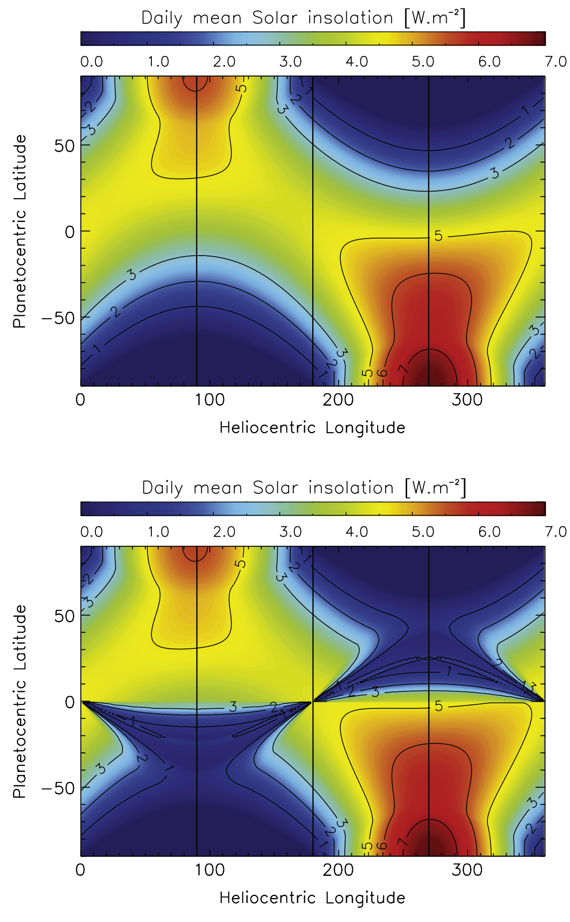

Fig. 9. Daily mean insolation in ($W\,m^{-2}$) as a function of planetocentric latitude and heliocentric longitude (i.e., seasons) received by a horizontal unit surface in Saturn's atmosphere. Ring shadowing is included in the lower panel. The black solid lines indicate the position of the solstices and equinoxes (see Fig. 1).

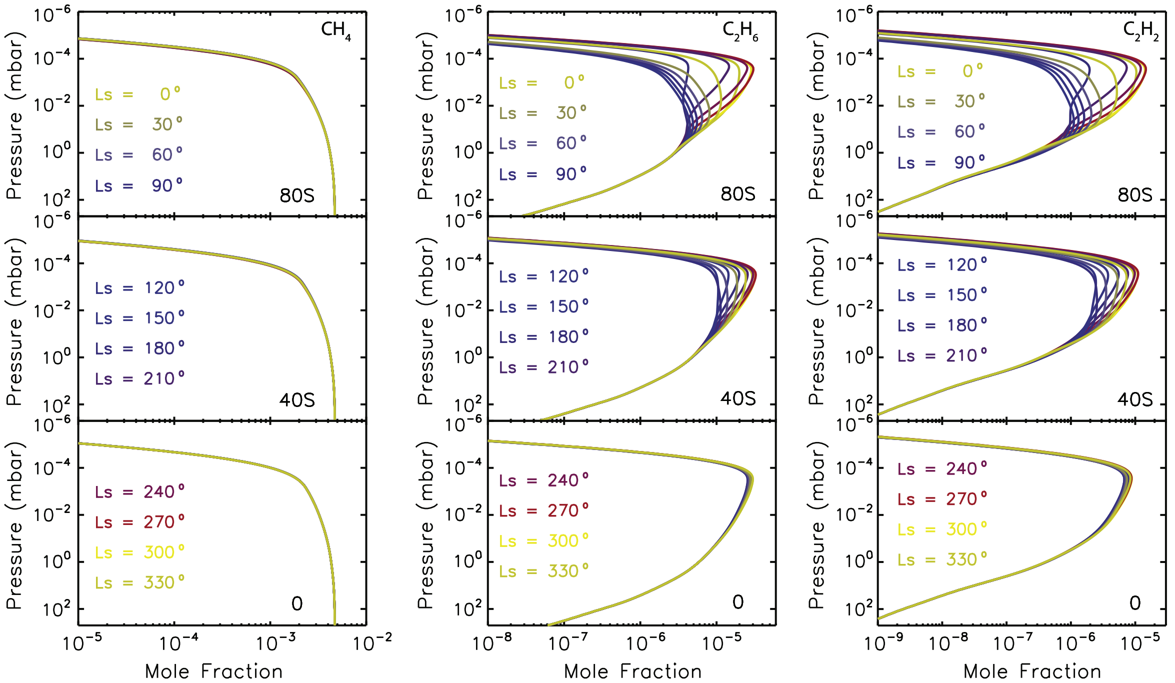

Fig. 10. Seasonal evolution of CH_4 (left), C_2H_6 (center) and C_2H_2 (right) vertical profiles computed for the whole Kronian year (360° in heliocentric longitude using a 30° step). Three latitudes are presented: 80°S (top), 40°S (middle) and the equator (bottom). CH_4 does not show any strong seasonal variability, even at high latitudes. Its shape is controlled by vertical mixing rather than photolysis (Romani and Atreya, 1988). The seasonal variability on C_2H_6 and C_2H_2 is clearly seen at low-pressure levels and high latitudes due to the large insolation variation at such latitudes over one Kronian year. The (U) thermal field has been used for these calculations.

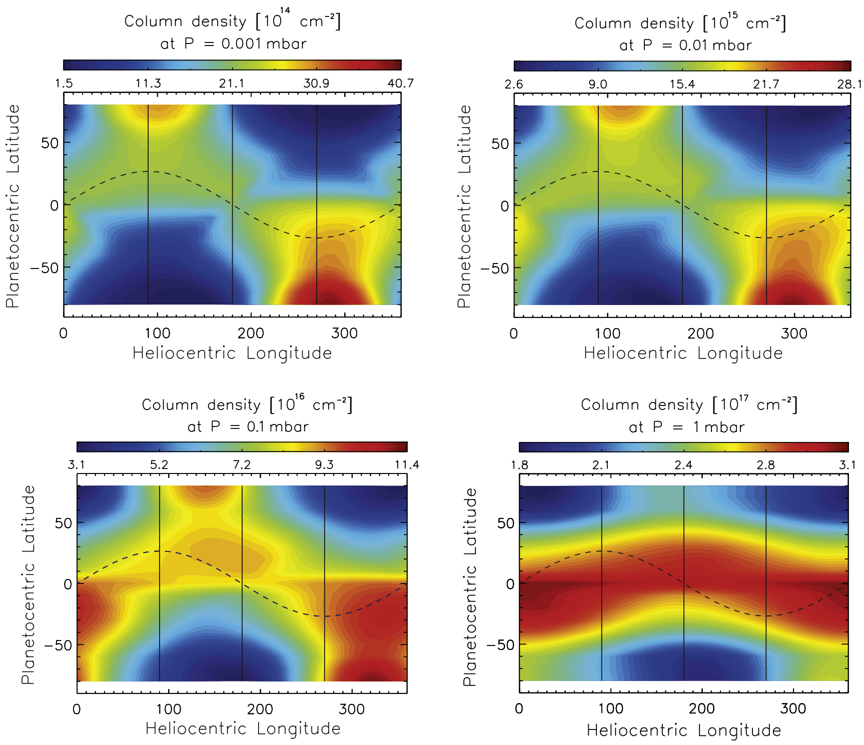

Fig. 11. C_2H_2 column density (cm^{-2}) above 10^{-3} mbar (top left), 10^{-2} mbar (top right), 0.1 mbar (bottom left), and 1 mbar (bottom right). Ring shadowing is clearly seen around the winter solstice in the winter hemisphere. The solid line indicate the solstices and equinoxes, while the dashed line indicates the position of the subsolar point along the year. The North–South asymmetry between the summer hemispheres is caused by Saturn's eccentricity, its perihelion occurring shortly after the southern summer solstice. In both summer hemispheres, after the summer solstice, the C_2H_2 column densities reach a maximum which is shifted in time with respect to the maximum insolation level, i.e., at the solstice itself.

methane, ethane and acetylene as they are the most important compounds with respect to the radiative heating/cooling of the atmosphere (Yelle et al., 2001).

4.1.1. Methane (CH_4), ethane (C_2H_6) and acetylene (C_2H_2)

The vertical profiles of CH_4, C_2H_6, and C_2H_2, using the spatially uniform temperature field, are displayed in Fig. 10.

CH_4 does not exhibit strong seasonal variations, as eddy mixing and molecular diffusion, rather than photolysis, are the major processes controlling the shape of its vertical distribution (Romani and Atreya, 1988). Indeed, due to its relatively high abundance, CH_4 is never depleted enough to show seasonal variations.

The seasonal variability on C_2H_6 is clearly seen at low-pressure levels. The shape of its vertical profile is mostly governed by reaction R20 ($CH_3 + CH_3 \rightarrow C_2H_6$). Methyl is produced from the CH_4 photolysis around 10^{-4} mbar. At higher pressures, C_2H_6 is mostly in diffusive equilibrium (see Zhang et al., 2013 for instance) and its shape is governed by the slow diffusion of C_2H_6 produced at lower pressure levels. The seasonal variability of this compound is correlated with insolation and is therefore maximum around the poles.

C_2H_2 shows a seasonal variability similar to C_2H_6, with some differences around the 1 mbar pressure level, because C_2H_2 has substantial production at this pressure level by reactions R21 ($C_2H + H_2 \rightarrow C_2H_2 + H$) and R6 ($H + C_2H_3 \rightarrow C_2H_2 + H_2$), and depletion by R48 ($C_2H_2 + h\nu \rightarrow C_2H + H$) and R5 ($H + C_2H_2 \rightarrow C_2H_3$).

4.1.2. Evolution of the C_2H_2 column density

The C_2H_2 column densities computed for pressures lower than 10^{-3} mbar, 10^{-2} mbar, 0.1 mbar and 1 mbar are presented in Fig. 11, as a comparison with Fig. 8 of Moses and Greathouse (2005). The results concerning the temporal evolution of this column density are in good agreement. The differences in the column density absolute values can be attributed to differences in the temperature/pressure background, the eddy diffusion profile or the chemical network. At 10^{-3} mbar, an asymmetry between northern and southern summer solstices is caused by Saturn's eccentricity. The maximum value in column density is reached around the southern summer pole, shortly after the southern summer solstice, at $L_s \approx 280°$. The signature of the rings is clearly visible at low latitudes near the solstices in the winter hemisphere. The amount of radicals (and therefore chemical compound produced from radicals) is reduced (see for instance Edgington et al., 2012) due to the partial absorption of the UV radiation by Saturn's rings. At higher pressure levels, the ring signature is damped, and disappears almost completely at 0.1 mbar. From that pressure level to higher ones, the abundance of C_2H_2 is mainly controlled by the downward diffusion of C_2H_2 produced at lower pressure levels. Therefore, from that pressure level, the column density features (e.g., maxima and minima) are increasingly phase-lagged with increasing pressure. These plots also show that the maximum value of the C_2H_2 column density is shifted from high latitudes to equatorial latitudes with increasing pressure in agreement with previous work of Moses and Greathouse (2005). Indeed, this column density mimics the seasonal solar actinic flux at high altitudes (around 10^{-3} mbar), while it follows the annually averaged actinic flux at lower altitudes (at 1 mbar and below) where the column density is maximum at the equator.

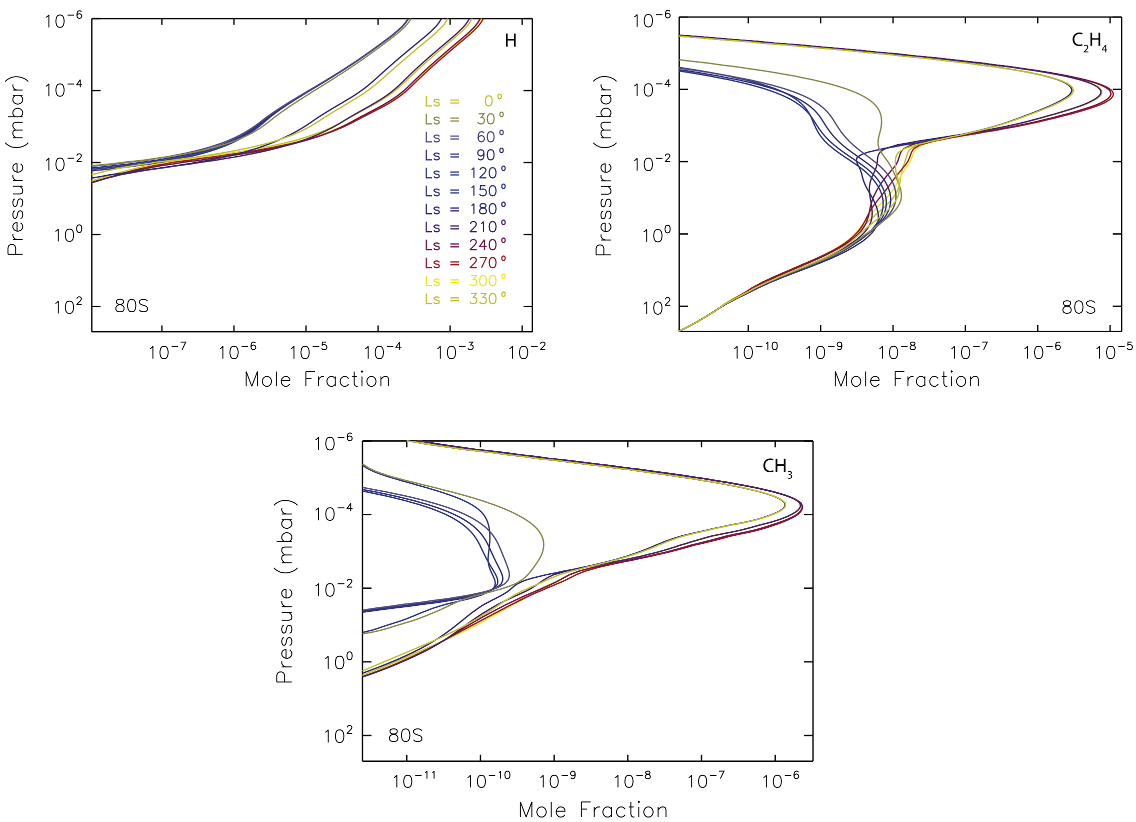

Fig. 12. Seasonal evolution of the mole fraction of atomic hydrogen (H, top left), ethylene (C_2H_4, top right), methyl (CH_3, bottom) as a function of pressure and heliocentric distance (L_s) at 80°S. The profiles are presented using a 30° step in L_s.

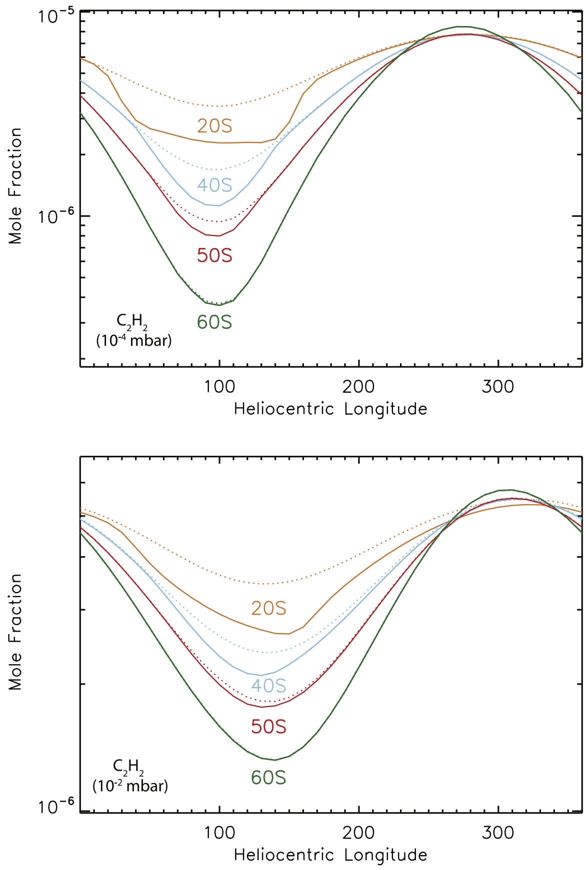

Fig. 13. C_2H_2 mole fraction at 10^{-4} mbar (top) and 10^{-2} mbar (bottom) as a function of heliocentric longitude. The solid lines include ring-shadowing effects, whereas the dotted lines do not include this effect. These effects are only visible from the equator to ±50°. High latitudes are alternately in polar day and polar night. The mole fraction minima and maxima are damped and phase-lagged at 10^{-2} mbar with respect to 10^{-4} mbar.

4.1.3. Other species

The seasonal evolution of the vertical profiles of several other compounds of interest are presented in Fig. 12 for 80°S, where variability is expected to be most noticeable. Radicals, such as atomic hydrogen (H) and methyl (CH_3), show a strong seasonal variability, as they mainly result from the photolysis of CH_4 and depend therefore on insolation conditions. These short-lived radicals undergo a drastic decrease in their abundances in winter conditions at this latitude, i.e., when CH_4 photolysis is stopped by the polar night. Ethylene (C_2H_4) also shows significant seasonal changes around 10^{-4} mbar as they mainly result from reactions involving CH radicals and methane (R13: $CH + CH_4 \rightarrow C_2H_4 + H$). Below that level, C_2H_4 production rate through reaction R7 ($H + C_2H_3 \rightarrow C_2H_4$) becomes increasingly important, consistently with Moses and Greathouse (2005), to be its main production process around 1 mbar.

4.1.4. Impact of the rings on chemistry

The impact of the UV absorption by the rings on the seasonal evolution of C_2H_2 and C_2H_6 mole fractions are depicted in Fig. 13 and 14. As expected from geometrical considerations, and given the latitudinal extent of the numerical cells of the model, the ring shadowing effect is maximum at latitudes below 50° in the winter hemisphere, at the solstice itself, i.e., when the shadow cast by the ring on the planet are the most extended in that hemisphere. The impact of the ring shadowing is more localised in time at a latitude of 40° than at a latitude of 20° in the winter hemisphere. At these latitudes, the main impact on chemistry of the ring shadowing effect comes from Saturn B ring. At a latitude of 20° in the winter hemisphere, the ring shadowing effects are effective over 140° in L_s, while at a latitude of 40°, they are effective over 80° in L_s. At higher pressure levels, and similarly to the column density, the mole fraction minima and maxima are damped and phase-lagged.

4.2. Accounting for the seasonal temperature field

In this section, we present results from the seasonal simulations using the seasonal (S) thermal profiles. The vertical profiles of CH_4, C_2H_6, and C_2H_2, using this thermal field are displayed in Fig. 15. These profiles have to be compared with Fig. 10, where the (U) thermal field was used.

Taking the (S) field into account leads to differences with respect to the (U) case in the amplitude of the seasonal variability of C_2H_2 and C_2H_6 at pressure levels ranging from 10^{-5} to 10^{-1} mbar. C_2H_2 now shows a small seasonal variability at pressure levels ranging from 0.5 to 10 mbar, which was not the case previously. The position of the homopause is also expected to vary, as the molecular diffusion coefficient has a thermal dependency ($D_i \propto T^{1.75}/p$). Using the (S) field, the homopause is generally shifted to a lower pressure, due to the fact that the (U) thermal field corresponds to summer conditions at latitude of 20° in the summer hemisphere.

The seasonal evolutions of the C_2H_2 and C_2H_6 mole fractions at three pressure levels (10^{-4}, 10^{-2} and 1 mbar) and considering the

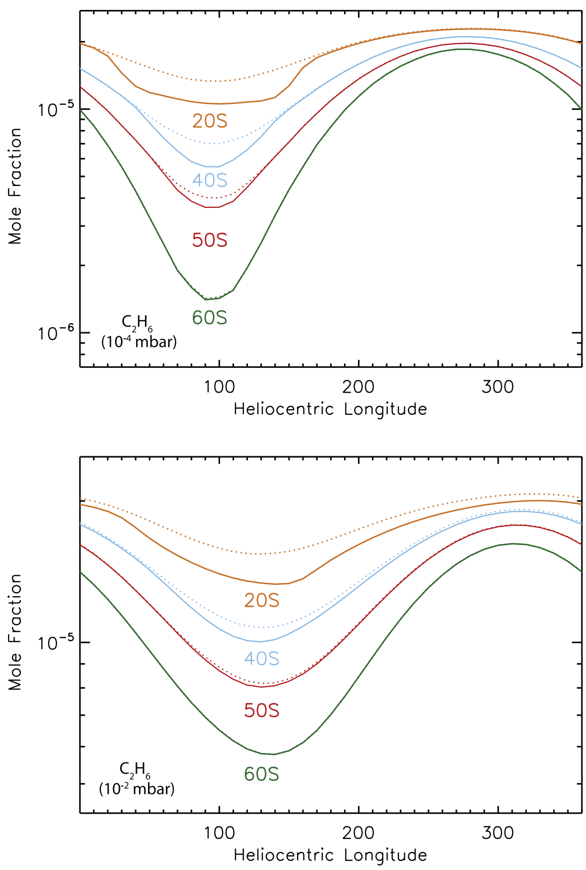

Fig. 14. Same as Fig. 13 for C_2H_6. Solid and dotted lines represent photochemical predictions with and without ring shadowing, respectively.

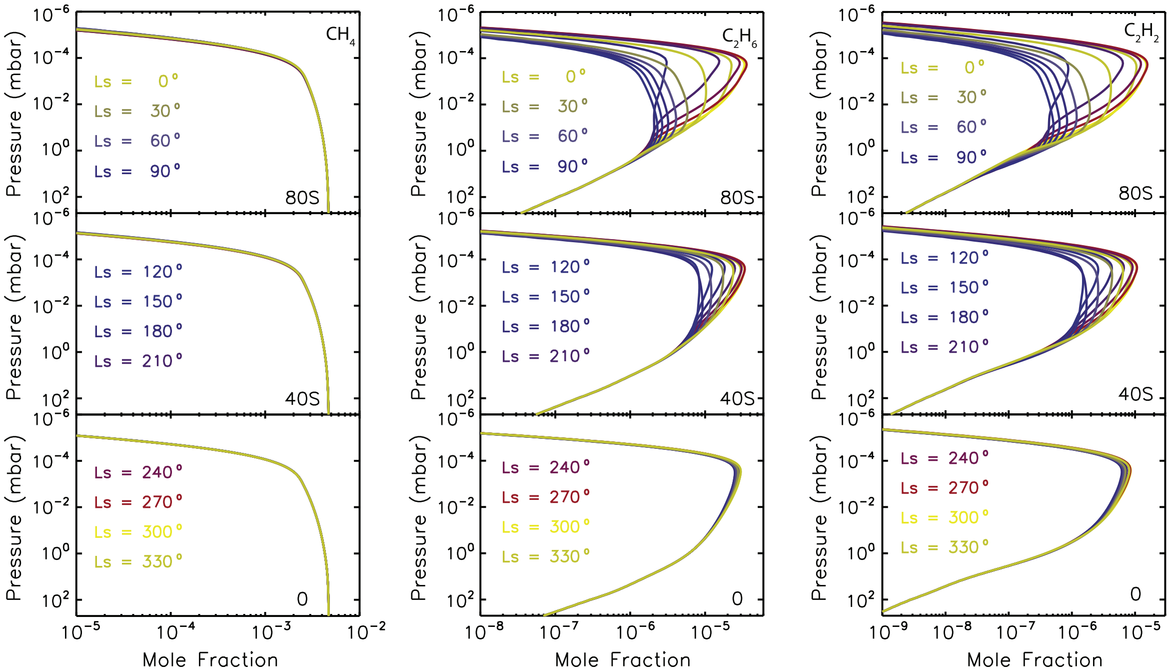

Fig. 15. Seasonal evolution of CH_4 (left), C_2H_6 (center) and C_2H_2 (right) vertical profiles computed for the whole Kronian year (360° in heliocentric longitude using a 30° step) and using the seasonal (S) thermal field.

(S) and (U) thermal fields are shown in Figs. 16, 18 and 20. For the sake of comprehension, the seasonal evolution of temperatures at these same pressure levels are shown alongside as well as the position of the different solstices and equinoxes. We only present these seasonal evolutions at a few latitudes in the southern hemisphere, although the same occurs in the northern hemisphere. Therefore, in what follows, summer and winter refer to these seasons in the southern hemisphere, if not otherwise specified.

• Fig. 16: At 10^{-4} mbar, C_2H_2 and C_2H_6 mole fractions, as predicted using both (S) and (U) thermal fields, evolve in phase. Around the summer solstice ($L_s = 270°$), the abundance of these compounds is increased when considering the (S) thermal field and they both show a positive abundance gradient from the equator to the south pole. Note that, when considering the (U) field, C_2H_6 shows a very small abundance gradient at the summer solstice.

The differences in C_2H_2 and C_2H_6 abundances between both (S) and (U) thermal field calculations never exceed 50% except at high latitudes at summer solstice where C_2H_2 and C_2H_6 abundances are enhanced by a factor of 1.4 and 1.5, respectively. The small bump observed at the equator with both thermal fields is due to the absence of ring shadowing due to the thin nature of the rings. The ring opacity on the UV field is averaged over the latitudinal extent of the numerical cells, which are 10°-wide here. A local maximum on the UV field is expected at the equator at $L_s = 0°$ and 180°, i.e., when the projection of the rings over Saturn's planetary disk is negligible, given the latitudinal extent of the numerical cells. The temperatures at 40°S for L_s ranging from 50° to 140° vary abruptly with times due to the shadowing from the different rings. The temperature of the (U) thermal field at this pressure level is 1 K warmer than the one of (S) thermal field at latitude of 80°S around the summer solstice.

At 10^{-4} mbar, the C_2H_2 production is mainly controlled by reactions R50 ($C_2H_4 + h\nu \rightarrow C_2H_2 + H_2$) and R51 ($C_2H_4 + h\nu \rightarrow C_2H_2 + H + H$) as displayed on Fig. 17 (left panel). The integrated production rates above that pressure level computed using the (S) thermal field are always greater than the ones computed with the (U) field. These differences are caused by the temperature which affects the position of the homopause and allows the UV radiation to penetrate deeper in the (U) thermal field case. This ultimately leads to an increase in the integrated production rate above 10^{-4} mbar of CH radical from methane photolysis. Since the (U) thermal field is hotter than the (S) thermal field at all times along the year, the integrated production rates of C_2H_2 and C_2H_6 above 10^{-4} mbar in the former case are always expected to be greater than the (U) case. From this radical, C_2H_4 is produced through reaction R13, and then photolysed through reactions R50 and R51. We note that the differences in the integrated production rates between these two thermal fields reach a minimum at 40°N around the northern winter solstice ($L_s = 270°$) while, at the same time, the C_2H_2 mole fraction becomes more important when considering the (U) thermal field than when using the (S) thermal field. These differences are produced by the decrease in the diffusion timescale due to the contraction of the atmospheric column which cools down around the winter solstice as explained below.

A similar behavior is observed for C_2H_6 (Fig. 17, right panel) whose integrated production rates are controlled by reaction R20. We can however note that, at 80°S and around the winter solstice ($L_s = 90°$) the integrated production rate considering the (S) thermal field is more important than the one using (U) thermal field, consistent with the predicted greater abundance of C_2H_6 at that time.

• Fig. 18: At 10^{-2} mbar, C_2H_2 is less abundant at every latitude when the (S) field is accounted for. Its abundance gradually increases with latitude from the equator to the south pole during the summer season. However, at this pressure level, the peak in the C_2H_2 and C_2H_6 abundances during summer is occurring earlier at high latitudes than at mid-latitudes due to Saturn's obliquity. C_2H_6 becomes as abundant with the (S) thermal field as it was with the (U) thermal field during the summer season. A slight dephasing is noted between

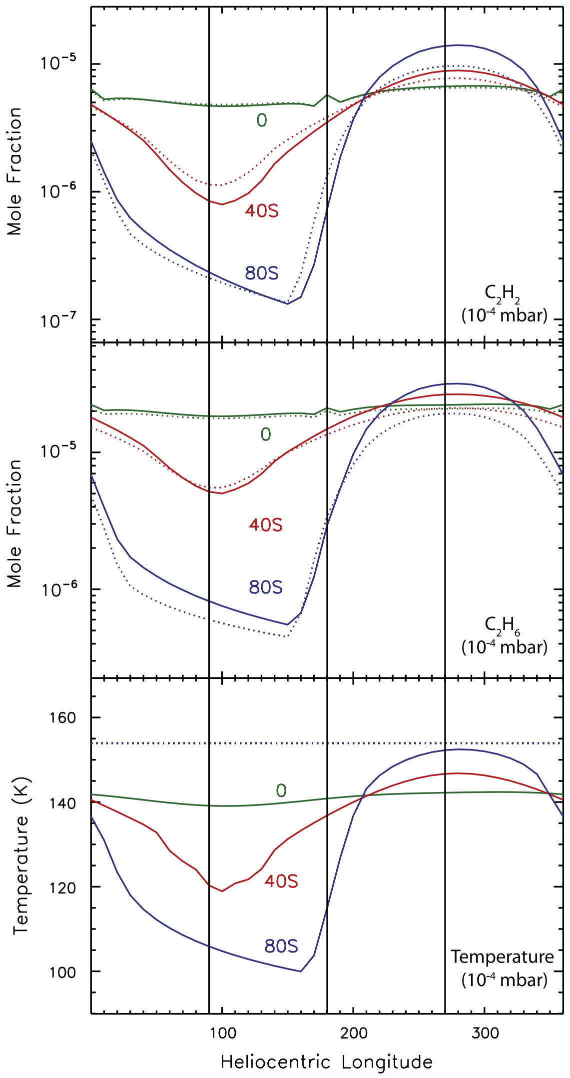

Fig. 16. Evolution of the C_2H_2 mole fraction (top panel), the C_2H_6 mole fraction (middle panel) and temperature (bottom panel) at 10^{-4} mbar. The evolution of mole fractions and temperature is plotted as a function of heliocentric longitude for latitudes of 80°S, 40°S and at the equator. Values obtained with the (S) and (U) thermal fields are displayed with solid and dotted lines, respectively. The black solid lines indicate the position of the solstices and equinoxes (see Fig. 1).

the two thermal field calculations when C_2H_2 and C_2H_6 reach both their maximal and minimal values. At 80°S, the abundance of C_2H_2 and C_2H_6 is decreased by a factor 2.3 and 2.1, respectively, during the winter season when we consider the (S) thermal field. At this pressure level, the temperatures of the (U) field are 2 K and 6 K warmer than the equatorial temperatures of the (S) field at the summer solstice and the winter solstice respectively.

At 10^{-2} mbar, the C_2H_2 production is mainly controlled by reaction R6. The seasonal evolution of the integrated production rate of this reaction above this pressure level is presented in Fig. 19 (left panel) at latitudes of 80°S and 40°N. Around the summer solstice ($L_s = 270°$ for 80°S and $L_s = 90°$ for 40°N), the integrated production rate of reaction R6 in the (U) and (S) cases are very similar, consistent with the predicted C_2H_2 mole fraction. Around the winter solstice ($L_s = 90°$ for 80°S and $L_s = 270°$ for 40°N), the (S) integrated production rate is higher than the (U) one, also consistent with the predicted C_2H_2 mole fractions.

Similarly to the situation at lower pressure levels, the integrated C_2H_6 production rate (Fig. 19, right panel) is controlled by reaction R20. The integrated production rates of this reaction are very similar between the two thermal field cases, all along the year except around the southern winter solstice at high latitudes. Indeed, the integrated production rate become less important in the (S) case than in the (U) case.

At this pressure level, the differences between the two thermal field cases observed in the C_2H_2 and C_2H_6 abundances are mainly controlled by two quantities. First, a higher integrated production rate above that level will produce a greater quantity of the considered molecule. At the same time, the contraction of the atmospheric column during the winter season will increase the diffusion of the produced hydrocarbons to higher pressure levels. This former effect is clearly noticed for C_2H_6 at 40°N during the northern winter season where its integrated production rate above that level with the (S) thermal field is slightly greater than the one with the (U) thermal field, while its predicted abundance is lower in the (S) case than in the (U) case.

- Fig. 20: At 1 mbar, C_2H_2 still shows seasonal variability while C_2H_6 seasonal variability is negligible with the (U) thermal field. The variability of these compounds persists at higher-pressure level when the (S) thermal field is accounted for. The dephasing between the two thermal field calculations which was observed at 10^{-2} mbar is now enhanced here. C_2H_6 is slightly more abundant at the equator using the (S) field, and has now a steeper abundance gradient toward the South pole. The temperature of the (U) field corresponds to temperatures of the (S) field at 40°S during the winter solstice.

Note that the resolution of the model in the pressure space varies with thermodynamic conditions as discussed in Section 2.3.2, while the vertical resolution of the model is constant. The altitudinal resolution of the model has been doubled in order to assess if the differences observed between the two thermal fields at high latitudes in the winter hemisphere where not due to numerical artifact. The results obtained were identical.

It is clear from Figs. 18 and 20 that accounting for the (S) thermal field leads to a decrease in the seasonal lag of C_2H_6 and C_2H_2 at pressure levels higher than 10^{-2} mbar. We also noted that these two compounds still show seasonal variability at 1 mbar while this variability has already vanished for C_2H_6 with the (U) thermal field. The temporal positions of the maximum and minimum abundance values as a function of pressure, corresponding to summer and winter conditions (hereafter called summer peak and winter hollow, respectively), are displayed in Fig. 21. We note an increase in the phase lag between the (U) and the (S) thermal field calculations with increasing pressure from the 10^{-2} mbar to the 1 mbar pressure level. At 1 mbar, the depletion in the C_2H_6 abundance due to low-insolation winter conditions (winter hollow) is occurring 90° in heliocentric longitude earlier with the (S) thermal field than with the (U) thermal field. Similarly, the increase in C_2H_6 abundance due to summer conditions (summer peak) is occurring 40° in heliocentric longitude earlier.

We can note here some discrepancies between both our study cases and the following statement previously made by Moses and Greathouse (2005): *"Our assumption of a constant thermal structure with time and latitude introduce mole-fractions errors of a few percent but will not affect our overall conclusions."* This statement seems to be clearly in disagreement with the results presented in Figs. 16, 18 and 20 where the differences between the (U) and (S) cases are well beyond a few percent. The fact that we did not reach the same conclusions lies in the different approach we had. In the present model, we assumed that the compounds mole fractions followed the atmospheric contraction/dilatation in the pressure space with changing thermodynamic conditions (see Section 2.3.3). Therefore, when the atmosphere column contracts,

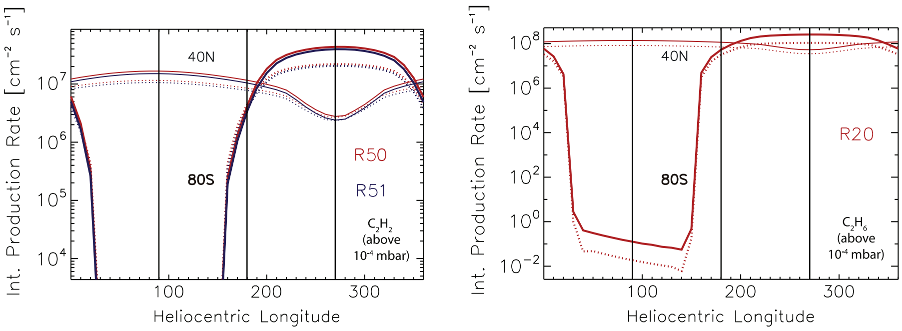

Fig. 17. Seasonal evolution of the integrated production rate above 10^{-4} mbar of the main reactions leading to the production of C_2H_2 (left panel) and C_2H_6 (right panel). For the sake of clarity these integrated production rates are presented at 80°S (thick lines) and 40°N (thin lines). Calculations that include the (S) and (U) thermal field are displayed with solid and dotted lines, respectively.

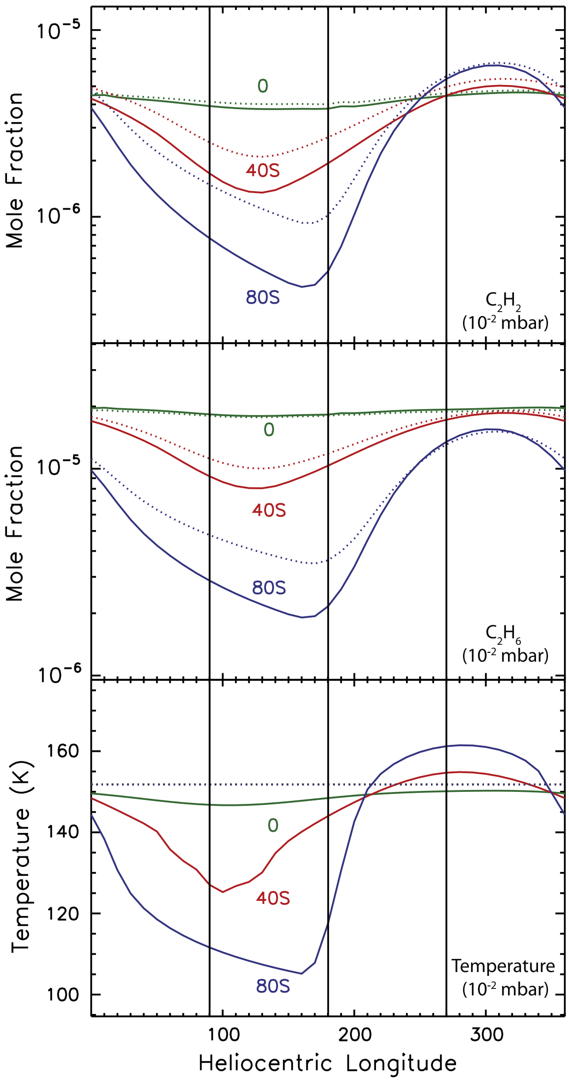

Fig. 18. Same as Fig. 16 at 10^{-2} mbar.

the mole fraction vertical gradients in altitude are increased and the diffusion to higher pressure levels becomes faster. On the other hand, when the thermal structure does not evolve with time (i.e., the (U) study case), our approach is identical to the work of Moses and Greathouse (2005).

The diffusion timescale is therefore decreased at all times in the (S) model with respect to the (U) model, due to the thermal evolution of the (S) model. Consequently, this decrease in the diffusion timescale shifts to higher pressures the level where the seasonal variations vanish. This effect is maximized at the poles where the seasonal variations in temperature are important.

We remind the reader that we assumed a seasonally and latitudinally constant eddy diffusion profile, due to the lack of constraint on this free-parameter.

5. Comparison with Cassini/CIRS data

After Cassini's arrival in the Saturn system, observations of hydrocarbons have been performed with an unprecedented spatial and temporal coverage, either with nadir (Howett et al., 2007; Hesman et al., 2009; Sinclair et al., 2013) or limb (Guerlet et al., 2009, 2010) observing geometries. Howett et al. (2007) reported the meridional variability of C_2H_6 and C_2H_2 from 15°S to almost 70°S at a pressure level around 2 mbar between June 2004 ($L_s \approx 292^\circ$) and November 2004 ($L_s \approx 298^\circ$) with Cassini/CIRS. The C_2H_2 distribution was found to peak around 30°S and decreases towards both the equator and the South Pole. C_2H_6 showed a rather different and puzzling behavior, with an increasing abundance southward from the equator, confirming the earlier findings of Greathouse et al. (2005) and Simon-Miller et al. (2005).

Sinclair et al. (2013) reported observations of C_2H_6 and C_2H_2 around the 2.1 mbar pressure level, acquired in nadir observing mode with a good spatial coverage, from South to North Pole. These observations range in time from March 2005 ($L_s \approx 307^\circ$) to September 2012 ($L_s \approx 37^\circ$). However, the most recent ones were contaminated with the signature of Saturn's 2011 Great Storm (Fletcher et al., 2011; Fischer et al., 2011; Sánchez-Lavega et al., 2011), which stratospheric aftermath was studied extensively by Fletcher et al. (2012). Their retrieval suggests that C_2H_2 is abundant at the equator and decreases toward the poles. Similarly to previous findings, C_2H_6 showed a behavior different from C_2H_2. The observed trend suggests an enrichment in C_2H_6 at high southern latitudes.

The observations retrieved by Guerlet et al. (2009, 2010) from Cassini/CIRS limb-scans, enabled constraining the vertical distributions of C_2H_2 and C_2H_6 from 5 mbar to 5 μbar. The retrieved mole fraction meridional profiles of C_2H_2 and C_2H_6 at 1 mbar are

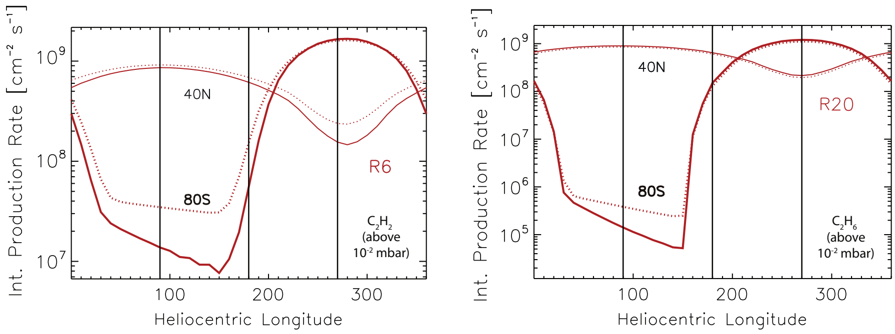

Fig. 19. Same as Fig. 17 for 10^{-2} mbar.

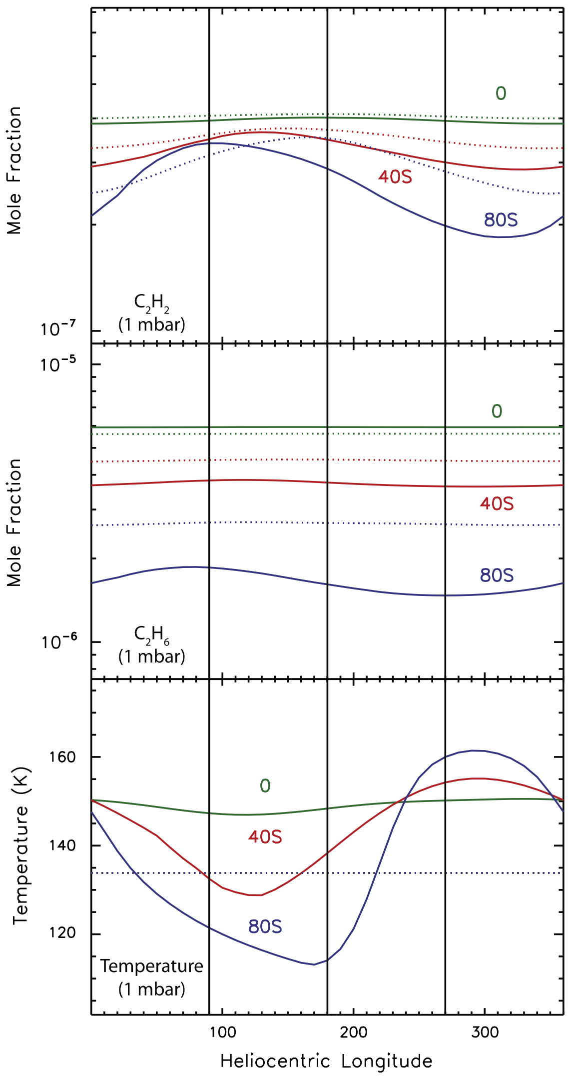

Fig. 20. Same as Fig. 16 at 1 mbar.

presented in Fig. 22 for a better comparison with already published nadir observations (Howett et al., 2007; Sinclair et al., 2013). When considering the meridional profiles only, the systematic errors are not considered and therefore the observational errors have been reduced of 20% in Fig. 22. We chose not to rescale our predictions to superimpose them to the observations, although it is occasionally observed in the literature. Dobrijevic et al. (2003, 2010a) showed that uncertainty propagations in giant planet photochemistry lead to uncertainties of about an order of magnitude in the C2 species' abundances at around the 1 mbar pressure level. Recent improvement on the chemical scheme greatly reduced these uncertainties (Hébrard et al., 2013; Dobrijevic et al., 2014; Loison et al., 2015) (see Fig. 7) by a factor of 1.8 for C_2H_6 and a factor of 4.2 for C_2H_2. The absolute differences between the photochemical predictions and the observations shall not be seen as a concern if it remains within the photochemical uncertainties. What can (and have to) be compared between observations and models are the general trends seen in the meridional distributions at the relevant pressure levels.

The Cassini limb-observations offer latitude and altitude information. The retrieved abundances of these two molecules over the pressure sensitivity range are presented in Fig. 23 at a few observed planetographic latitudes. We have selected these latitudes in order to display the different features noted when confronting these observations with the model, e.g., a large over-prediction of their abundance at high southern latitudes and low pressure level, a good agreement at mid-to-low latitudes, and an under-prediction at mid-to-high northern latitudes and high pressure levels, especially noted for C_2H_6. It is worth presenting a comparison with these data in two-dimensional plots for the sake of clarity. The relative differences between the Cassini observations of C_2H_6 and C_2H_2 from the photochemical predictions using

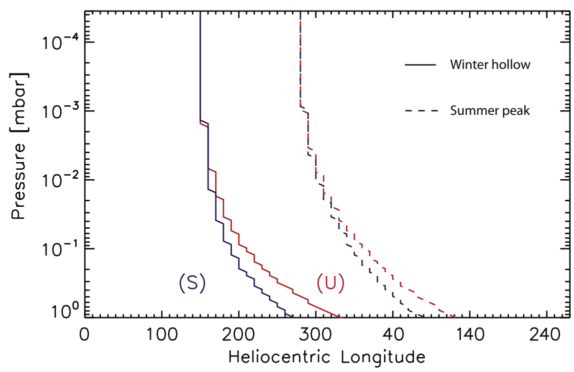

Fig. 21. Evolution of the seasonal maximum value (*summer peak*, dashed lines) and minimum value (*winter hollow*, solid lines) reached by the C_2H_6 mole fraction as a function of pressure at 80°S. Calculations using the (S) and the (U) thermal fields are denoted by blue and red colors, respectively. (For interpretation of the references to color in this figure legend, the reader is referred to the web version of this article.)

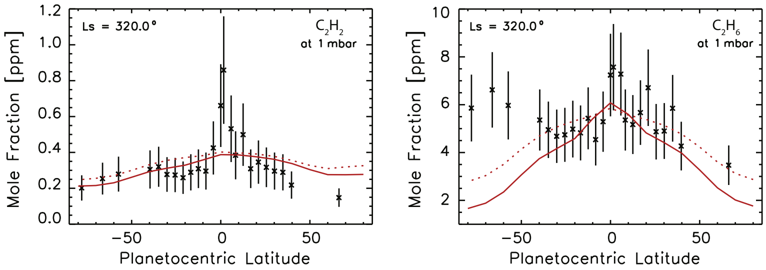

Fig. 22. Comparison between the Cassini/CIRS limb observations (Guerlet et al., 2009) for heliocentric longitudes ranging from $L_s \approx 300^\circ$ to $L_s \approx 340^\circ$ and the photochemical model predictions. Photochemical predictions are presented for a heliocentric longitude of 320°. C_2H_2 and C_2H_6 are respectively shown in the left and right panels. Model outputs using the (S) and (U) thermal fields are denoted by solid and dotted lines, respectively. No rescaling factors have been applied, see text for details.

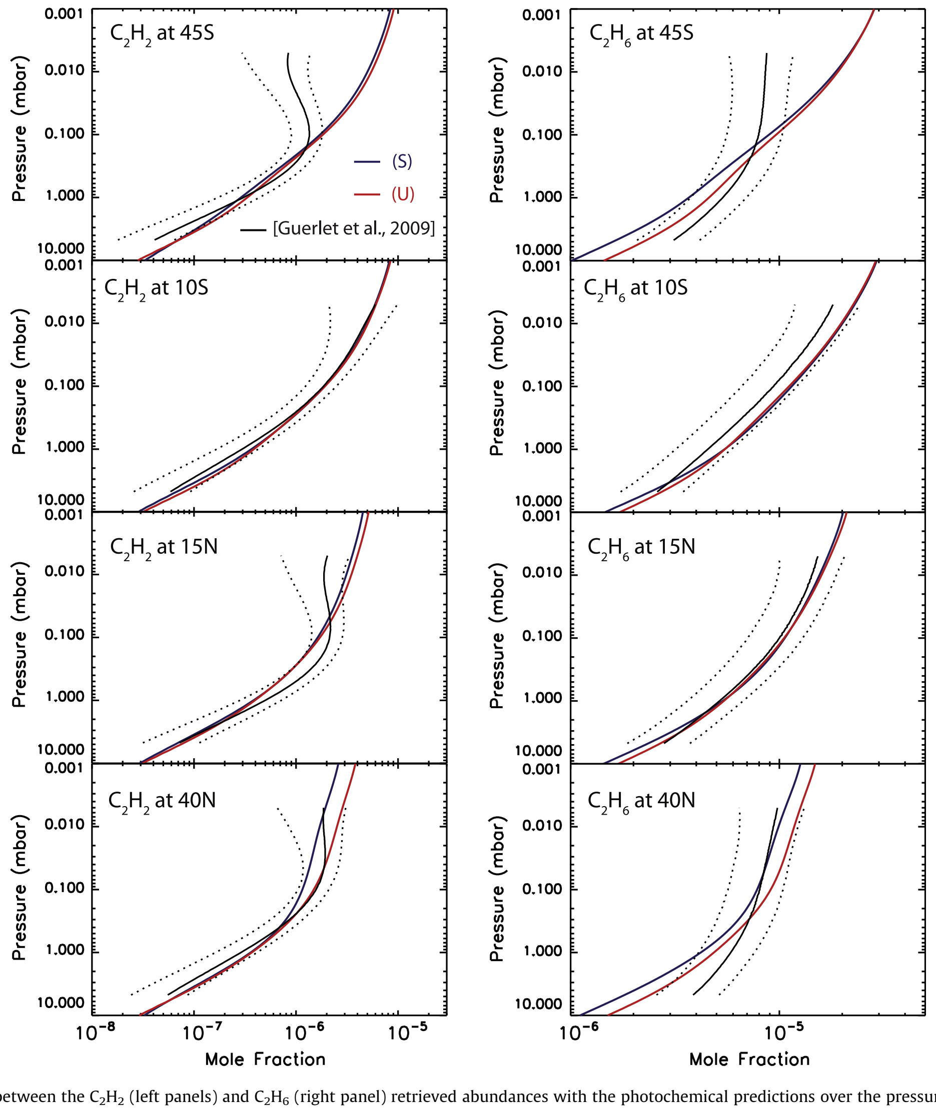

Fig. 23. Comparison between the C_2H_2 (left panels) and C_2H_6 (right panel) retrieved abundances with the photochemical predictions over the pressure sensitivity range at few observed planetographic latitudes. Photochemical predictions that uses the (S) and (U) thermal field are displayed by solid blue and red colors, respectively. Solid and dotted black lines represent the observed abundances of Guerlet et al. (2009) with the $1-\sigma$ uncertainties, respectively. Photochemical predictions are presented for a heliocentric longitude of 320°. (For interpretation of the references to color in this figure legend, the reader is referred to the web version of this article.)

(S) thermal field are displayed in Fig. 24 using a logarithmic scale. The positive and negative values therefore denote the regions where the photochemical model under and over-predicts the abundance of these compounds, respectively. The quantity $log(y_i^{CIRS}/y_i^{PM})$ is plotted as a function of the pressure range and the latitude, where y_i denotes respectively the mole fraction of

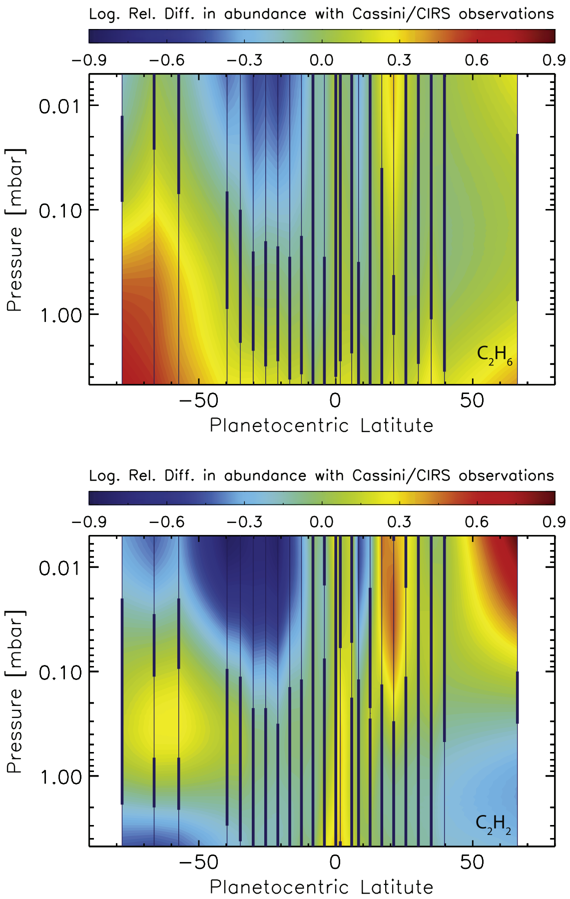

Fig. 24. Comparison between observations (Guerlet et al., 2009) and photochemical predictions as a function of the pressure sensitivity range of limb observations and planetocentric latitudes. C_2H_6 and C_2H_2 are presented in the upper and lower panel, respectively. The observing period ranges from $L_S = 300°$ and $L_S = 340°$. Observations are compared to photochemical predictions at $L_S = 320°$. The logarithm of the difference between Cassini observations of these compounds and the photochemical predictions that use (S) thermal field is plotted here. Positive/negative values denote an under/over-prediction of the photochemical models. The vertical lines denote the latitudes for which observations have been made. The thick portions of those lines show the region where the photochemical predictions are within the observation uncertainties. Uncertainties on the photochemical predictions are not taken into account. No scaling factor have been applied.

species *i*, while *PM* stands for photochemical model. Because the latitudinal coverage of Cassini limb-observations is limited, we have indicated the latitude of each observation by black vertical lines.

5.1. C_2H_2

At the 1 mbar pressure level (Fig. 22), our photochemical model simulations agree reasonably well with the meridional trend seen in the C_2H_2 meridional profiles, namely the poleward decrease of its abundance, as reported by Guerlet et al. (2009, 2010) and Sinclair et al. (2013). Differences are observed in the equatorial regions, at latitudes lower than 15° and Northward of 35°N.

Below the 0.1 mbar pressure level (see Fig. 24), the agreement with the C_2H_2 distribution reported by Guerlet et al. (2009) is within the uncertainty range of the observations from the equator to ± 40°. The agreement is however poor at lower-pressure levels and high-southern latitudes, where C_2H_2 abundance tends to be over-predicted.

In the equatorial zone, the differences between our photochemical predictions and the observations change sharply over a short latitudinal range. Fig. 22 shows that our model does not reproduce the equatorial peak of C_2H_2 abundance (between 5°S and 5°N roughly). This peak is thought to be caused by Saturn's thermal Semi-Annual Oscillation (SSAO) (Orton et al., 2008; Fouchet et al., 2008; Guerlet et al., 2009, 2011).

In the southern hemisphere, from 10°S to 50°S, we over-predict the C_2H_2 mole fraction at pressures lower than 0.1 mbar. This feature is also observed when comparing C_2H_6 predictions to observations and is discussed below.

5.2. C_2H_6

Moses and Greathouse (2005) have shown that the seasonal variability of C_2H_6 at pressures higher than 0.8 mbar was negligible, because the timescale driving this compound's abundance becomes longer than the Saturn year below that pressure level.

Due to the larger chemical evolution timescale of C_2H_6 with respect to C_2H_2, this compound is expected to be more sensitive to transport processes than the latter one. In addition to that, the uncertainties on the reactions involved in the production or destruction of C_2H_2 lead to an important error bar on its vertical

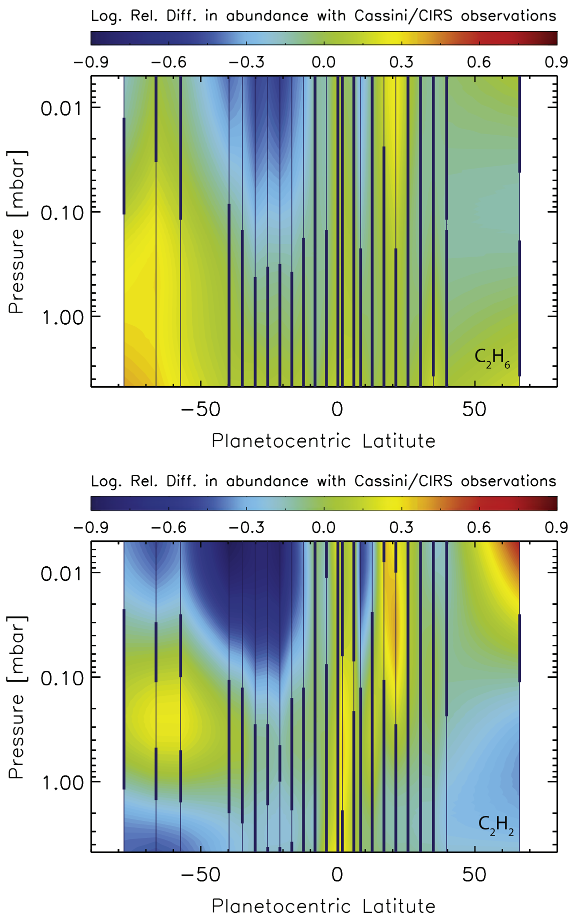

Fig. 25. Same as Fig. (24) using the photochemical predictions that use (U) thermal field.

profile (recall Fig. 7), whereas the predicted shape of C_2H_6 has smaller error bars. Therefore, C_2H_6 is a compound that should be first used to trace dynamics rather than C_2H_2. C_2H_6 is reasonably well reproduced from the equator to 40° in both hemispheres below the 0.1 mbar pressure level. An equatorial peak similar to the one observed in the C_2H_2 meridional profile (see Fig. 22), though with a smaller relative amplitude, is present in the C_2H_6 meridional profile and could also be caused by the SSAO. Similarly to C_2H_2, we underpredict C_2H_6 abundance from 40°S to south pole below the 0.1 mbar pressure level, and we overpredict its abundance at latitudes ranging from 10°S to 40°S above the 0.1 mbar pressure level. These similar over/under-prediction seen in C_2H_2 and C_2H_6 could be caused by large scale dynamical cell redistributing species meridionally in Saturn's stratosphere, as suggested by Guerlet et al. (2009, 2010), Sinclair et al. (2013).

At the 1 mbar pressure level (Fig. 22), the photochemical predictions that use the (S) thermal field predict a steeper equator-to-pole gradient, which arise from the faster diffusion to higher-pressure levels when considering the (S) thermal field. Fitting these meridional profiles with dynamical processes could help to constrain meridional mixing processes and will be the object of a forthcoming study.

5.3. Does accounting for the seasonal evolution of the thermal field better fit Cassini data?

Fig. 25 presents the comparison between Cassini-limb observations with photochemical predictions using the (U) thermal field in a similar way as Fig. 24. C_2H_6 is better predicted using (U) thermal field below 1 mbar while C_2H_2 is better predicted at all pressure levels using (S) thermal field. The region where C_2H_6 was widely under-predicted with the (S) thermal field from mid-southern latitude to South pole (recall Fig. 24), is now slightly reduced, but it remains significant.

The evolution of the Chi-Square goodness-of-fit between the predicted C_2H_2 and C_2H_6 abundance (using both thermal fields) and Cassini observations for every observed latitudes is shown in Fig. 26. These values are computed first by interpolation of the photochemical prediction on the observed latitudes and pressure levels, then the Chi-Square coefficient presented in Fig. 26 is computed and summed over the observed latitudinal range. Using the (S) thermal field in the predicted C_2H_6 profile represents a slight

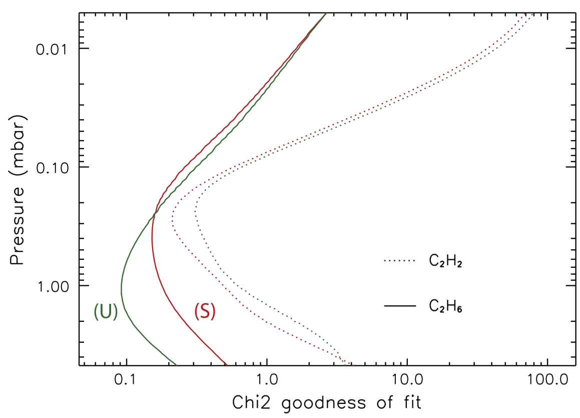

Fig. 26. Evolution of the χ square goodness-of-fit factor for C_2H_2 (dotted lines) and C_2H_6 (solid lines) over the sensitivity pressure ranges of the Cassini/CIRS limb observation mode. This factor is presented when using (S) and (U) thermal fields, denoted by the blue and red lines respectively. This factor is summed for all observed latitudes. (For interpretation of the references to color in this figure legend, the reader is referred to the web version of this article.)

improvement at pressures lower than 0.1 mbar. However, in the lower stratosphere, from 0.2 mbar to 5 mbar, the predicted C_2H_6 shape is better reproduced using the (U) thermal field. C_2H_2 is better reproduced using the (S) thermal field at all pressure levels.

5.4. Discussion

As noted above, it has been shown that both C_2H_6 and C_2H_2 were overpredicted at mid-southern latitudes and above 0.1 mbar, while C_2H_6 was underpredicted at high-southern latitudes and below 0.1 mbar (recall Fig. 24). It can be pointed out that the eddy diffusion coefficient used in this work was possibly not the most optimal one. We remind the reader that the coefficient used here was chosen so that it provides a satisfactory fit of the CH_4 vertical profile in comparison to Voyager/UVS and Cassini/CIRS data (Smith et al., 1983; Dobrijevic et al., 2011).

However, when looking carefully at the southern mid latitudes in Figs. 23 and 24, where we overpredict the C_2H_6 abundance above 0.1 mbar and underpredict its abundance below 1 mbar, a diffusion coefficient greater in the upper stratosphere (above 0.1 mbar) and smaller below that level might provide a better fit at these latitudes. We have performed a sensitivity study on that parameter by using several dozen different eddy diffusion coefficients. The seasonal model was run from the converged state with the nominal eddy diffusion profile presented in this work. From that point, the eddy diffusion profile was modified and several additional iterations over Saturn orbits were necessary for the system to converge, depending on the new eddy diffusion coefficient. Several different eddy diffusion coefficients provide a better fit of mid-latitudes in the southern hemisphere, but at the same time the good agreement in the northern hemisphere vanishes.

All along this study, we have assumed an eddy coefficient constant with latitudes. However, the sensitivity study on that free parameter has shown us that some latitudes that were not properly reproduced with an eddy diffusion coefficient based on globally averaged observations could be reproduced when adjusting this coefficient. In principle, it could therefore be possible to fit all the observed latitudes by finding the most adapted diffusion coefficient at each latitude. We have not explored this possibility more extensively since the meridional variability of that parameter has not yet been demonstrated with the observation of the latitudinal variability of CH_4 homopause.

Another likely possibility would be the existence of large scale meridional transport (diffusive and/or advective), as the associated atmospheric motions might be an important source of departure from the photochemical predictions (Moses and Greathouse, 2005; Guerlet et al., 2009, 2010; Friedson and Moses, 2012; Sinclair et al., 2013). However, it is difficult to assess the validity of this hypothesis without further numerical testing. Such work is deferred to a later paper. The recommended methodology would be first to retrieve the latitudinal variability of the CH_4 homopause in order to better constrain the latitudinal variability of the eddy diffusion coefficient before fitting the Cassini/CIRS observations with meridional transport.

Predictions of the existence of large-scale circulation have already been studied using numerical models. Conrath et al. (1990), using a 2D zonally averaged model, have predicted a summer-to-winter pole stratospheric circulation cell for Saturn at solstice with upwelling around the summer pole and downwelling around the winter pole. They also found a double circulation cell at equinox, with upwelling at equator and downwelling at both poles. However their calculations did not include aerosols heating which is known to impact the radiative budget in the atmosphere. Afterwards, West et al. (1992) included such heating for a jovian-like planet and showed that circulation was altered above 100 mbar, with downwelling at equator and upwelling at the poles. We note that they have not presented the effect of aerosol heating on a Saturn-like planet at solstice. Recently, Friedson and Moses (2012) predicted a seasonally reversing circulation cell using a 3D GCM, with upwelling at the equator and downwelling at low latitudes in the winter hemisphere. The next step of this study is to evaluate whether these predicted circulation patterns are sufficient for our full 2D photochemical model to reproduce the Cassini data.

6. Summary and perspectives

We have developed a latitudinally and seasonally variable photochemical model for giant planets and we have adapted it first to Saturn. The model takes into account photochemistry, vertical mixing, Saturn's obliquity, and variation of seasonally dependent orbital parameters such as subsolar latitude, heliocentric distance and ring shadowing. Meridional transport (both advective and diffusive) as well as vertical advective transport have been coded in the model but have been switched off for the current study. The present model is therefore run as a sum of 1D seasonally variable models calculated at different latitudes. This is the first step toward a full-2D model as it is already coupled to a full-3D radiative transfer model. This first paper is dedicated to the study of the photochemical effects involved by a seasonally variable thermal field, which relies on predictions from a radiative climate model (Greathouse et al., 2008).

Seasonal variability of C_2H_2 and C_2H_6 – The seasonal variations of the C2-hydrocarbon mole fractions such as C_2H_2 (acetylene) and C_2H_6 (ethane) are important at pressure levels lower than 0.1 mbar and at high latitudes. These compounds are known to act as the main stratospheric coolants (Yelle et al., 2001) and we therefore have emphasized their seasonal variabilities in this work. These hydrocarbons are produced by chemical reactions involving radicals which strongly depend on insolation. Including the ring shadowing effect generally results in lowering the mole fraction of hydrocarbons at latitudes that are under the shadow of the rings. The decrease in the mole fraction of these compounds caused by the rings is more important for C_2H_2 than for C_2H_6. This decrease tends to vanish at higher-pressure levels.

Accounting for a seasonally variable thermal field – We found that including a seasonally variable thermal field mainly impacts the seasonal evolution of the hydrocarbon mole fractions in two ways. First, the modification of the thermal field amplitude will affect the position of the methane homopause and will impact consequently the integrated production rates of radicals above the pressure level of 10^{-4} mbar. Then, accounting for a seasonally variable thermal field will affect the diffusion of these produced hydrocarbons through the contraction and dilatation of the atmospheric columns. This will compress the vertical distribution of the atmospheric compounds and will therefore increase the diffusion of these compounds to higher pressure levels. Because the former effect is correlated with the seasonal variation of temperature of the atmospheric column, it is therefore increased with increasing latitude, i.e., where the seasonal thermal gradients are strong. At 10^{-4} mbar, C_2H_2 and C_2H_6 seasonal abundance gradients are generally enhanced. At this pressure level and during the summer season, C_2H_6 shows a positive equator-to-summer pole (North or South) gradient. At 10^{-2} mbar, the seasonal abundance gradients are also increased: the abundance of C_2H_6 and C_2H_2 are respectively decreased by a factor of 2.1 and 2.3 at a latitude of 80° during winter, with respect to the (U) study case. We do not reach the same conclusions than Moses and Greathouse (2005) about the thermal sensitivity of the photochemical model. While our (U) study case is similar to their approach, our (S) study case is, on the other hand, different in a way that the compounds mole fractions are assumed to follow the atmospheric contraction/dilatation in the pressure space with changing thermodynamic conditions. This consequently affects the downward diffusion of the seasonally produced photochemical by-products.

Comparison with Cassini/CIRS data – The Cassini spacecraft has now provided an important amount of data that includes good spatial and temporal coverage (Sinclair et al., 2013) as well as good vertical sensitivity (Guerlet et al., 2009, 2010). Our model reproduces reasonably well the meridional distributions of C_2H_2 and C_2H_6 up to mid-latitudes, even without meridional circulation. However, the overall decrease of C_2H_6 from the south pole towards the north pole at $L_s = 320°$ is not reproduced. An interesting feature has been noted: our model tends to underpredict C_2H_6 abundance from 40°S to South pole at pressure levels ranging from 5 mbar to 0.1 mbar and overpredict its abundance at latitude ranging from 10°S to 40°S at pressure ranging from 5×10^{-3} to 0.1 mbar. These results are consistent with previous findings of Guerlet et al. (2009, 2010) and Sinclair et al. (2013). This interesting feature is also observed for C_2H_2, although in a less pronounced way. The forthcoming step is to turn on the meridional transport to evaluate if it can help better fit to the Cassini data.

Coupling radiative climate model and photochemical model Accounting for these results may have important implications for radiative climate models and GCMs because the predicted temperatures from these models are very sensitive to the amount of these coolants (Greathouse et al., 2008). From 0.1 to 10^{-4} mbar, where their seasonal variability is important, the increase in the amount of these coolants during the summer season will likely counteract the increase in the atmospheric heating caused by the increase in the solar insolation at high-latitudes. Depending on the relative magnitudes of the photochemical timescale over the thermal inertia timescale, the peak in the predicted temperatures at high-latitudes could happen earlier around the summer solstice than previously predicted using a radiative climate model which uses time-independent abundances of atmospheric coolants. The predicted temperatures are therefore expected to start decreasing earlier after summer solstice than what would be predicted with a model that held the amount of these atmospheric coolants constant over time. Moreover, the effect on the lower-stratosphere could be also interesting, as we showed that accounting for the seasonal evolution of the thermal field impacts the phase-lag and the seasonal variability in this region.

Acknowledgments

This work has been supported by the *Investissements d'avenir* program from *Agence Nationale de la Recherche* under the reference ANR-10-IDEX-03-02 (IdEx Bordeaux). Part of this work was done by V.H. at Southwest Research Institute, San Antonio. We thank Julianne Moses and an anonymous reviewer for their constructive comments on the manuscript. We thank Jean Brillet for providing his line-by-line radiative transfer model as well as for useful discussions. We thank Sandrine Guerlet for providing their published Cassini data and for useful discussions. We acknowledge Eric Hébrard for useful discussions on chemistry, Franck Selsis for interesting comments on photochemical models, James Sinclair, Christophe Cossou and Marcelino Agundez for useful comments and discussions. We thank Aymeric Spiga and Melody Sylvestre for useful discussions.

References

Agúndez, M. et al., 2014. Pseudo 2D chemical model of hot-Jupiter atmospheres: Application to HD 209458b and HD 189733b. Astron. Astrophys. 564, A73.
Banfield, D. et al., 1996. 2 μm spectrophotometry of jovian stratospheric aerosols–scattering opacities, vertical distributions, and wind speeds. Icarus 121, 389–410.

Bézard, B. 1986. Variations saisonnières de la structure thermique et composition chimique de jupiter, saturne et uranus. Ph.D. Thesis.
Bézard, B., Gautier, D., 1985. A seasonal climate model of the atmospheres of the giant planets at the Voyager encounter time. I – Saturn's stratosphere. Icarus 61, 296–310.
Bézard, B., Gautier, D., Conrath, B., 1984. A seasonal model of the Saturnian upper troposphere Comparison with Voyager infrared measurements. Icarus 60, 274–288.
Brillet, J. et al., 1996. A three-dimensional simulation of transmitted light through planetary atmospheres using Monte-Carlo methods. Adv. Space Res. 17, 223–226.
Brinkman, A.W., McGregor, J., 1979. The effect of the ring system of the solar radiation reaching the top of Saturn's atmosphere – Direct radiation. Icarus 38, 479–482.
Cavalié, T. et al. 2015. The photochemical response to the variation of temperature in Saturn's 2011–2012 stratospheric vortex. Astron. Astrophys. (revised).
Cess, R.D., Caldwell, J., 1979. A Saturnian stratospheric seasonal climate model. Icarus 38, 349–357.
Colwell, J.E. et al., 2010. Cassini UVIS stellar occultation observations of Saturn's rings. Astron. J. 140, 1569–1578.
Conrath, B.J., Gautier, D., 2000. Saturn helium abundance: A reanalysis of Voyager measurements. Icarus 144, 124–134.
Conrath, B.J., Pirraglia, J.A., 1983. Thermal structure of Saturn from Voyager infrared measurements – Implications for atmospheric dynamics. Icarus 53, 286–292.
Conrath, B.J., Gierasch, P.J., Leroy, S.S., 1990. Temperature and circulation in the stratosphere of the outer planets. Icarus 83, 255–281.
Courtin, R. et al., 1984. The composition of Saturn's atmosphere at northern temperate latitudes from Voyager IRIS spectra – NH_3, PH_3, C_2H_2, C_2H_6, CH_3D, CH_4, and the Saturnian D/H isotopic ratio. Astrophys. J. 287, 899–916.
Dobrijevic, M., Parisot, J.P., 1998. Effect of chemical kinetics uncertainties on hydrocarbon production in the stratosphere of Neptune. Planet. Space Sci. 46, 491–505.
Dobrijevic, M. et al., 2003. Effect of chemical kinetic uncertainties on photochemical modeling results: Application to Saturn's atmosphere. Astron. Astrophys. 398, 335–344.
Dobrijevic, M. et al., 2010a. Key reactions in the photochemistry of hydrocarbons in Neptune's stratosphere. Planet. Space Sci. 58, 1555–1566.
Dobrijevic, M. et al., 2010b. Comparison of methods for the determination of key reactions in chemical systems: Application to Titan's atmosphere. Adv. Space Res. 45, 77–91.
Dobrijevic, M., Cavalié, T., Billebaud, F., 2011. A methodology to construct a reduced chemical scheme for 2D-3D photochemical models: Application to Saturn. Icarus 214, 275–285.
Dobrijevic, M. et al., 2014. Coupling of oxygen, nitrogen, and hydrocarbon species in the photochemistry of Titan's atmosphere. Icarus 228, 324–346.
Dowling, T.E. et al., 2006. The EPIC atmospheric model with an isentropic/terrain-following hybrid vertical coordinate. Icarus 182, 259–273.
Dowling, T.E. et al. 2010. New radiative transfer capability in the EPIC atmospheric model with application to Saturn and Uranus. In: AAS/Division for Planetary Science Meeting Abstracts #42, vol. 42. Bulletin of the American Astronomical Society. p. 1021.
Edgington, S.G. et al. 2012. Photochemistry in Saturn's ring shadowed atmosphere: Production rates of key atmospheric molecules and preliminary analysis of observations. American Geophysical Union (Fall). Abstracts B1946.
Fischer, G. et al., 2011. A giant thunderstorm on Saturn. Nature 475 (7354), 75–77.
Flasar, F.M. et al., 2004. An intense stratospheric jet on Jupiter. Nature 427, 132–135.
Flasar, F.M. et al., 2005. Temperatures, winds, and composition in the Saturnian system. Science 307, 1247–1251.
Fletcher, L.N. et al., 2007. Characterising Saturn's vertical temperature structure from Cassini/CIRS. Icarus 189, 457–478.
Fletcher, L.N. et al., 2009. Methane and its isotopologues on Saturn from Cassini/CIRS observations. Icarus 199, 351–367.
Fletcher, L.N. et al., 2010. Seasonal change on Saturn from Cassini/CIRS observations, 2004–2009. Icarus 208, 337–352.
Fletcher, L.N. et al., 2011. Thermal structure and dynamics of Saturn's northern springtime disturbance. Science 332 (6036), 1413–1417.
Fletcher, L.N. et al., 2012. The origin and evolution of Saturn's 2011–2012 stratospheric vortex. Icarus 221, 560–586.
Fouchet, T. et al., 2008. An equatorial oscillation in Saturn's middle atmosphere. Nature 453, 200–202.
Fouchet, T., Moses, J.I., Conrath, B.J. 2009. Saturn: Composition and Chemistry. p. 83.
Friedson, A.J., Moses, J.I., 2012. General circulation and transport in Saturn's upper troposphere and stratosphere. Icarus 218, 861–875.
Fuller, E.N., Schettler, P.D., Giddings, J.C., 1966. New method for prediction of binary gas-phase diffusion coefficients. Ind. Eng. Chem. 58 (5), 18–27.
Fuller, E.N., Ensley, K., Giddings, J.C., 1969. Diffusion of halogenated hydrocarbons in helium. The effect of structure on collision cross sections. J. Phys. Chem. 73 (11), 3679–3685.
Gezari, D.Y. et al., 1989. New features in Saturn's atmosphere revealed by high-resolution thermal infrared images. Nature 342, 777–780.
Gillett, F.C., Orton, G.S., 1975. Center-to-limb observations of Saturn in the thermal infrared. Astrophys. J. 195, L47–L49.
Godunov, S., 1959. A difference scheme for numerical solution of discontinuous solution of hydrodynamic equations. Math. Sbornik 47, 271–306.
Greathouse, T.K. et al., 2005. Meridional variations of temperature, C_2 H_2 and C_2H_6 abundances in Saturn's stratosphere at southern summer solstice. Icarus 177, 18–31.
Greathouse, T.K. et al. 2008. A general radiative seasonal climate model applied to Saturn, Uranus, and Neptune. American Geophysical Union (Fall). Abstracts B6.
Guerlet, S. et al., 2009. Vertical and meridional distribution of ethane, acetylene and propane in Saturn's stratosphere from CIRS/Cassini limb observations. Icarus 203, 214–232.
Guerlet, S. et al., 2010. Meridional distribution of CH_3C_2H and C_4 H_2 in Saturn's stratosphere from CIRS/Cassini limb and nadir observations. Icarus 209, 682–695.
Guerlet, S. et al., 2011. Evolution of the equatorial oscillation in Saturn's stratosphere between 2005 and 2010 from Cassini/CIRS limb data analysis. Geophys. Res. Lett. 38, 9201.
Guerlet, S. et al., 2014. Global climate modeling of Saturn's atmosphere. Part i: Evaluation of the radiative transfer model. Icarus 238 (0), 110–124.
Guillot, T., 2005. The interiors of giant planets: Models and outstanding questions. Annu. Rev. Earth Planet. Sci. 33, 493–530.
Hanel, R. et al., 1981. Infrared observations of the Saturnian system from Voyager 1. Science 212, 192–200.
Hanel, R. et al., 1982. Infrared observations of the Saturnian system from Voyager 2. Science 215, 544–548.
Hartogh, P. et al., 2009. Water and related chemistry in the Solar System. A guaranteed time key programme for Herschel. Planet. Space Sci. 57, 1596–1606.
Hartogh, P. et al., 2011. Direct detection of the Enceladus water torus with Herschel. Astron. Astrophys. 532, L2.
Hébrard, E. et al., 2013. Photochemistry of C_3H_p hydrocarbons in Titan's stratosphere revisited. Astron. Astrophys. 552, A132.
Hesman, B.E. et al., 2009. Saturn's latitudinal C_2H_2 and C_2H_6 abundance profiles from Cassini/CIRS and ground-based observations. Icarus 202, 249–259.
Howett, C.J.A. et al., 2007. Meridional variations in stratospheric acetylene and ethane in the southern hemisphere of the saturnian atmosphere as determined from Cassini/CIRS measurements. Icarus 190, 556–572.
Ingersoll, A.P., Pollard, D., 1982. Motion in the interiors and atmospheres of Jupiter and Saturn – Scale analysis, anelastic equations, barotropic stability criterion. Icarus 52, 62–80.
Irwin, P., 2006. Giant Planets of Our Solar System: An Introduction. Springer Praxis Books/Astronomy and Planetary Sciences Series. Springer.
Li, L. et al., 2010. Saturn's emitted power. J. Geophys. Res. (Planets) 115, 11002.
Liang, M.-C. et al., 2005. Meridional Transport in the Stratosphere of Jupiter. Astrophys. J. 635, L177–L180.
Lindal, G.F., Sweetnam, D.N., Eshleman, V.R., 1985. The atmosphere of Saturn – An analysis of the Voyager radio occultation measurements. Astron. J. 90, 1136–1146.
Lindzen, R., 1971. Tides and gravity waves in the upper atmosphere (internal gravity waves and tidal oscillations excitation mechanism in upper atmosphere). In: Mesospheric Models and Related Experiments, 122130.
Lindzen, R.S., 1981. Turbulence and stress owing to gravity wave and tidal breakdown. J. Geophys. Res.: Oceans (1978–2012) 86 (C10), 9707–9714.
Loison, J.C. et al., 2015. The neutral photochemistry of nitriles, amines and imines in the atmosphere of titan. Icarus 247, 218–247. http://dx.doi.org/10.1016/j.icarus.2014.09.039.
Medvedev, A.S., Sethunadh, J., Hartogh, P., 2013. From cold to warm gas giants: A three-dimensional atmospheric general circulation modeling. Icarus 225, 228–235.
Moreno, R. et al., 2003. Long-term evolution of CO, CS and HCN in Jupiter after the impacts of Comet Shoemaker-Levy 9. Planet. Space Sci. 51, 591–611.
Moses, J.I., Greathouse, T.K., 2005. Latitudinal and seasonal models of stratospheric photochemistry on Saturn: Comparison with infrared data from IRTF/TEXES. J. Geophys. Res. (Planets) 110, 9007.
Moses, J.I. et al., 2000a. Photochemistry of Saturn's atmosphere. I. Hydrocarbon chemistry and comparisons with ISO observations. Icarus 143, 244–298.
Moses, J.I. et al., 2000b. Photochemistry of Saturn's atmosphere. II. Effects of an influx of external oxygen. Icarus 145, 166–202.
Moses, J.I. et al., 2005. Photochemistry and diffusion in Jupiter's stratosphere: Constraints from ISO observations and comparisons with other giant planets. J. Geophys. Res. 110, 8001.
Moses, J.I. et al. 2007. Meridional distribution of hydrocarbons on Saturn: Implications for stratospheric transport. In: Planetary Atmospheres. pp. 85–86.
Ollivier, J.L. et al., 2000a. Seasonal effects in the thermal structure of Saturn's stratosphere from infrared imaging at 10 microns. Astron. Astrophys. 356, 347–356.
Ollivier, J.L., Dobrijévic, M., Parisot, J.P., 2000b. New photochemical model of Saturn's atmosphere. Planet. Space Sci. 48, 699–716.
Orton, G.S. et al., 2008. Semi-annual oscillations in Saturn's low-latitude stratospheric temperatures. Nature 453, 196–199.
Pirraglia, J.A. et al., 1981. Thermal structure and dynamics of Saturn and Jupiter. Nature 292, 677–679.
Rieke, G.H., 1975. The thermal radiation of Saturn and its rings. Icarus 26, 37–44.
Romani, P.N., Atreya, S.K., 1988. Methane photochemistry and methane production on Neptune. Icarus 74, 424–445.
Sánchez-Lavega, A. et al., 2011. Deep winds beneath Saturn's upper clouds from a seasonal long-lived planetary-scale storm. Nature 475, 71–74.
Simon-Miller, A.A. et al. 2005. Cassini CIRS measurements of benzene, propane and carbon dioxide on Saturn. In: AAS/Division for Planetary Sciences Meeting Abstracts #37, vol. 37. Bulletin of the American Astronomical Society. p. 682.

Sinclair, J.A. et al., 2013. Seasonal variations of temperature, acetylene and ethane in Saturn's atmosphere from 2005 to 2010, as observed by Cassini-CIRS. Icarus 225, 257–271.
Sinclair, J.A. et al., 2014. From Voyager-IRIS to Cassini-CIRS: Interannual variability in Saturn's stratosphere? Icarus 233, 281–292.
Smith, B.A. et al., 1982. A new look at the Saturn system – The Voyager 2 images. Science 215, 504–537.
Smith, G.R. et al., 1983. Saturn's upper atmosphere from the Voyager 2 EUV solar and stellar occultations. J. Geophys. Res. 88, 8667–8678.
Tokunaga, A.T. et al., 1978. Spatially resolved infrared observations of Saturn. II – The temperature enhancement at the South Pole of Saturn. Icarus 36, 216–222.
West, R.A., Friedson, A.J., Appleby, J.F., 1992. Jovian large-scale stratospheric circulation. Icarus 100, 245–259.
Yelle, R.V., Griffith, C.A., Young, L.A., 2001. Structure of the jovian stratosphere at the Galileo probe entry site. Icarus 152, 331–346.
Zhang, X., Shia, R.-L., Yung, Y.L., 2013. Jovian stratosphere as a chemical transport system: Benchmark analytical solutions. Astrophys. J. 767, 172.

A&A 562, A33 (2014)
DOI: 10.1051/0004-6361/201322297

Astronomy & Astrophysics

The first submillimeter observation of CO in the stratosphere of Uranus*

T. Cavalié[1,2], R. Moreno[3], E. Lellouch[3], P. Hartogh[4], O. Venot[5], G. S. Orton[6], C. Jarchow[4], T. Encrenaz[3], F. Selsis[1,2], F. Hersant[1,2], and L. N. Fletcher[7]

[1] Univ. Bordeaux, LAB, UMR 5804, 33270 Floirac, France
e-mail: cavalie@obs.u-bordeaux1.fr
[2] CNRS, LAB, UMR 5804, 33270 Floirac, France
[3] LESIA – Observatoire de Paris, CNRS, Université Paris 06, Université Paris-Diderot, Meudon, France
[4] Max Planck Institut für Sonnensystemforschung, Katlenburg-Lindau, Germany
[5] Instituut voor Sterrenkunde, Katholieke Universiteit Leuven, Leuven, Belgium
[6] Jet Propulsion Laboratory, California Institute of Technology, Pasadena, USA
[7] Atmospheric, Oceanic and Planetary Physics, Clarendon Laboratory, University of Oxford, Parks Road, Oxford OX1 3PU, UK

Received 17 July 2013 / Accepted 7 November 2013

ABSTRACT

Context. Carbon monoxide (CO) has been detected in all giant planets and its origin is both internal and external in Jupiter and Neptune. Despite its first detection in Uranus a decade ago, the magnitude of its internal and external sources remains unconstrained.
Aims. We targeted CO lines in Uranus in the submillimeter range to constrain its origin.
Methods. We recorded the disk-averaged spectrum of Uranus with very high spectral resolution at the frequencies of CO rotational lines in the submillimeter range in 2011−2012. We used empirical and diffusion models of the atmosphere of Uranus to constrain the origin of CO. We also used a thermochemical model of its troposphere to derive an upper limit on the oxygen-to-hydrogen (O/H) ratio in the deep atmosphere of Uranus.
Results. We have detected the CO(8−7) rotational line for the first time with *Herschel*-HIFI. Both empirical and diffusion models results show that CO has an external origin. An empirical profile in which CO is constant above the 100 mbar level with a mole fraction of $7.1{-}9.0 \times 10^{-9}$, depending on the adopted stratospheric thermal structure, reproduces the data. Sporadic and steady source models cannot be differentiated with our data. Taking the internal source model upper limit of a mole fraction of 2.1×10^{-9} we find, based on our thermochemical computations, that the deep O/H ratio of Uranus is less than 500 times solar.
Conclusions. Our work shows that the average mole fraction of CO decreases from the stratosphere to the troposphere and thus strongly advocates for an external source of CO in Uranus. Photochemical modeling of oxygen species in the atmosphere of Uranus and more sensitive observations are needed to reveal the nature of the external source.

Key words. planets and satellites: individual: Uranus – planets and satellites: atmospheres – submillimeter: planetary systems

1. Introduction

The detection of water vapor (H_2O) and carbon dioxide (CO_2) in the stratospheres of the giant planets and Titan by Feuchtgruber et al. (1997), Coustenis et al. (1998), Samuelson et al. (1983), and Burgdorf et al. (2006) has raised several questions: what are the sources of oxygen to their upper atmospheres? And do the sources vary from planet to planet? Oxygen-rich deep interiors of the giant planets cannot explain the observations because these species are trapped by condensation below their tropopause (except CO_2 in Jupiter and Saturn). Therefore, several sources in their direct or far environment have been proposed: icy rings and/or satellites (Strobel & Yung 1979), interplanetary dust particles (IDP; Prather et al. 1978), and large comet impacts (Lellouch et al. 1995).

While the relative similarity of the infall fluxes inferred for H_2O by Feuchtgruber et al. (1997) may indicate that IDP could be the source for all giant planets (Landgraf et al. 2002), infrared and far-infrared observations have unveiled a quite different picture. Infrared Space Observatory, *Cassini, Odin*, and *Herschel* observations proove that the Jovian stratospheric H_2O and CO_2 originate from the Shoemaker-Levy 9 (SL9) comet impacts (Lellouch et al. 2002, 2006; Cavalié et al. 2008a, 2012, 2013), while *Herschel* recently shows that the external flux of water at Saturn and Titan is likely due to the Enceladus geysers and the water torus they feed (Hartogh et al. 2011; Moreno et al. 2012).

The situation is even more complex for carbon monoxide (CO). Because CO does not condense at the tropopauses of giant planets, oxygen-rich interiors are also a potential source. An internal component has indeed been observed in the vertical profile of CO in Jupiter by Bézard et al. (2002) and in Neptune, originally by Marten et al. (1993) and Guilloteau et al. (1993), while an upper limit has been set on its magnitude by Cavalié et al. (2009) and Fletcher et al. (2012) for Saturn. The measurement of the tropospheric mole fraction of CO can be used to constrain the deep oxygen-to-hydrogen (O/H) ratio (Lodders & Fegley 1994), which is believed to be representative of condensation processes of the planetesimals that formed the giant planets (Owen et al. 1999; Gautier & Hersant 2005). On the other hand, large comets seem to be the dominant external source, as

* *Herschel* is an ESA space observatory with science instruments provided by European-led Principal Investigator consortia and with important participation from NASA.

Table 1. Summary of the *Herschel*-HIFI observations of CO in Uranus.

Date	OD	Obs. ID	ν [GHz]	Δt [h]	θ_{HIFI} [$''$]	θ_{Uranus} [$''$]
2011-07-01	779	1342223423	921.800 GHz	1.82	23.0	3.53
2012-06-15	1128	1342247027	921.800 GHz	2.54	23.0	3.47
2012-06-15	1128	1342247028	921.800 GHz	2.54	23.0	3.47
2012-06-15	1128	1342247029	921.800 GHz	2.54	23.0	3.47

Notes. OD means operational day, ν is the CO line center frequency, Δt is the total integration time, θ_{HIFI} is the *Herschel*-HIFI telescope beamwidth, and θ_{Uranus} is the equatorial diameter of Uranus.

shown by various studies: Bézard et al. (2002) and Moreno et al. (2003), for Jupiter, Cavalié et al. (2010), for Saturn and Lellouch et al. (2005, 2010), Hesman et al. (2007), Fletcher et al. (2010) and Luszcz-Cook & de Pater (2013), for Neptune.

The first detection of CO in Uranus was obtained by Encrenaz et al. (2004) from fluorescent emission at 4.7 μm. They derived a mixing ratio of 2×10^{-8} by assuming a uniform distribution throughout the atmosphere. The authors tentatively proposed that CO was depleted below the tropopause, suggesting that CO would have an external origin. Despite this first detection almost a decade ago, the situation has remained unclear. Ground-based heterodyne spectroscopy has been used unsuccessfully in the past to try and detect CO in Uranus. Rosenqvist et al. (1992) first set an upper limit of 4×10^{-8} and subsequent attempts to detect CO have failed so far (Marten et al. 1993; Cavalié et al. 2008b). In this paper, we present observations of CO in Uranus carried out with the *Herschel* Space Observatory (Pilbratt et al. 2010) in 2011−2012, which led to the first detection of CO in Uranus in the submillimeter range.

In the following sections, we will describe the observations, their modeling, and our derivations of new constraints on the origin of CO in Uranus and its deep O/H ratio.

2. Observations

We observed the CO(8−7) line at 921.800 GHz with the Heterodyne Instrument for the Far-Infrared (HIFI, de Graauw et al. 2010) aboard *Herschel* (Pilbratt et al. 2010) on July 1, 2011, as part of the guaranteed time key program "Water and related chemistry in the solar system", also known as "*Herschel* solar system Observations" (HssO; Hartogh et al. 2009). The CO(8−7) line was targeted in Uranus for ~two hours. The resulting spectrum led us to a tentative detection of CO in Uranus at the level of $\sim 2.5\sigma$ (on the line peak) at native resolution and encouraged us to perform a deeper integration of this line.

We obtained an ~eight-hour integration (split into three observations of equal length) of the same line on June 15, 2012, as part of the *Herschel* open time 2 program OT2_tcavalie_6. We performed the observations in double-beam switch mode with the Wide-Band Spectrometer (WBS) at a nominal spectral resolution of 1.1 MHz (more details given in Table 1). We processed the data with the *Herschel* interactive processing environment (HIPE 9, Ott 2010) up to Level 2 for the horizontal (H) and vertical (V) polarizations and stitched the WBS subbands together. We determined the baseline ripple frequencies caused by the strong continuum emission of Uranus with a normalized periodogram (Lomb 1976) and we removed the three or four strongest sine waves. Those sine waves are caused by the hot and cold black bodies and by the local oscillator chain of the instrument and have periods of 90−100 MHz (Roelfsema et al. 2012). We corrected the double-sideband response of HIFI by assuming a sideband ratio of 1, i.e., a single sideband gain of 0.5

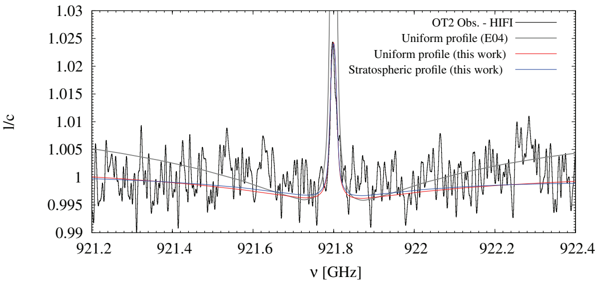

Fig. 1. *Herschel*-HIFI observation of the CO(8−7) line in Uranus on June 15, 2012, expressed in terms of line-to-continuum ratio (l/c, black line). This line can be modeled successfully with either empirical models: (i) a "uniform" profile with a constant mole fraction of 7.2×10^{-9} throughout the atmosphere (red line); and (ii) a "stratospheric" profile with a constant mole fraction of 7.1×10^{-9} above the 100 mbar level and zero below it (blue line). The spectrum resulting from the Encrenaz et al. (2004) uniform source profile is also shown for comparison (grey line, labeled "E04"). The synthetic lines are obtained with the thermal profile of Feuchtgruber et al. (2013).

(Roelfsema et al. 2012), and identical continuum levels in both sidebands. The uncertainty on the sideband ratio is 12% (3% on the single sideband gain), and the continuum levels in the two sidebands should differ by less than 1%, according to our model. Finally, we coadded the H and V polarizations after weighting them according to their respective noise levels (the V spectra were always noisier than the H spectra). We obtained a clear detection at the level of 7σ on the line peak, at a smoothed resolution of 8 MHz using a gaussian lineshape, on the combined eight-hour observation shown in Fig. 1. Because we have not performed any absolute calibration, we analyze this line in terms of line-to-continuum ratio (l/c). The observed continuum levels differ by 6% in the H and V polarizations, and so we have to account for an additional uncertainty of 3% on the continuum level of our averaged spectrum.

We note that we also targeted the CO (3−2) and (6−5) lines (at 345.796 GHz and 691.473 GHz, respectively) in Uranus using the Heterodyne Receiver Array Programme (HARP) receiver array and the D-band receiver, respectively, of the *James Clerk Maxwell* Telescope (JCMT) on October 15−16 and November 2, 2009, as part of the M09BI02 project. These observations resulted in the determination of an upper limit of 6×10^{-8} uniform with altitude up to the CO homopause for the CO mole fraction and will not be discussed further.

3. Models and results

3.1. Radiative transfer model

We performed all spectral line computations with the forward radiative transfer model detailed in Cavalié et al. (2008b, 2013), adapted to Uranus. This line-by-line model accounts for the elliptical geometry of the planet and its rapid rotation. Opacity due to H_2-He-CH_4 collision-induced absorption (Borysow et al. 1985, 1988; Borysow & Frommhold 1986) was included. Orton et al. (2007) published H_2-H_2 collision-induced coefficient tables, which reproduce the continuum of Uranus between 700 and 1100 cm^{-1} as observed by *Spitzer* better, but these coefficients do not differ significantly in the wavelength range of our observations. We used the JPL Molecular Spectroscopy catalog Pickett et al. (1998) and the H_2/He pressure-broadening parameters for CO lines from Sung & Varanasi (2004) and Mantz et al. (2005), i.e., a collisional linewidth at 300 K of 0.0661 cm^{-1} atm^{-1} for the CO(8−7) line and a temperature dependence exponent of 0.638. We used the thermal profiles of Feuchtgruber et al. (2013) and Orton et al. (2013a). They have the same tropopause temperature (53 K), but the profile of Feuchtgruber et al. (2013) is continuously warmer than the profile of Orton et al. (2013a) in the stratosphere (by 2 K at 10 mbar, 5 K at 1 mbar, and 11 K at 0.1 mbar). We present results for both thermal profiles hereafter. We smoothed all synthetic lines to the working resolution of 8 MHz using a gaussian lineshape.

The CO line is optically thin with $\tau = 0.04-0.25$ (depending on models) and probes the stratosphere of Uranus between the 0.1 and 5 mbar levels, allowing us to derive information on the CO abundance. The signal-to-noise ratio (S/N) of the observations results in error bars of 14%. By adding this uncertainty quadratically with other uncertainty sources (sideband ratio, continuum levels), we end up with an uncertainty of 19% on the results presented hereafter.

3.2. Empirical models

We tested two classes of empirical models: (i) uniform profiles (referred to as "uniform" hereafter); and (ii) uniform profiles in the stratosphere down to a cutoff pressure level (referred to as "stratospheric" hereafter). These profiles are not physically plausible mainly due to the low homopause in Uranus (see next subsection), but were considered for comparison with Encrenaz et al. (2004) and Teanby & Irwin (2013). Our results are described hereafter and are summarized in Table 2.

The uniform distribution of Encrenaz et al. (2004) with a CO mole fraction of 2×10^{-8} overestimates the observed line core by a factor of 2.5−3. The observed line can be fitted with a "uniform" profile in which the CO mole fraction is 7.2×10^{-9} with the profile of Feuchtgruber et al. (2013), or 9.3×10^{-9} with the profile of Orton et al. (2013a).

The line can be fitted equally well with a "stratospheric" profile in which the CO is constant above the 100 mbar level with a CO mole fraction of 7.1×10^{-9} with the thermal profile of Feuchtgruber et al. (2013), or 9.0×10^{-9} with the profile of Orton et al. (2013a). For comparison with other papers (e.g., Encrenaz et al. 2004; Cavalié et al. 2008b; Teanby & Irwin 2013), we set this transition level to 100 mbar, but our computations show this level could be located anywhere between ∼3 and 1000 mbar. Our results in terms of mole fraction would be affected by less than 10%. If set above the 3 mbar level, then more CO would be needed.

From these empirical models, it is not possible to favor an internal or an external origin for CO in the atmosphere of Uranus because the models cannot be distinguished (see Fig. 1).

Fortunately, Teanby & Irwin (2013) recently published *Herschel*-SPIRE observations at CO line wavelengths. These observations are sensitive to the 10−2000 mbar range, with a contribution function peak at 200 mbar (see their Fig. 2b), and they did not result in any detection. Those authors have set a stringent upper limit of 2.1×10^{-9} on the CO mole fraction in their internal source model. This is ∼3−5 times lower than required by our observations. It is thus a clear indication that the HIFI line is caused by external CO.

Table 2. Summary of the empirical and diffusion model results.

	Empirical model		
Thermal profile	Uniform	Stratospheric	
Feuchtgruber	7.2×10^{-9}	7.1×10^{-9}	
Orton	9.3×10^{-9}	9.0×10^{-9}	
	Diffusion model		
Thermal profile	Internal source	External source	
	y_{CO}	ϕ_{CO}	y_0
Feuchtgruber	1.9×10^{-8}	2.2×10^5	3.1×10^{-7}
Orton	2.7×10^{-8}	2.7×10^5	3.9×10^{-7}

Notes. All results are mole fractions, except ϕ_{CO} (in cm^{-2} s^{-1}). The cutoff level in the "stratospheric" empirical model is at 100 mbar. The internal source value of y_{CO} in the diffusion model enables fitting the CO line core amplitude, but the line is too broad and additional broad wings incompatible with the data are generated.

3.3. Diffusion model

Uranus has the lowest homopause amongst the giant planets (Orton et al. 1987; Moses et al. 2005). It is located around the 1 mbar level, where submillimeter observations generally probe. Therefore, we computed more realistic CO vertical profiles by accounting for diffusion processes to see how our previous results are impacted by the low homopause of Uranus. Such modeling also shows how the various external sources can be parametrized.

The vertical profile of CO primarily depends on the sources of CO, but it is also influenced by other oxygen sources. Indeed, O produced by H_2O photolysis reacts with CH_3 and other hydrocarbons to produce CO (Moses et al. 2000). The magnitude of the H_2O flux is still quite uncertain, mostly due to limitations in the knowledge of the thermal structure and eddy mixing at the time of the observations of Feuchtgruber et al. (1997). For the sake of simplicity, we ignored (photo-)chemical processes.

We adapted the 1D time-dependent model of Dobrijevic et al. (2010, 2011) to Uranus and removed all photochemical processes. Orton et al. (2013b) constrained the stratospheric K_{zz} within [1000:1500] cm^2 s^{-1} (vertically constant) with CH_4 and C_2H_6 *Spitzer* observations. We took their best fit value (1200 cm^2 s^{-1}) in our model. We tested three sources of CO, representing simple cases: (i) an internal source; (ii) a steady flux of micrometeorites (IDP); and (iii) a single large comet impact[1]. The three sources tested are controlled by a few parameters: (i) the tropospheric CO mole fraction y_{CO} for an internal source; (ii) the flux ϕ_{CO} at the upper boundary of the model atmosphere for a steady source; and (iii) the equivalent mole fraction of CO y_0 deposited by a comet and averaged over the planet. We assumed that all the CO was deposited at levels higher than 0.1 mbar in analogy to the SL9 impacts (Lellouch et al. 1995; Moreno et al. 2003) and that the impact time $\Delta t \sim 300$ years as it roughly corresponds to the diffusion

[1] This does not exclude a combination of internal and external sources, or any intermediate situation between a continuum of micrometeoritic impacts and a single impact event.

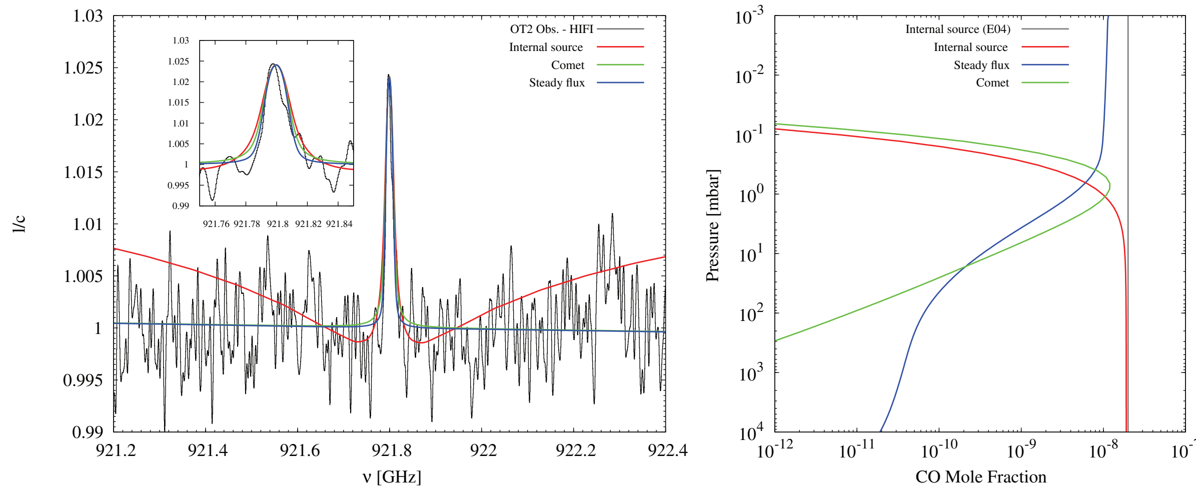

Fig. 2. *Left*: *Herschel*-HIFI observation of the CO(8−7) line in Uranus on June 15, 2012, expressed in terms of line-to-continuum ratio (l/c, black line). For each source, the models that best fit the emission core are displayed: an internal source yielding a mole fraction of 1.9×10^{-8} in the upper troposphere (red line), a steady external flux (due to IDP or a local source) of 2.2×10^5 cm^{-2} s^{-1} (blue line), and a comet with a diameter of 640 m depositing 3.4×10^{13} g of CO above the 0.1 mbar level ∼300 years ago (green line). These models were computed with the thermal profile of Feuchtgruber et al. (2013). The internal source model overestimates the line core width and produces a broad absorption that is not observed in the data. The external source models can barely be differentiated. *Right*: vertical profiles associated with the spectra.

time down to 1 mbar in Uranus in our model, but other combinations of deposition time and level are possible. To infer the mass and diameter of the comet, we assumed the comet density was 0.5 g cm^{-3} (Weissman et al. 2004; Davidsson et al. 2007) and that the comet yielded 50% CO at impact (Lellouch et al. 1997).

The vertical profiles and resulting spectra corresponding to the three sources, as obtained with the thermal profile of Feuchtgruber et al. (2013), are displayed in Fig. 2. The best fits to the spectrum are obtained for external source models. Despite resulting in different vertical profiles, a steady flux $\phi_{CO} = 2.2 \times 10^5$ cm^{-2} s^{-1} and a 640 m diameter comet depositing 3.5×10^{13} g of CO ($y_0 = 3.1 \times 10^{-7}$) result in lines that are indistinguishable from the standpoint of our observations. Such impact at Uranus occurs every ∼500 years with a factor of 6 uncertainty (Zahnle et al. 2003). Such timescales are fully compatible with our assumption on Δt. With the thermal profile of Orton et al. (2013a), we obtain slightly higher values because of lower stratospheric temperatures: $\phi_{CO} = 2.7 \times 10^5$ cm^{-2} s^{-1} and $y_0 = 3.9 \times 10^{-7}$ (i.e., a 700 m diameter comet). All fit parameters are listed in Table 2. These values remain to be confirmed by more rigorous (photochemical) modeling and higher S/N data.

The amplitude of the CO emission peak is reproduced with an internal source model in which $y_{CO} = 1.9 \times 10^{-8}$ (see Fig. 2). With the thermal profile of Orton et al. (2013a), $y_{CO} = 2.7 \times 10^{-8}$. We note that ∼three times more tropospheric CO is needed in this model, compared to the "uniform" empirical model value derived in Sect. 3.2. This is due to the fact that the observed emission line probes the mbar level, i.e., where the CO vertical profile sharply decreases because of the low homopause in the atmosphere of Uranus. As a result, a stronger internal source is required to reach a sufficient level of abundance of CO around the mbar level. The main outcome of this model is that it now overestimates the line core width and results in additional broad absorption because CO is much more abundant in the lower stratosphere than in the external source models (by as much as two orders of magnitude at 10 mbar). The absence of such a broad CO absorption in the data cannot be caused by our sinusoidal ripple removal procedure because we have removed sine waves of much shorter period than the total width of such broad absorption wings. We can rule out the internal source model because the width of the line core is not fitted, there is no broad absorption in the spectrum, and the derived y_{CO} values are an order of magnitude larger than the upper limit set by *Herschel*-SPIRE observations of this region of the atmosphere (Teanby & Irwin 2013). Thus, as long as there is no significant photochemical source of CO in the stratosphere, the HIFI line is caused by external CO.

3.4. An upper limit on the deep O/H ratio in Uranus

Thermochemistry in the deep interior of Uranus links the CO abundance to H_2O abundance and thus to the internal O/H ratio (Fegley & Prinn 1988; Lodders & Fegley 1994) with the following net thermochemical equilibrium reaction,

$$H_2O + CH_4 = CO + 3H_2.$$

The upper tropospheric mole fraction of CO is fixed at the level where the thermochemical equilibrium is quenched by vertical diffusion.

The upper limit of Teanby & Irwin (2013) on the internal source ($y_{CO} = 2.1 \times 10^{-9}$) can be further used to try and constrain the deep atmospheric O/H ratio in Uranus. Their observations probe between 10 and 2000 mbar, i.e., well below the homopause level (see Fig. 2 right). As a consequence, this upper limit is valid even if the authors have not accounted for the low homopause of Uranus.

We have adapted the thermochemical model developed by Venot et al. (2012) to Uranus to constrain the O/H ratio. This model accounts for C, N, and O species. We extended our thermal profile to high pressures following the dry adiabat. The profiles of Feuchtgruber et al. (2013) and Orton et al. (2013a) are similar in the upper troposphere and thus give similar deep tropospheric profiles. We constrained the O/H and C/H ratios by fitting the following upper tropospheric mole fractions with errors

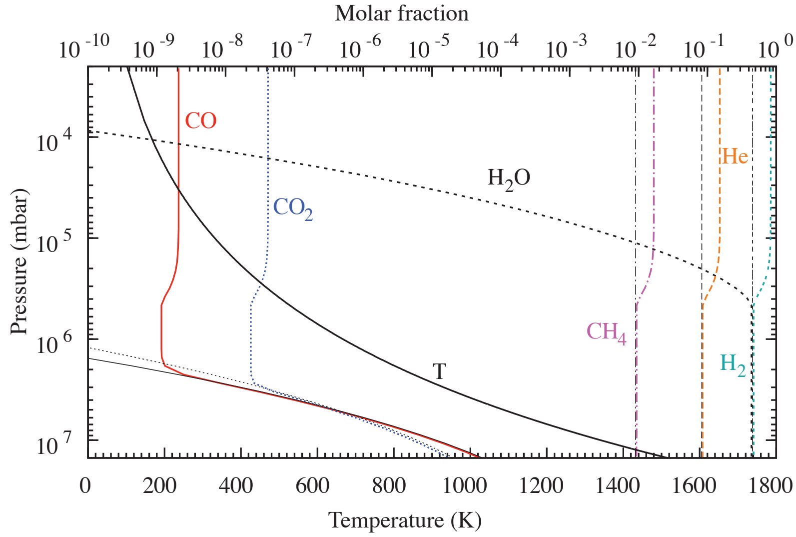

Fig. 3. Molar fraction profiles in the troposphere of Uranus obtained with the model of Venot et al. (2012), targeting the 2.1×10^{-9} upper limit on the upper tropospheric CO mole fraction obtained by Teanby & Irwin (2013). The temperature profile in the troposphere is shown with a solid black line. Thermochemical equilibrium profiles are plotted in black with the same layout as their corresponding species. CO and CO_2 are quenched around $2-3 \times 10^6$ mbar. H_2O departs from thermochemical equilibrium because of condensation and causes an increase of other species mole fractions (the sum of all mole fractions is normalized to unity at all levels). The model parameters are: O/H $= 501\odot$, C/H $= 18\odot$, and $K_{zz} = 10^8$ cm^2 s^{-1}.

lower than 4%: 0.152 for He (Conrath et al. 1987), 0.016 for CH_4 (Baines et al. 1995; Sromovsky & Fry 2008), and the 2.1×10^{-9} upper limit for CO. The level at which CO is quenched depends not only on the temperature profile and the deep O/H ratio, but also on the deep K_{zz}. By assuming Uranus' interior is convective, we estimate K_{zz} from the planet's internal heat flux (Stone 1976). Following Pearl et al. (1990), $K_{zz} \sim 10^8$ cm^2 s^{-1}, within one order of magnitude (Lodders & Fegley 1994). The resulting tropospheric vertical profiles for this nominal model are shown in Fig. 3. The elemental ratios in this model are 501 times solar for O/H and 18 times solar for C/H (with solar abundances, $\odot$ hereafter, taken from Asplund et al. 2009). The N species have no significant impact on the C and O species. We also computed the elemental ratios in a series of additional models to evaluate the influence of parameters like K_{zz} and the upper tropospheric CH_4 mole fraction on the O/H ratio. The results are displayed in Table 3. We find that the deep O/H is lower than $\sim 500\odot$ (nominal model), but could be even below $340\odot$ to be in agreement with the CO tropospheric upper limit in all cases. On Neptune, Luszcz-Cook & de Pater (2013) find that "an upwelled CO mole fraction of 0.1 ppm implies a global O/H enrichment of at least 400, and likely more than 650 times the protosolar value".

Table 3. Summary of the thermochemical model results.

Model	K_{zz} cm^2 s^{-1}	y_{CH_4} $\times 10^{-2}$	C/H $\times\odot^a$	y_{CO} $\times 10^{-9}$	O/H $\times\odot^b$
Nominal	10^8	1.6^c	18	2.1	501
CH_4-rich	10^8	3.2^d	40	2.1	417
low K_{zz}	10^7	1.6	13	2.1	631
high K_{zz}	10^9	1.6	23	2.1	339

Notes. We obtained values so as to reach the 2.1×10^{-9} upper limit of Teanby & Irwin (2013) for the CO upper tropospheric mole fraction. [(a)] Solar C/H volume ratio: 2.69×10^{-4} (Asplund et al. 2009). [(b)] Solar O/H volume ratio: 4.90×10^{-4} (Asplund et al. 2009). [(c)] Baines et al. (1995) and Sromovsky & Fry (2008). [(d)] Fry et al. (2013); Sromovsky et al. (2011); and Karkoschka & Tomasko (2009).

4. Discussion and conclusion

We detected the CO(8−7) line at 921.800 GHz in Uranus with *Herschel* and we constrained its possible sources.

Herschel-HIFI (this work) and *Herschel*-SPIRE (Teanby & Irwin 2013) results show that the average CO mole fraction is decreasing from the stratosphere to the troposphere. This suggests the deep interior is not the source of the observed CO. Our diffusion model calculations confirm that the internal source hypothesis is not valid and show that Uranus has an external source of CO as long as there is not a significant photochemical source of CO in the stratosphere. The data can be successfully fitted with an empirical model in which CO has a mole fraction of $7.1-9.0 \times 10^{-9}$ above the 100 mbar level (value depending on the chosen thermal profile). There is a contradiction between this model's mole fraction values and the mole fraction reported by Encrenaz et al. (2004) (3×10^{-8} in their external source model). Regarding this apparent discrepancy, we note that modeling LTE emission from CO rotational lines is much simpler than inferring an abundance from non-LTE fluorescence (e.g., López-Valverde et al. 2005). At any rate, a reanalysis of the Encrenaz et al. (2004) data in the light of CO distributions proposed in this paper should be performed.

Comet and steady source models, in which diffusion processes are accounted for, give very similar fit to the data. These results should be confirmed with more elaborate models, i.e., photochemical models and more sensitive observations. Oxygen photochemistry computations, taking nearly concomitant measurements of the thermal profile (Feuchtgruber et al. 2013; Orton et al. 2013a), of the influx of H_2O (Jarchow et al., in prep.), and of the influx of CO_2 (Orton et al. 2013b), into account would enable us to draw better constraints on the external source of oxygen. It would certainly reduce the external flux of CO or the mass of the impacting comet we obtained from a simple diffusion model because the chemical conversion of H_2O into CO would already provide a significant part of the observed stratospheric column of CO.

We used the internal source upper limit derived by Teanby & Irwin (2013) ($y_{CO} = 2.1 \times 10^{-9}$), which also contradicts the detection level of Encrenaz et al. (2004) (2×10^{-8} in their internal source model), to derive an upper limit on the deep O/H ratio of Uranus. Our thermochemical simulations show that the deep O/H ratio is lower than $500\odot$, which provides a y_{CO} value lower than 2.1×10^{-9}. A dedicated probe, as in the mission concepts proposed by Arridge et al. (2014) and Mousis et al. (2014) in response to the ESA 2013 Call for White Papers for the Definition of the L2 and L3 Missions in the ESA Science Programme, or radio observations might be the only way to measure the deep O/H ratio in Uranus.

Acknowledgements. T. Cavalié acknowledges funding from the Centre National d'Études Spatiales (CNES). T. Cavalié and F. Selsis acknowledge support from the European Research Council (Starting Grant 209622: E_3ARTHs). O. Venot acknowledges support from the KU Leuven IDO project IDO/10/2013 and from the FWO Post-doctoral Fellowship programme. G. Orton acknowledges funding from the National Aeronautics and Space Administration to the Jet Propulsion Laboratory, California Institute of Technology. L. N. Fletcher was supported by a Royal Society Research Fellowship at the University of Oxford. The authors thank M. Hofstadter for his constructive review. HIFI has been designed and built by a consortium of institutes and university departments from across Europe, Canada, and the United States under the leadership of SRON Netherlands Institute for Space Research, Groningen, The Netherlands, and with major contributions from Germany, France, and the US. Consortium members are: Canada: CSA, U.Waterloo; France: CESR, LAB, LERMA, IRAM; Germany: KOSMA, MPIfR, MPS; Ireland, NUI Maynooth; Italy: ASI, IFSI-INAF, Osservatorio Astrofisico di Arcetri-INAF; Netherlands: SRON, TUD; Poland: CAMK, CBK; Spain: Observatorio Astronómico Nacional (IGN), Centro de Astrobiología (CSIC-INTA). Sweden: Chalmers University of Technology – MC2, RSS & GARD; Onsala Space Observatory; Swedish National Space Board, Stockholm University – Stockholm Observatory; Switzerland: ETH Zurich, FHNW; USA: Caltech, JPL, NHSC. The *James Clerk Maxwell* Telescope is operated by the Joint Astronomy Centre on behalf of the Science and Technology Facilities Council of the UK, the National Research Council of Canada, and the Netherlands Organisation for Scientific Research.

References

Arridge, C., Agnor, C., Ambrosi, R. M., et al. 2014, Planet. Space Sci., submitted
Asplund, M., Grevesse, N., Sauval, A. J., & Scott, P. 2009, ARA&A, 47, 481
Baines, K. H., Mickelson, M. E., Larson, L. E., & Ferguson, D. W. 1995, Icarus, 114, 328
Bézard, B., Lellouch, E., Strobel, D., Maillard, J.-P., & Drossart, P. 2002, Icarus, 159, 95
Borysow, A., & Frommhold, L. 1986, ApJ, 304, 849
Borysow, J., Trafton, L., Frommhold, L., & Birnbaum, G. 1985, ApJ, 296, 644
Borysow, J., Frommhold, L., & Birnbaum, G. 1988, ApJ, 326, 509
Burgdorf, M., Orton, G., van Cleve, J., Meadows, V., & Houck, J. 2006, Icarus, 184, 634
Cavalié, T., Billebaud, F., Biver, N., et al. 2008a, Planet. Space Sci., 56, 1573
Cavalié, T., Billebaud, F., Fouchet, T., et al. 2008b, A&A, 484, 555
Cavalié, T., Billebaud, F., Dobrijevic, M., et al. 2009, Icarus, 203, 531
Cavalié, T., Hartogh, P., Billebaud, F., et al. 2010, A&A, 510, A88
Cavalié, T., Biver, N., Hartogh, P., et al. 2012, Planet. Space Sci., 61, 3
Cavalié, T., Feuchtgruber, H., Lellouch, E., et al. 2013, A&A, 553, A21
Conrath, B., Hanel, R., Gautier, D., Marten, A., & Lindal, G. 1987, J. Geophys. Res., 92, 15003
Coustenis, A., Salama, A., Lellouch, E., et al. 1998, A&A, 336, L85
Davidsson, B. J. R., Gutiérrez, P. J., & Rickman, H. 2007, Icarus, 187, 306
de Graauw, T., Helmich, F. P., Phillips, T. G., et al. 2010, A&A, 518, L6
Dobrijevic, M., Cavalié, T., Hébrard, E., et al. 2010, Planet. Space Sci., 58, 1555
Dobrijevic, M., Cavalié, T., & Billebaud, F. 2011, Icarus, 214, 275
Encrenaz, T., Lellouch, E., Drossart, P., et al. 2004, A&A, 413, L5
Fegley, B., & Prinn, R. G. 1988, ApJ, 324, 621
Feuchtgruber, H., Lellouch, E., de Graauw, T., et al. 1997, Nature, 389, 159
Feuchtgruber, H., Lellouch, E., Orton, G., et al. 2013, A&A, 551, A126
Fletcher, L. N., Drossart, P., Burgdorf, M., Orton, G. S., & Encrenaz, T. 2010, A&A, 514, A17
Fletcher, L. N., Swinyard, B., Salji, C., et al. 2012, A&A, 539, A44
Fry, P. M., Sromovsky, L. A., Karkoschka, E., et al. 2013, in AAS/Division for Planetary Sciences Meeting Abstracts, 45, #312.18
Gautier, D., & Hersant, F. 2005, Space Sci. Rev., 116, 25
Guilloteau, S., Dutrey, A., Marten, A., & Gautier, D. 1993, A&A, 279, 661
Hartogh, P., Lellouch, E., Crovisier, J., et al. 2009, Planet. Space Sci., 57, 1596
Hartogh, P., Lellouch, E., Moreno, R., et al. 2011, A&A, 532, L2
Hesman, B. E., Davis, G. R., Matthews, H. E., & Orton, G. S. 2007, Icarus, 186, 342
Karkoschka, E., & Tomasko, M. 2009, Icarus, 202, 287
Landgraf, M., Liou, J.-C., Zook, H. A., & Grün, E. 2002, AJ, 123, 2857
Lellouch, E., Paubert, G., Moreno, R., et al. 1995, Nature, 373, 592
Lellouch, E., Bézard, B., Moreno, R., et al. 1997, Planet. Space Sci., 45, 1203
Lellouch, E., Bézard, B., Moses, J. I., et al. 2002, Icarus, 159, 112
Lellouch, E., Moreno, R., & Paubert, G. 2005, A&A, 430, L37
Lellouch, E., Bézard, B., Strobel, D. F., et al. 2006, Icarus, 184, 478
Lellouch, E., Hartogh, P., Feuchtgruber, H., et al. 2010, A&A, 518, L152
Lodders, K., & Fegley, Jr., B. 1994, Icarus, 112, 368
Lomb, N. R. 1976, Ap&SS, 39, 447
López-Valverde, M. A., Lellouch, E., & Coustenis, A. 2005, Icarus, 175, 503
Luszcz-Cook, S. H., & de Pater, I. 2013, Icarus, 222, 379
Mantz, A. W., Malathy Devi, V., Chris Benner, D., et al. 2005, J. Mol. Struct., 742, 99
Marten, A., Gautier, D., Owen, T., et al. 1993, ApJ, 406, 285
Moreno, R., Marten, A., Matthews, H. E., & Biraud, Y. 2003, Planet. Space Sci., 51, 591
Moreno, R., Lellouch, E., Lara, L. M., et al. 2012, Icarus, 221, 753
Moses, J. I., Lellouch, E., Bézard, B., et al. 2000, Icarus, 145, 166
Moses, J. I., Fouchet, T., Bézard, B., et al. 2005, J. Geophys. Res., 110, 8001
Mousis, O., Fletcher, L. N., Lebreton, J.-P., et al. 2014, Planet. Space Sci., submitted
Orton, G. S., Aitken, D. K., Smith, C., et al. 1987, Icarus, 70, 1
Orton, G. S., Gustafsson, M., Burgdorf, M., & Meadows, V. 2007, Icarus, 189, 544
Orton, G. S., Fletcher, L. N., Moses, J. I., et al. 2013a, Icarus, submitted
Orton, G. S., Moses, J. I., Fletcher, L. N., et al. 2013b, Icarus, submitted
Ott, S. 2010, in Astronomical Data Analysis Software and Systems XIX, eds. Y. Mizumoto, K.-I. Morita, & M. Ohishi, PASP, 434, 139
Owen, T., Mahaffy, P., Niemann, H. B., et al. 1999, Nature, 402, 269
Pearl, J. C., Conrath, B. J., Hanel, R. A., & Pirraglia, J. A. 1990, Icarus, 84, 12
Pickett, H. M., Poynter, I. R. L., Cohen, E. A., et al. 1998, J. Quant. Spectr. Rad. Transf., 60, 883
Pilbratt, G. L., Riedinger, J. R., Passvogel, T., et al. 2010, A&A, 518, L1
Prather, M. J., Logan, J. A., & McElroy, M. B. 1978, ApJ, 223, 1072
Roelfsema, P. R., Helmich, F. P., Teyssier, D., et al. 2012, A&A, 537, A17
Rosenqvist, J., Lellouch, E., Romani, P. N., Paubert, G., & Encrenaz, T. 1992, ApJ, 392, L99
Samuelson, R. E., Maguire, W. C., Hanel, R. A., et al. 1983, J. Geophys. Res., 88, 8709
Sromovsky, L. A., & Fry, P. M. 2008, Icarus, 193, 252
Sromovsky, L. A., Fry, P. M., & Kim, J. H. 2011, Icarus, 215, 292
Stone, P. H. 1976, in Proc. Colloq. Jupiter: Studies of the Interior, Atmosphere, Magnetosphere and Satellites, ed. T. Gehrels (Univ. of Arizona Press), 586
Strobel, D. F., & Yung, Y. L. 1979, Icarus, 37, 256
Sung, K., & Varanasi, P. 2004, J. Quant. Spectr. Rad. Transf., 85, 165
Teanby, N. A., & Irwin, P. G. J. 2013, ApJ, 775, L49
Venot, O., Hébrard, E., Agúndez, M., et al. 2012, A&A, 546, A43
Weissman, P. R., Asphaug, E., & Lowry, S. C. 2004, in Comets II, eds. M. C. Festou, H. U. Keller, & H. A. Weaver (Univ. of Arizona Press), 337
Zahnle, K., Schenk, P., Levison, H., & Dones, L. 2003, Icarus, 163, 263

A&A 553, A21 (2013)
DOI: 10.1051/0004-6361/201220797

Astronomy & Astrophysics

Spatial distribution of water in the stratosphere of Jupiter from *Herschel* HIFI and PACS observations⋆,⋆⋆

T. Cavalié[1,2], H. Feuchtgruber[3], E. Lellouch[4], M. de Val-Borro[5,6], C. Jarchow[5], R. Moreno[4], P. Hartogh[5], G. Orton[7], T. K. Greathouse[8], F. Billebaud[1,2], M. Dobrijevic[1,2], L. M. Lara[9], A. González[5,9], and H. Sagawa[10]

[1] Univ. Bordeaux, LAB, UMR 5804, 33270 Floirac, France
e-mail: cavalie@obs.u-bordeaux1.fr
[2] CNRS, LAB, UMR 5804, 33270 Floirac, France
[3] Max Planck Institut für Extraterrestrische Physik, 85741 Garching, Germany
[4] LESIA–Observatoire de Paris, CNRS, Université Paris 06, Université Paris–Diderot, 5 place Jules Janssen, 92195 Meudon, France
[5] Max Planck Institut für Sonnensystemforschung, 37191 Katlenburg-Lindau, Germany
[6] Department of Astrophysical Sciences, Princeton University, Princeton, NJ 08544, USA
[7] Jet Propulsion Laboratory, California Institute of Technology, CA 91109 Pasadena, USA
[8] Southwest Research Institute, San Antonio, TX 78228, USA
[9] Instituto de Astrofísica de Andalucía (CSIC), 18008 Granada, Spain
[10] National Institute of Information and Communications Technology, 4-2-1 Nukui-kita, Koganei, Tokyo 184-8795, Japan

Received 27 November 2012 / Accepted 13 February 2013

ABSTRACT

Context. In the past 15 years, several studies suggested that water in the stratosphere of Jupiter originated from the Shoemaker-Levy 9 (SL9) comet impacts in July 1994, but a direct proof was missing. Only a very sensitive instrument observing with high spectral/spatial resolution can help to solve this problem. This is the case of the *Herschel* Space Observatory, which is the first telescope capable of mapping water in Jupiter's stratosphere.

Aims. We observed the spatial distribution of the water emission in Jupiter's stratosphere with the Heterodyne Instrument for the Far Infrared (HIFI) and the Photodetector Array Camera and Spectrometer (PACS) onboard *Herschel* to constrain its origin. In parallel, we monitored Jupiter's stratospheric temperature with the NASA Infrared Telescope Facility (IRTF) to separate temperature from water variability.

Methods. We obtained a 25-point map of the 1669.9 GHz water line with HIFI in July 2010 and several maps with PACS in October 2009 and December 2010. The 2010 PACS map is a 400-point raster of the water 66.4 μm emission. Additionally, we mapped the methane ν_4 band emission to constrain the stratospheric temperature in Jupiter in the same periods with the IRTF.

Results. Water is found to be restricted to pressures lower than 2 mbar. Its column density decreases by a factor of 2−3 between southern and northern latitudes, consistently between the HIFI and the PACS 66.4 μm maps. We infer that an emission maximum seen around 15 °S is caused by a warm stratospheric belt detected in the IRTF data.

Conclusions. Latitudinal temperature variability cannot explain the global north-south asymmetry in the water maps. From the latitudinal and vertical distributions of water in Jupiter's stratosphere, we rule out interplanetary dust particles as its main source. Furthermore, we demonstrate that Jupiter's stratospheric water was delivered by the SL9 comet and that more than 95% of the observed water comes from the comet according to our models.

Key words. planets and satellites: individual: Jupiter – planets and satellites: atmospheres – submillimeter: planetary systems

1. Introduction

Thermochemistry, photochemistry, vertical and horizontal transport, condensation, and external supplies are the principal physico-chemical processes that govern the 3D distributions of oxygen compounds in giant planet atmospheres. There are several sources of external supply for oxygen material in the atmospheres of the outer planets: interplanetary dust particles (IDP; Prather et al. 1978), icy rings and satellites (Strobel & Yung 1979), and large comet impacts (Lellouch et al. 1995). The vertical and horizontal distributions of oxygen compounds are a diagnostic of their source(s). The temporal evolution of these distributions can also contain the signature of a given source, especially if sporadic (as in the case of a comet impact).

Water in the atmospheres of the outer planets has both an internal and an external source (e.g., Larson et al. 1975 and Lellouch et al. 2002 for Jupiter). These sources are separated by a condensation layer, the tropopause cold trap, which acts as a transport barrier between the troposphere and the stratosphere. Thus, the water vapor observed by the Infrared Space Observatory (ISO) in the stratosphere of the giant planets has an external origin (Feuchtgruber et al. 1997). While Saturn's water seems to be provided by the Enceladus torus (Hartogh et al. 2011), the water origin in Uranus and Neptune remains unclear. For Jupiter, IDP or the Shoemaker-Levy 9 (SL9) comet, which collided with the planet in July 1994 at 44 °S, are the main candidates (Landgraf et al. 2002; Bjoraker et al. 1996).

⋆ *Herschel* is an ESA space observatory with science instruments provided by European-led Principal Investigator consortia and with important participation from NASA.
⋆⋆ Figures 1 and 3 are available in electronic form at http://www.aanda.org

Several clues or indirect proofs have suggested a cometary origin for the source of external water in Jupiter. First, Lellouch et al. (2002) analyzed the water and carbon dioxide (CO_2) observations by ISO. They could only reconcile the short-wavelength spectrometer (SWS) and the long-wavelength spectrometer (LWS) water data by invoking an SL9 origin but failed at reproducing the Submillimeter Wave Astronomy Satellite (SWAS) observation with their water vertical profile. In parallel, they showed that the meridional distribution of CO_2, produced from the photochemistry of water, was a direct proof that CO_2 was produced from SL9 (higher abundance in the southern hemisphere). Then, the analysis of the SWAS and Odin space telescope observations seemed to indicate that the temporal evolution of the 556.9 GHz line of water was better modeled assuming the aftermath of a comet impact (Cavalié et al. 2008b, 2012). However, IDP models have never been completely ruled out by these studies because the signal-to-noise ratio (S/N) and/or spatial resolution were never quite good enough.

The reason why some doubts have remained on the source of water in Jupiter's stratosphere is in the first place the lack of observations prior to the SL9 impacts. Since then, the lack of very high S/N and spectrally/spatially resolved observations prevented differentiating the SL9 source from any other source. High-sensitivity observations in the (sub)millimeter and in the infrared have led to converging clues for carbon monoxide (CO), advocating for a regular delivery of oxygen material to the giant planet atmospheres by large comets (Bézard et al. 2002 and Moreno et al. 2003 for Jupiter; Cavalié et al. 2009, 2010 for Saturn; Lellouch et al. 2005, 2010 and Hesman et al. 2007 for Neptune). High-sensitivity (sub)millimeter line spectroscopy performed with the *Herschel* Space Observatory now offers the means to solve this problem for water. Indeed, the very high spectral resolution in heterodyne spectroscopy enables the retrieval of line profiles and thus vertical distributions, while the horizontal distributions can be recovered from observations carried out with sufficient spatial resolution. Obviously, temporal monitoring of these distributions can be achieved by repeating the measurements.

In this paper, we report the first high S/N spatially resolved mapping observations of water in Jupiter carried out with the ESA *Herschel* Space Observatory (Pilbratt et al. 2010) and its Heterodyne Instrument for the Far Infrared (HIFI; de Graauw et al. 2010) and Photodetector Array Camera and Spectrometer (PACS; Poglitsch et al. 2010) instruments. These observations have been obtained in the framework of the guaranteed time key program "Water and related chemistry in the solar system", also known as "*Herschel* solar system Observations" (HssO; Hartogh et al. 2009b). We also present spatially resolved IRTF observations of the methane ν_4 band, obtained concomitantly, to constrain the stratospheric temperature. In Sects. 2 and 3, we present the various Jupiter mapping observations and models we used to analyze the water maps. We describe our results on the distribution of water in Sect. 4 and discuss the origin of this species in Sect. 5 in view of these results. We finally give our conclusions in Sect. 6.

2. Observations

2.1. *Herschel* observations

2.1.1. *Herschel*/HIFI map

The HIFI mapping observation (Observation ID: 1342200757) was carried out on July 7, 2010, operational day (OD) 419, in dual beam switch mode (Roelfsema et al. 2012). We obtained a 5×5 pixels raster map with a $10''$ separation between pixels, that is, covering a region of $40'' \times 40''$, centered on Jupiter. More details are given in Table 1.

We targeted the water line at 1669.905 GHz (179.5 μm) with a half-power beam width of $12\farcs7$. Because of the fast rotation of Jupiter, the line is Doppler shifted. Because the bandwidth of the High Resolution Spectrometer (HRS) was too narrow to encompass the whole water line, we only used the Wide Band Spectrometer (WBS) data, whose native resolution is 1.1 MHz. We processed the data with the standard HIPE 8.2.0 pipeline (Ott 2010) up to level 2 for the H and V polarizations. The HIPE-8-processed data are displayed in Fig. 1 and the pixel numbering (following the raster observation order) is also presented in this figure.

We extracted the 50 spectra (25 pixels, two polarizations) independently. Because we performed no absolute calibration, we analyzed the lines in terms of line-to-continuum ratio (l/c), after correcting the data for the double sideband (DSB) response of the instrument and assuming a sideband ratio of 0.5 (Roelfsema et al. 2012). Each pixel was treated for baseline-ripple removal when necessary by using a Lomb (1976) algorithm. Then, we checked if the observations had suffered any pointing offset. While the relative pointing uncertainty within the map should be very low, the position of the whole map with respect to Jupiter's center is subject to the pointing uncertainty of *Herschel*. The reason why we had to determine the true pointing for the map was to avoid confusing thermal/abundance variability effects with purely geometrical effects on the l/c. For instance, the effect of a pointing offset in a given direction leads to an increase/decrease of the line peak intensity in connection with limb-brightening in the line and limb-darkening in the continuum compared to what is obtained with the desired pointing. Retrieving the true pointing offset can be achieved by measuring the relative continuum level in the 50 spectra and comparing it to model predictions. For each polarization we measured the continuum in each pixel of the map and adjusted the pointing offset to minimize the residuals between the observations and the model in the 25 pixels. According to Roelfsema et al. (2012), the H and V receivers are misaligned by less than $1''$. We found that the continuum patterns seen in H and V could be reproduced with mean pointing offsets of ($-0\farcs7$, $-0\farcs7$) in right ascension and declination with differences between H and V of $\sim 0\farcs3$. The difference is small enough compared to the beam size that we averaged the H and V maps to improve on the noise.

Finally, we smoothed the 25 remaining spectra to a 12 MHz resolution to increase the S/N. As a result, the water line is detected in each pixel. The S/N we observe has a lowest value of 3.5 in pixels 1 and 21, generally ranges between 20 and 30, and reaches a maximum of 60 in pixel 17 (per 12 MHz channel).

2.1.2. *Herschel*/PACS maps

We first observed the full-range spectrum of Jupiter with the PACS spectrometer. This part of the instrument consists of an array of 5×5 detectors that covers $50'' \times 50''$ on the sky. The extreme far-infrared flux of Jupiter does not allow one to observe it with PACS in any standard mode. To avoid detector saturation, the spectrometer readout electronics were configured to the shortest possible reset intervals of 1/32 s. These observations (Observation ID: 1342187848) were carried out with the PACS spectrometer on December 8, 2009 (OD 208). Although these data, which cover the $\sim$50–200 μm range, will be published extensively in another paper (Sagawa et al., in prep.), we present

Table 1. Summary of *Herschel* observations of water in Jupiter.

OD	Obs. ID	UT start date	Int. time [s]	Freq. or Wav.	Instrument	Map properties	Beam size [″]	Size of Jupiter[a] [″ × ″]
208	1342187848	2009-12-08 13:07:58	23 538	58.7 μm & 65.2 μm	PACS	full range scan 2 × 2 raster & 28″ steps 100 points	9.4	36.94 × 34.54
419	1342200757	2010-07-07 08:16:36	2255	1669.904 GHz	HIFI	5 × 5 raster & 10″ steps 25 points	12.7	42.35 × 39.60
580	1342211204	2010-12-15 10:21:20	3001	66.4 μm	PACS	line scan 4 × 4 raster & 6.″5 steps 400 points	9.4	40.85 × 38.20

Notes. [(a)] Equatorial × Polar apparent diameter.

here two maps of the water emission at 58.7 μm and 65.2 μm, both extracted from the full-range spectrum. PACS has a spatial pixel (spaxel, hereafter) size of 9.″4 at these wavelengths. More details of these observations are given in Table 1. The line peak intensity ($l/c-1$, in % of the continuum) maps presented in Fig. 2 suggest that the water lines were a factor of 2 fainter in the north polar region than in the other limb regions. We took that as a possible clue for the horizontal distribution of water.

However, these observations were not optimized for mapping Jupiter's disk and will not be analyzed quantitatively below. Indeed, the observation consisted of a 2×2 raster with a stepsize of 28″ to have the disk seen once by every spaxel. Consequently, the planetary disk contains only a few pixels. These observations were also full grating scans with much time between the up-scan and the down-scan for a given line, which implies larger systematics in the data. The dominant source for the "noise" may be the spacecraft pointing jitter, which mainly affects spaxels that see parts of the limb or are close to the limb, because even small jitter can cause significant flux variations within a spaxel. Moreover, the observed line width varies from one pixel to another in the PACS maps. The key for the variation is the source position and source extension within the spectrometer slit. A point source will by default have a narrower profile than an extended source. For an extended source, even if 25 spatial spectra are taken at the same time, the profiles will depend on how each of the spaxels is filled by the source. In this way, there are certainly limb effects when observing planets like Jupiter and Saturn. For instance, there is up to a factor of 2 difference between the highest and lowest line width in the 58.7 μm map. Indeed, the mean values and standard deviations of the observed line widths are 0.0153 μm and 0.0041 μm at 58.7 μm and 0.0100 μm and 0.0022 μm at 65.2 μm. Such high values for the standard deviations with regard to the mean values prevent any meaningful quantitative analysis and interpretation of these maps. However, these rough mapping observations definitely encouraged us to perform a deeper integration with a dedicated and optimized mapping observation of a stronger water line.

We obtained a water map at 66.4377 μm (=4512 GHz) with PACS (Observation ID: 1342211204) on December 15, 2010 (OD 580). The spaxel size was also 9.″4 at this wavelength. To cover the entire disk of Jupiter and slightly beyond in the best way, we defined a 4 × 4 raster with a stepsize of 6.″5. At each raster position a single grating up/down scan around the 66.4377 μm water line was executed in unchopped mode to avoid transient effects at this extreme flux range. The duration of the entire raster including overheads was 3001 s (more details in Table 1). Given the PACS beam FWHM of 9.″4 at 66.4 μm and the enormous signal, the water line could be measured at all raster positions, even to about 10″ beyond the limb.

The response of the PACS Ge:Ga detectors increases with the strength of the cosmic radiation field, but at the same time it decreases because of the strong infrared illumination. Therefore the response is continuously drifting throughout the entire Jupiter measurement and an absolute flux calibration of the spectra cannot be achieved within any reasonable uncertainty. However, when expressing the line spectra in terms of l/c, the uncertainty in the absolute response cancels out and opens the path to a relevant analysis.

The data reduction started from the Level 0 products that were generated according to the descriptions in Poglitsch et al. (2010). Level 1 processing was run within HIPE 8.0 through all standard steps for unchopped observations. All additional processing (flat-fielding, outlier removal and rebinning) was carried out with standard IDL tools.

The astrometric coordinates of Jupiter, taken from the JPL Horizons database, were subtracted from the product coordinates after interpolating them to the respective sample times. For each spectrum and spaxel of the integral field spectrometer, a single averaged relative (with respect to Jupiter's center) coordinate was computed and used for the spectral image reconstruction. As in the HIFI map reduction, we retrieved the true pointing. The observed line width values are much more uniform over the entire map: its mean value and standard deviation is 0.0105 μm and 0.0010 μm. To exclude these small variations, we adapted the spectral resolution in our radiative transfer computations to the value measured in each pixel.

Using all spaxels at the 16 raster positions, a total of 400 spectra were recorded with a resolving power ($R = \lambda/\Delta\lambda$) of 6400 on average. The resulting map is presented in Fig. 3. The S/N in the map is generally ~30 but reaches values twice as high at some positions. The spectra were then divided by a third order polynomial fit to the continuum, excluding the range of the water line. Because the line profiles are purely instrumental at this resolving power, they were analyzed by fitting with a Gaussian line profile. Therefore, all abundance and temperature information is contained in the line peak + line width, i.e., in the line area, in the map.

Below, we analyze the PACS and HIFI data according to their l/c. Because the *Herschel* mapping observations of water are sensitive to the temperature and water abundance distributions, we have monitored the temperature over the Jovian disk

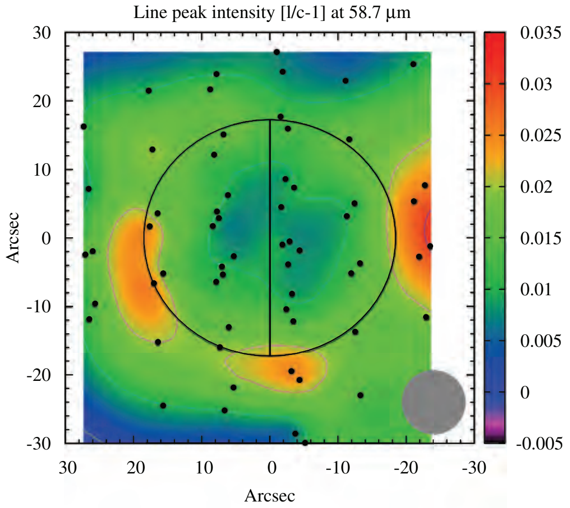

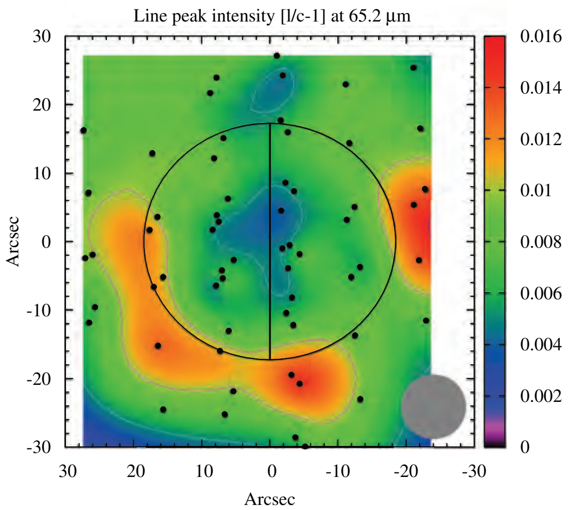

Fig. 2. Water maps of the line peak intensity (=l/c-1, thus in % of the continuum) at 58.7 and 65.2 μm observed by the PACS spectrometer on December 8, 2009. Jupiter is represented by the black ellipse, and its rotation axis is also displayed. The beam is represented by a gray filled circle. Both maps indicate that there is less emission in the northern hemisphere than in the southern (best seen in the limb emission).

and carried out complementary ground-based observations at the NASA Infrared Telescope Facility (IRTF) in 2009 and 2010.

2.2. IRTF observations

2.2.1. IRTF/TEXES maps

On May 31 and October 17, 2009, we performed observations with the Texas Echellon cross-dispersed Echelle Spectrograph (TEXES; Lacy et al. 2002), mounted on the NASA IRTF atop Mauna Kea. By achieving a spectral resolving power of ~80 000 in the ν_4 band of methane (CH_4) between 1244.8 and 1250.5 cm^{-1} (see Fig. 4), we were able to resolve the pressure-broadened methane emission wing features, which give detailed information on the vertical temperature profile from 0.01

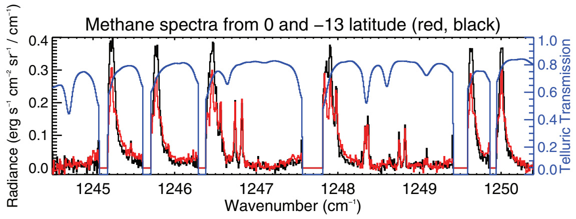

Fig. 4. Methane emission spectra from 13 °S latitude (black) and from the equator (red) showing the different spectral shape and strength from the May 2009 observations with TEXES. The spectra are at an airmass between 1 and 1.2. The blue curve represents the telluric transmission. Owing to the high Jupiter/Earth velocity and the high spectral resolution achieved by TEXES, we were able to easily separate the Jovian methane emission from the telluric methane absorption. Gaps in the data are caused by telluric transmission regions that are too opaque to retrieve useful data. The red and black spectra have been flat-fielded by the black chopper wheel minus the sky emission, which performs a first-order division of the atmosphere.

to 30 mbar. The data were reduced through the TEXES pipeline reduction software package (Lacy et al. 2002), where they were sky-subtracted, wavelength-calibrated, and flux-calibrated by comparing them to observations of a black chopper wheel made at the beginning of each set of four scan observations. We subsequently processed the pipelined data through a purpose built remapping software program to co-add all scan observations and solve for the latitude[1] and west longitude of each mapped step and spaxel along the TEXES slit length. The data were then zonally averaged and binned into latitude and airmass bin sizes of 1−1.2, 1.2−1.5, 1.5−2.0, and 2.0−3.0 Jovian airmass. The latitude bins (Nyquist-sampled spatial resolution) varied from 2 degrees at the sub-Earth point to 5 degrees at −60 degrees latitude.

2.2.2. IRTF/MIRSI maps

In addition to the TEXES observations, we recorded two sets of radiometric images of Jupiter's stratospheric thermal emission observed through a discrete filter with a FWHM of 0.8 μm, centered at a wavelength of 7.8 μm with the Mid-Infrared Spectrometer and Imager (MIRSI; Kassis et al. 2008) that is also mounted on the NASA IRTF. The radiance at this wavelength is entirely controlled by thermal emission from the ν_4 vibrational-rotational fundamental of methane and emerges from a broad pressure region in the middle of Jupiter's stratosphere, 1−40 mbar (see Fig. 2 of Orton et al. 1991). Because methane is well-mixed in Jupiter's atmosphere, any changes of emission are the result of changes in temperature around this region of Jupiter's stratosphere. The images were made (i) on 25 June−1 July 2010, very close in time to the July 7 HIFI observations, and (ii) on 5−6 December 2010, very close in time to the December 15 PACS observations. An example of these observations is shown in Fig. 5.

The data were reduced with the standard approach outlined by Fletcher et al. (2009), in which they were sky-subtracted with both short- (chop) and long-frequency (nod) reference images on the sky. The final results were co-additions of five individual images with the telescope pointing dithered around the field of view to fill in bad pixels in the array and minimize the effects of non-uniform sensitivities of pixels across the array. Before coadding, the individual images were flat-fielded using a

[1] All latitudes in this paper are planetocentric latitudes.

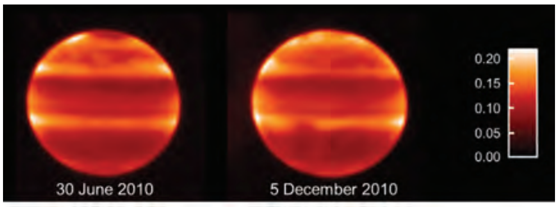

Fig. 5. IRTF/MIRSI radiance observations at 7.8 μm in the ν_4 rotational-vibrational band of methane in Jupiter. These radiance images, recorded on June 30 (*left*) and December 5 (*right*), 2010, are essentially sensitive to the stratospheric temperature between 1 and 40 mbar. The radiances are given in erg/s/cm^2/cm^{-1}/ster.

reference to observations of a uniform heat source, a part of the telescope dome. The images were also calibrated for absolute radiance by convolving the filter function with spectra taken by the Voyager IRIS and Cassini CIRS experiments, also described in detail by Fletcher et al. (2009).

3. Modeling

3.1. Herschel data modeling

We analyzed the *Herschel* maps with a 1D radiative transfer model that was improved from the model presented in Cavalié et al. (2008a). Our code is written in ellipsoidal geometry and accounts for the limb emission and the sub-observer point position. We included the opacity caused by the H_2-He-CH_4 collision-induced absorption spectrum (Borysow et al. 1985, 1988; Borysow & Frommhold 1986) and by the far wings of ammonia (NH_3) and phosphine (PH_3) lines. We used the JPL Molecular Spectroscopy catalog (Pickett et al. 1998) as well as H_2/He pressure-broadening parameters parameters for water lines from Dutta et al. (1993) and Brown & Plymate (1996).

As baseline, we used the same temperature profile as in Cavalié et al. (2008b) and Cavalié et al. (2012), which was taken from Fouchet et al. (2000) (see Fig. 6). The PACS observations probe pressures lower than 2 mbar (see Fig. 7). In this way, we constructed a series of thermal profiles, based on our nominal profile, with 1-K-step temperature deviations at pressures lower than 2 mbar to determine the necessary temperature deviations from our nominal profile to fit the observations. These deviations were then checked for consistency with our IRTF thermal maps. The deviations from our nominal thermal profile are initiated at 10 mbar to obtain a smooth transition toward the modified thermal profile compared to our nominal profile (and to avoid introducing a temperature inversion layer in the 1−10 mbar pressure range for negative deviations). For each thermal profile, we recomputed the pressure-altitude relationship assuming hydrostatic equilibrium. The resulting thermal profiles are shown in Fig. 6.

Retrieving the water vertical profile from the HIFI spectra will be the object of a forthcoming paper (Jarchow et al., in prep.) and therefore will not be addressed here. We used profiles that are qualitatively representative of the IDP and SL9 sources. For the IDP source, we took the profile published in Cavalié et al. (2008b), which corresponds to a water input flux of 3.6×10^6 cm^{-2} s^{-1}. This profile was obtained with a photochemical model that used the same thermal profile as our nominal profile and a standard $K(z)$ profile (Moses et al. 2005). This profile enables one to reproduce the average line intensity on the HIFI map. For the SL9 source, we took an empirical profile in

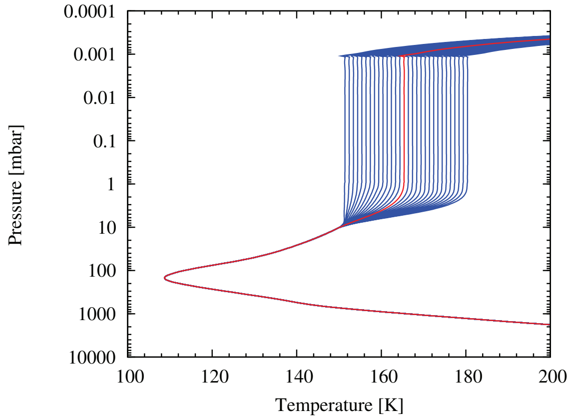

Fig. 6. Examples of temperature profiles used in this study. Our nominal profile is displayed in red. The thermal profiles displayed in blue correspond to cases in which the temperature at pressures lower than 2 mbar is increased or decreased with 1-K steps from −14 to +15 K. The deviations from our nominal thermal profile are initiated at 10 mbar to smooth the transition from the nominal profile at higher pressures toward the modified thermal profile at lower pressures.

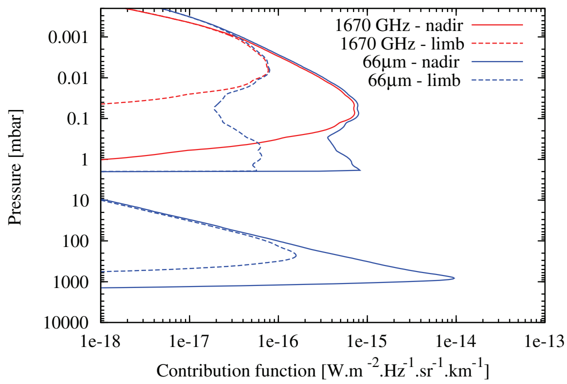

Fig. 7. Contribution functions of the water lines at 1669.9 GHz and 66.4 μm at their respective observed spectral resolutions for a pencil-beam geometry. These profiles have been obtained with the water profile used in this work (all water constrained to pressures lower than 2 mbar).

which water is restricted to pressures lower than a given pressure level p_0 (to be determined by our analysis). Both profiles are shown in Fig. 8.

The effect of the rapid rotation of the planet, which can clearly be seen as red or blue Doppler shifts of the water lines on the HIFI spectra (see Fig. 1) was taken into account, as well as the spatial convolution due to the beams of the HIFI and PACS instruments. Although the model assumes homogeneous temperature and water abundance within a HIFI or PACS beam, the geometry was fully treated. Indeed, the entire Jupiter disk was divided into small elements, including the limb. We solved the radiative transfer equation at each point and accounted for the Doppler shifts caused by the rapid rotation of Jupiter before finally performing the spatial convolution by the instrument beam.

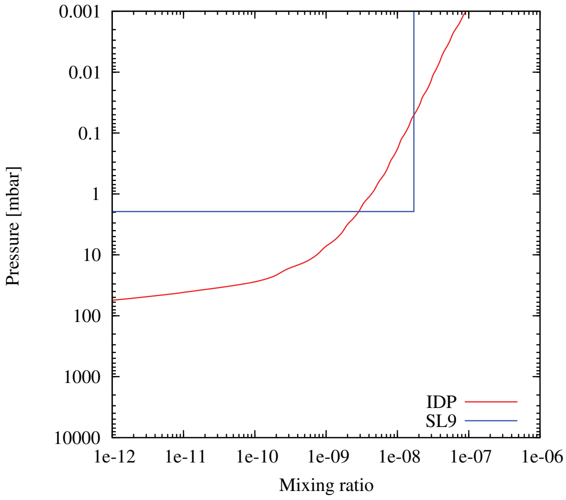

Fig. 8. Nominal water vertical profiles used in the analysis of the HIFI and PACS maps. The IDP profile (red solid line) was computed with the photochemical model of Cavalié et al. (2008b), using the nominal thermal profile of Fig. 6 and a standard $K(z)$ profile from Moses et al. (2005). In the SL9 profile, a cut-off level was set to $p_0 = 2$ mbar. This is the highest value of p_0 that enables reproducing all the HIFI lines. In this profile, the water mixing ratio is 1.7×10^{-8} as in the central pixel (number 13) of the HIFI map.

3.2. IRTF data modeling

Methane emission can be used to probe Jupiter's stratospheric temperatures because (i) the ν_4 band of methane emits on the Wien side of Jupiter's blackbody curve; (ii) methane is well-mixed throughout Jupiter's atmosphere and only decreases off at high altitudes because of diffusive separation (Moses et al. 2000); (iii) the deep volume mixing ratio is known from the Galileo probe re-analysis results of Wong et al. (2004) to be equal to $2.37 \pm 0.57 \times 10^{-3}$, resulting in a mole fraction of $2.05 \pm 0.49 \times 10^{-3}$. For the TEXES data, we used the photochemical model methane mole fraction profile from Moses et al. (2000) with a deep value of 1.81×10^{-3} taken from the initial Galileo probe results paper by Niemann et al. (1998) because it agrees within errors with Wong et al. (2004). Moreover, the Moses et al. (2000) model has been shown to agree with previous observations of Jupiter.

To infer Jupiter's stratospheric temperatures from the TEXES maps, we employed the automated line-by-line radiative transfer model described in Greathouse et al. (2011). This model uses the pressure-induced collisional opacity of H_2-H_2, H_2-He, and H_2-CH_4 as described by Borysow et al. (1985, 1988) and Borysow & Frommhold (1986) and the molecular line opacity for $^{12}CH_4$, $^{13}CH_4$, and CH_3D from HITRAN (Rothman et al. 1998). It also varies the vertical temperature profile to reproduce the observed methane emission spectra. The resulting zonally averaged temperature maps are displayed in Fig. 9. The pressure range we are sensitive to with these observations is 0.01–30 mbar.

A second approach to deriving stratospheric temperatures, which we applied to our MIRSI maps, consists of using the radiometrically calibrated versions of the 7.8 μm images. Although these maps yield only temperatures at a single level (between 1 and 40 mbar), they can differentiate between the thermal models shown in Fig. 6. Therefore, we simulated the 7.8 μm radiance we would expect from the range of temperature profiles from Fig. 6 to create a table of radiance vs. emission angle. Then we determined the upper-stratospheric temperature corresponding to the profile that most closely produced the observed radiance at each latitude/emission angle pair along the central meridian for each date. Orton et al. (1991) used a similar approach in their analysis of raster-scanned maps of Jupiter. The result is the temperature maps that are shown in Fig. 10. The zonal variability is much smaller than the meridional variability in each image, validating the approach taken in examining the zonal-averaged temperatures from the TEXES data shown in Fig. 9.

The *Herschel* observations are sensitive to pressures lower than 2 mbar. This is why we created the range of thermal profiles shown in Fig. 6, in which the profiles start to differ from one another at pressures lower than 10 mbar. This introduces the main limitation in our temperature derivation from the MIRSI images, because these observations are sensitive to levels ranging from 1 to 40 mbar. To encompass the range of observed radiances that are generated by higher temperatures in the 1–40 mbar range, we therefore had to increase the range over which we were perturbing the temperatures at pressures lower than 10 mbar. As a result, the temperatures derived from the MIRSI images are excessively high at latitudes corresponding to bright bands. Therefore, only the trend in the latitudinal variation of the temperature can be relied on rather than the values themselves.

4. Results

4.1. HIFI map

At 1669.9 GHz and with the spectral resolution of HIFI, we probed altitudes up to the 0.01 mbar pressure level, depending on the observation geometry (see Fig. 7). The line opacity at the central frequency at the observed spectral resolution but at infinite spatial resolution is ~10 at the nadir and ~250 at the limb. We first tested the IDP profile (presented in the previous section) that fitted the SWAS and Odin observations in Cavalié et al. (2008b, 2012). At Jupiter, this source should be steady and spatially uniform (Selsis et al. 2004). In the case of a steady local source, it would either show high concentrations at high latitudes (for material transported in ionic form) or at low latitudes (for material transported in neutral form). We detected neither of these cases in the observations, although this diagnostic is limited by the relatively low spatial resolution. The result of the IDP model is displayed in Fig. 11. The IDP profile fails to reproduce the observations in several aspects. Indeed, it can be seen that this model produces lines that are too strong in most of the northern hemisphere (pixels 6, 7, 15 and 16). Figure 12 shows that if the water flux attributed to IDP is lowered to $\sim 2.0 \times 10^6$ cm^{-2} s^{-1}, the model matches the observations in terms of l/c but still overestimates the line width. The main problem of this model is that the line wings are too broad in most of the pixels. The only pixels in which the line wings could be compatible with the data are pixels with the highest noise. This means that the bulk of the stratospheric water is not located just above the condensation level, i.e., at ~20–30 mbar as in the IDP model, but higher in altitude. The line shape of the 556.9 GHz water line as observed by SWAS and Odin already suggested that the IDP source was unlikely (Cavalié et al. 2008b). Consequently, the IDP model can be ruled out. In contrast, the SL9 profile gives much better results in the line wings (see Fig. 11). We found that all line wings could be reproduced

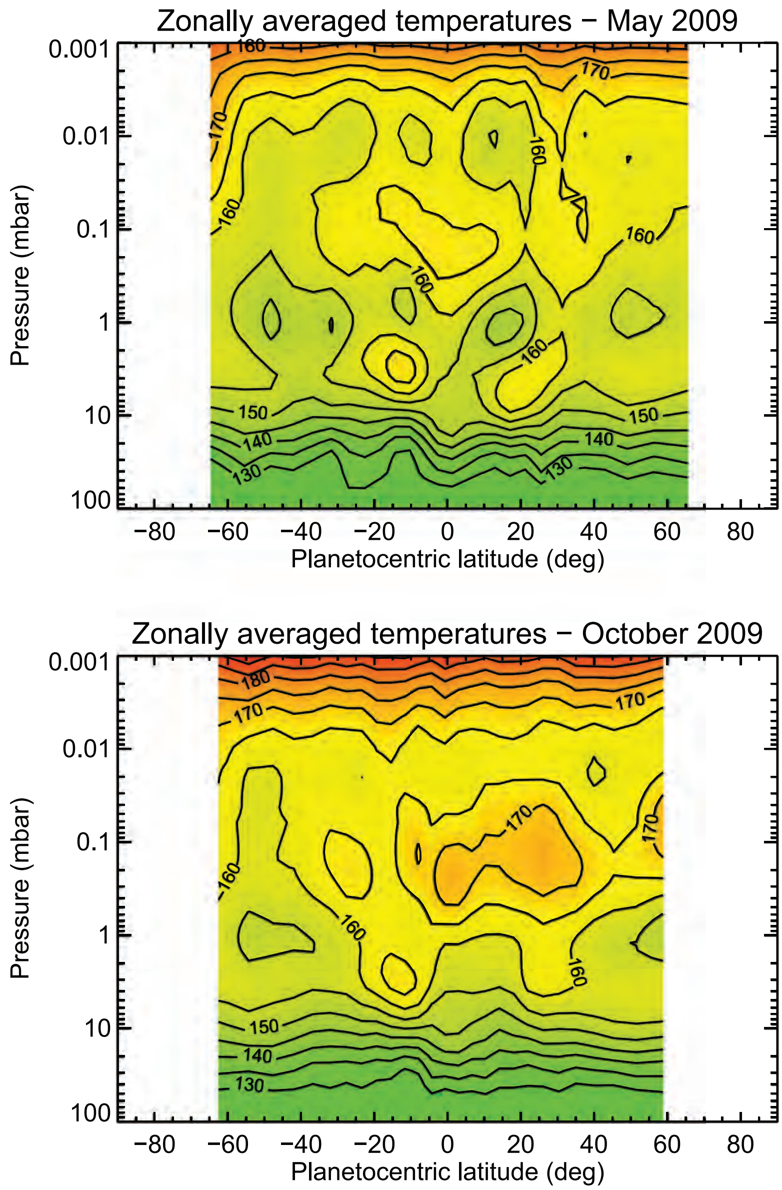

Fig. 9. Zonally averaged thermal maps as retrieved from IRTF/TEXES observations of the ν_4 band of methane carried out on May 31 and October 17, 2009. The sensitivity ranges from 0.01 to 30 mbar.

provided that the p_0 level was not set at pressures higher than 2 mbar[2]. For the remainder of the paper, we have set the p_0 level to this value.

Before we more quantitatively analyze the SL9 model results with regard to the HIFI observations, we focus on the PACS map analysis using the information on the p_0 level we derived above. Because we already ruled out the IDP model at this stage, we do not use it further in the analysis.

[2] The value of p_0 can be set to pressures lower than 2 mbar and still reproduce the observations reasonably well, provided that additional water was included in the model. Indeed, Doppler broadening is about equal to pressure broadening around the 1 mbar level in Jupiter's atmosphere. Therefore, the line widths will be almost the same in models with a value of p_0 lower than 2 mbar.

4.2. PACS maps

We now use the PACS maps to separate the temperature and water vapor variability. First, we can see that the line peak intensity ($=l/c-1$) maps (Figs. 2 and 3) present the same spatial structure. The highest emission is concentrated at the limb due to limb-brightening in the line and limb-darkening in the continuum. The main feature seen in these maps is the lack of emission around the northernmost region compared to the southernmost region. However, we have to keep in mind that because the observations are not spectrally resolved, all information on the temperature and water column abundance is contained in the line area. The line peak intensity alone only contains part of the information. Therefore, we fitted the line peak with an adjustable line width in the model, which is the same as fitting the line area. The line opacity at the central frequency at the observed spectral

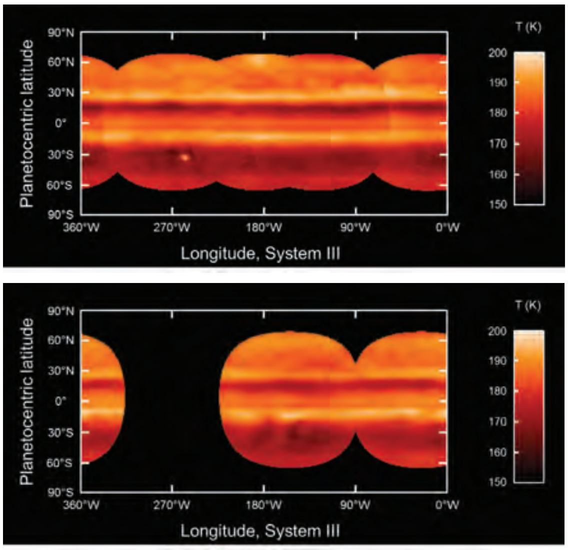

Fig. 10. IRTF/MIRSI radiance observations at 7.8 μm in the ν_4 rotational-vibrational band of methane, carried out on 25 June−1 July 2010 (*top*) and 5−6 December 2010 (*bottom*). These observations are essentially sensitive to the stratospheric temperature between 1 and 40 mbar. The color scale gives the correspondence between radiances and stratospheric temperatures at 2 mbar, according to our derivation procedure (see text for limitations). These maps suggest that the northern hemisphere is generally warmer than the southern hemisphere. The bright belt seen around 15 °S in both maps (as well as in the TEXES data; see Fig. 9) is a possible explanation for the ~4 K increase seen in the PACS 66.4 μm map between the equator and 25 °S. The bright dot seen in the 25 June−1 July 2010 map is Io and had only marginal effects on the zonal mean results.

resolution but at infinite spatial resolution is ~3 at the nadir and ~100 at the limb.

To investigate whether this north-south asymmetry is caused by the stratospheric temperature distribution or by the column density spatial distribution, we analyzed the 66.4 μm emission map considering two cases:

- We determined the spatial distribution of the temperature deviation from the nominal profile at pressures lower than 2 mbar from our nominal thermal profile considering a spatially uniform distribution of water. In this case, we set the water mixing ratio to 2×10^{-8} for $p \leq 2$ mbar, corresponding to a column abundance of 3.7×10^{15} cm^{-2}. This choice roughly corresponds to the average column found in this map. Its choice is thus arbitrary to some extent but does not affect the result, because we are interested in relative contrasts in temperature over Jupiter's disk, not in absolute values of them.
- We determined the spatial distribution of the column density considering a spatially uniform temperature profile (i.e., our nominal profile).

4.2.1. Map of the stratospheric temperature deviation from the nominal profile

We used the thermal profiles shown in Fig. 6 to check whether latitudinal temperature variations could cause the line peak emission distribution observed in Fig. 3, assuming a spatially uniform distribution of water. To do this, we fitted the line in each pixel of the map by finding the most appropriate thermal profile and retained the temperature deviation from the nominal profile associated to each pixel. The temperature deviation map associated to the 66.4 μm observations is shown in Fig. 13. The uncertainty on the line peak values is in the range of 3−10%, which translates into an uncertainty of 1−3 K on the derived temperature deviation. Another way to evaluate the uncertainty on the temperature is to see the variations of the temperature around a given latitude. Although the atmosphere radiative timescale is 3 orders of magnitude longer than the rotation period (Flasar 1989), variations of several K in the zonal temperatures at 1 mbar, probably caused by a Rossby wave trapped at certain latitudes, have been reported by Flasar et al. (2004). However, at our spatial resolution, the temperature should be smoothed in longitude compared to Flasar et al.'s observations. After checking the temperatures in several narrow latitudinal bands, we found a scatter of ~3 K on the temperature, which agrees with the uncertainty range we derived.

The 66.4 μm map in Fig. 13 shows two interesting structures that can also be better seen in a representation of the temperature deviation from the nominal profile as a function of latitude. Such a latitudinal section is shown in Fig. 14.

First, a north-south contrast of 10−15 K (with higher temperatures in the southern hemisphere) is required to reproduce the global north-south asymmetry seen in the line peak emission. This picture contradicts the TEXES maps from 2009 (see Fig. 9). In these maps, we see large meridional variations at 2 mbar (see Fig. 14), of the same order of magnitude as in our PACS map (~10 K). These variations correlate quite well with those seen by Fletcher et al. (2011) at 5 mbar in 2009−2010. But there is no evidence for a global meridional asymmetry. Moreover, there clearly are changes in the stratospheric temperature field between 2009 and 2010, as shown by the thermal maps we retrieved from the 7.8 μm IRTF/MIRSI images we captured a few days before the HIFI and PACS maps were produced (see in Fig. 10). However, these changes do not work in favor of the temperature variability hypothesis to explain the water emission maps. On the contrary, the Jovian quasiquadriennial oscillation (Leovy et al. 1991) creates a bright band north of the equator that we only marginally see in Fig. 13. Accordingly, the MIRSI observations even suggest that there the temperatures are higher in the northern hemisphere than in the southern hemisphere in the pressure range we are sensitive to. The opposite would have been necessary to explain the water emission maps. Consequently, the asymmetry we see in the water emission maps has to be due to an hemispherical asymmetry in the water distribution.

The second structure we see in the 66.4 μm map is a temperature increase of ~4 K between 25 °S and the equator. There is a good correlation between this feature and a warm temperature belt seen consistently between 1 and 30 mbar in the MIRSI and TEXES data and in Fletcher et al. (2011) around 15 °S. This feature likely results from the spatial convolving of this warm belt (see Fig. 14). We discuss it in Sect. 5.1.

Now that we have proven that a global latitudinal temperature variation is not the cause for the north-south asymmetry seen in the line peak intensity maps, we can derive the column density map that reproduces the observations.

4.2.2. Column density map

Here, we assumed that our nominal temperature profile is valid at any latitude/longitude and locally rescaled the water vertical profile, i.e., the water column density, to fit the line in each pixel. The computed column densities are representative of averages

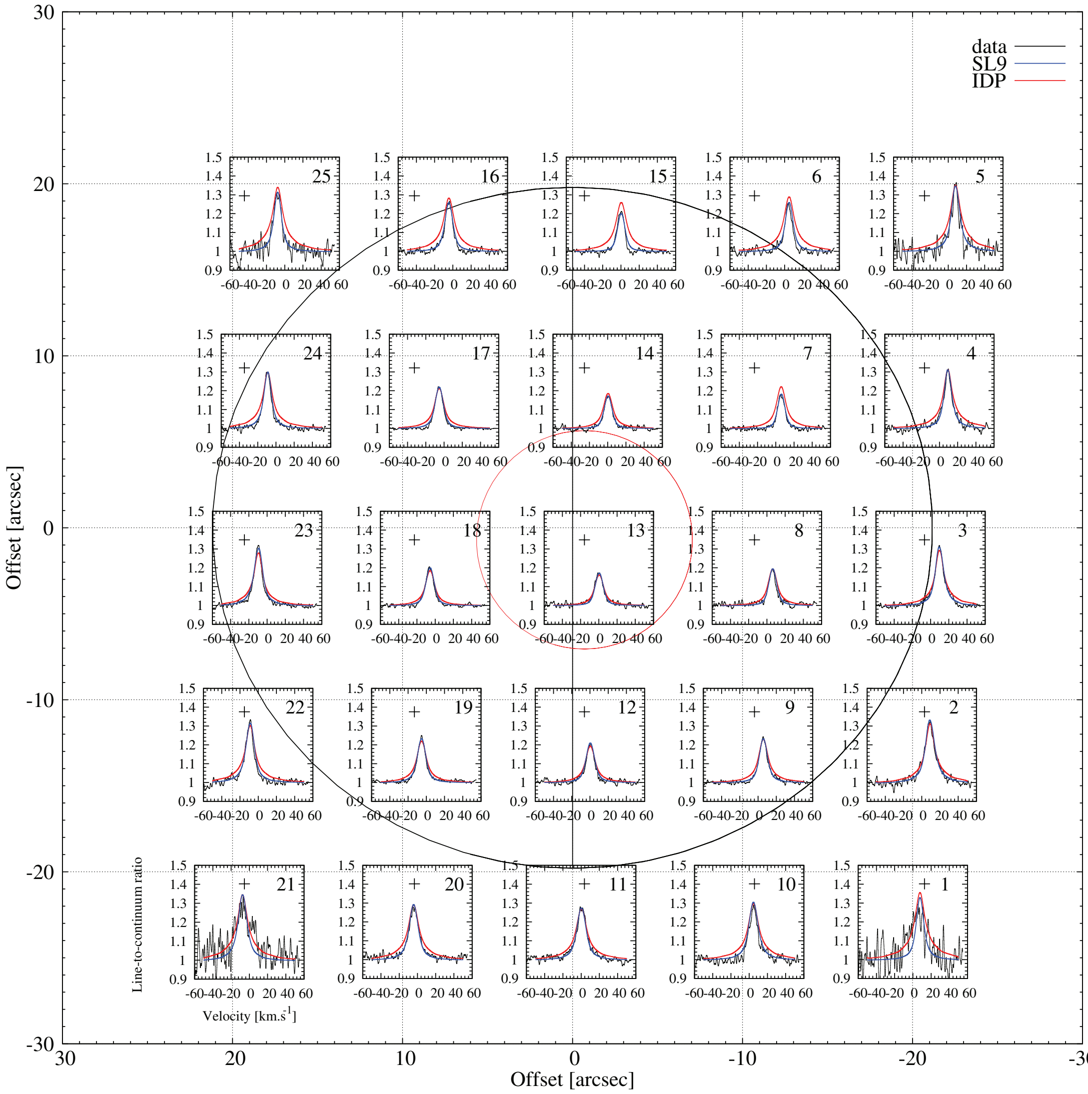

Fig. 11. Water 5 × 5 raster map at 1669.9 GHz obtained with *Herschel*/HIFI on July 7, 2010, expressed in terms of l/c and smoothed to a spectral resolution of 12 MHz (observation are plotted in black). Jupiter is represented with the red ellipse, and its rotation axis is also displayed. The black crosses indicate the center of the various pixels after averaging the H and V polarizations. The beam is represented for the central pixel by the red dotted circle.These high S/N observations rule out the IDP source model (red lines) because they result (i) in narrower lines than the ones produced by the IDP model; and (ii) in a non-uniform spatial distribution of water. Even if the flux in the northernmost pixels is adjusted to lower values to fit the l/c, the IDP model fails to reproduce the line wings (see Fig. 12). By adjusting the local water column density by rescaling the SL9 vertical profile, we find that an SL9 model (blue line), in which all water resides at pressures lower than 2 mbar, enables one to reproduce the observed map.

over the PACS beam. The resulting maps are displayed in Fig. 15 and a latitudinal section taken from the 66.4 μm map is shown in Fig. 16. The uncertainty on the line peak values translates into an uncertainty of up to 20% on the column density values. This is consistent with the scatter we find in narrow latitudinal bands (~15%). If we had used a physical profile for the SL9-material evolution instead of an empirical one for water, we could have ended up with column density values different by a factor of up to 2 (with the same level of uncertainties). One needs to know the true vertical profile to retrieve the true values of the local water column.

The 66.4 μm map and the corresponding latitudinal section show a general trend in the latitudinal distribution of the derived column densities. Indeed, we see an increase by a factor of 2−3 from the northernmost latitudes to the southern latitudes. This kind of distribution was anticipated by Lellouch et al. (2002), though with a much lower contrast, from their SL9 model. They expected a contrast of only 10% between 60 °S and 60 °N at infinite spatial resolution in 2007. Here, we observe a factor of 2−3 contrast between 60°S and 60 °N after spatial convolution by the instrument beam. This should translate into an even stronger contrast at infinite spatial resolution.

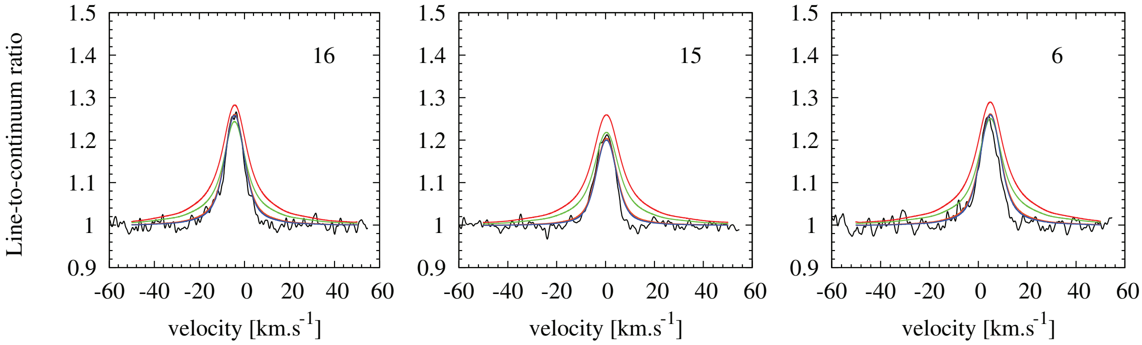

Fig. 12. Zoom on the northernmost pixels 6, 15 and 16 of the HIFI map. The SL9 model is displayed in blue, while the IDP model with a flux of 3.6×10^6 cm^{-2} s^{-1} is plotted in red. The IDP model overestimates both the l/c and the line width in each pixel. Even if the IDP flux is lowered to 2.0×10^6 cm^{-2} s^{-1} (green line) to roughly fit the l/c, it still fails to fit the wings. A model based on the philosophy of the "hybrid" model of Lellouch et al. (2002) with the SL9 source and a background IDP source with a flux of 8×10^4 cm^{-2} s^{-1}, corresponding to the upper limit placed on the IDP source by the authors, is shown in orange. This model can barely be distinguished from the pure SL9 model, which means that an IDP background source is compatible with our observations.

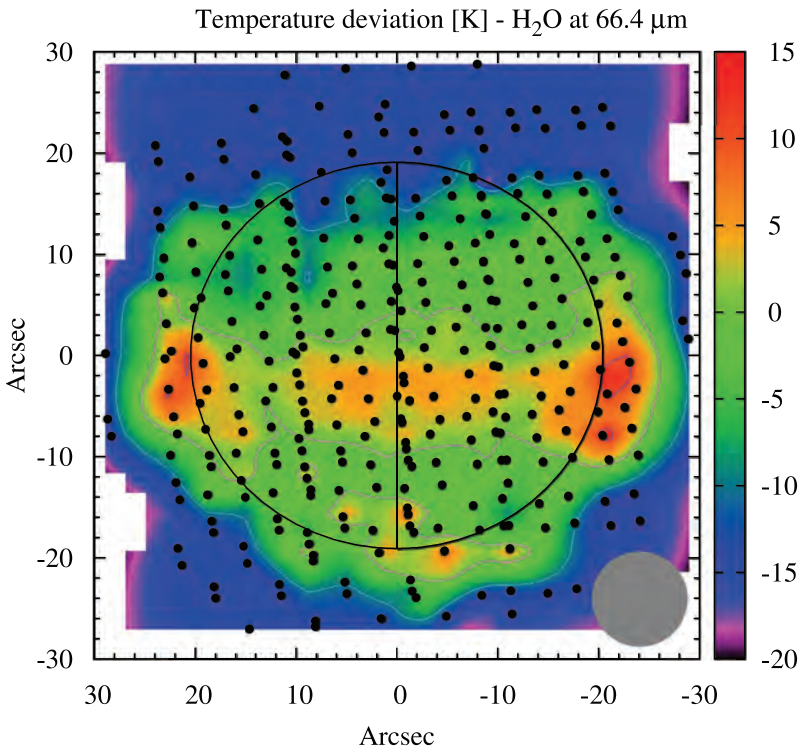

Fig. 13. Map of the temperature deviation (in K) from the nominal thermal profile assuming a spatially uniform distribution of water, as derived from the 66.4 μm map. Jupiter is represented by the black ellipse, and its rotation axis is also displayed. The beam is represented by the gray filled circle. A relative difference of 10–15 K in the high stratospheric temperatures between the northern and southern latitudes is required to reproduce the observations. A warm south equatorial region (0–25 °S) of ~4 K higher stratospheric temperatures is identified in this map (see also Fig. 14).

We applied the same methodology as for the PACS map to derive the local column density from the HIFI map, still assuming a spatially uniform temperature. The resulting map is shown in Fig. 17. The uncertainty on the column abundance derivation is on the order of 20% in the HIFI pixels despite the high S/N, because the line is optically thick. We find that the column abundance increases from the northernmost latitude to the southern latitudes by a factor of ~3. The general trend as a function of latitude as well as the highest values of the water column ($4{-}5 \times 10^{15}$ cm^{-2}) fully agree with the PACS results obtained at 66.4 μm and therefore confirm our results.

5. Discussion

5.1. A local temperature maximum or an additional source of water around 15° S?

In the 66.4 μm map analysis (Sect. 4.2.1), we found that the emission between the equator and 25 °S could be explained by either an about 4 K warmer stratospheric temperature and/or a higher water column density (or even a combination of both), over the PACS beam.

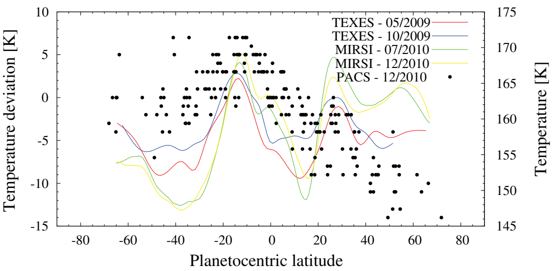

Fig. 14. Latitudinal section of the temperature deviation from the nominal profile as derived from the 66.4 μm map (black points), assuming a spatially uniform distribution of water. Only the pixels within the planetary disk are represented here. The temperatures at a pressure of 2 mbar as retrieved from our IRTF/TEXES observations are also displayed (red line for the May 2009 data and blue line for the October 2009 data) as well as the temperatures derived from our IRTF/MIRSI data (green for July 2010 and yellow for December 2010). The temperatures derived from the MIRSI images are averages for the pressure range the observations are sensitive to (1−40 mbar). We applied to these values an offset of −20 K to bring them to the same scale as the TEXES values (see Sect. 3.2 for the reasons why we obtained these high values from the MIRSI data). The warm temperature belt seen around 15 °S is the most probable cause for the enhanced emission seen at these latitudes in our 66.4 μm map (see Fig. 13). There is only marginal evidence in the water emission observations for the warm belt seen in the IRTF/MIRSI data around 30 °N.

The IRTF/MIRSI images unveil a warm belt around 15 °S at pressures between 1 and 40 mbar (see Fig. 5), also seen in the data of Fletcher et al. (2011) at 5 mbar. The temperature maps retrieved from the IRTF/TEXES data locate such a belt at this latitude in the 1−10 mbar pressure range (see Fig. 9) and it is most obvious at 2 mbar (see Fig. 14). Given that the temperature excess needed over the PACS beam to fit the data is ~4 K, this warm belt is probably sufficient to explain the enhanced water emission in this latitudinal range. This warm belt also implies that the water condensation level is located at a slightly lower altitude, allowing higher column densities of water at these latitudes.

On the other hand, if the warm belt is not sufficient and if the water column is indeed higher at these latitudes (independently of any temperature effect), this means that this extra water is provided by an additional source. What kind of source could that be? A local source (rings/satellites) that would generate these spatial properties seems unlikely. If the material were transported from the source to Jupiter in neutral form, the deposition latitude should be centered on the equator. According to Hartogh et al. (2011), this is how the Enceladus torus feeds Saturn's stratosphere in water. A second possibility is the deposition of ionized material (with a high charge-to-mass ratio) at latitudes that are magnetically connected to the source(s), as proposed by Connerney (1986). According to his work, a source depositing material at ~10 °S would probably need to be located at 1.1 planetary radii, in the case of Saturn. Because Jupiter's magnetic field is 20 times stronger than Saturn's, this would imply that a hypothetical source depositing material around 15 °S would need to be even closer to the planet than 1.1 Jupiter radii, a zone where there is no such source. There is no reason why a source like the IDP would deposit material only around 15 °S. In addition to that, an increase by a factor of ~2 of the water column due to a local source or an IDP source should result in broader line widths in the pixels centered on the equator in the HIFI map, an effect evidently absent from Fig. 11. Finally, another possible source is an additional comet impact. The only known events are two impacts that have been detected in Jupiter between the SL9 event and our 2010 PACS observation. The first one occurred on July 19, 2009, but at a planetocentric latitude of 55 °S (Sánchez-Lavega et al. 2010; Orton et al. 2011). Interestingly, the second observed impact occurred on June 3, 2010, at a planetocentric latitude of 14.°5 S (Hueso et al. 2010). According to Hueso et al. (2010), this impactor had a size of 8−13 m. According to Fig. 16, the excess of H_2O column in this latitude region is on the order of $\sim 10^{15}$ cm^{-2}. The latitudinal band extending from 25 °S to the equator has a surface area of 1.35×10^{20} cm^2. The excess of water then corresponds to 4×10^9 kg of water, i.e., ~3500 times the mass of a 3 m impactor consisting of pure water. It is thus unlikely that this extra water (if any) located between 25 °S and the equator is due to an additional external source.

Finally, we recall that the highest emission seen between 25 °S and the equator can most probably be attributed to the temperature increase in this region as seen in the MIRSI and TEXES maps (Figs. 9, 10 and 14).

5.2. Spatial distribution of water in Jupiter

The HIFI and PACS maps contain horizontal information on the water distribution in Jupiter's stratosphere. Because HIFI resolves the line shapes of the water emission at 1669.9 GHz, the HIFI map also contains information on the vertical distribution of the species if they are located at pressures lower than 1 mbar.

As stated previously, the precise shape of the vertical water profile will be retrieved from the 556.9, 1097.4 and 1669.9 GHz water lines observed at very high S/N with HIFI in the framework of the HssO Key Program and shall therefore be discussed in detail in a future dedicated paper (Jarchow et al., in prep.). However, we tested profiles that are qualitatively compatible with the IDP and SL9 sources. The spectral line shapes observed with the HIFI very high resolution confirm that the bulk of water resides at lower pressure levels (i.e., at pressures lower than 2 mbar) than would be the case with a steady IDP source. This result agree well with the prediction of Moreno et al. (2003) for the p_0 level (1 mbar) for CO, hydrogen cyanide (HCN), and carbon monosulfide (CS) 20 years after the SL9 impacts. Cavalié et al. (2012) studied the temporal evolution of the disk-averaged water line at 556.9 GHz with the Odin space telescope for almost a decade. They developed two models that could fit the tentatively seen decrease in the line contrast. In a first model, they tentatively increased the vertical eddy diffusion $K(z)$ by a factor of 3 at 1 mbar to remove more water by condensation. The line profiles in the HIFI map now show that this hypothesis is not valid and that the bulk of water remains at higher levels ($p_0 \leq 2$ mbar) than in their model, where the bulk of water had spread quite uniformly as a function of pressure down to the condensation level (see their Fig. 10). This means that the decrease of the line-to-continuum ratio at 556.9 GHz that they have tentatively observed has to be explained by the removal of water at the mbar and submbar levels and not by condensation. In a second model, Cavalié et al. (2012) approximately incorporated dilution effects from horizontal diffusion and chemical losses due to conversion of OH radicals (photolytical product of H_2O) into CO_2 based on the predictions of Lellouch et al. (2002) for their previously published temporal evolution model (Cavalié et al. 2008b). The water vertical profile used in Cavalié et al. (2008b) was based on the philosophy of the "hybrid model" of Lellouch et al. (2002), which took into account a low IDP flux of 4×10^4 cm^{-2} s^{-1}. This second model of Cavalié et al. (2012) has several advantages in

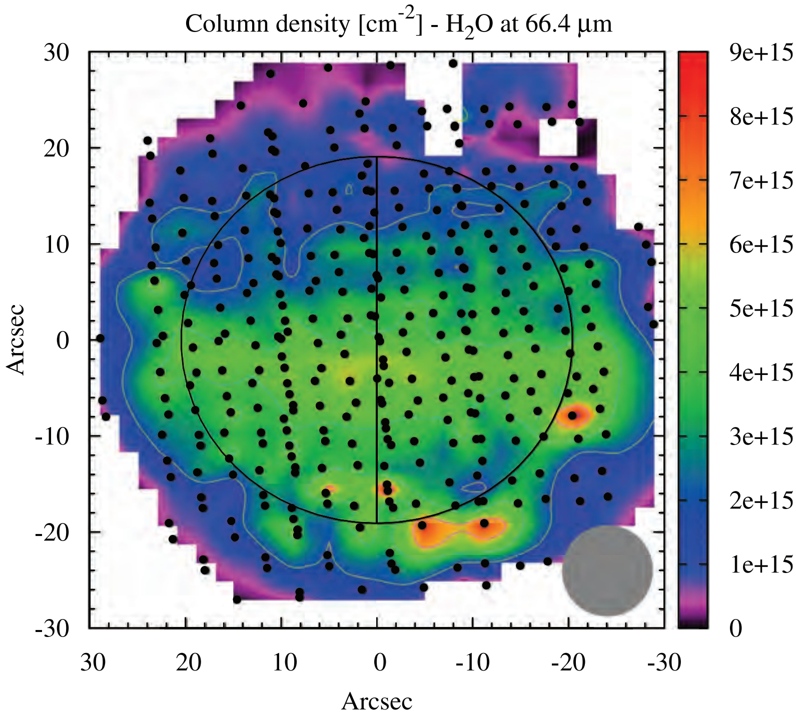

Fig. 15. Column density of water (in cm^{-2}), as derived from the 66.4 μm map. Jupiter is represented by the black ellipse, and its rotation axis is also displayed. The beam is represented by the gray filled circle. In the south equatorial region (0−25 °S), the emission maximum identified in this map is most probably caused by a temperature effect and not by a local maximum of the column density.

that enough water is lost as a function of time to reproduce the temporal evolution of the 556.9 GHz line, and it keeps a standard $K(z)$ profile and thus keeps the bulk of water at pressures compatible with our HIFI results. In this sense, it reconciles the Odin and our HIFI submillimeter observations of water with the infrared observations of ISO. Another advantage is that this model also accounts for a background IDP source with a flux of 4×10^4 cm^{-2} s^{-1}. According to our computations, adding an IDP source of that magnitude is not inconsistent with our observations, because such a low flux only marginally affects the line shape at 1669.9 GHz and 66.4 μm (e.g., Fig. 12). Even a model accounting for a background source due to IDP with a flux corresponding to the upper limit derived by Lellouch et al. (2002) (8×10^4 cm^{-2} s^{-1}) remains compatible with our data[3] (see Fig. 12). We are thus able to quantify how much of the observed water can be attributed to the SL9 impact. The disk-averaged column density of this SL9 + background IDP model (with a flux of 8×10^4 cm^{-2} s^{-1}) is $\sim 3 \times 10^{15}$ cm^{-2}, while the column density of the background IDP source alone is $\sim 10^{14}$ cm^{-2}. This means that more than 95% of the observed water comes from SL9 according to our models. These results are somewhat different from those obtained by Lellouch et al. (2002). These authors found a disk-averaged column of 1.5×10^{15} cm^{-2} from their SL9 + background IDP model and 4.5×10^{14} cm^{-2} for their background IDP model with a flux of 8×10^4 cm^{-2} s^{-1}, implying that up to 30% of the water could be due to IDP. These differences may arise from a different choice of chemical scheme, temperature, and vertical eddy mixing profiles. But both results essentially show that SL9 is by far the main source of water in Jupiter's stratosphere.

The HIFI and the 66.4 μm PACS maps consistently show a north-south asymmetry that cannot be attributed to a hemispheric asymmetry in the stratospheric temperatures but to an asymmetry in the water column abundance. If we omit the 25 °S-to-equator band from the meridional distribution observed by PACS shown in Fig. 16, which is most probably a result of a local temperature increase, we see that the water column looks roughly constant in the southern hemisphere and decreases linearly by a factor of 2−3 poleward in the northern hemisphere. This behavior is not expected from a IDP source but is consistent with the SL9 source, because the comet has hit the planet at 44 °S. Although the observations have taken place more than 15 years after the SL9 impacts, a remnant of the latitudinal asymmetry that was predicted by Lellouch et al. (2002) is now demonstrated, thus validating the SL9 source.

We have to keep in mind that, unlike Lellouch et al. (2006) for HCN and CO_2, we do not have access to latitudes higher than ~60° because of the observation geometry and beam convolution. It would thus be hazardous to directly compare of the water distribution with the distributions of HCN and CO_2 previously observed by Lellouch et al. (2006). They also correspond to different post-impact observation dates.

Lellouch et al. (2002) used a horizontal model that accounted for meridional eddy diffusion and a simplified chemical scheme for oxygen species to model the temporal evolution of the water column as a function of latitude. They derived a horizontal eddy diffusion coefficient of $K_h = 2 \times 10^{11}$ cm^2 s^{-1}, constant in latitude, and a H_2O/CO ratio of 0.11 from their observed CO_2 horizontal distribution and disk-averaged water column. According to the results of this model, the contrast predicted for 2007 (i.e., even earlier than our *Herschel* maps) was ~10% at infinite spatial resolution. The contrast measured with PACS at 66.4 μm is

[3] This possible additional background source could also be attributed to a flow of smaller comets that would have impacted Jupiter at random latitudes in the last tens to a couple of hundreds of years, for which the vertical distribution of water would resemble that of a background IDP source.

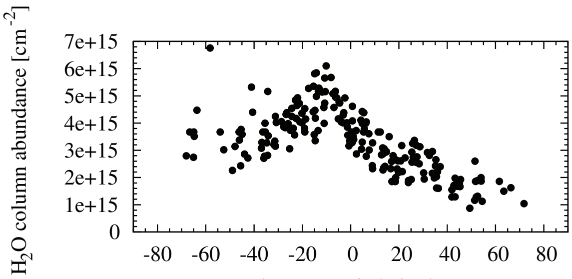

Fig. 16. Latitudinal section of the beam-convolved column density of water as derived from the 66.4 μm map. Only the pixels within the planetary disk are represented here. The peak values around 15 °S can most probably be attributed to the warmer temperatures observed around this latitude. The marginal increase seen around 30 °N could be due to the bright band detected at these latitudes in 2010 in the IRTF/MIRSI observations (see Fig. 14).

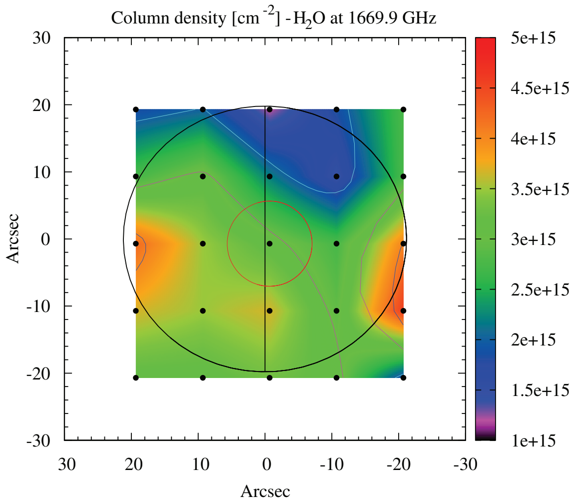

Fig. 17. Beam-convolved column density of water (cm^{-2}) map as derived from the HIFI observations at 1669.9 GHz. The beam is represented for the central pixel by the red circle.

already higher despite the beam convolution, which results in its attenuation. The deconvolution of the observed contrast to constrain horizontal transport is beyond the scope of this paper. However, we anticipate that if it were only due to eddy diffusion, the meridional distribution of water in Jupiter's stratosphere would require lower values for K_h. Lellouch et al. (2006) showed that the HCN meridional distribution in December 2000 (6.5 years after the impacts) could not be reproduced by using the latitudinally constant meridional eddy diffusion coefficient K_{yy} of Griffith et al. (2004). They rather had to invoke not only a K_{yy} variable in latitude (θ) with peak values of $K_{yy} \sim 2.5 \times 10^{11}$ cm^2 s^{-1}, consistent with low spatial resolution measurements of Moreno et al. (2003), and a significant decrease of K_{yy} by an order of magnitude poleward of 40°, but also equatorward advective transport with wind velocities of ~7 cm s^{-1}. The equatorward advective wind results in a slower contamination of the northern hemisphere. According to this work and to Moreno et al. (2003), water and HCN are located at the same pressure level. If confirmed, they should be subject to the same horizontal transport regime. The philosophy of the transport model of Lellouch et al. (2006) seems to agree with our observations, but more modeling work is needed to check the consistency of their $K_{yy}(\theta)$ and wind velocity profiles.

We recall that the water column density values derived in this paper correspond to values convolved by the PACS beam. Because the 66.4 μm water line targeted for the mapping with PACS, from which the column densities were derived, is optically thick, there is no linear relation between the column densities and the observed lines. Therefore, it is not possible to simply spatially convolve the results of a diffusion model to compare it with our observation results. The confirmation of the validity of the horizontal model from Lellouch et al. (2006) with those data thus requires reproducing the observed map with a 2D (for geometry) radiative transfer model that could be fed with the water latitude-dependent distribution output of the diffusion+advection model. The problem is even more complicated because of the sensitivity of water to photolysis in Jupiter's high stratosphere and to condensation in the low stratosphere. Accordingly, unlike HCN and CO_2, water is not chemically stable and cannot be considered as an ideal tracer for horizontal dynamics. A 2D/3D photochemical model including oxygen chemistry is therefore necessary to derive constraints on $K_{yy}(\theta)$ and on advection in Jupiter's stratosphere at the mbar level. Such a model would also enable one to retrieve a reliable mass of the water that was initially deposited by the comet from these *Herschel* observations. Recent work by Dobrijevic et al. (2010, 2011) now enables reducing the size of chemical schemes to acceptable sizes to extend existing 1D photochemical models to 2D/3D by identifying key reactions in the more complete chemical schemes of 1D models. These reduced chemical schemes will facilitate the emergence of 2D/3D photochemical models because they reduce the computational time for chemistry by one to two orders of magnitude.

6. Conclusion

We have performed the first spatially resolved observations of water in the stratosphere of Jupiter with the HIFI and PACS instruments of the *Herschel* Space Observatory in 2009−2010 to determine its origin. In parallel, we monitored the stratospheric temperature in Jupiter with the NASA IRTF in the same periods to separate temperature from water variability in the *Herschel* maps.

We found that the shape of the water lines at 1669.9 GHz in the HIFI map recorded at very high spectral resolution proves that the bulk of water resides at pressures lower than 2 mbar. This rules out any steady source, like the IDP source, in which water would be present down to the condensation level (~20−30 mbar). A uniform source is also ruled out by both the HIFI and PACS maps. Indeed, the observations show a north-south asymmetry in the emission. The water column is roughly constant in the southern hemisphere and decreases linearly by a factor of 2−3 poleward in the northern hemisphere, at the spatial resolution of the observations. This distribution cannot be attributed to a hemispheric asymmetry in the stratospheric temperatures, according to our IRTF observations, but rather to meridional variability of the water column abundance. Thus, the spatial distribution of water in Jupiter's stratosphere is clear evidence that a recent comet, i.e., the Shoemaker-Levy 9 comet, is the principal source of water in Jupiter. What we observe today is a remnant of the oxygen delivery by the comet at 44 °S in July 1994.

It is possible that other sources like IDP or icy satellites may coexist at Jupiter, but, as demonstrated by this work, with other spatial distribution properties and lower magnitudes than the SL9 source. The upper limit derived for an IDP source by Lellouch et al. (2002) (with a flux of 8×10^4 cm^{-2} s^{-1}) is consistent with the *Herschel* observations, meaning that at least 95% of the observed water comes from the SL9 comet and subsequent (photo)-chemistry in Jupiter's stratosphere according to our models, as of today.

Although they reached their objective of determining the origin of the bulk of stratospheric water in Jupiter, the mapping observations we presented have insufficient latitudinal resolution and a lack of information at latitudes higher than ~60° to assess the relative magnitude of all possible water sources at Jupiter. The Submillimetre Wave Instrument (Hartogh et al. 2009a) is an instrument proposed for the payload of the recently selected Jupiter Icy Moon Explorer (JUICE), an L-class mission of the ESA Cosmic Vision 2015−2025 program, which is to be launched in 2022 and will study the Jovian system for 3.5 years starting in 2030. This instrument has several key objectives, one of which is to map in 3D SL9-derived species in the stratosphere of Jupiter with scale height vertical resolution and 1° resolution in latitude. It also proposes to measure the isotopic ratios in water and CO. The combination of these measurements will enable us to separate the spatial and isotopic signatures of all possible sources and their relative magnitude at Jupiter.

Acknowledgements. T. Cavalié wishes to thank J. Brillet for providing him with his baseline ripple removal tool for the purposes of this work. T. Cavalié acknowledges funding from the Centre National d'Études Spatiales (CNES). M. de Val-Borro acknowledges support from the Special Priority Program 1488 of the German Science Foundation, and grants NSF AST-1108686 and NASA NNX12AH91H. G. Orton acknowledges funding from the National Aeronautics and Space Administration to the Jet Propulsion Laboratory, California Institute of Technology. T. Greathouse acknowledges funding from NASA PAST grant NNX08AW33G and was supported as a Visiting Astronomer at the Infrared Telescope Facility, which is operated by the University of Hawaii under Cooperative Agreement no. NNX-08AE38A with the National Aeronautics and Space Administration, Science Mission Directorate, Planetary Astronomy Program. F. Billebaud wishes to thank the Programme National de Planétologie (PNP) of the Institut National des Sciences de l'Univers (INSU) for pluri-annual funding on this project. HIFI has been designed and built by a consortium of institutes and university departments from across Europe, Canada and the United States under the leadership of SRON Netherlands Institute for Space Research, Groningen, The Netherlands and with major contributions from Germany, France and the US. Consortium members are: Canada: CSA, U.Waterloo; France: CESR, LAB, LERMA, IRAM; Germany: KOSMA, MPIfR, MPS; Ireland, NUI Maynooth; Italy: ASI, IFSI-INAF, Osservatorio Astrofisico di Arcetri-INAF; Netherlands: SRON, TUD; Poland: CAMK, CBK; Spain: Observatorio Astronómico Nacional (IGN), Centro de Astrobiología (CSIC-INTA). Sweden: Chalmers University of Technology − MC2, RSS & GARD; Onsala Space Observatory; Swedish National Space Board, Stockholm University − Stockholm Observatory; Switzerland: ETH Zurich, FHNW; USA: Caltech, JPL, NHSC. PACS has been developed by a consortium of institutes led by MPE (Germany) and including UVIE (Austria); KUL, CSL, IMEC (Belgium); CEA, OAMP (France); MPIA (Germany); IFSI, OAP/AOT, OAA/CAISMI, LENS, SISSA (Italy); IAC (Spain). This development has been supported by the funding agencies BMVIT (Austria), ESA-PRODEX (Belgium), CEA/CNES (France), DLR (Germany), ASI (Italy), and CICT/MCT (Spain). Data presented in this paper were analyzed using HIPE is a joint development by the *Herschel* Science Ground Segment Consortium, consisting of ESA, the NASA *Herschel* Science Center, and the HIFI, PACS and SPIRE consortia. This development has been supported by national funding agencies: CEA, CNES, CNRS (France); ASI (Italy); DLR (Germany). Additional funding support for some instrument activities has been provided by ESA. We are grateful to an anonymous referee for the constructive comments about this manuscript.

References

Bézard, B., Lellouch, E., Strobel, D., Maillard, J.-P., & Drossart, P. 2002, Icarus, 159, 95
Bjoraker, G. L., Stolovy, S. R., Herter, T. L., Gull, G. E., & Pirger, B. E. 1996, Icarus, 121, 411
Borysow, A., & Frommhold, L. 1986, ApJ, 304, 849
Borysow, J., Trafton, L., Frommhold, L., & Birnbaum, G. 1985, ApJ, 296, 644
Borysow, J., Frommhold, L., & Birnbaum, G. 1988, ApJ, 326, 509
Brown, L. R., & Plymate, C. 1996, J. Quant. Spec. Radiat. Transf., 56, 263
Cavalié, T., Billebaud, F., Biver, N., et al. 2008a, Planet. Space Sci., 56, 1573
Cavalié, T., Billebaud, F., Fouchet, T., et al. 2008b, A&A, 484, 555
Cavalié, T., Billebaud, F., Dobrijevic, M., et al. 2009, Icarus, 203, 531
Cavalié, T., Hartogh, P., Billebaud, F., et al. 2010, A&A, 510, A88
Cavalié, T., Biver, N., Hartogh, P., et al. 2012, Planet. Space Sci., 61, 3
Connerney, J. E. P. 1986, Geophys. Res. Lett., 13, 773
de Graauw, T., Helmich, F. P., Phillips, T. G., et al. 2010, A&A, 518, L6
Dobrijevic, M., Cavalié, T., Hébrard, E., et al. 2010, Planet. Space Sci., 58, 1555
Dobrijevic, M., Cavalié, T., & Billebaud, F. 2011, Icarus, 214, 275
Dutta, J. M., Jones, C. R., Goyette, T. M., & De Lucia, F. C. 1993, Icarus, 102, 232
Feuchtgruber, H., Lellouch, E., de Graauw, T., et al. 1997, Nature, 389, 159
Flasar, F. M. 1989, NASA Spec. Publ., 494, 324
Flasar, F. M., Kunde, V. G., Achterberg, R. K., et al. 2004, Nature, 427, 132
Fletcher, L. N., Orton, G. S., Yanamandra-Fisher, P., et al. 2009, Icarus, 200, 154
Fletcher, L. N., Orton, G. S., Rogers, J. H., et al. 2011, Icarus, 213, 564
Fouchet, T., Lellouch, E., Bézard, B., et al. 2000, A&A, 355, L13
Greathouse, T. K., Richter, M., Lacy, J., et al. 2011, Icarus, 214, 606
Griffith, C. A., Bézard, B., Greathouse, T., et al. 2004, Icarus, 170, 58
Hartogh, P., Barabash, S., Bolton, S., et al. 2009a, EPSC Abstracts, 4, EPSC2009
Hartogh, P., Lellouch, E., Crovisier, J., et al. 2009b, Planet. Space Sci., 57, 1596
Hartogh, P., Lellouch, E., Moreno, R., et al. 2011, A&A, 532, L2
Hesman, B. E., Davis, G. R., Matthews, H. E., & Orton, G. S. 2007, Icarus, 186, 342
Hueso, R., Wesley, A., Go, C., et al. 2010, ApJ, 721, L129
Kassis, M., Adams, J. D., Hora, J. L., Deutsch, L. K., & Tollestrup, E. V. 2008, PASP, 120, 1271
Lacy, J. H., Richter, M. J., Greathouse, T. K., Jaffe, D. T., & Zhu, Q. 2002, PASP, 114, 153
Landgraf, M., Liou, J.-C., Zook, H. A., & Grün, E. 2002, AJ, 123, 2857
Larson, H. P., Fink, U., Treffers, R., & Gautier, III, T. N. 1975, ApJ, 197, L137
Lellouch, E., Paubert, G., Moreno, R., et al. 1995, Nature, 373, 592
Lellouch, E., Bézard, B., Moses, J. I., et al. 2002, Icarus, 159, 112
Lellouch, E., Moreno, R., & Paubert, G. 2005, A&A, 430, L37
Lellouch, E., Bézard, B., Strobel, D. F., et al. 2006, Icarus, 184, 478
Lellouch, E., Hartogh, P., Feuchtgruber, H., et al. 2010, A&A, 518, L152
Leovy, C. B., Friedson, A. J., & Orton, G. S. 1991, Nature, 354, 380
Lomb, N. R. 1976, Ap&SS, 39, 447
Moreno, R., Marten, A., Matthews, H. E., & Biraud, Y. 2003, Planet. Space Sci., 51, 591
Moses, J. I., Lellouch, E., Bézard, B., et al. 2000, Icarus, 145, 166
Moses, J. I., Fouchet, T., Bézard, B., et al. 2005, J. Geophys. Res., 110, 8001
Niemann, H. B., Atreya, S. K., Carignan, G. R., et al. 1998, J. Geophys. Res., 103, 22831
Orton, G. S., Friedson, A. J., Caldwell, J., et al. 1991, Science, 252, 537
Orton, G. S., Fletcher, L. N., Lisse, C. M., et al. 2011, Icarus, 211, 587
Ott, S. 2010, in Astronomical Data Analysis Software and Systems XIX, eds. Y. Mizumoto, K.-I. Morita, & M. Ohishi, PASP, 434, 139
Pickett, H. M., Poynter, I. R. L., Cohen, E. A., et al. 1998, J. Quant. Spectr. Rad. Trans., 60, 883
Pilbratt, G. L., Riedinger, J. R., Passvogel, T., et al. 2010, A&A, 518, L1
Poglitsch, A., Waelkens, C., Geis, N., et al. 2010, A&A, 518, L2
Prather, M. J., Logan, J. A., & McElroy, M. B. 1978, ApJ, 223, 1072
Roelfsema, P. R., Helmich, F. P., Teyssier, D., et al. 2012, A&A, 537, A17
Rothman, L. S., Rinsland, C. P., Goldman, A., et al. 1998, J. Quant. Spectr. Rad. Trans., 60, 665
Sánchez-Lavega, A., Wesley, A., Orton, G., et al. 2010, ApJ, 715, L155
Selsis, F., Brillet, J., & Rapaport, M. 2004, A&A, 416, 783
Strobel, D. F., & Yung, Y. L. 1979, Icarus, 37, 256
Wong, M. H., Mahaffy, P. R., Atreya, S. K., Niemann, H. B., & Owen, T. C. 2004, Icarus, 171, 153

Pages 15 to 16 are available in the electronic edition of the journal at http://www.aanda.org

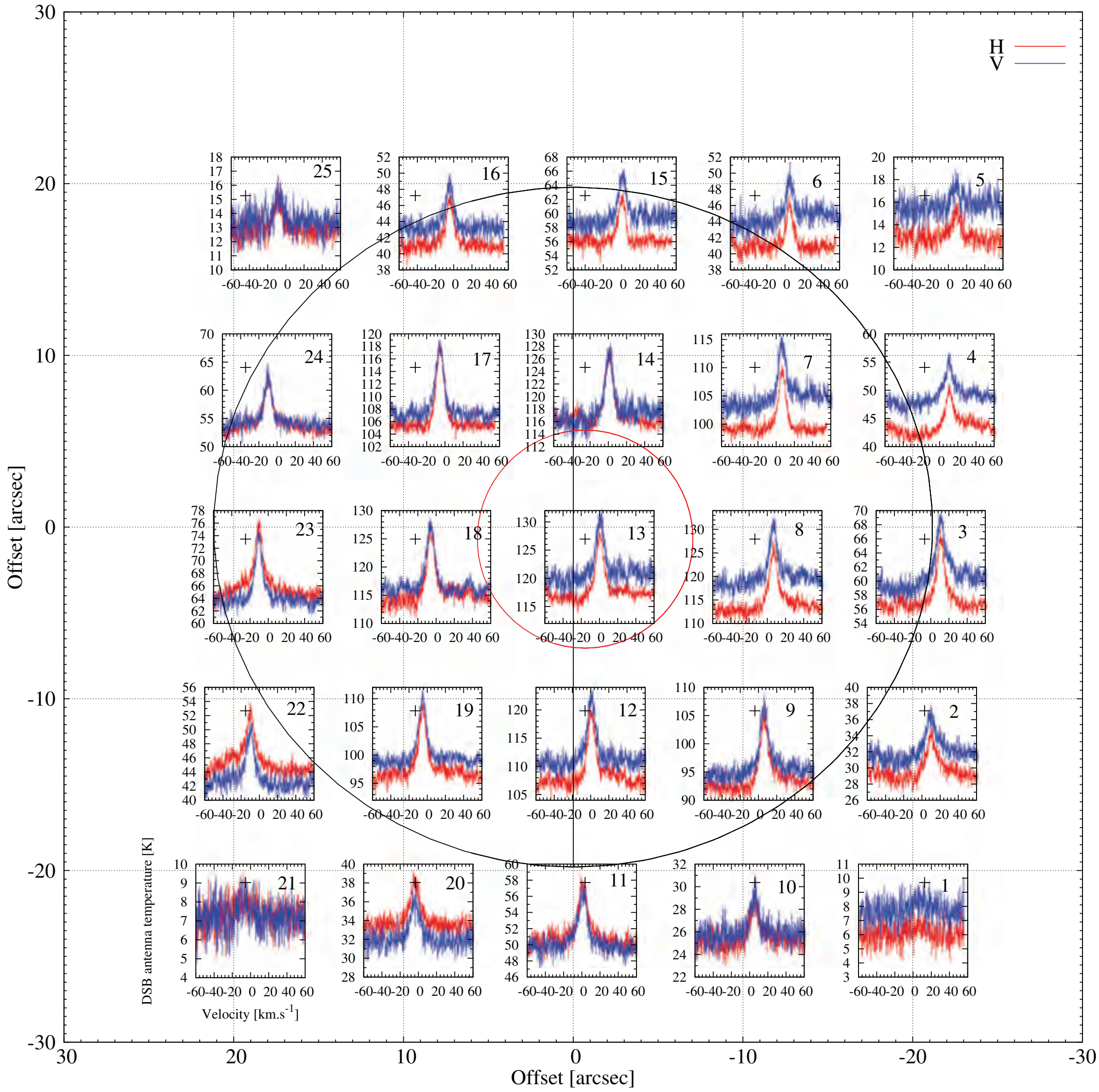

Fig. 1. Water 5×5 raster map at 1669.9 GHz obtained with *Herschel*/HIFI on July 7, 2010, after reducing the raw data with the HIPE 8.2.0 pipeline. The data are shown at their native resolution (1.1 MHz). The pixels are numbered according to the raster observation numbering. The H (red line) and the V (blue line) polarizations of the WBS are both presented. Jupiter is represented with the black ellipse, and its rotation axis is also displayed. The black crosses indicate the center of the various pixels according to the H/V mean positions retrieved from the modeling of the continuum emission. The beam is represented for the central pixel by the red circle.

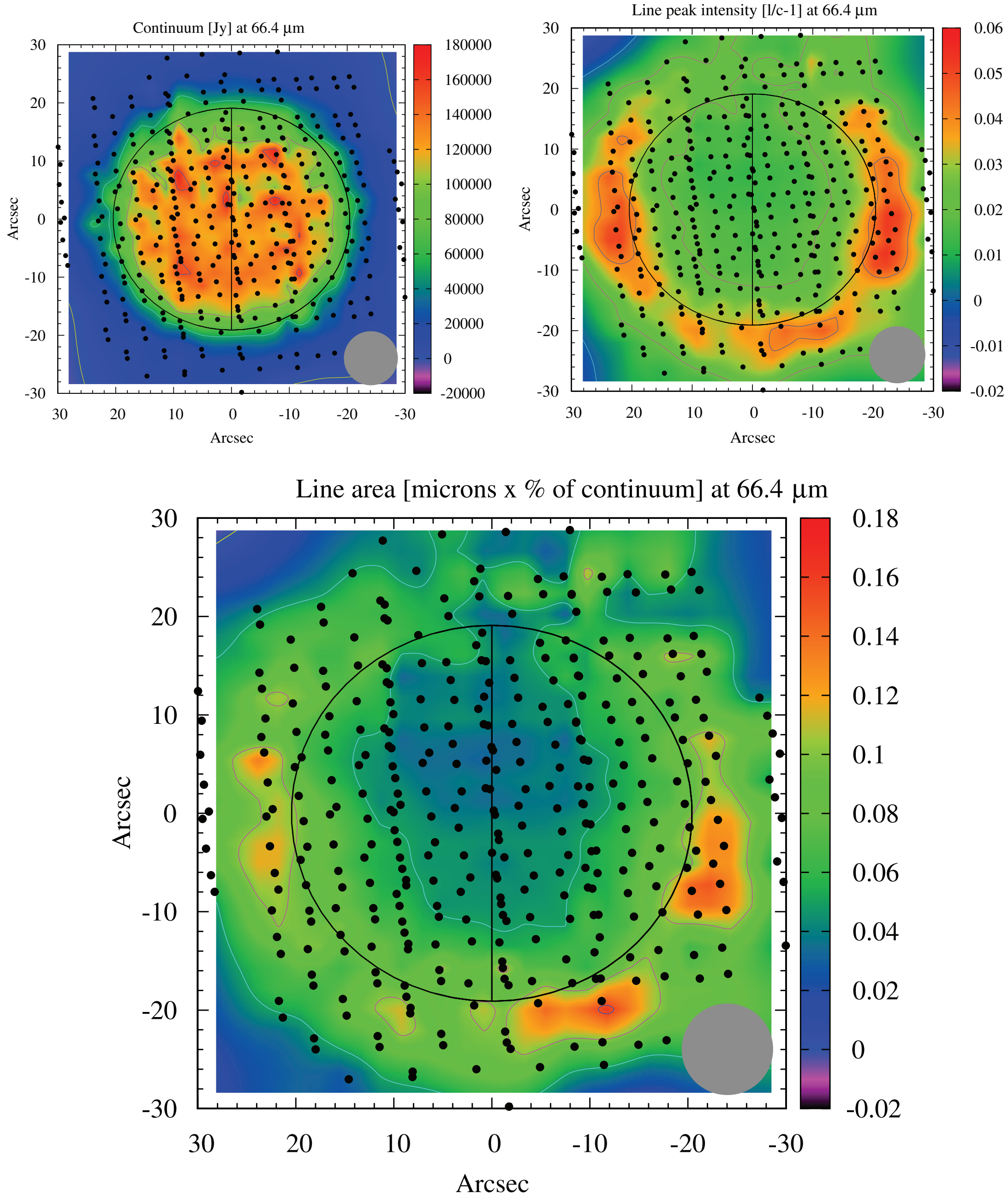

Fig. 3. Water map at 66.4 μm observed by the PACS spectrometer on December 15, 2010. Jupiter is represented by the black ellipse, and its rotation axis is also displayed. The beam is represented by a gray filled circle. The continuum (in Jy), the line peak intensity (=l/c-1), and the line area (in microns × % of the continuum) are displayed. While the line peak intensity and line area values can be relied on, the absolute flux values cannot (see text for more details). This map confirms the lack of emission at mid-to-high latitudes in the northern hemisphere (best seen at the limb).

A&A 510, A88 (2010)
DOI: 10.1051/0004-6361/200912909

Astronomy & Astrophysics

A cometary origin for CO in the stratosphere of Saturn?

T. Cavalié[1], P. Hartogh[1], F. Billebaud[2,3], M. Dobrijevic[2,3], T. Fouchet[4], E. Lellouch[4], T. Encrenaz[4], J. Brillet[2,3], and G. H. Moriarty-Schieven[5]

[1] Max Planck Institute für Sonnensystemforschung, 37191 Katlenburg-Lindau, Germany
e-mail: cavalie@mps.mpg.de
[2] Université de Bordeaux, Laboratoire d'Astrophysique de Bordeaux (LAB), France
[3] CNRS/INSU, UMR 5804, 33271 Floirac Cedex, France
[4] LESIA, Observatoire de Paris, 92195 Meudon, France
[5] National Research Council, Herzberg Institute of Astrophysics, Victoria, BC V9E 2E7, Canada

Received 17 July 2009 / Accepted 24 November 2009

ABSTRACT

Context. The CO(3–2) line has been observed in the atmosphere of Saturn. The CO(3–2) observation proves that an external source of CO exists in the stratosphere of the planet.

Aims. We attempt to constrain the type and magnitude of the external source of CO in the atmosphere of Saturn, by observing the emission core of the CO(6–5) line.

Methods. We observed the CO(6–5) line at the limbs of Saturn. We analysed the observations by means of a 1-D transport model of the atmosphere of Saturn, coupled with a radiative transfer model.

Results. We obtained a high signal-to-noise ratio spectrum that confirms the existence of an external source of CO in the stratosphere of Saturn. We demonstrated that a cometary origin of CO is the most probable, an impact occurring 220 ± 30 years ago and depositing $(2.1 \pm 0.4) \times 10^{15}$ g of CO above 0.1 mbar. However, we cannot totally reject the possibility of CO originating (at least partially) in a steady source.

Conclusions. Complete photochemical modelling of the oxygen compounds is required to determine realistic error bars of the inferred quantities and to conclude on the origin of CO.

Key words. planets and satellites: individual: Saturn – radio lines: planetary systems

1. Introduction

The detection of H_2O and CO_2 by the Infrared Space Observatory and Spitzer in the stratosphere of the giant planets and Titan (Feuchtgruber et al. 1997; Coustenis et al. 1998; Lellouch et al. 2002; Burgdorf et al. 2006) has proven the existence of an external source of oxygen in the outer Solar System that could be in the form of infalling interplanetary dust particles (IDP), ring and/or satellite particles, or large comets. In contrast, observing CO in the stratosphere of a giant planet does not automatically imply an external origin of this species. There is no condensation sink at the tropopause for CO so that it can be transported to the stratosphere from the deep hot interior of the planet. Therefore, CO can either have an internal origin, an external origin or a combination of both.

A dual origin of CO has already been observed in the atmosphere of Jupiter from infrared spectroscopy (Bézard et al. 2002) and tentatively in the atmosphere of Neptune from (sub)millimetre spectroscopy (Lellouch et al. 2005; Hesman et al. 2007). In both planets, observations and their analysis have led to the conclusion that CO, originating in an external source, was provided to the atmospheres of the planets by large comet impacts, the most recent being the impact of the Shoemaker-Levy 9 (SL9) comet in the atmosphere of Jupiter (Lellouch et al. 1995, 1997; Bézard et al. 2002).

While the situation is still unclear in the atmosphere of Uranus (Encrenaz et al. 2004; Cavalié et al. 2008a), Cavalié et al. (2009) demonstrated using their observations of the CO(3–2) rotational line at 345 GHz that there is an external source of CO in Saturn (not excluding an internal source that is probably weaker than in Jupiter). From their analysis, the authors concluded that this external source possibly had an SL9-like comet impact origin, but they did not reject the possibility of a steady source (interplanetary dust particles or grains from the rings and/or satellites). This first observation of CO in Saturn at submillimetre wavelengths has motivated the observations that we present in this paper. We have targeted the central emission core of a CO line at an even higher frequency (691.473 GHz) to directly probe the stratosphere of Saturn around 1 mbar and thus the external source of CO, while our previous attempt at 345 GHz probed a layer around 10–30 mbar (line in absorption). These observations aim to confirm the presence of an external source of CO and determine the most plausible source: a steady source or a sporadic source.

In this paper, we present the first observations of the CO(6–5) line in Saturn using heterodyne spectroscopy. In Sect. 2, we describe the observations and the data reduction. We then describe our atmospheric and radiative transfer models in Sect. 3 and the results obtained from our modelling in Sect. 4. We discuss them in Sect. 5 and finally present our conclusions in Sect. 6.

2. Observations

2.1. Data acquisition

Observations of Saturn at the frequency of the CO(6–5) line (ν_{6-5} = 691.4730763 GHz) were performed using the *D*-band

Table 1. Summary of Saturn's observations.

Date	τ(183 GHz)	Number of limb scans	% of used scans	Remarks
23 Jan. 2009	0.04–0.05			Observing strategy tests
27 Jan. 2009	0.05–0.06	2	100%	Observing strategy tests and validation
30 Jan. 2009	0.05–0.06	2	50%	50% of the scans lost due to bad pointing
13 Mar. 2009	0.05–0.06	4	50%	50% of the scans lost due to bad pointing
14 Mar. 2009	0.04–0.05	4	75%	25% of the scans lost due to bad pointing

Notes. Indicated: the date of the observations, the zenithal opacity conditions at 183 GHz during the observations, the number of limb scans that have been recorded, the percentage of the scans that have been used in the analysis, and remarks about the performed observations.

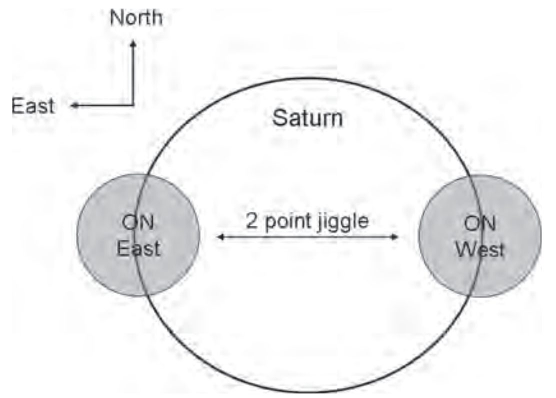

Fig. 1. On-scale scheme representing the 2-point jiggle-map observing mode. The larger disk represents Saturn's disk, while the smaller and filled ones correspond to the antenna beam in each of ON observed positions. The centre of the 7″ beam is alternately centred on the eastern and western limbs and then a common OFF position is observed 60″ away from Saturn's centre in the eastern direction. Eastern and western limb observations were carried out at equatorial latitudes, the sub-earth point latitude being [−3°; −1°] during the observations. *Note:* The rings are not displayed on the figure for simplicity, as they were close to edge-on.

receiver of the James Clerck Maxwell Telescope (JCMT) on 23, 27, and 30 January 2009, and on 13–14 March 2009. The zenithal opacity conditions at 183 GHz (JCMT data) and 225 GHz (Caltech Submillimeter Observatory data) were in the 0.04–0.06 range, i.e., 0.9–1.2 mm of precipitable water vapour, for every single observation, well within the specifications for observations at this frequency (see Table 1).

We carried out the observations with the *D*-band receiver in dual polarization and single-side band mode over a bandwidth of 250 MHz. Our strategy consisted in taking advantage of the relatively small beam (7″) compared to Saturn's size (19.5″ × 17.5″) and the rapid rotation of the planet, to observe alternately the eastern and western limbs of the planet and then subtract one resulting spectrum from the other. This was performed using a customized 2-point jiggle-map observing mode, in which the eastern and western limbs are observed consecutively as ON positions, both of them sharing a common OFF position observed afterwards (see Fig. 1). Both lines, Doppler-shifted by the rapid rotation of the planet, are thus present in the final spectrum, one with a positive amplitude and the other with a negative amplitude.

The multiple advantages of this "limb-switching" observing technique are the following: i) stronger line contrast; ii) reduction in the amplitude of the baseline ripples; and iii) isolation of the stratospheric line core formed at stratospheric pressure levels around 1 mbar by subtracting the tropospheric wide absorption feature. This technique obviously requires good pointing precision to balance both limb observations efficiently and equilibrate at best the continuum levels. This is why we have not included the spectra for which the difference between the two limbs was too large in our analysis. In the end, 2/3 of the observations were usable (see Table 1).

We also performed short disk-centred observations to measure the continuum level at the frequency of interest. This value is needed to establish a proper flux reference, the continuum level value at the limb being too sensitive to the pointing. Our subsequent analysis was then performed in terms of line-to-continuum ratio.

The *D*-band receiver has two independent channels (A and B). The JCMT staff reported on 27 March 2009 that channel B had a persistent difference in flux with channel A after 20 January 2009, probably caused by the partial vignetting of channel B, that led to a loss of 40% of the flux. From our calibration observations, we established that this difference between the channels has remained constant (within a 5% error bar) over the entire observation period. So, both the disk-centred and the limb observations were affected by the same flux losses in channel B. This is why we chose not to reduce independently the data of the two channels before averaging them, the loss in the disk-centred observations being proportionally the same as the loss in the limb observations.

2.2. Data reduction

The data were processed with the Starlink software of the JCMT. Before combining the different observations, we accounted for the Earth-Saturn relative velocity in the individual spectra (from $-20\ \mathrm{km\,s^{-1}}$ in January 2009 to $3\ \mathrm{km\,s^{-1}}$ in March 2009).

After combining the observations, each limb was treated separately before applying the subtraction. The antenna temperature of the continuum at the eastern and western limbs and at the disk-centre are 15.2 K, 11.6 K, and 29.4 K, respectively. The limb values show that there is a small westwards pointing shift, because the difference between them cannot be caused by atmospheric temperature differences at the limbs. By comparing the observed continuum with theoretical computations of the continuum over the planetary disk, we estimate that the average pointing offset on the eastern and western limbs is ∼0.5″. The ratio of the average of the limb values to the disk-centre value is equivalent to the predicted value to within 4%. We rescaled each limb spectrum continuum to the average of the limb continuum values, i.e., 13.4 K, to account for small pointing errors. We then subtracted the western limb spectrum from the eastern limb one and removed a polynomial baseline of third order to obtain the final

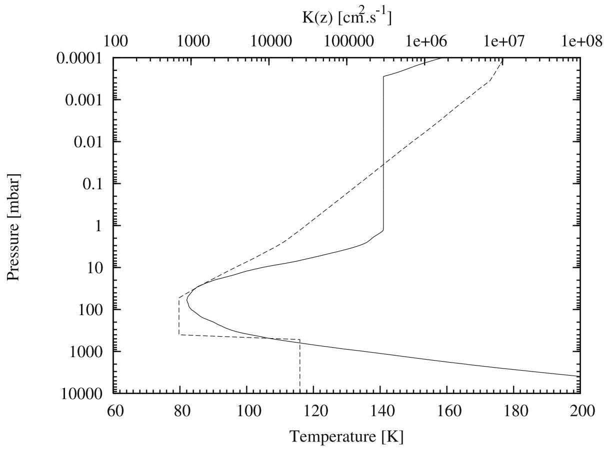

Fig. 2. Temperature (solid line) and eddy diffusion coefficient (dashed line) vertical profiles used in the computations. The $T(z)$ and $K(z)$ profiles come from Ollivier et al. (2000) and Moses et al. (2000a), respectively.

spectrum. Since the width of the line is ~17 MHz, we adopted a spectral resolution of 4 MHz to increase the signal-to-noise ratio (*S/N*) without lowering the quality of the lineshape.

We rescaled the continuum of the disk-centred observations to the continuum of our model. So, the final spectrum we present is expressed in terms of the brightness temperature difference between the western and eastern limbs $(\Delta T_{\mathrm{b}}(\nu))_{\mathrm{limbs}}$ and

$$(\Delta T_{\mathrm{b}}(\nu))_{\mathrm{limbs}} = (\Delta T^{*}_{\mathrm{a}}(\nu))_{\mathrm{limbs}} \times \left(\frac{T_{\mathrm{b}}}{T^{*}_{\mathrm{a}}}\right)_{\mathrm{disk-centre}} \tag{1}$$

where $(\Delta T^{*}_{\mathrm{a}}(\nu))_{\mathrm{limbs}}$ is the difference between the western and eastern limbs on the antenna temperature scale and $(T_{\mathrm{b}}/T^{*}_{\mathrm{a}})_{\mathrm{disk-centre}}$ is the ratio of the model brightness temperature to the observed antenna temperature in the continuum at the disk-centre.

3. Radiative transfer and atmospheric models

The model we used to perform our radiative transfer analysis was described in Cavalié et al. (2008a) and Cavalié et al. (2009). It is a 1D line-by-line model that accounts for the ellipticity of the planet. The limb emission is taken into account. Here, we chose, for simplicity, not to account for the absorption and emission of the rings, because the ring inclination was always lower than 3°.

We compared the synthetic spectra computed from our radiative transfer model with our observations. The shape of the synthetic spectra depends on the vertical profile of CO. The vertical profile that enabled us to retrieve the CO abundance at the levels that we probed were generated by the 1D time-dependent transport model of the atmosphere of Saturn of Cavalié et al. (2009). The parameters that we fixed prior to our analysis were the CO mixing ratio at the lower boundary q_{co}, the atmospheric thermal profile $T(z)$, and the eddy diffusion coefficient vertical profile $K(z)$. The value of q_{co} was set to be zero in every case, except in the internal-source-only model (see Sect. 4). The $T(z)$ profile was taken from Ollivier et al. (2000) and the $K(z)$ profile from Moses et al. (2000a). Both profiles are displayed in Fig. 2. The effect of the uncertainties on $T(z)$ and $K(z)$ will be discussed in Sects. 4 and 5.

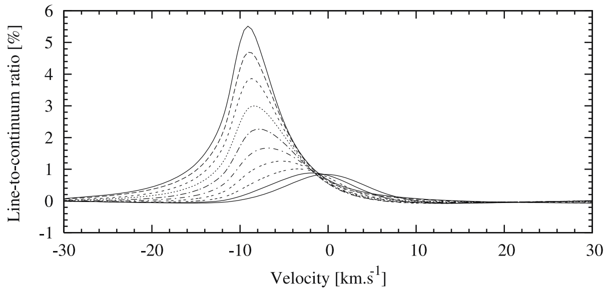

Fig. 3. Beam-integrated spectra, expressed in terms of line-to-continuum ratio, obtained for different lines of sight. The spectrum in solid line with a peak maximum at -9.2 km s^{-1} corresponds to an eastern limb line-of-sight. Other spectra correspond to increasing offsets towards the disk-centre in steps of 1″. The last spectrum (solid line with peak at 0 km s^{-1}) corresponds to a disk-centre line-of-sight. The situation is symmetric on the western side of the disk. This plot shows that the more the beam is pointed towards the disk-centre, the more the line amplitude decreases and the more the line position is shifted towards 0 km s^{-1}. To obtain lines centred around -8.7 km s^{-1} and $+7.7$ km s^{-1}, offsets of 2″ from the eastern limb line-of-sight position and of 5″ from the western limb line-of-sight position, respectively, would be needed.

We considered two types of external source models: a steady source model and a sporadic source model. We used the same formalism as Cavalié et al. (2009). In the case of the steady source model, we attempted to derive the disk-averaged CO external flux from the observations, while we tried to derive the impact time t_0 and the CO mixing ratio q_0 that would be deposited above 0.1 mbar by an SL9-like comet. The value of q_0 is also disk-averaged (see Cavalié et al. 2008b; and Cavalié et al. 2009, for further details of the modelling).

4. Results

The line was unambiguously detected independently on both limbs ($S/N > 5$ for each observing date). In the final spectrum, we obtain a peak-to-peak *S/N* of 25 at 4 MHz resolution. The eastern limb peak occurs at -8.7 km s^{-1} (close to the predicted velocity of -9.2 km s^{-1}), while the western limb peak is centred on $+7.7$ km s^{-1}. This result is not caused by the averaged pointing offset of ~0.5″. To obtain this velocity shift, the beam centre of the eastern observation would have to be shifted by 5″ towards the centre of the disk (see Fig. 3). This seems inconsistent because continuum values show that the pointing error is lower than 1″ on both limb observations. This shift could be caused by strong stratospheric winds. However, the prograde stratospheric thermal winds measured by Cassini/CIRS (Liming et al. 2008) are inconsistent with those inferred from our observations, possibly indicating that the forcing of the circulation in Saturn's atmosphere is not purely thermal. We need to include retrograde winds of ~450 m s^{-1} at the eastern limb and ~850 m s^{-1} at the western limb to reproduce the lines. Finally, the shift could also be partly caused by the subtraction process and the limitation in the *S/N* of the observations. We are presently unable to say unambiguously why this shift is observed. So, in our analysis, we fitted both limbs as if they were located at their predicted velocity.

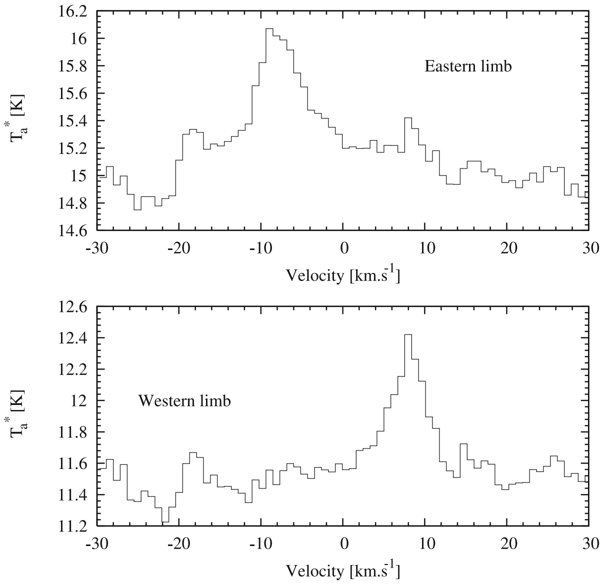

Fig. 4. Raw spectra at the eastern (*top*) and western (*bottom*) limbs of Saturn at the CO(6–5) frequency in terms of antenna temperature as a function of velocity.

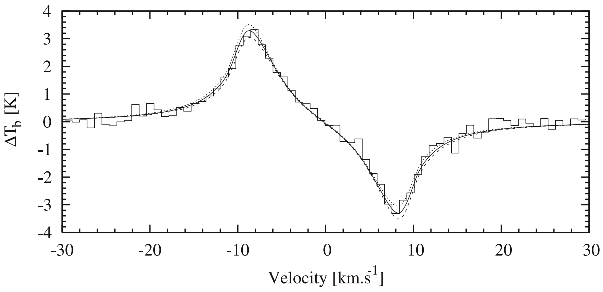

Fig. 5. Effects of a pointing error of −0.5″ (dashed line) and +0.5″ (dotted line) on the modelled spectrum. The solid line represents a comet-impact model with $(q_0, t_0) = (3.5 \times 10^{-6}, 220$ years). We note that the centre of the peaks is shifted only by $\sim\pm0.1$ km s^{-1} with these pointing shifts.

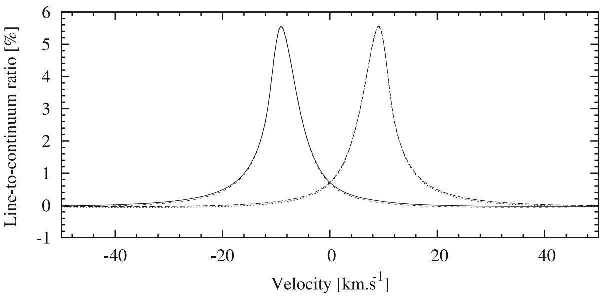

Fig. 6. Spectra of the CO(6–5) line for at the eastern and western limbs for two models, expressed in terms of line-to-continumm ratio. The spectra have been computed for a comet impact model (eastern limb in solid line and western limb in long-dashed line) and for the same comet impact model in which an internal source of CO with a deep mixing ratio of 10^{-9} has been added (eastern limb in short-dashed line and western limb in dotted line). These plots show that an internal source only changes the line-to-continuum ratio in a negligible way since the results for the different models are hardly distinguishable.

4.1. Uncertainty analysis

The main source of uncertainty in the CO abundance measurement comes from the pointing uncertainty of ∼0.5″. Depending on the pointing accuracy, the antenna temperature continuum level at the disk-centre varies slightly. The relative uncertainty in the observed brightness temperature contrast of the line $(\Delta T_\mathrm{b})_\mathrm{limbs}$ depends linearly on the relative uncertainty in the antenna temperature at the disk-centre $(T^*_\mathrm{a})_\mathrm{disk-centre}$ and on the uncertainty in the peak-to-peak line contrast $(\Delta T^*_\mathrm{a})_\mathrm{limbs}$. From Eq. (1), we derive

$$\frac{\sigma\left[(\Delta T_\mathrm{b})_\mathrm{limbs}\right]}{(\Delta T_\mathrm{b})_\mathrm{limbs}} = \frac{\sigma\left[(\Delta T^*_\mathrm{a})_\mathrm{limbs}\right]}{(\Delta T^*_\mathrm{a})_\mathrm{limbs}} + \frac{\sigma\left[(T^*_\mathrm{a})_\mathrm{disk-centre}\right]}{(T^*_\mathrm{a})_\mathrm{disk-centre}}. \quad (2)$$

The peak-to-peak *S/N* being 25, the value of the first term in the equation is 4%. From our repeated measurements, we find a relative uncertainty of 10.5% in the value of $(T^*_\mathrm{a})_\mathrm{disk-centre}$, leading to a total relative uncertainty in the brightness temperature line contrast of 15%.

This pointing uncertainty also causes some uncertainty in the modelling of the line. So, we checked how the modelled line strength is influenced by pointing errors of ±0.5″. We modelled the limb emission on both limbs with pointing shifts of ±0.5″ and applied the same subtraction procedure as applied to the data to obtain values that could be compared. In the end, a pointing error of 0.5″ in the modelling produces an uncertainty corresponding to 5% of the line contrast (see Fig. 5).

The subtraction process removes information contained in the far wings of the line and thus about the abundance of CO and/or the temperature at altitude levels lower than those probed by the emission core. However, we note that the first observations were performed for a 1 GHz band and that no wide feature could be observed from the individual limb observations.

We also checked whether neglecting the CO produced by a potential internal source (by modelling the CO distribution due to the external source only) would generate an error in the line-to-continuum ratio or not. We therefore computed the line for two kinds of models, the first being the comet impact model with no internal source, and the second the comet impact model with an internal source characterized by a mixing ratio of 10^{-9}, which corresponded to the upper limit derived by Cavalié et al. (2009) and the mixing ratio necessary to account for the 5 μm observations in the case of the internal origin model for CO of Noll & Larson (1991), to check whether the line-to-continuum ratio was changed. Figure 6 shows that the line-to-continuum ratio of each limb changes only negligibly.

The thermal profile of Saturn shows more variations as a function of latitude at low pressures than at higher pressures (Fletcher et al. 2007). Given the size of the antenna beam (7″), that we target the eastern and western limbs, and that the sub-Earth point latitude was always between −1° and −3°, we considered the variations in temperature between −30° and 30°: $\Delta T \sim 2$–3 K if $p > 35$ mbar, and $\Delta T \sim 5$ K if $p < 6$ mbar (Fletcher et al. 2007). An uncertainty of 5 K in the thermal profile seems therefore to be reasonable. By shifting the entire thermal profile by ±5 K, the relative uncertainty in the modelled line contrast is about 4%. If we shift only the upper part ($p < 1$ mbar) of the thermal profile by ±5 K, then the uncertainty in the modelled line contrast reaches 11%. This is still lower than the error bars related to our observing technique.

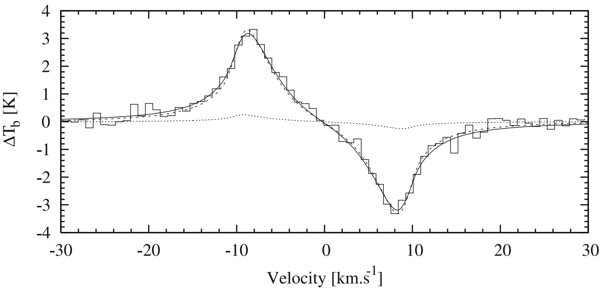

Fig. 7. Limb-switched spectrum of Saturn centred around Saturn's velocity compared to various models. From the observations, an external source is evident since an internal source of CO ($q_{co} = 10^{-9}$, uniform with altitude) results in the dotted line synthetic spectrum. A steady flux of CO of $\phi_{co} = 4.1 \times 10^6$ cm^{-2} s^{-1} results in the dashed line. An SL9-like comet impact model with the parameters $(q_0, t_0) = (3 \times 10^{-6}, 200$ years) is shown in solid line.

Another source of uncertainty in the derivation of model parameters is the $K(z)$ profile in the stratosphere. The $K(z)$ profile was set so as to produce abundance vertical profiles that result in the closest possible match with the observations of hydrocarbons (Moses et al. 2000a). However, the constraints placed on $K(z)$ by hydrocarbons strongly depend on the set of chemical constants that are used in the chemical scheme of the photochemical model. The retrieved $K(z)$ depends on the uncertainties in the chemical constants of the photochemical model as shown by Dobrijevic et al. (2003). The uncertainty in the $K(z)$ profile can reach an order of magnitude. In this work, we did not investigate the effect of this uncertainty. We will investigate the uncertainty in the $K(z)$ profile in a future paper, where we will also take all the photochemical processes into account.

4.2. Determination of external source parameters

First, we underline that the CO line is unambiguously produced by an external source of CO. Figure 7 compares the data with the synthetic line data computed from an internal source model in which the CO mixing ratio is 10^{-9} and uniform with altitude (upper limit derived by Cavalié et al. 2009; as well as mixing ratio necessary to account for the 5 μm observations in the case of the internal origin model for CO of Noll & Larson 1991). This model produces a line that is ~20 times fainter than that inferred from the observed line contrast. So, the contribution of an internal source is negligible in the spectrum. Hereafter, we will focus on models with an external source only and derive the parameters of these models (i.e., flux or comet mass and impact time).

For a steady flux of CO generated by either interplanetary dust particles or a local source, we derive a ϕ_{co} value of $(4.1 \pm 0.6) \times 10^6$ cm^{-2} s^{-1} (see spectrum in Fig. 7). When the CO originates from an SL9-like event, the CO line is mainly sensitive to two parameters, the volume mixing ratio q_0 deposited above the 0.1 mbar level and the time elapsed since the impact t_0. The values that provide the best fit to the CO(6–5) spectrum are $(q_0, t_0) = ([3.0 \pm 0.6] \times 10^{-6}, 200^{+50}_{-40}$ years).

5. Discussion

The central emission core of the CO(6–5) rotational line that we have observed is sensitive only to the stratospheric CO distribution (see Fig. 8). We have shown that an internal source only of

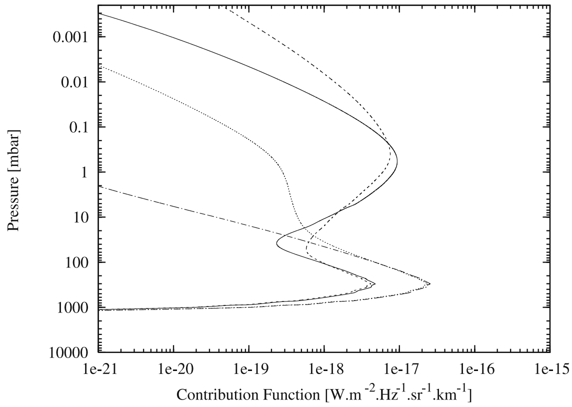

Fig. 8. Contribution functions (not integrated over the beam) of the central emission core of the CO(6–5) line as a function of pressure, computed for a limb line-of-sight (at the centre of the beam) and smoothed to a resolution of 4 MHz. The solid line corresponds to the SL9-like comet impact model ($q_0 = 3 \times 10^{-6}$, t_0 = 200 years), which reproduces the CO(6–5) observation. The dashed line correponds to the best-fit steady source model for the CO(6–5) observation (flux of 4.1×10^6 cm^{-2} s^{-1} CO molecules). For comparison, the contribution function for the internal source model ($q_{co} = 10^{-9}$) and a model without any CO are represented by the dotted and dashed-dotted lines, respectively.

CO ($q_{co} = 10^{-9}$) cannot account for the line contrast that we have observed. Therefore, we cannot place any additional constraint on the strength of the internal source of CO in the atmosphere of Saturn.

Prior to a discussion about the external source of CO in Saturn, we need to understand what the contribution functions tell us for the CO(6–5) line. Because we also used the results presented in Cavalié et al. (2009), we analysed the contribution functions of the CO(3–2) lines. The contribution functions corresponding to the central frequency of the CO(6–5) line at the planetary limb (beam central line-of-sight) are shown in Fig. 8. They show where the observed emission core is formed. We computed the contribution functions both for the internal and external source models and for a CO free atmosphere model (for comparison). The contribution functions of the CO(6–5) line clearly show that the emission line is formed at pressures of ~1 mbar. The second peak of these functions, which is centred between 100 and 1000 mbar, causes the continuum emission. Theoretically, the CO(3–2) line centre probes also up to the same region. The central emission seen in the external models of the line in Cavalié et al. (2009, see their Figs. 9 and 11) is formed in this region. However, because the S/N is low, it is not possible to constrain the CO abundance in this region as precisely as with the CO(6–5) line presented in this paper, whose S/N is much higher. Most of the central emission peak contrasts modelled for the CO(3–2) are smaller than the noise level. On the other hand, the CO(3–2) line shows a distinctive absorption feature in disk-centre geometry[1]. To show where the CO(3–2) absorption is formed, we have computed the contribution functions at 20 MHz from the line centre on a disk-centred line-of-sight for several models presented in Cavalié et al. (2009), from which we have subtracted the contribution function obtained from a CO free atmosphere model (see Fig. 9). This has enabled us to remove the

[1] The line forms in a region where the temperature is lower than the continuum temperature, leading to an absorption feature.

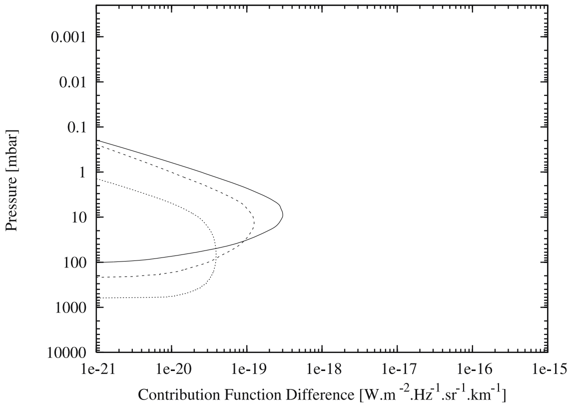

Fig. 9. The different lines plotted result from the subtraction of the contribution function obtained for a CO free atmosphere in the contribution functions obtained from several models for a disk-centred line-of-sight. We have plotted these functions at 20 MHz from the central frequency to focus on the observed absorption feature. Here, the curves corresponding to a comet impact ($q_0 = 3 \times 10^{-6}$, $t_0 = 250$ years) and to an external steady source of CO ($\phi_{co} = 1.5 \times 10^6$ cm^{-2} s^{-1}) are the solid and the dashed lines, respectively. The dotted curve refers to an internal source model ($q_{co} = 10^{-9}$). *Note:* The contribution functions used here have not been integrated over the beam but have been smoothed to the spectral resolution of the observation (16 MHz).

continuum contribution and thus focus on the CO contribution. We have chosen to plot the contribution functions at 20 MHz from the central frequency to avoid the central emission core. In Cavalié et al. (2009), the models that most successfully reproduce the line are a cometary model for which $q_0 = 3 \times 10^{-6}$ and $t_0 = 250$ years (solid line in Fig. 9) and a steady source model for which $\phi_{co} = 1.5 \times 10^6$ cm^{-2} s^{-1} (dashed line in Fig. 9). Finally, these contribution functions indicate where the observed absorption line originates: it is formed around 10 mbar. In the end, the CO(6–5) observation probes pressures centred around 1 mbar on the limb, while the 20 MHz wings of the CO(3–2) line at the disk-centre probe a layer centred around 10 mbar. So, using both observations enables us to retrieve vertical information about the CO distribution at two different pressure levels.

From the SL9-like comet impact model, an entire set of (q_0, t_0) couples, shown in Fig. 10, produces models that match the line. At the frequency of the CO(6–5) line, the higher q_0, the longer t_0 must be to provide a satisfactory fit to the data. In contrast, the lower q_0, the longer t_0 must be to match the CO(3–2) spectrum obtained by Cavalié et al. (2009). So, the possible values of t_0 as a function of q_0 exhibit different behaviour depending on the observed line (see Fig. 10). This result comes from the pressure levels that are probed by these lines being different, as mentioned previously. The abundance of CO decreases with time at the pressure levels probed by the CO(6–5) emission line, whereas it increases with time at the pressure levels probed by the CO(3–2) absorption line.

Figure 10 shows that the set of values for (q_0, t_0) that we derive for the CO(6–5) line overlaps with the set of values derived from the observations of the CO(3–2) line by Cavalié et al. (2009). This overlap is close to the location of our preferred values for (q_0, t_0), i.e., ([$3.5 \pm 0.5] \times 10^{-6}$, 220 ± 30 years). The corresponding CO mixing ratio vertical profile is shown in Fig. 11, and the resulting spectra at the CO(3–2) and CO(6–5) frequencies are shown in Fig. 12. This result confirms that a cometary origin for the CO present in the stratosphere of Saturn is possible. The mass of CO deposited by the comet would be $(2.1 \pm 0.4) \times 10^{15}$ g, corresponding to approximately 3 times the mass of SL9 (Moreno et al. 2003). Collisions of such comets with Saturn occur once every ~750 years, according to Zahnle et al. (2003).

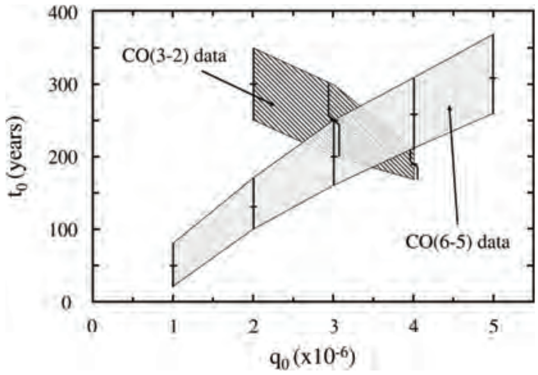

Fig. 10. Parameters q_0 and t_0 in the case of an SL9-like comet impact derived from the CO(6–5) observations (red dotted area, this work). The parameters retrieved by Cavalié et al. (2009) from CO(3–2) observations using the same modelling are also shown for cross-comparison (blue dashed area).

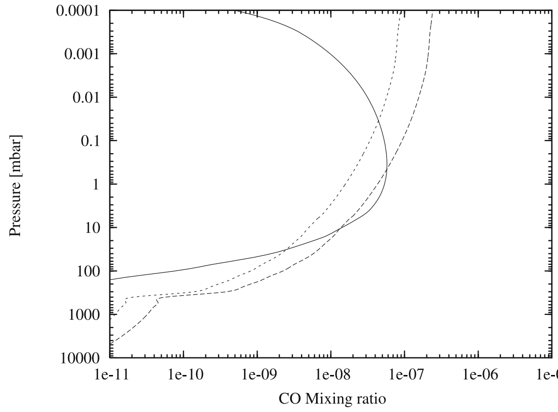

Fig. 11. CO mixing ratio vertical profiles of several external source models. The solid line corresponds to the profile obtained for a comet impact 220 years ago, with $q_0 = 3.5 \times 10^{-6}$. This model reproduces the CO(3–2) observations and the CO(6–5) observation as well. The long-dashed and short-dashed lines correspond to steady source models with $\phi_{co} = 4.1 \times 10^6$ cm^{-2} s^{-1} (CO(6–5) line best match) and $\phi_{co} = 1.5 \times 10^6$ cm^{-2} s^{-1} (CO(3–2) line closest match), respectively.

For a steady source of CO, a flux of $\phi_{co} = (4.1 \pm 0.6) \times 10^6$ cm^{-2} s^{-1} is required to fit the CO(6–5) line observations (vertical profile shown in Fig. 11). This value is inconsistent with the flux retrieved with the same model from the CO(3–2) observations, i.e., $\phi_{co} = (1.5 \pm 0.4) \times 10^6$ cm^{-2} s^{-1} (Cavalié et al. 2009). Figure 12 clearly shows that a flux of 4.1×10^6 cm^{-2} s^{-1} results in far too deep absorption at the CO(3–2) frequency and that a flux of 1.5×10^6 cm^{-2} s^{-1} underestimates the CO(6–5) emission. This inconsistency is caused by different layers being probed by the two observed lines, so that the fluxes needed to account for the observed CO at each layer are also different. So, using the assumed $K(z)$ eddy-diffusion coefficient vertical-profile ensures that a steady source seem less likely, compared to the comet impact model results.

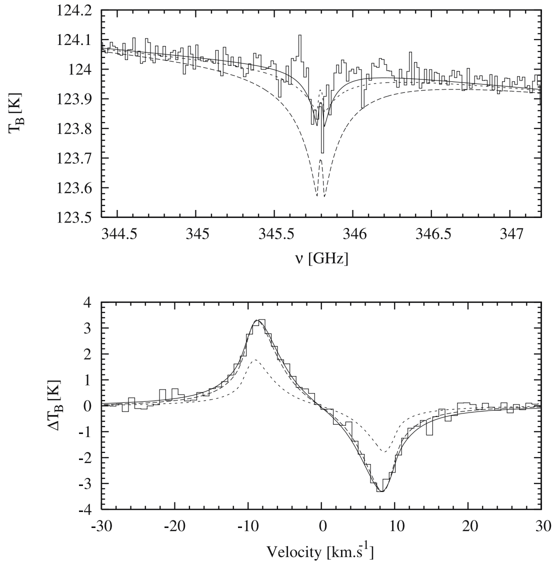

Fig. 12. Spectra of the CO(3–2) line (*top*) and the CO(6–5) line (*bottom*). The only model that fits both lines is the comet impact model in which $(q_0, t_0) = (3.5 \times 10^{-6}$, 220 years). It is plotted as a solid line. The external steady source model fails to reproduce both lines with the same flux. A flux of 1.5×10^6 cm^{-2} s^{-1} CO molecules would be needed at the CO(3–2) frequency (short-dashed line), whereas a flux of 4.1×10^6 cm^{-2} s^{-1} CO molecules would be needed at the CO(6–5) frequency (long-dashed line). *Note*: The layout for each model corresponds to that of Fig. 11, where the corresponding vertical profiles are shown.

6. Conclusion

We have obtained the first observation of the CO(6–5) line in the atmosphere of Saturn from "limb-switching" observations with the JCMT. We have analysed our data by applying a 1-D transport model coupled with a radiative transfer model and tested several hypothese for the possible origin of CO in the atmosphere of the planet.

The first outcome of this work is that an internal source of CO with $q_{\rm co} = 10^{-9}$, corresponding to the upper limit determined by Cavalié et al. (2009), cannot explain the observed emission features, thus confirming that there is an external source of CO in the stratosphere of Saturn. A steady flux of CO of $(4.1 \pm 0.6) \times 10^6$ cm^{-2} s^{-1} produces a synthetic line that matches the observations as well as a sporadic input of CO that would have been caused by the collision of a SL9-like comet ~200 years ago.

We have then compared our results with the results obtained by observing the CO(3–2) absorption line by Cavalié et al. (2009). Because these lines probe different pressure levels, we have been able to constrain the CO vertical profile more precisely than possible before. Our analysis now clearly favours a cometary origin for CO in the stratosphere of Saturn with model parameters $q_0 = (3.5 \pm 0.5) \times 10^{-6}$ and $t_0 = 220 \pm 30$ years, resulting in a deposition of $(2.1 \pm 0.4) \times 10^{15}$ g of CO. In contrast, the steady source model infers inconsistent values for the CO flux for the CO(3–2) and CO(6–5) observations.

However, we cannot firmly reject the possibility that CO originates (at least partially) in a steady source, because accounting for the photochemistry of H_2O would result in the production of CO (Moses et al. 2000b) and would thus modify the CO vertical profile and affect the flux values. It is unclear at which levels the CO is produced from H_2O, but the effects of CO production from H_2O photochemistry on the spectrum of Saturn at 345 GHz and 691 GHz should depend on the CO production rate vertical profile and on the $K(z)$ profile. Confirmation of this is beyond the scope of this present paper and is left to future analysis.

At the frequencies of H_2O and CO, observations of Saturn will be conducted by the HIFI instrument of the Herschel Space Observatory (Hartogh et al. 2009). These observations should produce very high *S/N* observations of H_2O and CO that will enable us to obtain their vertical profiles with unprecedented accuracy. Photochemical modelling of the oxygen compounds in the atmosphere of Saturn will thus gain precision and enable us to test the validity of the models presented in this paper.

Acknowledgements. T. Cavalié would like to thank the people at JCMT who helped in achieving this project: B. Warrington and J. Hoge for successfully operating the observations, T. Jenness and S. Hart for creating the customized 2-point jiggle mapping observation procedure, J. Dempsey, P. Friberg and K. Brown for re-commissioning the *D*-band receiver in the months prior to our run, and finally I. Coulson for supporting the project from the scheduling phase until the data reduction phase. We also thank the anonymous reviewer for constructive comments on the manuscript.

References

Bézard, B., Lellouch, E., Strobel, D., Maillard, J.-P., & Drossart, P. 2002, Icarus, 159, 95
Burgdorf, M., Orton, G., van Cleve, J., Meadows, V., & Houck, J. 2006, Icarus, 184, 634
Cavalié, T., Billebaud, F., Fouchet, T., et al. 2008a, A&A, 484, 555
Cavalié, T., Billebaud, F., Biver, N., et al. 2008b, Planet. Space Sci., 56, 1573
Cavalié, T., Billebaud, F., Dobrijevic, M., et al. 2009, Icarus, 203, 531
Coustenis, A., Salama, A., Lellouch, E., et al. 1998, A&A, 336, L85
Dobrijevic, M., Ollivier, J. L., Billebaud, F., Brillet, J., & Parisot, J. P. 2003, A&A, 398, 335
Encrenaz, T., Lellouch, E., Drossart, P., et al. 2004, A&A, 413, L5
Feuchtgruber, H., Lellouch, E., de Graauw, T., et al. 1997, Nature, 389, 159
Fletcher, L. N., Irwin, P. G. J., Teanby, N. A., et al. 2007, Icarus, 189, 457
Hartogh, P., Lellouch, E., Crovisier, J., et al. 2009, Planet. Space Sci., 57, 1596
Hesman, B. E., Davis, G. R., Matthews, H. E., & Orton, G. S. 2007, Icarus, 186, 342
Lellouch, E., Paubert, G., Moreno, R., et al. 1995, Nature, 373, 592
Lellouch, E., Bézard, B., Moreno, R., et al. 1997, Planet. Space Sci., 45, 1203
Lellouch, E., Bézard, B., Moses, J. I., et al. 2002, Icarus, 159, 112
Lellouch, E., Moreno, R., & Paubert, G. 2005, A&A, 430, L37
Liming, L., Gierasch, P. J., Achterberg, R. K., et al. 2008, Geophys. Res. Lett., 35, 23208
Moreno, R., Marten, A., Matthews, H. E., & Biraud, Y. 2003, Planet. Space Sci., 51, 591
Moses, J. I., Bézard, B., Lellouch, E., et al. 2000a, Icarus, 143, 244
Moses, J. I., Lellouch, E., Bézard, B., et al. 2000b, Icarus, 145, 166
Noll, K. S., & Larson, H. P. 1991, Icarus, 89, 168
Ollivier, J. L., Dobrijevic, M., & Parisot, J. P. 2000, Planet. Space Sci., 48, 699
Zahnle, K., Schenk, P., Levison, H., et al. 2003, Icarus, 163, 263

Appendix C

List of acronyms

Institutes, agencies, etc.

ASP	Atmosphères et Surfaces Planétaires
CENBG	Centre d'études Nucléaires de Bordeaux-Gradignan
CNES	Centre National d'Études Spatiales
CNRS	Centre National de la Recherche Scientifique
DFG	Deutsche Forschungsgemeinschaft (German Ministry of Research)
ESA	European Space Agency
IdEx	Initiative d'Excellence
IN2P3	Institut National de Physique Nuclaire et de Physique des Particules
ISM	Institut des Sciences Moléculaires
LAB	Laboratoire d'Astrophysique de Bordeaux
LAM	Laboratoire d'Astrophysique de Marseille
LESIA	Laboratoire d'Études Spatiales et d'Instrumentation en Astrophysique
LISA	Laboratoire Interuniversitaire des Systèmes Atmosphériques
LMD	Laboratoire de Météorologie Dynamique
LRGP	Laboratoire Réactions et Génie des Procédés
MPS	Max Planck Institute for Solar System Research
NASA	National Aeronautics and Space Administration
NRAO	National Radio Astronomy Observatory
SF2A	Société Française d'Astronomie et d'Astrophysique
SFP	Société Française de Physique
SwRI	Southwest Research Institute
UB	Université de Bordeaux
UM	Université de Montpellier

Observatories, missions, and instruments

ALMA	Atacama Large Millimeter/Submillimeter Array
CIRS	Composite Infrared Spectrometer
CRIRES	Cryogenic high-Resolution InfraRed Echelle Spectrograph
CSHELL	Cryogenic Echelle Spectrograph
HIFI	Heterodyne Instrument for the Far Infrared
INMS	Ion and Neutral Mass Spectrometer
IRAM-30m	30m telescope of the Institut de Radio Astronomie Millimtrique

IRTF	InfraRed Telescope Facility
ISO	Infrared Space Observatory
JCMT	James Clerk Maxwell Telescope
JUICE	Jupiter Icy Moons Explorer
JWST	James Web Space Telescope
MWR	Microwave Radiometer
NOEMA	NOrthern Extended Millimeter Array
PACS	Photodetector Array Camera and Spectrometer
SMA	SubMillimeter Array
SOFIA	Stratospheric Observatory For Infrared Astronomy
SPIRE	Spectral and Photometric Imaging Receiver
STIS	Space Telescope Imaging Spectrograph
SWAS	Submillimeter Wave Astronomy Satellite
SWI	Submillimetre Wave Instrument
TEXES	Texas Echelon Cross-Echelle Spectrograph
UVS	UltraViolet Spectrometer (Juno or JUICE)
VISIR	VLT Imager and Spectrometer for mid-InfraRed
VLT	Very Large Telescope

JUICE

3GM	Gravity & Geophysics of Jupiter and Galilean Moons
ACS	Autocorrelator Spectrometer
CCH	Continuum Channels
CTS	Chirp Transform Spectrometer
DPU	Digital Processing Unit
EM	Engineering Model
GALA	GAnymede Laser Altimeter
GCO	Ganymede Circular Orbit
GEO	Ganymede Elliptical Orbit
GOI	Ganymede Orbit Insertion
IDS	Interdisciplinary Scientist
JANUS	Jovis, Amorum ac Natorum Undique Scrutator (visible and near-infrared camera)
JOI	Jupiter Orbit Insertion
J-MAG	JUICE MAGnetometer
MAJIS	Moons And Jupiter Imaging Spectrometer
MAPPS	Mapping and Planning Payload Science
MOC	Mission Operation Center
OPT	SWI Observation Planning Tool
PEP	Particle Environment Package
PRIDE	Planetary Radio Interferometer & Doppler Experiment
PS	Project Scientist
RIME	Radar for Icy Moons Exploration
RPWI	Radio & Plasma Wave Investigation
SOC	Science Operation Center
SWI	Submillimetre Wave Instrument
SWT	Science Working Team
UVS	UltraViolet imaging Spectrograph
WG	Working Group

Others

A&A	Astronomy and Astrophysiqucs
CASA	Common Astronomy Software Applications
GCM	General Circulation Model
HssO	Herschel Solar System Observations
IDP	Interplanetary Dust Particles
LTE	Local Thermodynamical Equilibrium
QBO	Quasi-Biennal Oscillation
QPO	Quasi-Periodic Oscillation (also referred to as Semi-Annual Oscillation)
QQO	Quasi-Quadriennal Oscillation
SAO	Semi-Annual Oscillation (also referred to as Quasi-Periodic Oscillation)
SL9	Shoemaker-Levy 9 (comet D/1993 F2)
S/C	Spacecraft
S/N	Signal-to-noise ratio